Micro-computed Tomography for High Resolution Soft Tissue Imaging; Applications in the Normal and Failing Heart

Thesis submitted in accordance with the requirements of

The University of Liverpool

for the degree of

Doctor in Philosophy

by

Robert S Stephenson, BSc (Hons)

September 2013

DECLARATION

I declare that this thesis is the result of my own work and has not been submitted in any form for another degree or diploma at any university or other institution. Information derived from published or unpublished work of others has been acknowledged in the text and a list of references is given.

The research was carried out in the Department of Musculoskeletal Biology at The University of Liverpool

ACKNOWLEDGEMENTS

There are many people who have contributed towards my work whom I would like to thank.

Firstly, I would like to acknowledge my supervisor, Professor Jonathan Jarvis for his guidance and support in both practical and written aspects of my research over the last four years.

I thank Alder Hey Children's NHS foundation trust for their support, collaboration and generous funding by award of the Cardiac Surgery Research Award.

I would also like to thank members of Musculoskeletal Biology II, who have provided a supportive and encouraging working environment. I thank Dr Nathan Jeffery for providing me with training in the use of Micro-CT. I also thank my collaborators at the University of Manchester- Professor George Hart, Professor Mark Boyett, Dr Halina Dobryznski and Dr Theodora Nikolaidou, and Queen Mary's University London- Professor Alan Boyde, the research opportunities and academic insight they provided were invaluable.

I also thank Professor Bruce Smaill and Dr Jichao Zhao for the invitation to work in their lab at the University of Auckland. Without the skill, expertise and teachings of Dr Jichao Zhao the extraction of fibre orientation from my data would not of been possible. I also thank them for their continuing support and collaboration.

Lastly, I would like to acknowledge the continuing dedicated support of friends and family, especially my parents, and my partner Shauna.

ABSTRACT

The normal structure and function of the heart, the common pathological changes that cause abnormal function and the interventions proposed to improve or restore its function are fundamentally based on cardiac anatomy. Therefore in all these areas a detailed and accurate understanding of 3D structure is essential. However there is still disparity over some aspects of the form and function of the healthy heart. Furthermore, in heart failure (HF) the transition from compensated to decompensated HF is poorly understood, and details of ventricular, and particularly atrial, remodelling and their effects on cardiac function are yet to be fully elucidated. In addition little is known on how the 3D morphology of the cardiac conduction system is affected in disease, and further knowledge is required on the structural substrates for arrhythmogenesis associated with HF.

Here we have developed contrast enhanced micro-CT for soft tissue imaging, allowing non-invasive high resolution (~5 μm attainable) differentiation of multiple soft tissue types including; muscle, connective tissue and fat. Micro-CT was optimised for imaging of whole intact mammalian hearts and from these data we reveal novel morphological and anatomical detail in healthy hearts and in hearts after experimental HF (volume and pressure overload). Remodelling of the myocardium in HF was dramatic with significant hypertrophy and dilatation observed in both atria and ventricles. The atria showed a 67% increase in myocardial volume, with the left atrium showing a 93% increase. The pectinate muscle: wall thickness ratio was significantly increased in both atria ($p=<0.05$), and total cavity volume of the atria was increased by 119% ($p=<0.05$). An 84% ($p=<0.05$) and 28% ($p=<0.01$) increase in myocardial volume was seen in the right and left ventricles (RV and LV) respectively. The LV cavity increased to 231% of control ($p=<0.001$). Regional remodelling occurred in the LV with the base and mid-wall of the heart undergoing eccentric hypertrophy and the apex undergoing mixed hypertrophy. Longitudinal in vivo analysis by echocardiography revealed progressive loss of function pre termination (41% reduction in fractional shortening, $p=< 0.001$).

We have imaged the major regions of the cardiac conduction system (CCS) in single intact hearts and we present the data as high resolution 3D renderings. This is the first time that such data has been shown for any species. In HF all regions of the CCS

underwent dramatic morphological changes, with all regions undergoing hypertrophy and stretch. The sinoatrial node showed an 85% increase in volume ($p=0.08$) and 51% increase in surface area ($p=<0.05$). The atrioventricular node increased in both volume (52% $p=< 0.05$) and 3D length (14% $p=< 0.05$). The free running Purkinje fibre network showed an 85% increase in volume ($p=<0.05$); 3D filament analysis revealed the free running length was increased by 62% ($p=<0.05$), and was strongly correlated with the increase in LV cavity volume.

Applying a novel technique for the extraction of 3D fibre orientation from micro-CT data we showed that significant changes occur in HF. The technique was first validated in skeletal muscle and then applied to the heart. Fibre orientation in the ventricles was consistent with previous findings, and novel insight into the complex and heterogeneous fibre orientation of the atria and their accompanying muscle bands was obtained. In HF significant changes in fibre orientation were seen in regions of dilatation; in the LV fibres became more vertical at the endocardium and this coincided with a reduction in the transverse angle; in the transmural mid-wall of both the LV and interventricular septum the percentage of circumferential fibres was reduced, and fibres became more disordered. Based on changes in morphology and 3D fibre orientation we present the idea of regional specific compensated and decompensated HF in the presence of volume and pressure overload.

Data presented here provides new information on remodelling of the heart in HF, giving insight into the mechanisms underlying the contractile and electrical pathologies associated with HF.

LIST OF ABBREVIATIONS

ATP	Adenosine tri phosphate
AF	Atrial fibrillation
Ag target	Silver X-ray target
AVCA	Atrioventricular conduction axis
AVN	Atrioventricular node
BB	Bachmann's bundle
BSSEM	Back scattered scanning electron microscopy
Ca^{2+}	Calcium ions
CCS	Cardiac conduction system
CN	Compact node
CS	Coronary sinus
Cx	Connexin
Cu target	Copper X-ray target
CT	Crista terminalis
DT-MRI	Diffusion tensor magnetic resonance imaging
EF	Ejection fraction
FO	Fossa ovalis
FS	Fractional shortening
HF	Heart failure
HCN4	Hyperpolarization activated cyclic nucleotide-gated potassium channel 4
IAS	Interatrial septum
*I*ca	Inward Ca^{2+} current
I_2KI	Iodine crystals (I_2), potassium iodide (KI), added to 10% PBFS
INE	Inferior nodal extension
IVC or ICV	Inferior vena cava
IVS	Interventricular septum

LAA	Left atrial appendage
LBB, RBB	Left and right bundle branches
LSARB, RSARB	Left and right sinoatrial ring bundles
LV	Left ventricle
LVFW	Left ventricular free wall
LVPW	Left ventricular posterior wall
Micro-CT	Micro-computed tomography
Mo target	Molybdenum target
NF-M	Neurofilament middle
Na^+	Sodium ions
PA	Pulmonary artery
PcMs	Pectinate muscles
PV	Pulmonary vein
PBFS	Phosphate buffered formal saline
PMMA	Polymethylmethacrylate
RA	Right atrium
RAA	Right atrial appendage
ROI	Region of interest
RV	Right ventricle
RVOT	Right ventricular outflow tract
SAN	Sinoatrial node
SR	Sarcoplasmic reticulum
SS	Septum spurium
SVC or SCV	Superior vena cava
SV	Stroke Volume
K^+	Potassium ions
TCE micro-CT	Targeted contrast enhanced micro-CT
W target	Tungsten target

LIST OF FIGURES

Chapter 1 Pages 1-57

Chapter 8 Pages 232-295

LIST OF TABLES

Chapter 8 Pages 232-295

APPENDICES Page 316-

Fibre orientation analysis

Published papers appended:

Stephenson RS, Boyett MR, Hart G, et al. (2012) Contrast Enhanced Micro-Computed Tomography Resolves the 3-Dimensional Morphology of the Cardiac Conduction System in Mammalian Hearts. *PLoS ONE*, **7,** e35299.

Jeffery NS, **Stephenson RS**, Gallagher JA, Jarvis JC, Cox PG (2011) Micro-computed tomography with iodine staining resolves the arrangement of muscle fibres. *Journal of Biomechanics*, **44,** 189-192.

Jarvis J, **Stephenson RS.** (2013) Studying the microanatomy of the heart in 3 dimensions: a practical update. *Frontiers in Paediatric Cardiology*, doi: 10.3389/fped.2013.00026.

Zhao J, **Stephenson RS**, Sands GB, et al. (2013) Atrial Fibrosis and Atrial Fibrillation: A Computer Simulation in the Posterior Left Atrium. *FIMH,* 400–408.

Aslanidi O, Nikolaidou T, Zhao J, Smaill BH, Gilbert SH, Holden AV, Lowe T, Withers PJ, **Stephenson RS**, et al. (2012) Application of Micro-Computed Tomography with Iodine Staining to Cardiac Imaging, Segmentation and Computational Model Development. Medical Imaging, IEEE Transactions on, 32(1):8-17.

CHAPTER 1

Introduction

1.1 Motivation for the project

Heart failure (HF) is a clinical syndrome which is characterised by the inability of the heart to pump sufficient blood to meet the metabolic needs of the body (McDonagh et al., 2011, Leonard et al., 2012). Despite recent advances in our treatment of HF, the condition has a considerable morbidity, affecting over 900,000 people in the UK (NHS, 2012), and has a mortality rate of 5 years (annual mortality rate 10-50%), which rivals most cancers (Stewart et al., 2001). In the western world, HF affects 1-2% of the population (Brown and Cleland, 1998), contributing to 5% of all hospital admissions, and complicating ~15% of all admissions (Khand et al., 2000). The overall prevalence of clinically evident HF is around 5–20 cases/1,000 population, however this figure rises to >100 cases/1,000 population in subjects aged >65 years (Heart Failure Society of America, 2006). The number of patients with heart failure is ever increasing (McDonagh et al., 2011). This is due to our ageing population and improved survival rates in patients.

Cardiac arrhythmias are a common complication associated with HF, the most common being atrial fibrillation (AF). The prevalence of AF approximately doubles with each advancing decade of age, from 0.5% at age 50–59 years to almost 9% at age 80–89 years (National Collaborating Centre for Chronic Conditions, 2006). Radiofrequency catheter ablation is widely considered to be best practice, especially for patients resistant to pharmacological and electrical cardioversion (Brooks et al., 2010). However, success rates are relatively poor; single procedure freedom from atrial arrhythmia at long-term follow-up is ~53%, ~54% in paroxysmal AF (Ganesan et al., 2013), and~28% for persistent AF even with one “optimally” combined ablation procedure (Brooks et al., 2010). Multiple procedures do improve these figures but treatment of arrhythmias is an increasing economic burden in health care; it costs ~£12,500 per catheter ablation procedure in Europe.

The normal structure and function of the heart, the common pathological changes that cause abnormal function and the interventions proposed to improve or restore its function are fundamentally based on structure. Therefore in all these areas a detailed and accurate understanding of 3D cardiac anatomy is essential. However there is still disparity over the form and function of mural architecture in the healthy heart (Anderson et al., 2008, Buckberg et al., 2008, Jouk et al., 2000, LeGrice et al., 1995,

Lunkenheimer et al., 2006a, Schmid et al., 2007, Torrent-Guasp et al., 2005). Furthermore, in HF the transition from compensated to decompensated HF is poorly understood, and details of ventricular, and particularly atrial, remodelling and their effects on cardiac function are yet to be elucidated. In addition little is known on how the 3D morphology of the cardiac conduction system is affected in disease, and further knowledge is required on the structural substrates for arrhythmogenesis associated with HF.

Therefore, further insight into the detailed morphology and structure of the heart in health and disease will; a) aid our understanding of the aetiology of HF and its associated mechanical and electrical dysfunction; b) provide information on fibre orientation within heart, thus improving knowledge of cardiac contraction and pathways of conduction; c) inform the development of 'virtual hearts'- anatomically and biophysically-detailed mathematical models of the heart for education, research, planning surgical treatments and drug discovery; d) inform cardiac ablation procedures; and e) guide the planning of implantation and reconstructive surgeries to avoid damage to structures integral to the form and function of the heart, thus reducing the need for pacemakers.

A true grasp of this information is essential for targeted clinical and scientific research, which ultimately could contribute to the creation and improvement of therapeutic approaches.

1.2 The heart structure and function

In this section the gross anatomy of the heart is described in the context of its primary function. In Chapter 5 the detailed 3D anatomy of the heart including its fibre orientation is investigated using contrast enhanced micro-CT.

1.2.1 Gross anatomy and function of the heart

The heart is a muscular pump composed of myocardium (cardiac muscle) which functions to; (1) collect de-oxygenated blood from the tissues of the body and pump it to the lungs to be oxygenated; and (2) collect the oxygenated blood from the lungs and pump it to all the tissues of the body. The mammalian heart is made up of four

chambers; two upper chambers (atria) and two lower chambers (ventricles). The upper chambers are divided from one another by a wall of myocardium known as the interatrial septum (IAS). A similar structure divides the lower chambers and is known as the interventricular septum (IVS). The fibrous skeleton of the heart; a non-myocardial structure made of connective tissue, acts to divide the upper and lower chambers (see below). Functionally the heart can be split into the left and right sides; the right atrium and ventricle collect blood from the body and pump it to the lungs, while the left atrium and ventricle collect blood from the lungs and distribute it to the body. The movement of blood through the heart is a 'one-way' flow, this is achieved and maintained by valves; the two atrioventricular valves (tricuspid and bicuspid) and the semilunar valves of the outflow tracts (pulmonary and aortic) (figure 1.1) (Iaizzo et al., 2009). The right and left heart pumps function in series, but contract simultaneously (Loushin et al., 2009).

In life the heart lies in the thorax, protected by the overlying sternum and costal cartilages. The heart lies between the lungs in the middle mediastinum covered by a serous membrane- the pericardium, and its inferior border sits on the superior surface of the diaphragm (Levick, 2003, Drake et al., 2005)

.

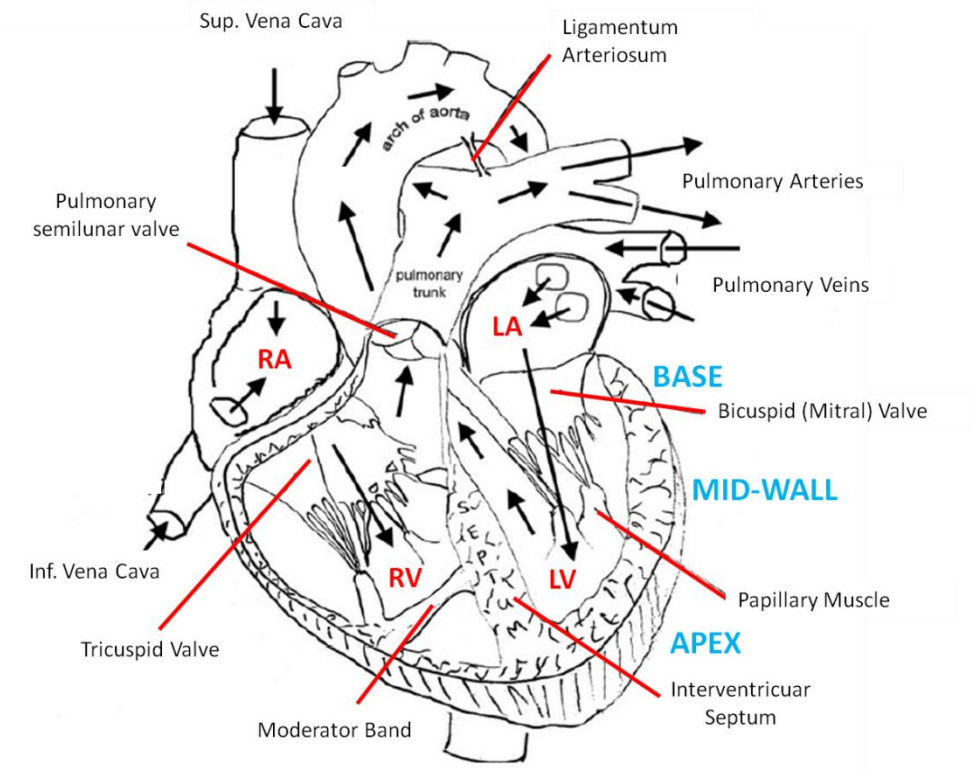

Figure 1.1 Schematic representation of a longitudinally sectioned heart. Showing the major anatomical landmarks, the 4 chambers (labelled red), and the regions of the ventricle (labelled blue). Blood flow through the heart is represented by arrows. LA- left atrium, LV- left ventricle, RA- right atrium, RV- right ventricle. (Modified from Iaizzo 2009)

1.2.2 The right atrium

There are anatomical features characteristic of both atria; each has an appendage, venous component, a vestibule, and the interatrial septum (IAS) separating them. The appendages are pouch-like extensions of the atria, and are characterised by the presence of pectinate muscles (PcMs) on their endocardial surface - numerous bands of muscle which run parallel with one another (figure 1.2). The right atrium (RA) is dominated by its appendage, this in contrast to the common belief that only the tip of the atrium constitutes the appendage. The appendage actually forms the majority of the free wall, since the PcMs characterising the appendage, are associated with the tricuspid valve vestibule throughout its course around the free wall. An immediate transition from the trabeculation of the PcMs to the smooth walled venous component occurs in the posterior right atrium (figure 1,2). This transition is

demarcated on the endocardium by the crista terminalis (CT) or terminal crest; a thick band of muscle running lateral to the opening of the superior vena cava (SVC or SCV figure 1.2), obliquely down, like a twisted 'C', to the opening of the inferior vena cava (IVC or ICV figure 1.2). Close to its origin the CT is joined by another thick muscle bundle - the septum spurium (SS), which extends anterolaterally into the appendage (Ho et al., 2002, Iaizzo et al., 2009). Both the CT and SS provide the origin for the PcMs.

The venous component houses the majority of the named structures of the right atrium. The SVC and IVC open to the top and bottom of this region respectively. The coronary sinus (CS) also opens into the region, inferior and lateral to the IVC. The Thebesian and Eustachian valves occupy the CS and IVS respectively (figure 1.2), in human these structures vary from large to almost absent, and from membranous to muscular-like. Anteriorly the two valves come together to form the fibrous tendon of Todaro which eventually inserts into the membranous septum. The distal ramification of the CT with the coronary sinus is often referred to as the 'flutter isthmus', because of its arrhythmogenic properties. Medial to the CS and IVC openings is the fossa ovalis (FO) (figure 1.2), a remnant of the foramen ovale (crucial in embryonic circulation). It appears as a depression, occupied by the flap valve of the IAS, it is surrounded by extensive muscular rims, and is the major constituent of the IAS (Ho et al., 2002, Iaizzo et al., 2009).

Internal features of the RA provide the landmarks for the triangle of Koch, which serves as a surgical guide for locating conducting tissues involved in atrioventricular conduction (Ho et al., 2002). In human, attitudinally, the Eustachian ridge containing the tendon of Todaro forms the posterior border, and the hinge point of the tricuspid valve leaflet forms the anterior border (Inoue and Becker, 1998). At the base of triangle is the CS, and the apex is formed at the point where the anterior and posterior borders meet (Figure 1.2).

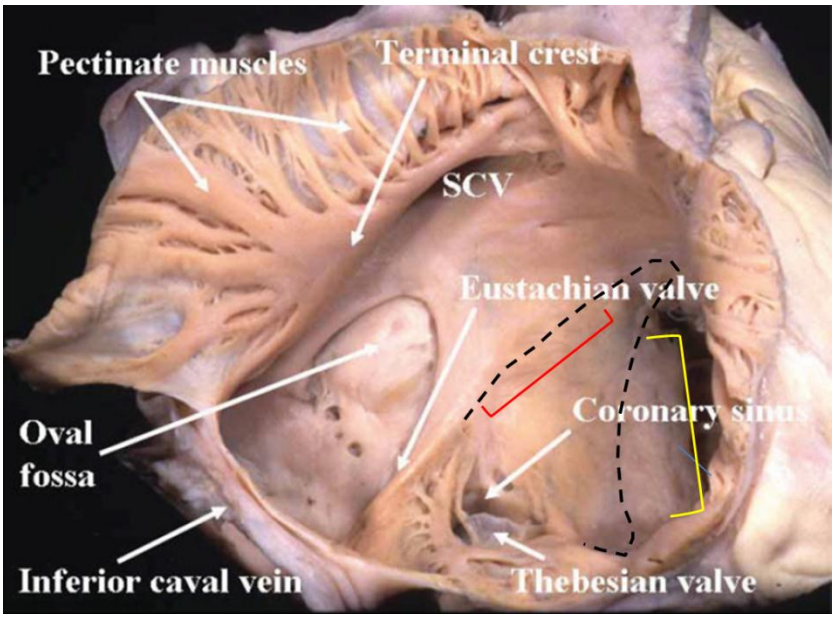

Figure 1.2 Prosection showing the internal anatomy of the right atrial cavity in human. The free wall of the right atrium is reflected, red bracket represents the tendon of Todaro, yellow bracket represents the tricuspid valve., black dotted line indicates the boudaries of the triangle of Koch. SCV- superior vena cava. (Modified from Anderson 2007)

1.2.3 The right ventricle

The ventricles are characterised by possessing an inlet, apical trabeculae and outlet components, but are incomplete when lacking an inlet, outlet or both (Anderson et al., 2011). The right ventricle (RV) receives blood from the RA and pumps it to the lungs via the outflow tract to the pulmonary trunk. The outflow tract or infundibulum, which carries the blood in a anterosuperior fashion out of the RV is smooth walled. In contrast, the majority of the endocardial surface is characterised by a complex arrangement of coarse muscle bundles called trabeculae carnae. These trabeculae are found in both ventricles and are analogous to the PcMs of the atria, the most prominent in the RV is the moderator band (figure 1.1). When the RV contracts (systole) blood is prevented from flowing back into the RA by closure of the tricuspid valve. The pressure increase within the RV opens the pulmonary valve and allows blood to leave the heart via the pulmonary artery (PA) (figure 1.1). The function of valves is reversed in diastole, with the tricuspid valve open and the pulmonary valve closed (Iaizzo et al., 2009).

1.2.4 The left atrium

Like the RA, the LA has an appendage, venous component, vestibule, and IAS. The LA lacks a structure analogous to the CT, therefore there is no obvious demarcation between the appendage and the pulmonary venous component. The free wall and PcMs of the LA are thicker and more pronounced than in the RA, but the PcMs can still be seen associated with the vestibule of the bicuspid (mitral) valve throughout its course around the free wall (Ho et al., 2012). Posteriorly the venous component is void of PcMs and is dominated by the pulmonary veins (PVs). In human there are usually four PVs, but variation in their number is common in human and animals (figure 1.1) (Ho et al., 1999). The detailed morphology of the atria are considered in detail in Chapter 5, and changes in the failing heart are assessed in Chapter 8.

1.2.5 The left ventricle

Blood passes from the RA into the left ventricle (LV), where it is pumped from the ventricular cavity through the aorta to supply the tissues of the body. The wall of the LV is trabeculated but is much thicker than the RV and can thus produce a greater contractile force. The IVS appears continuous with the curvature of the LV and as a result bulges into the RV cavity, giving the RV its distinctive crescent shape and the LV its cone-like appearance. When the LV contracts, closure of the mitral valve prevents backflow into the LA, and the aortic valve opens to allow blood to leave the heart and enter the systemic circulation. The function of the valves is reversed in diastole, with the mitral valve open and the aortic valve closed. Like the pulmonary valve the aortic valve consists of three semilunar shaped cusps. During diastole, due to the increased pressure in the aorta, these cusps are occluded and act as upside down parachutes with their respective sinuses filling with blood residing in the aorta. Within two of the sinuses are ostia (openings) into the coronary arteries that supply the myocardium. Due to the great pressure difference blood flows through these vessels during diastole (Anderson et al., 2011, Iaizzo et al., 2009).

1.2.6 The fibrous skeleton

Passing through the transverse plane at the base of the heart is a dense framework of connective tissue known as the fibrous skeleton. The functions of this static scaffold are (1) anchor the valves of the heart, preventing overstretching of the valve

apparatus, and (2) electrically insulate the atria from the myocardium, preventing direct spread of the propagation wave to the ventricles from the atria. The fibrous skeleton is made up of four interconnecting rings, with two trigones and an inferior projection . The central ring supports the aortic valve, while the anterior ring supports the pulmonary valve. The two larger posterior rings support the bicuspid and mitral valves respectively. The strongest part of the skeleton is the central fibrous body or the right fibrous trigone, this triangle is formed at the junction between the aortic valve and the medial aspects of the atrioventricular valves. The central fibrous body is associated with the specialised atrioventricular conducting tissue (see below). The left fibrous trigone is smaller and lies at the junction of the aortic valve and the anterior cusp of the mitral valve. The inferior projection of the skeleton is called the membranous interventricular septum, a continuation of the central fibrous body forming an attachment with the muscular interventricular septum below. Medially the membranous septum provides attachment for the right coronary cusp of the aortic valve, and superiorly is continuous with the interatrial membranous septum (Iaizzo et al., 2009, Anderson et al., 1991). The true extent of the fibrous skeleton has been debated due to the difficulty in appreciating its 3D morphology using dissection or histology (as described by Anderson et al., 1991).

1.2.7 The myocardial wall

Transmurally the myocardial walls are made up of a number of layers. Superficially the heart is covered by the pericardium; its outermost layer is the dense and fibrous parietal pericardium, while the visceral layer of the pericardium adheres to the surface of the myocardium (epicardium) (figure 1.3). The pericardial cavity between these two layers is filled with serous fluid (secreted from mesothelial cells) allowing the visceral layer to smoothly glide over the outer parietal pericardium during cardiac contraction. The middle myocardium forms the muscular component of the wall, and itself is subdivided into the subepicardium, transmural mid-wall and subendocardium. However, the epicardium and subepicardium are sometimes collectively referred to as the epicardium, and the same can be said of the endocardium. Finally the endocardial surface is formed by a connective tissue and endothelial layer (figure 1.3) (Iaizzo et al., 2009).

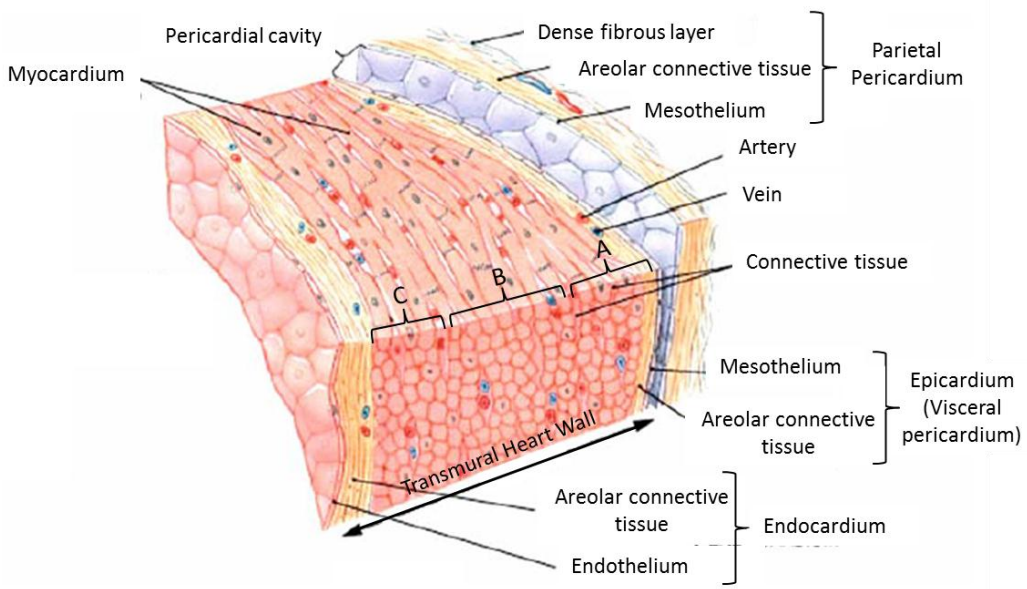

Figure 1.3 Schematic representation of a transmural ventricular segment and its association with the pericardium. a-subepicardium, b-transmural mid-wall, c-subendocardium. (Modified from Iaizzo 2009) Note: The orientation of the fibres making up the myocardium is not as simple as this figure suggests. The 3D arrangement of muscle fibres within the whole heart is explored in Chapter 5,7,8.

1.2.8 The Myocyte

The coordinated contraction is the basis of the hearts function; such contractions are produced by the muscle cells of the heart- the cardiac myocytes. Unlike other types of muscle cells, myocytes are branched and join together with neighbouring myocytes at complex junctions called intercalated discs. This arrangement creates the so-called functional syncytium of the heart. Unlike skeletal muscle, myocytes are not typically referred to as fibres, rather the term fibre refers to a row of multiple adjoining myocytes. The diameter of the roughly cylindrical myocyte can range from 10-20µm, and lengths vary from 50-100µm (Barnett and Iaizzo, 2009, Levick, 2003). Although myocytes contain the organelles common to all muscle cells, their internal volume is predominantly made up of a cytoskeletal lattice of contractile proteins. This gives the cells a characteristic striated appearance when viewed under a microscope (Barnett and Iaizzo, 2009, Levick, 2003).

Intercalated discs contain adheren junctions that hold the cells together mechanically. These membrane bound proteins form structural associations between adjoining myocytes, and can be composed of various proteins (Colaco and Evans, 1981, Kaplan et al., 2004). Most crucially they allow force to be transmitted across the myocardium. At the intercalated discs gap junctions form electrical communications between cells (Beauchamp et al., 2006), allowing the synchronised flow of ions, and thus the transmission of electrical propagation that stimulates myocyte contraction. Gap junctions are usually formed by the assembly of 6 proteins called connexins (Cx), which collectively form a hemi-channel called a connexon. These channels are found on the sarcolemma of the myocyte and form complete gap junctions when they dock with the connexon of a neighbouring myocyte.

The sarcolemma is also penetrated by membrane lined channels called transverse tubules (T-tubules). These channels are filled with extracellular fluid and invaginate into the sarcoplasm and run around the myofibrils. T-tubules form a diad with the organelle specialised to store and release calcium for cardiac contraction, the sarcoplasmic reticulum. This close association allows rapid transmission of the electrical impulse inside the cell and helps couple action potentials with the release of internal calcium stores and thus myocyte contraction (see below) (Bers, 2002, Levick, 2003).

The arrangement of the contractile proteins within a myocyte is similar to that found in skeletal muscle, the contractile subunits are called myofibrils, and each myofibril is made up of multiple sarcomeres, the smallest functional unit of muscle (figure 1.4). The myofibrils are mainly composed of the proteins actin and myosin. Primarily these form thin (actin) and thick (myosin) filaments, which overlap to some extent when the muscle is at rest. These filaments repeat along the length of the myofibril in sections known as sarcomeres. Although there has been some suggestion of long term cell turnover in cardiac muscle (Bergmann 2009), the nuclei of mammalian myofibres are entirely postmitotic and cannot replace themselves (Charge and Rudnicki, 2004, Ahunja 2007). However in certain conditions, for example increased load, the myocytes can increase cross sectional area and lay down more sarcomeres, a process called hypertrophy (Leonard 2012-Drazner 2012). In addition when myocytes are under abnormal tension they stretch, increasing their length (Gaasch

2011, Opie 2006, Leonard (Smaill) 2012-Ryan 2007). Both these responses are discussed in the setting of the failing heart below (section 1.4).

Muscles contract by ATP-driven conformational changes in the myosin head, often referred to as the sliding filament mechanism. The sarcomere consists of central bidirectional thick filaments (myosin) flanked by six actin filaments, orientated in opposite directions (figure 1.4). Each actin subunit has multiple binding sites for the myosin head, which act as an actin-based molecular motor to convert chemical energy released from the hydrolysis of adenosine tri phosphate (ATP) into mechanical force (Barnett and Iaizzo, 2009). In diastole myosin ATPase binds ATP hydrolysing it and producing ADP and energy. However due to the inhibitory effects of tropomyosin-troponin complexes on actin filaments, the energy formed cannot be used, but is stored. During systole calcium floods into the sarcoplasm via numerous channel proteins (Bers, 2002), and the calcium binds to the troponin C present on the actin filaments (Gillis et al., 2007). The troponin then allosterically modulates the tropomyosin. Under normal circumstances, the tropomyosin obstructs the binding sites for myosin on the actin filament, but once calcium binds to the troponin C this causes an allosteric change in the troponin protein, unblocking the binding sites (Gillis et al., 2007).This allows the myosin head to bind to actin and form a crossbridge. Force and movement are generated by a change in angle of the myosin head facilitated by the stored energy. This advances the filament 5-10nm, the myosin head then disengages and this process repeats itself at a new actin site further along the filament. This process occurs at numerous myosin heads along the filament. The myosin and actin filaments therefore slide over one another, bringing the z-discs towards each other, shortening the I-band, H zone and overall sarcomere (A Band) length (figure 1.4). Therefore contractile performance is strongly linked to intracellular calcium concentration, and this depicted by the force-calcium relationship (Barnett and Iaizzo, 2009).

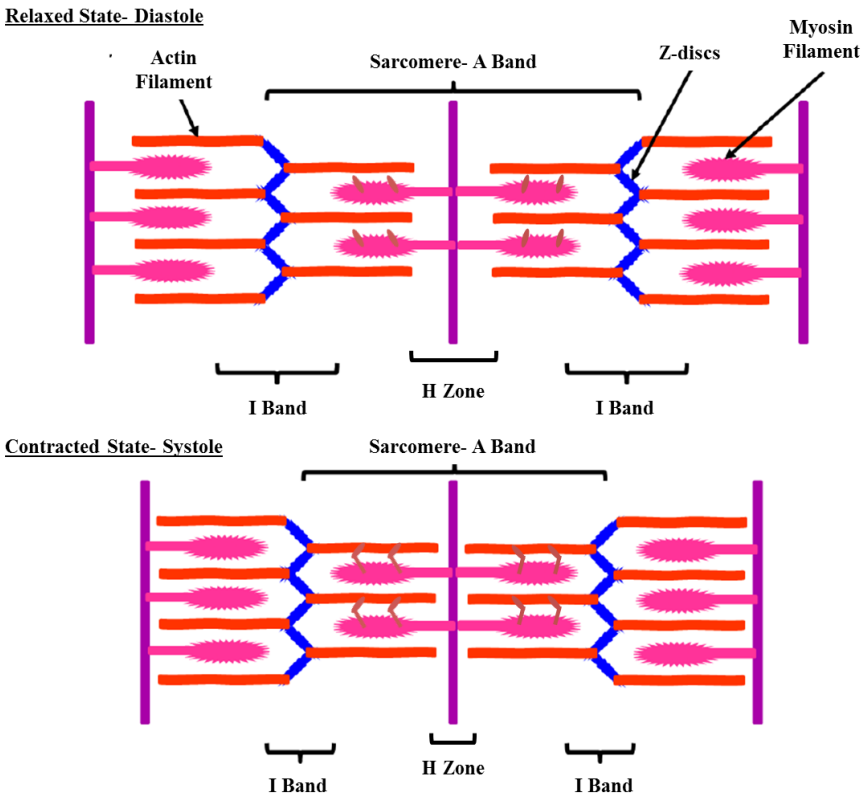

Figure 1.4 Diagrammatic representation of a sarcomere and the sliding filament Theory. Showing the sarcomeres conformational change from diastole (upper panel) to systole (lower panel). (Modified with the permission of Dr Andrew Fisher)

1.2.9 Fibre orientation

The arrangement of muscle fibres within the heart is much more complex than that observed in most skeletal muscles. Unlike the single cell fibres found in skeletal muscle, the cardiac mass is made up of short (50-100μm) axially coupled myocytes forming continuous 'fibres' which are embedded in a fibrous tissue matrix. In the heart, myocytes are often seen to branch at their extremities and give off lateral off shoots forming multiple connections with adjacent cells (Costa et al., 1999, LeGrice et al., 1995). The result is a detailed mesh of branching and anatomosing cells (Anderson et al., 2006). Any future reference to 'fibres' in the heart refers to these axially coupled aggregations of myocytes. The detailed study of Pettigrew (Pettigrew, 1864) showed that the long axis angulation of the myocytes changes across the ventricular wall relative to the equator (figure 1.5A). This so-called helical

arrangement came to prominence due to the histological investigations of Streeter (Streeter and Bassett, 1966, Streeter et al., 1969). The fibre angle rotates clockwise from ~-80° at the epicardium to ~+80° at the endocardium, with the mid-wall consisting of fibres primarily running circumferentially (Greenbaum et al., 1981, Streeter et al., 1969) (figure 1.5A). Globally a left-handed helical pattern is formed in epicardial regions of the left ventricle, and a reciprocal right-handed helical pattern dominates the endocardium (Nielsen et al., 2009, Smerup et al., 2009) (figure 1.5A). This helical fibre orientation is preserved in many different species (Costa et al., 1999, Geerts et al., 2002, Greenbaum et al., 1981, Streeter and Bassett, 1966). However, the progressive depth-related change in helical angle does vary in different regions of the heart (Costa et al., 1999, Dorri et al., 2007, Schmid et al., 2007, Streeter et al., 1969). The 3D morphology of the helical arrangement cannot be fully appreciated using histology (Greenbaum et al., 1981, Streeter et al., 1969) or peeling (Dorri et al., 2007). But such studies have shown fibre orientation must be described in terms of both inclination (helical) and transverse (intrusion) angle (figure 1.5B), and should be considered as a anisotropic mesh of fibres which functions with the connective tissue network (Lunkenheimer et al., 2006b). This 3D arrangement of fibres has since been validated using diffusion tensor magnetic resonance imaging (DT-MRI- described below), albeit with poor spatial resolution (Nielsen et al., 2009, Rohmer et al., 2007, Helm et al., 2005a).

The transverse angle was first described by Frank 1901 (Schmid et al., 2007). These fibres can be described as intruding, as their transverse angle represents the degree to which the fibre intrudes in a epicardial to endocardial direction (figure 1.5B). Many studies of cardiac contraction ignore such fibres, although their existence is well accepted (Geerts et al., 2002, Lunkenheimer et al., 2006a). Transverse angled fibres have been shown to have angles as great as 40° (Lunkenheimer et al., 2006a), with other studies suggesting up to 12% of their population exceed 45° (Schmid et al., 2007). These fibres are thought to play important roles in; (1) effective torsional movements (see below) and force generation in both systole and diastole (Adhyapak and Parachuri, 2009, Lunkenheimer et al., 2004), (2) cyclic rearrangement of myoctes in three dimensions (3D) in diastole, (3) shape stabilization, (4) ventricular thickening (Anderson et al., 2006, Lunkenheimer et al., 2006a), (5) and antagonism

of constrictive forces, although previously refuted, has recently been revisited (Lunkenheimer et al., 2004).

These traditional views have been challenged by other theories, particularly the idea that the myocardium is composed of distinct 'bands'. The concept of a unique myocardial band has been proposed (Torrent-Guasp et al., 2005), and the view of ''nested pretzels'' has been also been postulated (Jouk et al., 2000). However these ideologies have not been validated by anatomical, developmental or histological examinations of the whole ventricular mass (Smerup et al., 2009).

The fibre orientation within the atria is not so well understood, but the muscle bands within the atria (discussed below), for example PcMs and CT, dictate fibre orientation due to the fact that fibres run predominantly in the longitudinal axis of these structures (Ho et al., 2002, Wang et al., 1995). Although some data exists on fibre orientation in the SAN (Chandler et al., 2011, Dobrzynski et al., 2005), most studies focus on the PVs due to their arrhymogenic properties (Hocini et al., 2002, Hocini et al., 1998, Zhao et al., 2012). The lack of investigation into global fibre orientation of the atria coincides with the lack of knowledge of how the atria contract. In Chapter 5 the complex global 3D fibre orientation of the atria is investigated and regional heterogeneities are highlighted.

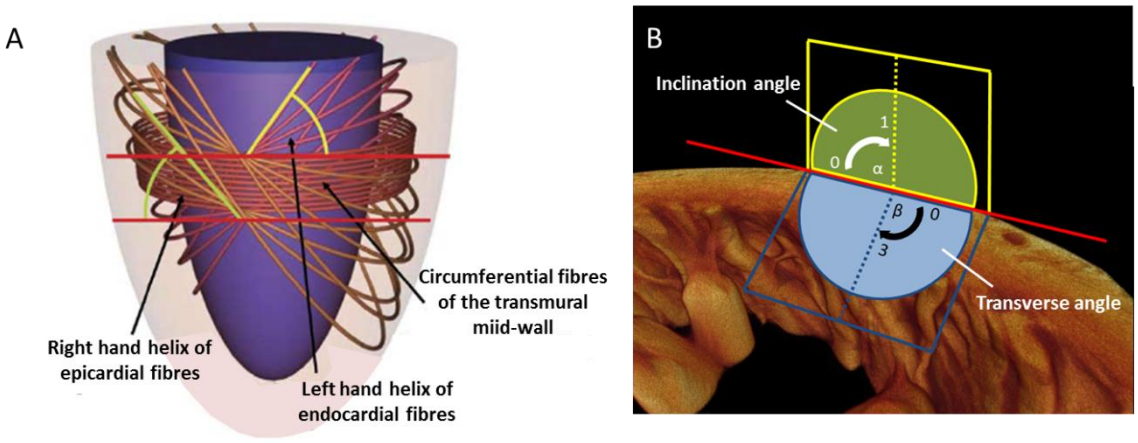

Figure 1.5 Fibre orientation in the ventricles. Simplified 3D representation of the helical arrangement of fibre across the ventricular wall (A) (modified from Anderson 2005). Schematic showing the angles recorded (inclination and transverse) to find the true 3D orientation of a fibre (B). (for further explanation see figures 2.1 and 2.2)

1.2.10 Laminar sheets

The existence of laminar sheet structures within the ventricles was debated for some time, however 3D investigations of ventricular myocardium have confirmed their existence (Gilbert et al., 2009, LeGrice et al., 1995). The laminae are formed by stacks of myocytes (4-6 cells thick) arranged end to end on their long axis, and transmurally they showed branching and abrupt changes in organisation (LeGrice et al., 1995, Gilbert et al., 2012). The transmural extent of the clefts or planes formed by the laminae is still disputed (LeGrice et al., 1995, Lunkenheimer and Niederer, 2012). The long axes of the myocytes within the sheets are arranged helically (as described above). However little is known regarding their contribution to ventricular contraction; it is thought myocytes contraction within the laminar sheets induces shearing forces (Smerup et al., 2013b), which allow laminae to slide over one another, contributing to myocardial thickening in systole (Costa et al., 1999). Within sheets, connective tissue surrounds individual fibres and forms branches between fibres, but a less dense network is present between sheets. This arrangement is thought to facilitate sheet shearing (Costa et al., 1999, LeGrice et al., 1995). In terms of conduction it has been postulated that they are involved in the spread of electrical propagation (Hooks et al., 2007), and also function to increase the safety factor of the myocardium by constraining passive current load locally (Smaill et al., 2013). The anatomy of the laminar sheets is investigated in Chapter 5 using non-invasive imaging techniques, and novel details regarding regional differences are revealed.

1.2.11 Connective tissue

Skeletal muscle is made up of many individual cells known as muscle fibres (myofibres), fibre orientation is usually uniform across the muscle and a fine layer of connective tissue called endomysium covers each individual fibre. Individual fibres are bundled together into fascicles, each surrounded by a layer of connective tissue called the perimysium. Many fascicles combined make up a muscle, and a connective sheath called the epimysium surrounds the entire muscle providing a pathway for blood vessels and nerves (Figure 1.6A) (Salmons, 1995). In Chapter 4 we present a non-invasive method for 3D imaging of skeletal muscle in which the connective tissue can be discriminated from the muscle fibres.

Collagen is the major structural component of the extra cellular matrix in the myocardium, and like in skeletal muscle has been classified into three components (figure 1.6B) : the endomysium surrounds each myocyte providing it with the supportive frame work, coordinates the transmission of force and prevents slippage between adjacent cells; the perimysium a network of thicker connective tissue surrounds groups of myocytes (laminar sheets), its weave structure bears the shearing forces between groups of myocytes and its lateral strands prevent malalignment between sheets (Ho, 2009, Pope et al., 2008); and the epimysium surrounds the entire muscle (Ho, 2009). The connective tissue network has been shown to play important roles in ventricular contractions and transmural thickening (Lunkenheimer et al., 2006b). Recent studies using 3D imaging techniques have shown transmural differences in the 3D distribution of connective tissue (Pope et al., 2008). It is postulated these differences have functional and morphological implications; Pope et al. showed laminar sheets were present throughout the subendocardium and midwall where perimysial collagen was present mainly in the form of extensive sheets. But Laminar sheets were not present in the subepicardium where perimysial collagen is mostly composed of regularly spaced cords (Pope et al., 2008).

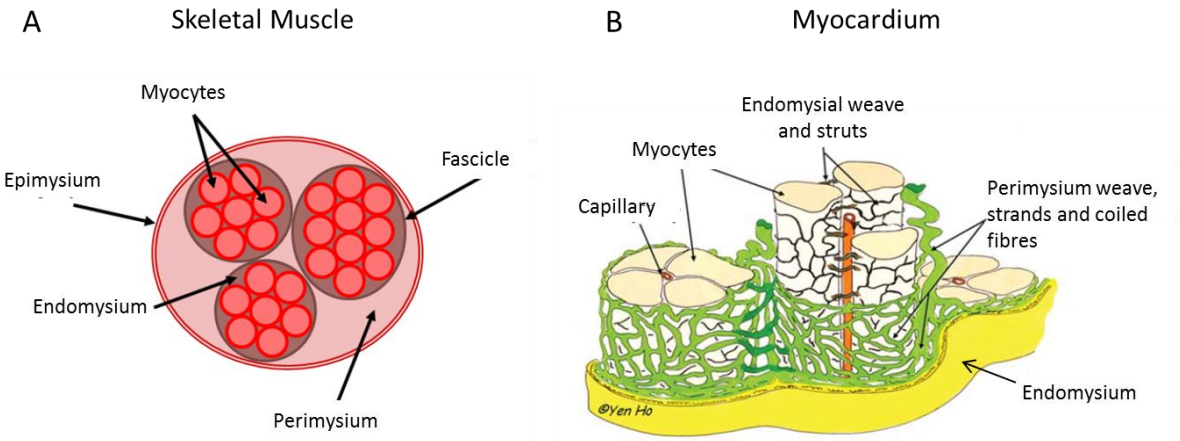

Figure 1.6 Schematic representations of the connective tissue arrangement in skeletal muscle and myocardium. Showing the hierarchy of connective tissue in skeletal muscle (A), and the myocardium (B). (B- Modified from Ho 2009)

1.2.12 Cardiac contraction

Systolic contraction causes complex deformation of the LV, and is a combination of long axis shortening, circumferential constriction, wall thickening and long axis torsion (Anderson et al., 2005, Smerup et al., 2009). Myocyte contractions are constrained to a 14-16% shortening (Rodriguez et al., 1992, Lehto and Tirri, 1980), however systolic strains in the LV can greatly exceed this value (Arts et al., 1984, Arts et al., 1979). Fibre shortening only causes a 8% increase in myocyte diameter which does not explain the 40% radial wall thickening and ~60% ejection fraction in systole (Arts et al., 1979). This suggests the myocardial mesh (myocytes and connective tissue) is able to produce greater deformation than its active constituents. It is postulated that this is achieved by the dualistic function of ventricular torsion (angular difference in reciprocal twisting of apex and base), this intricate pattern of motion utilizes the complex fibre architecture of the heart creating tangential and radial forces (Greenbaum et al., 1981, Lunkenheimer et al., 2004, Smerup et al., 2013b). This 'wringing' motion during myocardial contraction was first described by Lower 1669 (Ingels, 1997). Observed functional deformation shows an initial counter-clockwise twist globally (as seen looking from below the heart), with accompanied narrowing (isovolumic phase) prior to blood ejection. During ejection the counter-clockwise twisting continues at the apex, while clockwise twisting occurs at the base along with longitudinal shortening. Then the apex rotates rapidly in a clockwise manner (isovolumic untwisting), thus the ventricle lengthens and the cavity slightly widens, no blood enters or leaves the heart at this stage (Buckberg et al., 2008, Buckberg et al., 2006, Jung et al., 2006, Notomi et al., 2008). As untwisting continues there is a pressure decay (Notomi et al., 2008), and rapid filling occurs due to both suction and the created pressure gradient (Thomas and Popovic, 2006, Notomi et al., 2008). The final phase is relaxation (diastole), where widening of the heart continues and filling is slowed. The cycle is reinitiated by atrial contraction in the next synchronised heartbeat. The mode of contraction is therefore determined by the orientation of the oblique running fibres at the epi and endocardium (Russel et al., 2009).

As stated by Anderson et al., 2008 to fully explain transmural thickening of the ventricles, it is necessary to postulate rearrangement of the individual myocytes relative to each other (Anderson et al., 2008). It has been shown the myocytes do

realign themselves transmurally during systole, with up to 40% more myocytes packed transmurally than is seen in diastole (as described by Anderson et al., 2008). Also the work of Lunkenheimer et al., 2004 and 2006a suggests the functional contribution of transverse angled fibres to wall thickening should always be considered. It is also postulated wall thickening is produced by sliding of the Laminar sheets (as described above) (Costa et al., 1999, LeGrice et al., 1995). All these theories are believed to be supported by the morphology and mechanics of the connective tissue network (Ingels, 1997, Lunkenheimer et al., 2006b).

The dualistic motion of the LV acts to equalise fibre stress and strain throughout the heart, and reduce transmural gradients of fibre work (Arts et al., 1979, Ingels, 1997). Furthermore the rapid untwisting during early diastole is believed to assist LV filling (Notomi et al., 2008, Rademakers et al., 1992), and torsion has been shown to generate realistic ejection fractions in modelling studies (Sallin, 1969, Smerup et al., 2013b). However there is still disparity over the form and function of the ventricles (Anderson et al., 2008, Buckberg et al., 2008, Torrent-Guasp et al., 2005), and how the ventricles function in HF is yet to be elucidated. In Chapter 8 changes in fibre orientation in the failing heart are assessed and effects on contractile performance are discussed.

Less is known about the contractions of the atria. Inferences regarding contraction have been made with reference to the atria's muscular bands (described below); the PcMs are thought to play an important role in deformation of the atrial chamber during atrial systole (Ho et al., 2002, Ho and Sánchez-Quintana, 2009, Wang et al., 1995). This lack of understanding is mostly due to the absence of high fidelity 3D geometries; 3D fibre orientation has not been described in the atria as it has in the ventricles. In Chapter 5 we investigate the global 3D fibre orientation within the atria, and make inferences regarding differential systolic deformation of the RA and LA.

1.2.13 Action potentials of the working myocytes

The electrical activation of myocytes is essential for the normal contractile function of the heart; this relationship is referred to as excitation-contraction coupling (Barnett and Iaizzo, 2009, Bers, 2002, Iaizzo et al., 2009). Myocytes create a charge gradient

through the action of various ion pumps and ion selective channels (Barnett and Iaizzo, 2009, Bers, 2002), the charge difference between the cell and extracellular space is known as the membrane potential. In the resting state the cell carries a negative charge relative to the outside, but the initiation of a cardiac action potential changes the cells' permeability to sodium (Na^+), calcium (Ca^{2+}) and potassium ions (K^+), causing the cell to depolarise (figure 1.7). Calcium ions are considered the most important in excitation-contraction coupling as Ca^{2+} is a direct activator of myocyte contraction (see above) (Bers, 2002). As a result Ca^{2+} mishandling contributes to contractile and electrical dysfunction in pathophysiological conditions (Bers, 2002, Pogwizd et al., 2001). During the cardiac action potential, inward Ca^{2+} current (*I*ca) increases due to depolarization-activated Ca^{2+} channels, this contributes to the action potential plateau (Figure 1.7). Ca^{2+} entry and ryanodine receptor activation triggers Ca^{2+} release from the sarcoplasmic reticulum (SR), in a process known as calcium induced calcium release. The combination of influx and release raises the free intracellular concentration, allowing Ca^{2+} to bind to the myofilament protein troponin C, which then switches on the contractile machinery (see above) (figure 1.4 and 1.7). For relaxation, Ca^{2+} is transported out of the cell by various pathways; SR Ca^{2+}-ATPase, sarcolemmal Na^+/ Ca^{2+} exchange, sarcolemmal Ca^{2+}-ATPase or mitochondrial Ca^{2+}- uniport. This reduces *I*Ca allowing Ca^{2+} to dissociate from troponin (Barnett and Iaizzo, 2009, Bers, 2002, Levick, 2003).

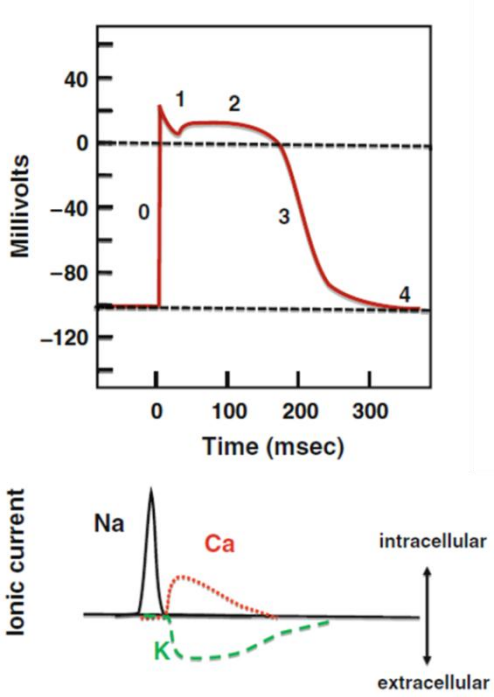

Figure 1.7 Cardiac action potential of a working myocyte and the corresponding ionic currents. The inward Na current associated with the opening of the voltage-gated Na-channels causes upstroke (phase 0). The closing of the Na-channels causes initial repolarization (phase 1). The depolarization of the cell causes opening of the voltage-gated Ca-channels and the voltage-gated K-channels, whose ionic currents are in balance during plateau (phase 2). The closing of the Ca-channels while the K-channels are still passing an outward current causes the repolarization (phase 3) and return to the resting membrane potential (phase 4). (Modified from Barnett 2009)

1.3 The cardiac conduction system

This section will cover the gross and micro anatomy of the cardiac conduction system (CCS), and highlight its function and dysfunction in health and disease. In Chapter 6 we present a technique that permits non-invasive imaging of the major regions of the CCS for the first time in a fully intact heart. Changes in the 3D morphology of the CCS with HF are investigated using the same technique in Chapter 7.

1.3.1 The anatomy of the cardiac conduction system

Synchronised contraction of the atria and ventricles is regulated by the propagation of electrical impulses travelling through a complex network of modified myocytes, collectively called the CCS (Laske et al., 2009). These subpopulations of specialised myocytes are interposed within the working myocardium, and have the ability to spontaneously generate electrical impulses (pacemake). They act to preferentially conduct impulses throughout the heart in a rapid and coordinated fashion (Laske et al., 2009).

The components and morphology of the CCS in humans is similar to that found in most commonly used lab animals, however interspecies and intraspecies variations have been described (Sanchez-Quintana and Yen Ho, 2003, Atkinson et al., 2011, Stephenson et al., 2012, Ho et al., 1995). The CCS is composed of; the sinoatrial node (SAN), the main pacemaker of the heart; the atrioventricular conduction axis (AVCA), forming the only functional connection between the atria and ventricles; and the Purkinje network, which allows fast and coordinated conduction to the ventricles (figure 1.8) (Boyett, 2009, Sanchez-Quintana and Yen Ho, 2003). However recently other regions of specialised tissues have been described, namely the atrioventricular ring tissues (Yanni et al., 2009a) and the ventricular outflow tracts (Monfredi et al., 2010) (figure 1.8).

To be deemed a specialised conducting cell, myocytes need to match three criteria, first proposed by Aschoff and Monckeberg in 1910 (Anderson et al., 2013): (1) they should be histologically discrete from working myocardium; (2) should be traceable in serial sections; and (3) the cells should be insulated by fibrous tissue from the working myocardium. More recently molecular phenotyping of both the CCS and working myocardium has allowed further distinction of the specialised tissues (reviewed by Dobrzynski et al., 2013).

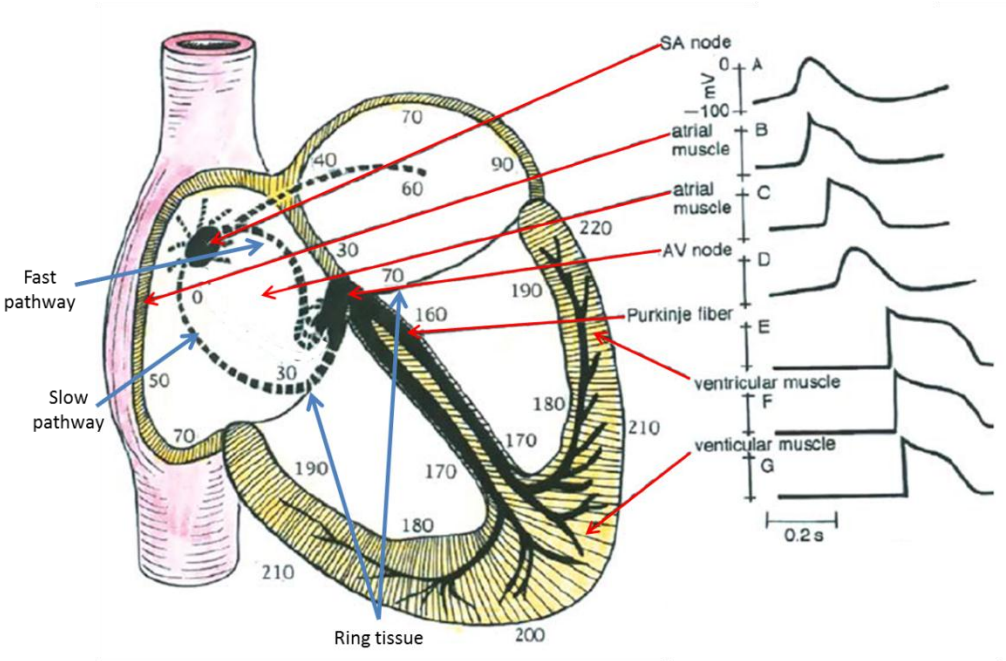

Figure 1.8 Schematic representation of the cardiac conduction system (CCS) in a longitudinally sectioned heart, with corresponding activation sequence and regional action potentials. Black dotted lines indicate inter-nodal and inter-atrial conduction. Activation time in milliseconds. (Modified from Laske 2009)

1.3.1.1 The sinoatrial node

The SAN serves as the natural pacemaker of the heart, and is thus responsible for generating normal cardiac rhythm (Laske et al., 2009). The SAN was first discovered in 1907 by Keith and Flack (Keith and Flack, 1907) who distinguished the node in many mammals including humans. The SAN is located in the subepicardial intercaval region of the heart, and in contrast to many textbook descriptions (figure 1.8), runs from the opening of the SVC down alongside the CT extending towards the IVC (Anderson and Ho, 1998, Dobrzynski et al., 2005). The nodal myocytes are smaller than the working myocytes, and have no spatial order, few mitochondria, sparse myofilaments, and are embedded in a dense connective tissue network (Boyett et al., 2000, Christoffels et al., 2010, Sanchez-Quintana and Yen Ho, 2003). At the periphery of the node is the paranodal region, a region distinct from the SAN and working myocardium. Paranodal cells are embedded in fat not connective tissue (SAN), and are loosely packed not densely packed like the myocardium (Chandler et

al., 2009, Dobrzynski et al., 2013). However it does contain a mixture of atrial and nodal myocytes (Chandler et al., 2009), the precise function of the region is unknown but it is postulated that it plays an important role in normal atrial activation (Aslanidi et al., 2011, Chandler et al., 2009). The SAN therefore only satisfies two of the criteria established in 1910; histologically discrete and traceable in serial sections.

1.3.1.2 Internodal conduction

Controversy has long surrounded the issue of how the electrical impulse within the RA travels from the SAN to the atrioventricular node (AVN). Dual pathway physiology is generally accepted, with both anatomical and functional evidence supporting their existence (Hucker et al., 2008a, Zhang et al., 2001). The two pathways are classified as 'slow' and 'fast' (figure 1.8); the slow pathway normally passes the isthmus between the CS and vestibule to join the proximal aspect of the AVCA, and has a longer conduction time but a shorter effective refractory period than the fast; The fast pathway runs superiorly across to the IAS, before descending the IAS to meet the AVCA at the common node, and has a faster conduction rate, but a longer effective refractory period than the slow pathway (Laske et al., 2009). Therefore during normal conduction the fast pathway is preferential, however during higher heart rates or premature beats slow conduction occurs through the slow pathway.

Some support the existence of specialised tracts (James, 1963), while others favour the idea that the arrangement of myocytes (fibres) is responsible for the fast preferential conduction between the nodes (Sanchez-Quintana et al., 1997). It is argued studies of specialised tracts ignore the criteria of 1910 (Anderson et al., 1981). However some histological studies do describe insulated tracts containing both histologically definable Purkinje like cells and nerve cells, such tracts matching the anatomical positions of the slow and fast pathways have been described in rabbit and pig (Bojsen-Moller and Tranum-Jensen, 1971, Bojsen-Moller and Tranum-Jensen, 1972, Paes De Carvaho et al., 1953). These are the left and right sino-atrial ring bundles (SARBs), they form a fine ring of tissue which encircles the smooth intercaval region. Inferiorly the right SARB runs through the eustachian and thebesian valves into the region of the AVCA. Superiorly the right SARB gives off branches to the PcMs, while the left SARB branches across to the IAS eventually

running inferiorly to, like the right SARB, join with the AVCA (Roberts, 1991, Bojsen-Moller and Tranum-Jensen, 1972). Studies of the tracts electrophysiology using micro electrodes suggest, like Purkinje cells, they have slow diastolic depolarisation (pacemaker potential) and a fast upstroke (Hiraoka and Sano, 1976, Paes De Carvalho et al., 1953). Paes de Carvalho et al., 1953 suggested the SARBs are the first to be excited by the SAN and offer the fastest route for internodal conduction, however more recent studies have questioned the role of the SARBs suggesting the CT is the first to be excited, and offers the route for preferential conduction due to its superior conduction velocity (Masuda and Paes de Carvalho, 1975, Hiraoka and Sano, 1976). The existence of specialised internodal tracts is considered in Chapter 5; 3D anatomy, molecular expression and fibre orientations in the region are investigated.

1.3.1.3 The atrioventricular conduction axis

The principle function of the AVCA is to conduct action potentials from the atria to the ventricles. Conduction through the AVCA is slow allowing atrial systole to precede ventricular systole and thus permit ventricular filling. The AVCA was originally discovered by Tawara (Tawara, 2000), and has atrial, penetrating and ventricular components (Anderson et al., 2013, Tawara, 2000). The majority of the atrial component lies within the RA in the triangle of Koch (figure 1.2 and 1.9). The compact node (CN) lies at the apex of the triangle; proximally, the inferior nodal extension (INE) projects between the CS and tricuspid valve hinge (septal isthmus), and constitutes part of the slow pathway (Hucker et al., 2008b, Li et al., 2008). A transitional zone of cells surrounds the CN at the region where the fast pathway enters the conduction axis, and their presence may act to increase the safety factor in the region (Dobrzynski et al., 2013). The penetrating part of the AVCA is formed anterior to the CN when the axis becomes insulated from the atrial tissue by the fibrous skeleton (figure 1.9). Running within the central fibrous body this region is deemed the penetrating bundle. It is insulated for only a short distance before emerging anteriorly on the superior aspect of the IVS, first as a short non-branching bundle, before becoming the branching bundle giving rise to the right and left bundle branches (Dobrzynski et al., 2013, Sanchez-Quintana and Yen Ho, 2003) (figure 1.9).

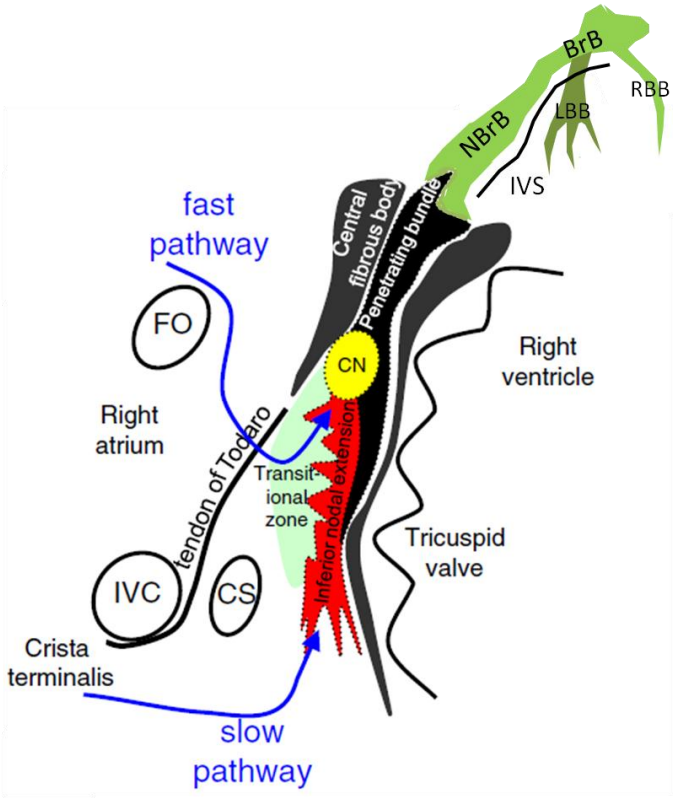

Figure 1.9 Diagrammatic representation of the atrioventricular conduction axis and its association with surrounding structures. Blue arrows indicate the entry points of the fast and slow pathways into the axis. CS- coronary sinus, CN- compact node, FO- foramen ovale, IVC- inferior vena cava, IVS- interventricular septum, NBrB- non-branching bundle, BrB- branching bundle, LBB and RBB- left and right bundle branches. (Modified from Mazgalev et al., 2002)

1.3.1.4 The atrioventricular ring tissue

Recently additional specialised tissues have been identified at the atrioventricular junctions. These histologically specialised rings take origin form the INE of the AVCA and encircle the orifices of the atrioventricular valves forming a figure-of-eight (Yanni et al., 2009a). One ring projects leftwards to encircle the orifice of mitral valve, while the rightward projecting ring encircles the tricuspid valve. Anteriorly the right ring passes over the AVCA, and is therefore not associated with the central fibrous body, but joins with the left ring to form the retroaortic node. The retro aortic node is found posterior to the aortic root within the atrial wall (Yanni et al., 2009a). The ring tissues satisfy two of the three criteria for specialised tissues

(Aschoff and Monckeberg 1910), and are thus justified in been classified specialised. The function of the atrioventricular ring tissues is yet to be elucidated, however this tissue does have portential pacemaking capabilities (Dobrzynski et al., 2013), and is also thought to play a role in arrhythmogenesis in the adult heart (Boyett, 2009), making it an ablation target for patients with atrial tachycardia (Kistler et al., 2006).

1.3.1.5 The Purkinje network

There is an on-going debate over atrial conduction, however there is no doubt that insulated specialised conducting tissue distributes the cardiac impulse through the ventricles. Collections of insulated rapid conducting cells known as Purkinje fibres act as preferential conduction pathways, providing fast and coordinated excitation of the ventricles (Laske et al., 2009, Sanchez-Quintana and Yen Ho, 2003) (figure 1.8). The Purkinje fibres first described by Jan Evangelista Purkinje in sheep ventricles in 1845 (Eliška, 2006), are continuous with the bundle branches of the branching bundle (figure 1.9). The right and left bundle branches (RBB,LBB) have asymmetric morphologies; the LBB is typically fan-like and divided into 3 fascicles, while the RBB is more cord like and projects anteriorly (Ansari et al., 1999, Atkinson et al., 2011, Miquerol et al., 2004). The Purkinje fibres in both sides of the heart form complex subendocardial and free running networks which project towards the apex down the IVS, and form extensive connections with the papillary muscles of the valves and the ventricular free walls (Ansari et al., 1999, Atkinson et al., 2011, Miquerol et al., 2004). The SAN, INE and CN all have transitional cells at their junctions with the atrial myocardium (see above). Transitional cells have also been described at the Purkinje-LV wall junctions (Severs, 2000). Such cells are expected to facilitate smooth propagation of electrical impulses, thus reducing source-sink mismatch.

1.3.1.6 The right ventricular outflow tract

The right ventricular outflow tract is a muscular region which connects the working myocardium of the RV infundibulum and the pulmonary trunk. This region also gives attachment to the pulmonary valve leaflets (Monfredi et al., 2010). Recently it has been shown that the tract contains cells with a nodal-like phenotype (Monfredi et al., 2010, Yanni et al., 2009a) and pacemaker-like activity (Dobrzynski et al., 2013).

It is thought that the presence of these ‘nodal’ cells plays an important role in the high susceptibility of the region to arrhythmias(Yanni et al., 2009a).

1.3.2 Propagation of the wave of depolarisation

The electrical activation of nodal cells and myocytes is essential for the normal contractile function of the heart, this relationship is referred to as excitation-contraction coupling (Bers, 2002, Iaizzo et al., 2009) (see above). The generation of action potentials is facilitated by the electrical permeability of various ion channels and the cell-cell communications created by gap junctions. This section will highlight how action potential morphology and propagation differs in the CCS and working myocardium.

1.3.2.1 Action potentials- cardiac conduction system vs myocardium

The principles behind the generation of action potentials are the same in both nodal and working myocytes, but the time course and morphology of the action potentials is considerably different (Iaizzo et al., 2009, Laske et al., 2009, Levick, 2003). Nodal cells are characterised by the ability to spontaneously depolarize to generate an action potential (pacemake). Nodal cells (SAN and AVN) can also be characterised by their action potential morphology (figure 1.10); in comparison to the working myocardium they have a slower initial upstroke, a lower amplitude overshoot, and usually lack an early phase of repolarization (phase 1), but do have a prominent plateau (phase 2). The repolarisation is slower, and as a result, the sinus node action potential is longer than that of the surrounding atrial muscle (Boyett et al., 1999, Laske et al., 2009).

The Purkinje cells can also be characterised by automaticity and action potential morphology, but also by their rapid conduction; they have a rapid upstroke, a prominent early phase of rapid repolarization (phase 1), and a stable plateau and repolarisation phase. The working myocardium is also fast conducting, with an action potential morphology similar to that of the Purkinje cells (figure 1.10). However they do have a shorter action potential duration, which ensures that they are out of the refractory period before the onset of the next heart beat (Laske et al., 2009).

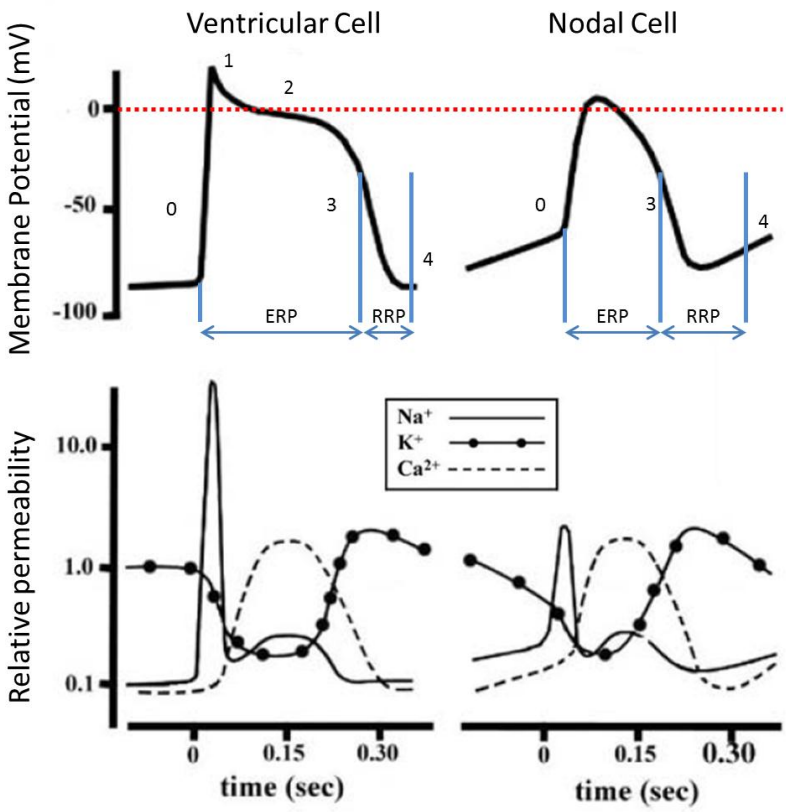

Figure 1.10 Ventricular cell action potential vs Nodal cell action potential. Top row shows typical action potential morphology of ventricular cell (left) and nodal cell (right), 0- upstroke (depolarisation), 1- initial repolarisation, 2- plateau, 3- repolarisation,4- resting potential. Bottom row shows corresponding ionic currents. ERP- effective refractory period, RRP- relative refractory period. (Modified from Laske 2009)

1.3.3 Pathways for conduction

The CCS

The speed at which a wave of depolarisation propagates through tissue is termed- conduction velocity (CV). Different conduction velocities are observed in different tissue types and regions across the heart, and are related to ion channel and gap junction expression (see above), but are also dependent on myocyte size and organization.

The cellular architecture of the different regions of the CCS contributes to their characteristic conduction velocities. In the SAN CV is considerable slower (a few

cm/s in the rabbit) than in the surrounding atrial muscle (~70 cm/s in the rabbit) (figure 1.10) (Boyett et al., 2000). This is in part due to the small cell size associated with the SAN, also cells within the node are sparse and heterogeneously arranged in dense connective tissue (Boyett et al., 2000, Dobrzynski et al., 2005), all factors which contribute to slow conduction. The AVN is predominantly slow-conducting (1-5 cm/s) with regional changes in CV. Proximal to the CN, cells are small (2-3 μm- around 10 times smaller than working myocytes) and arranged in spiralling fascicles surrounded by connective tissue. The CN cells are interwoven and the 'tortuous' pathways created are thought to be a major contributor to atrioventricular conduction delay (Laske et al., 2009, Levick, 2003). In the penetrating and non-branching and branching bundles cells are also arranged in fascicles but are generally larger with a greater population of spindle cells present (faster conducting). In contrast CV in the Purkinje cells is the fastest in the heart with a conduction velocity of 230 cm/s as compared to 75 cm/s in the 'fast conducting' ventricular muscle (Desplantez et al., 2007). This is mostly due to fact that Purkinje cells are the widest cells in the heart (40-80 μm) and have strong cell-cell coupling (Laske et al., 2009, Levick, 2003).

The ventricles

In the fast conducting working myocardium, muscular contraction and electrical conduction is strongly dictated by myocardial architecture (Spach and Kootsey, 1983, Dorri et al., 2010). The helical and transverse angled populations of the cells form a spiracle arrangement of fibres which coupled with the CCS allow for fast and synchronised conduction, facilitating the complex dualistic motion or torsion of the heart (see above).

The atria

Muscular bands and sleeves of varying prominence exist within the atria, and have been studied by dissection (Ho et al., 2002, Wang et al., 1995). These structures play a vital role in the preferential propagation of action potentials and effective muscular contraction of the atria. In the RA they include the CT, Eustachian ridge and the multiple ridges of myocardium associated with the FO (structures described above). Bands which are common in both atria include the PcMs, and the vestibules surrounding the atrioventricular valves (Ho et al., 2002, Ho and Sánchez-Quintana, 2009).

Bands also exist on the epicardial surface of the RA; the intercaval bundle covers the surface of the venous sinus between the posterior interatrial groove and sulcus terminalis. Bachmann's Bundle (BB) forms the most important 'inter-atrial' band; the CT gives rise to BB in the atrial roof anterior to the opening of the SVC. BB runs anteriorly on the surface of the inter-atrial groove as a prominent band of transverse running fibres. There are often further bands running inferiorly in the inter-atrial grove (Ho et al., 2002, Ho and Sánchez-Quintana, 2009). On the posterior wall there is an inter-atrial band, aptly named the posterior inter-atrial band which runs between the CS and LA (Chauvin et al., 2000, Ho and Sánchez-Quintana, 2009) (figure 1.11).

The circumferential bands or bundles encircle the base of the RA and form the vestibule. The internal circumferential band commences anteriorly at the IAS and runs posteriorly around the right vestibule. The external circumferential band originates from the right side of the anterior inter-atrial bundle, and posteriorly is continuous with the intercaval bundle (Wang et al., 1995). The circumferential bundles of the LA are more prominent than in the RA, but also lie predominantly in the vestibule. The principle bundle is a leftward continuation of BB; as it reaches the appendage it gives off upper and lower branches which encircle the left atrial appendage. The upper branch gives off further branches to the LA free wall, while the lower branch courses the vestibule, both branches continue posteriorly and insert into the posterior inter-atrial groove. In the LA the septopulmonary bundle is analogous to the intercaval bundle of the RA. In the human heart it originates at the posterior inter-atrial groove and runs superiorly towards the anterior wall, here it gives off multiple bundles, the largest of which runs leftwards and intermingles with the BB (Wang et al., 1995) (figure 1.11).

Located in the posterior wall or venous component of the LA (Which is larger than in RA) are the pulmonary vein sleeves, these short tubes of circumferentially running myofibres anchor the 2-4 pulmonary veins to the LA (Anderson and Cook, 2007, Ho et al., 2002) (figure 1.11). The junctions between the muscle sleeves and LA are complex with heterogeneous fibre orientation. It is believed that this anisotropic arrangement of myocytes contributes to the high prevalence of arrhythmias in this region in the setting of fibrosis and ageing (Hocini et al., 2002, Spach et al., 1982, Zhao et al., 2012). In Chapter 5 the 3D fibre orientation of these bands are

investigated, with emphasis placed on their junctions with the adjacent structures and atrial wall.

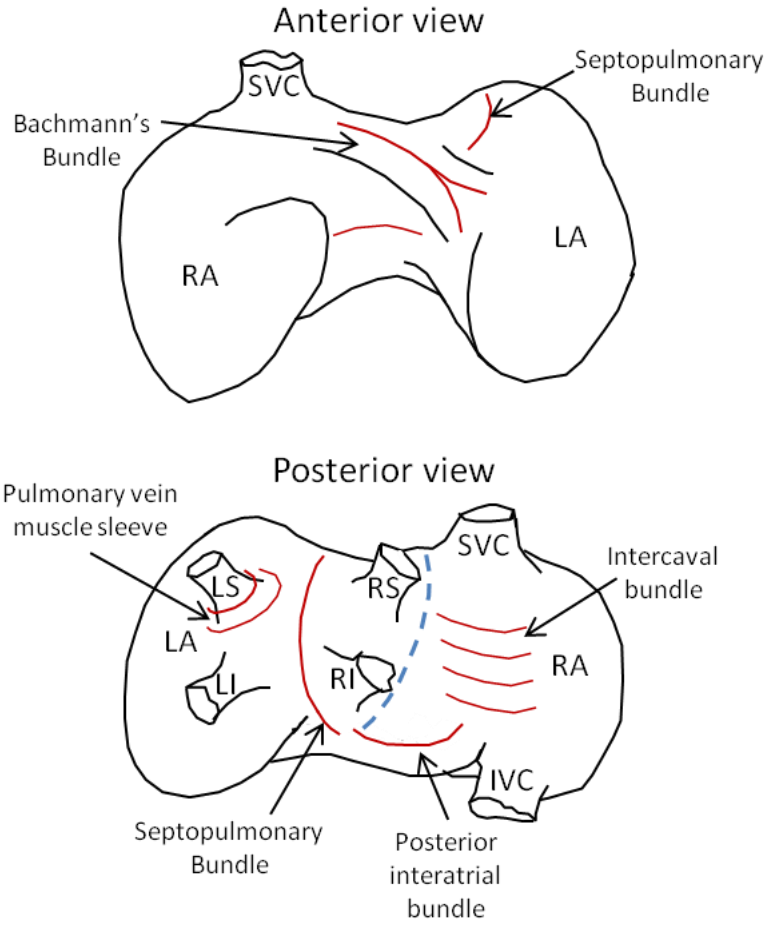

Figure 1.11 Diagrammatic representation of the atrial muscle bands. Showing the major muscle bands and sleeves of the atria (red lines) from anterior (top) and posterior (bottom) views. LA- left atrium, LI,LS,RI,RS- left and right inferior and superior pulmonary veins, IVC- inferior vena cava, RA- atrium, SVC- superior vena cava.

1.4 The failing heart

Heart failure (HF) is a clinical syndrome which is characterised by inability of the heart to pump sufficient blood to meet the body's metabolic needs (Leonard et al., 2012). The overall prevalence of clinically evident HF is around 5–20 cases/1,000 population, however this figure rises to >100 cases/1,000 population in subjects aged

>65 years (National Collaborating Centre for Chronic Conditions, 2006). This section will highlight morphological and functional changes in HF, including changes to fibre orientation and the CCS, with emphasis placed on the effects of volume and pressure overload.

1.4.1 Causes and predispositions

Many changes in morphology and physiology of the cardiovascular system can increase an individual's risk of developing HF including: Increased preload (the end volumetric pressure acting of the heart), normally caused by volume overload due to insufficiency of the valves and increased venous and pulmonary pressures; increased afterload (described as the pressure the ventricle has to overcome to eject blood), normally attributed to pressure overload of the heart due to increased arterial pressure or hypertension due to vessel stenosis and occlusion; myocardial infarction, in this acute syndrome an area of the heart becomes starved of its blood supply normally due to blockage of a coronary artery, resulting in myocardial ischemia which causes hypoxia and if untreated necrosis of the myocardium. Risk factors for HF include; gender, age, ethnicity, genetic predisposition, and lifestyle risk factors such as obesity, smoking, alcoholism and sedentary existence (Jessup and Brozena, 2003).

1.4.2 Morphological changes disease

Multifactorial morphological changes offer a basis for classifying HF, but classifications are often conflicting (Gaasch and Zile, 2011, Opie et al., 2006). For example; the idea of a common end-stage for all HF syndromes has recently been challenged (Leonard et al., 2012). However HF for the most part is a progressive process characterised by changes in the morphology and shape of the chamber due to dilatation and/or hypertrophy – a process referred to as 'cardiac remodelling' (Gaasch and Zile, 2011, Opie et al., 2006) (figure 1.12). Remodelling has been shown to be dependent on the type and severity of overload (volume or pressure) (Gaasch and Meyer, 2008), and can be compensated (improve function) or decompensated (cause dysfunction). The usual response in a chronic setting is for the heart to take on a compensated phenotype, but left untreated the progression to

decompensated HF is unavoidable, and currently this transition between states is poorly understood.

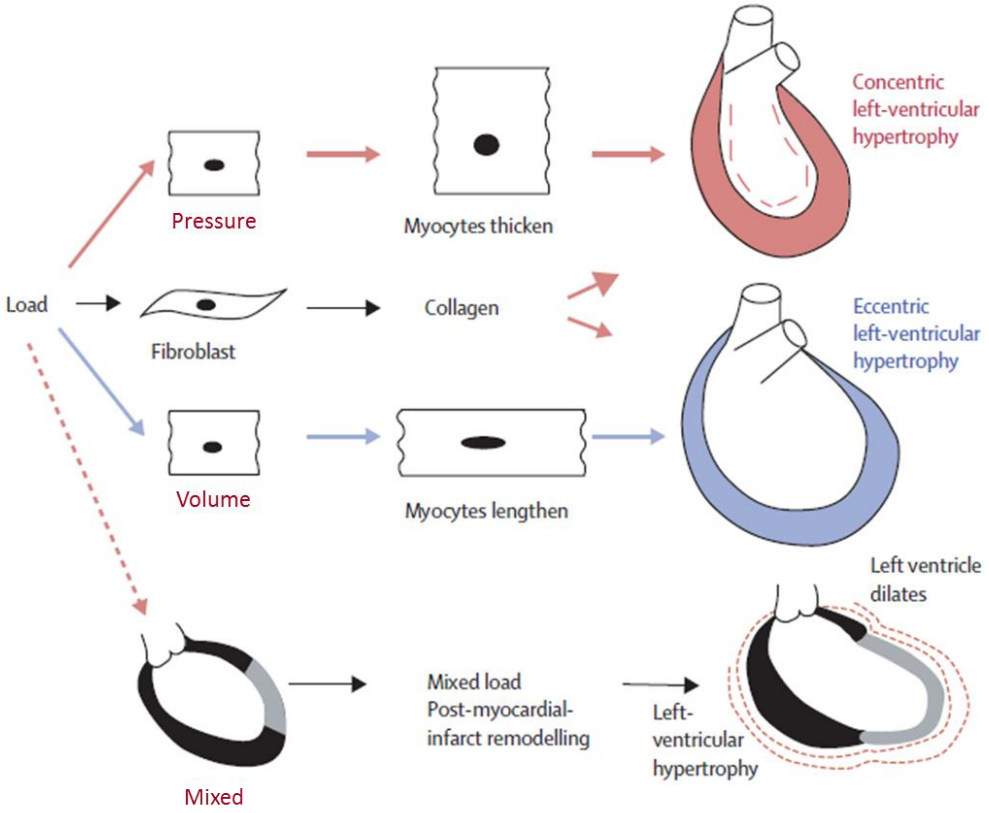

Figure 1.12 Schematic representation of cardiac remodelling in response to overload. Showing the classic response to pressure overload (top row), volume overload (middle row) and myocardial infarction (bottom row). (Modified from Opie 2006)

1.4.2.1 Response to volume overload

The general response to volume overload is eccentric hypertrophy, in which increased preload causes myocyte stretching and addition of sarcomeres, thus causing chamber dilatation (Figure 1.12). This is usually accompanied by mild hypertrophy but a decrease in the relative wall thickness (RWT)- the ratio between wall thickness and chamber radius (Opie et al., 2006, Gaasch and Meyer, 2008).

1.4.2.2 Response to pressure overload

The general response to pressure overload is concentric hypertrophy, increased afterload causes hypertrophy of the myocardium which is associated with an increased myocyte cross-sectional area due to addition of sarcomeres (figure 1.12) (Drazner, 2011). According to Linzbach (Gaasch and Zile, 2011) in concentric hypertrophy there is "no change in the size of the internal cavity", however recently more detailed classifications of HF have been proposed, for example hypertrophy in the presence of dilatation and increased RWT is termed mixed hypertrophy (Gaasch and Zile, 2011) (figure 1.13).

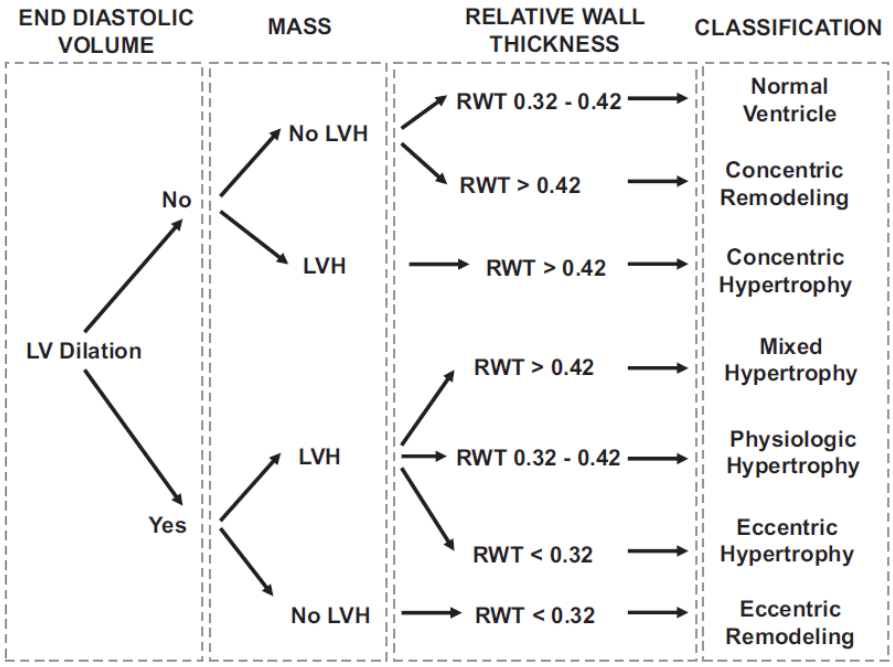

Figure 1.13 Flow chart for classification of cardiac remodelling. Detailed categorisation of cardiac remodelling using dilatation, hypertrophy and relative wall thickness as criteria. LVH- left ventricular hypertrophy, RWT- relative wall thickness. (Modified from Gaasch 2011)

1.4.2.3 Changes to the CCS in disease

In contrast to the working myocardium, changes in the gross morphology of the CCS in disease are not well understood, however changes in cell structure and remodelling

at a molecular level in HF are much better represented. The CCS has been confirmed as plastic (Boyett, 2009), and has been shown to be more sensitive to change than myocardium (Chandler et al., 2009) (Yanni et al., unpublished).

Histological studies have shown all regions of the CCS undergo hypertrophy (Harris et al., 2012, Okada and Fukuda, 1981)(Yanni et al., unpublished), and show an increased deposition of ECM in HF (Yanni et al., 2009b). Significant remodelling of ion channels, gap junctions and calcium handling proteins has been described in the CCS in HF. A downregulation of funny current (I_f) and slow delayed rectifying potassium current ($I_{K,s}$) has been observed in the sinus node in rabbit (Verkerk et al., 2003), and widespread remodelling of ion channels has been observed in the sinus node of infarcted (Yanni et al., 2011) and pulmonary hypertensive rats (described in Dobrzynski et al., 2013). Studies of the AVCA electrophysiology in failure are limited, slowing of atrioventricular conduction has been shown in a study of isolated atrioventricular junction preparations, in a rabbit model of HF induced by myocardial infarction (Muir et al., 2005). In the Purkinje fibres significant downregulation of ion channels has been described in both rabbit (HF) and dog (ventricular tachy pacing) models: downregulation of funny channels (HCN4), Na+ channels ($Na_v1.5$), Ca^{2+} channels ($Ca_v1.2$, $Ca_v1.3$), K+ channels ($K_{ir}2.1$), Ca^{2+}-handling proteins (RYR2, SERCA2 and NCX1) and connexins (Cx40, Cx43) were common in both models (Maguy et al., 2009)(Yanni et al., unpublished data). However contrasting findings have been presented in a pressure overload model of HF in rat (Harris et al., 2012). In chapter 7 we investigate the effects of experimental HF on the major regions of the CCS.

1.4.2.4 Changes in fibre orientation

There is dispute as to the arrangement of the muscle fibres in the normal heart (Greenbaum et al., 1981, Jouk et al., 2000, Streeter et al., 1969, Torrent-Guasp et al., 2005), as a result the effects of cardiac remodelling on fibre orientation is poorly understood, and conflicting results can be found in the literature. Pearlman et al. conducted a histological study looking at fibre orientation in various stages of heart disease, and concluded that the orientation of the myocardial strands was unaltered (Pearlman et al., 1981), this is consistent with the findings of Neilsen et al. using DT-

MRI, but spatial resolution was poor (1.33mm^3) (Nielsen et al., 2009). In contrast, subsequent studies suggest fibre orientation is altered in HF; histological studies of hypertrophic hearts suggest the proportion of longitudinal fibres is increased while circumferential fibres are reduced (Carew and Covell, 1979, Kuribayashi and Roberts, 1992). These findings are consistent with studies using DT-MRI to map fibre orientation in hypertrophic (Tseng et al., 2006) and dilated hearts (Eggen et al., 2009). Studies have also highlighted the increased variability of fibre orientation in HF and show regional differences between the base and apex (Adhyapak and Parachuri, 2009, Eggen et al., 2009, Schmitt et al., 2009). However most studies only concentrate on changes in the helical angle, with few studies looking at changes in the transverse or intrusion angle. Lunkenheimer et al. suggests these intruding fibres will become more erect in response to hypertrophy (Lunkenheimer et al., 2006b), using using difussion tensor magnetic resonance imaging (DT-MRI) Schmitt et al. described an increase in the angle of intruding fibres in the LV free wall and IVS in hypertrophy (Schmitt et al., 2009).

Changes to 3D fibre orientation in failed hearts is investigated in Chapter 8; areas of hypertrophy are examined, however few descriptions of changes in dilated myocardium exist in the literature, therefore emphasis is placed on regions of dilatation.

1.4.3 Functional changes in heart disease

Functional changes to the heart are usually assessed using echocardiography. Measures include stroke volume, ejection fraction and fractional shortening. Stroke Volume (SV) is defined as the volume ejected between the end of diastole and the end of systole. Ejection Fraction (EF) is a global index of LV fibre shortening and is generally considered as one of the most meaningful measures of the LV pump function. It is defined as the ratio of the SV to the end diastolic volume. Fractional shortening (FS) is the percentage change in LV cavity dimension with systolic contraction (Frangi et al., 2001).

1.4.3.1 Laws of the heart

Starling's law of the heart states that the force of contraction by the myocardium is proportionate to the length of the muscle fibre pre-contraction, therefore the more a myocyte is stretched the greater the force of the contraction it produces (figure 1.14A). Starling's law is therefore related to the length tension relationship (figure 1.14C), and as a result excessive stress will eventually result in plateau and decline of contractility (figure 1.14A,C) (Levick, 2003, Loushin et al., 2009).

Laplace's law states that internal pressure is proportional to wall tension (wall stress x wall thickness) and inversely proportional to internal radius. Therefore as a chamber increases in size and the wall thins, stroke volume decreases (figure 1.14B). In Laplace's law afterload is the 'wall stress' during ejection and depends on wall thickness and arterial pressure, and is therefore related to the after-load shortening relationship (figure 1.14D), which shows how excessive afterload can cause decreased contractility (Levick, 2003, Loushin et al., 2009).

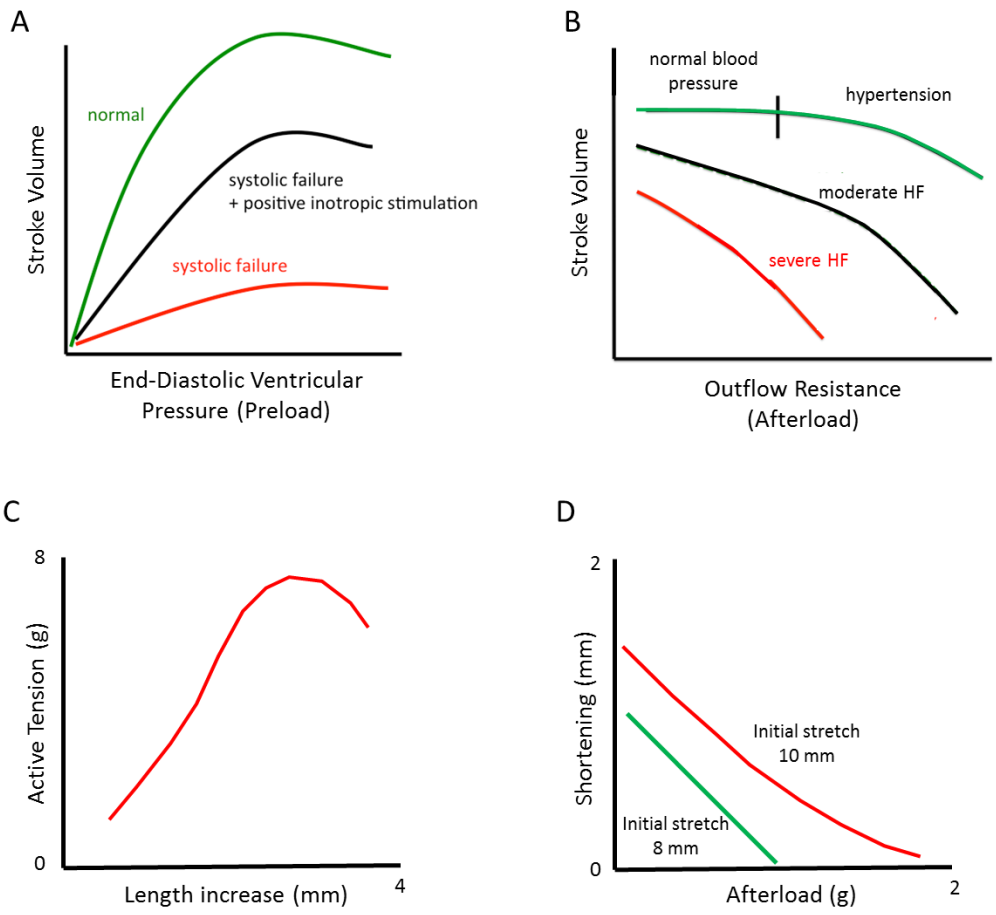

Figure 1.14 Functional laws of the heart. Line graphs representing: Starling's law (A), the effects of increased afterload (B), the length tension relationship (C) and the afterload shortening curve (D). (adapted from Levick 2003 and Sonnenblick 1962)

1.4.3.2 Functional changes in heart failure

Volume overload

As mentioned above vast morphological changes occur in the presence of overload, with the severity and time-scale of overload dictating the level of remodelling. Usually the initial response to volume overload is compensated; dilatation acts to increase end diastolic pressure and preload is increased. As a result contractility and stroke volume are increased due to Starling's law and the length-tension relationship (figure 1.14A,C) (Barnett and Iaizzo, 2009, Levick, 2003, Loushin et al., 2009). At this point a balance is maintained between Starling's law and Laplace's, however as HF is progressive the severity of symptoms, particularly dilatation, increase and the

heart becomes decompensated; Laplace's law dominates and increases in chamber radius cause little/no increase in contractility. At this point Starling and length-tension curves reach plateau (figure 1.14A,C), and the increase in ventricular radius reduces the systolic pressure generated through Laplace's law and thus stroke volume declines (figure 1.14B,D) (Levick, 2003, Loushin et al., 2009).

Pressure overload

Loss of function in pressure overload is also seen to be progressive and dependent on severity. In pressure overload the heart is presented with increased afterload; to overcome this the heart must increase contractility, this is achieved by a hypertrophic response. Increasing wall thickness and reducing wall radius results in increased stroke volume due to Laplace's law- the heart becomes compensated. However the heart becomes decompensated in excessive hypertrophy due to Starling's law; the compliance of the myocardium is reduced so that the myocytes operate on the low tension part of the length-tension curve and the reduced cavity size means end-diastolic pressure is reduced (figure 1.14A,C). In addition excessive afterload is associated with reduced stroke volume (figure 1.14B), and reduced muscle shortening (figure 1.14D) and shortening velocity (Levick, 2003, Sonnenblick, 1962).

Fibre orientation

Changes in fibre orientation in HF are still not fully understood (see above), and how the fibre orientation contributes to contraction in the control heart is yet to be fully elucidated. However it is postulated that a reduction in circumferential fibres will reduce transmural thickening, and because these fibres make the greatest contribution to pressure generation stroke volume will be reduced (Buckberg et al., 2008). Furthermore in the biphasic motion of the heart the helical and transverse angled fibres work together but have specific role in producing torsion (Lunkenheimer et al., 2004). Therefore it is thought deviation from the 'normal' orientation will contribute to a reduction in the ability to both constrict and dilate the ventricles (Buckberg et al., 2008, Lunkenheimer et al., 2004). Models of cardiac mechanics which incorporate 3D fibre orientation can be used to investigate how changes in fibre orientation affect cardiac function (Dorri et al., 2010). Dorri et al. 2010 showed cardiac function was robust in the presence of small changes in fibre orientation. But highlighted severe

loss of function at angle deviations of ~30°, and showed transverse angles exceeding 45° cause mural contractions which counteract systolic thickening and reduces EF%.

1.4.3.3 Electrical dysfunction in disease

CCS dysfunction is present in HF, atrial fibrillation, aged hearts and possibly diabetes (Boyett, 2009). A considerable proportion of HF patients die of bradyarrhythmias, sinus bradycardia, prolonged AVCA conduction, left bundle branch block and complete heart block.

The substantial morphological changes in HF can act as a substrate for electrical dysfunction. Stretch has been shown to cause changes in ion channel expression (Jeyaraj et al., 2007), and animal studies have demonstrated that atrial dilation, through various mechanisms, results in a shortened atrial refractory period and a prolonged atrial conduction time (Marin-Garcia, 2010). Also ventricular remodelling in humans is associated with electrical dysfunction such as ventricular tachycardia (VT) (Marin-Garcia, 2010).

Impulse propagation across the heart depends on: physiology of individual cardiomyocytes, impulse transmission between adjacent cells, and the 3D arrangement of cells. Perturbation in the function of any of these factors can give rise to rhythm disturbances and re-entry activation (Smaill et al., 2013). Re-entry occurs when an abnormal myocardial conduction pathway causes the wave of excitation to travel in a repetitive and continual circus (Levick, 2003). As a result myocytes emerging from their refractory period are instantly re-excited , re-entry is thought to contribute to tachycardia generation, maintenance of atrial fibrillation and triggering of afterdepolarisations (Levick, 2003, Smaill et al., 2013).

Conduction in all regions of the heart is determined by the balance between current source and passive current load, known as source-sink matching (Smaill et al., 2013). Depolarised cells act as the source of current, which diffuses into surrounding polarised tissues- the sink (Nikolaidou et al., 2012). Abrupt changes in both wall thickness and fibre orientation have been shown to contribute to source sink mismatch (reviewed in Smaill et al., 2013). In addition abrupt tissue expansions

result in a change in; wave front curvature, conduction slowing and even conduction block (reviewed in Smaill et al., 2013). Furthermore, modelling studies have suggested increased fibrosis plays a significant role in electrical dysfunction and arrhythmogenesis (Zhao et al., 2013b).

1.4.4 Models of heart failure

The function and morphology of the heart in health and disease is often investigated using animal models. Numerous animal models exist in the literature and are extensively reviewed by Hasenfuss (Hasenfuss, 1998). It is clear that many studies have been conducted to investigate electrical dysfunction, and the effects of volume or pressure overload on the heart. However there are very few studies into the longitudinal, morphological and molecular changes to the heart when presented with both volume and pressure overload simultaneously. Here, with colleagues (Professor George Hart, Dr Antonio Corno, Dr Xue Cai, Dr Caroline Jones, Professor Jonathan Jarvis), we have developed a HF model in rabbit which encompasses both volume and pressure overload (methods 2.2). Longitudinal (*in vivo*), morphological and molecular changes were subsequently analysed.

1.5 Imaging of muscle tissue

The desire for true and accurate 3D representations of soft tissue structures has been ever present in the scientific community. Developmental, comparative and functional investigation of animal tissue morphology necessitates accurate visualisation and analysis of 3D tissue structure. In addition, modern genomic and mutational investigations into morphogenesis are equally dependent on 3D visualisation and interpretation of global morphological change. These all require 3D images that accurately preserve 3D relationships within samples.

1.5.1 Invasive *ex vivo* imaging techniques

Traditionally, knowledge on the gross morphology of muscle came from careful dissection (Pettigrew, 1864, Vesalius, 1544), with fine morphological knowledge coming from histological studies (Harman and Gwinn, 1949, Hoagland et al., 1944).

Both techniques are still frequently implemented in the investigation of muscle tissue but do have limitations. Histology is labour intensive, and only permits analysis of small sample preparations, meaning analysis of gross morphological changes in a large sample size is impractical. Dissection suffers, although to a lesser degree, from similar limitations, and the discrimination of different tissue types is difficult using dissection. Histology does allow for staining of specific structures, for example muscle fibre types (Tunell and Hart, 1977) and connective tissue networks (Dolber and Spach, 1987).

Confocal microscopy (Semwogerere and Weeks, 2005) and scanning electron microscopy (SEM) (LeGrice et al., 1995) provide suitable data, but are hampered by the fact that a sample depth of only a few hundred microns is viable, and again sample preparations are small. To address some of the issues which hamper the aforementioned modalities, techniques such as episcopic microscopy (Mohun and Weninger, 2011, Weninger et al., 2006), extended volume confocal (Pope et al., 2008, Sands et al., 2005) and surface imaging microscopy (Gerneke et al., 2007) have been developed. These techniques address the issue of registration of sections and poor z-plane depth, although access of specific stains to individual cells is problematic if samples are embedded. Further drawbacks include; long acquisition times, only small samples can be processed, and the destructive nature of the techniques mean artefacts due to tissue damage are inevitable.

1.5.2 Clinical non-invasive *in vivo* imaging of the heart

Non-invasive imaging describes a technique where the sample is intact, and not damaged during the acquisition process. As a result if resolution and safety permits, images of muscle can be obtained *in vivo*, and in some cases allowing analysis of function as well as morphology. In a clinical setting many imaging techniques are used in this way to image the heart, and are reiewed by Frangi et al., 2002: Two-dimensional (2D) echocardiography uses ultrasound waves and allows the anatomy and motion of cardiac structures to be visualised noninvasively, and also allows quantification of heart morphology and function (SV, EF, FS). The use of Doppler in 2-D echocardiography allows the direction and degree of blood flow to be investigated. 2D echocardiography and colour Doppler were used to make longitudinal morphological and functional measurements of our HF model-see

chapter 8. Cardiac MRI is another non-invasive imaging technique which can provide information on morphology and function of the cardiovascular system. Advantages of cardiac MRI include a wide topographical field of view, visualisation of multiple planes, and high soft-tissue contrast between the flowing blood and myocardium. MRI has been used to assess global and regional RV and LV form and function, SV, EF, LV mass, wall-thickening, myocardial motion, and circumferential shortening can all be measured. MRI *tagging* was introduced independently by Zerhouni and Axel, this allows tracking of material points in 2D and 3D, and subsequently strain analysis can be conducted.

Many imaging techniques use the non-invasive properties of electromagnetic radiation. Angiocardiography involves the use of X-rays to image hearts following injection of a radio-opaque contrast medium. This technique provides 2-D images which can be used to delineate lesions, and assess EF and myocardial volumes. Isotope imaging (e.g single positron emission computed tomography-SPECT) can be used to investigate cardiac function (EF) and regional wall motion. SPECT is often used to study myocardial perfusion in cases of myocardial infarction, and to assess the viability of the affected region. Conventional computed tomography (CT) has 'virtually no place in cardiovascular examinations'. However Spiral CT is commonly used for cardiac imaging, with image quality equalling that of MRI. DSR (Dynamic spatial reconstructor) uses multiple X-ray sources to produce "real time" cross sections with similar acquisition times to ultrafast CT but is not commercially available. Ultrafast CT is both relatively inexpensive and can provide 3D images of cardiac cavities anatomy and function, and coronary calcium deposits (plaque). Data obtained from CT and MRI is more accurate than that derived from 2D techniques, where the calculations are based on the notion that the LV is ellipsoidal. Volume measurements by CT and MRI are independent of cavity shape, with the area or motion calculated from automatically aligned contiguous slices in quantifications.

Similar techniques are often adopted in scientific research; high resolution echo is used to show regional strain (Notomi et al., 2008, Sengupta et al., 2006), and speckle tracking to look at torsion (Thomas and Popovic, 2006).

1.5.3 Non-invasive *ex vivo* imaging of muscle

1.5.3.1 Current techniques

Many non-invasive imaging techniques can be applied to *ex vivo* imaging of muscle, but when the goal is to obtain high resolution images non-invasively with high inter tissue contrast micro-MRI is considered most suited (Damon et al., 2011, Driehuys et al., 2008, Gilbert et al., 2012, Johnson et al., 2002). However recent studies into contrast enhancement in micro-CT imaging (Faraj et al., 2009, Metscher, 2009a) suggest that micro-CT, which has previously been disregarded due to its inferior soft tissue contrast, could become the superior method for soft tissue imaging. In addition micro-CT has many advantages over micro-MRI and these are discussed at length in Chapters 3 and 4.

1.5.3.2 Micro-computed tomography

Micro-computed tomography (micro-CT) is an imaging technique in which thousands of individual X-ray projections are acquired at small increments around the central axis of a sample. From this data, using a tomographic reconstruction algorithm, a 3D tomographic stack of multiple contiguous transaxial slices is generated (Ritman, 2011). These slices are made up of fully isometric voxels with spatial resolutions of ~5μm attainable. The system normally comprises an X-ray source (micro focus tube), sample gantry and an X-ray imaging array/detector (Ritman, 2011, Stauber and Mueller, 2008). These tomographic images are fully 3D, and although made up of multiple X-ray projections, do not suffer from the superimposition of overlying structures as in conventional radiography. Micro-CT was first developed in the early 1980s (Flannery et al., 1987, Elliott and Dover, 1982), however the development of the cone-beam reconstruction algorithm by Feldkamp et al. (Feldkamp et al., 1984), which is used to magnify the X-ray beam, facilitated the development of high resolution lab-based and desk-top systems. Micro-CT non-invasively produces high resolution 3D data sets in a cost and time efficient manner. Furthermore sample size is limited by both chamber and detector size, therefore the development of larger bay systems with large flat panel detectors means samples as big a 20cm^3 can be imaged at resolutions of ~100μm in a single 20 minute scan. In addition multiple scans from the same sample can be concatenated, in this case sample size is only limited by the chamber size, and resolution only by

time and scanner geometry. As a result the use of micro-CT for both *in vivo* and *in vitro* imaging of biological samples continues to grow in biomedical research. The wide range of applications and developments of micro-CT are reviewed in the literature (Holdsworth and Thornton, 2002, Ritman, 2004, Ritman, 2011). Here using micro-CT we have developed a technique for high resolution soft tissue imaging *in vitro*. We apply this technique to image skeletal muscle in Chapters 3 and 4, and cardiac tissue (working myocardium and CCS) in Chapters 5,6,7,8.

Geometry

Scanner geometry describes the source to object distance (SOD) and object to detector distance (ODD), varying these distances ultimately affects image quality (independent of the X-ray source and detector technology).

In short scanner geometries the sample is moved close to the X-ray source, therefore the ODD exceeds the SOD allowing the image to be projected onto the detector and thus magnified (figure 1.15). This hugely improves the spatial resolution of the scan, but also decreases the field of view at a proportional rate; as a result for high magnifications large detectors are required. The development of bay systems (as used in the present study) that can house large flat panel displays and allow for a high ODD solve this problem. Magnification penumbral blurring is amplified with increased magnification (figure 1.15), therefore in short geometries a micro-focus X-ray tube should be used with a small focal spot size to ensure a narrow X-ray beam. Short geometries are used in the data presented here to allow for optimal spatial resolution.

In long scanner geometries the SOD and ODD are roughly the same, long geometries are more often implemented in longitudinal *in vivo* studies as in this geometry the radiation dose can be reduced. However this is at the expense of spatial resolution (figure 1.15), and to gain sufficient contrast resolution a high flux or high exposure times must be used (Bartling et al., 2007).

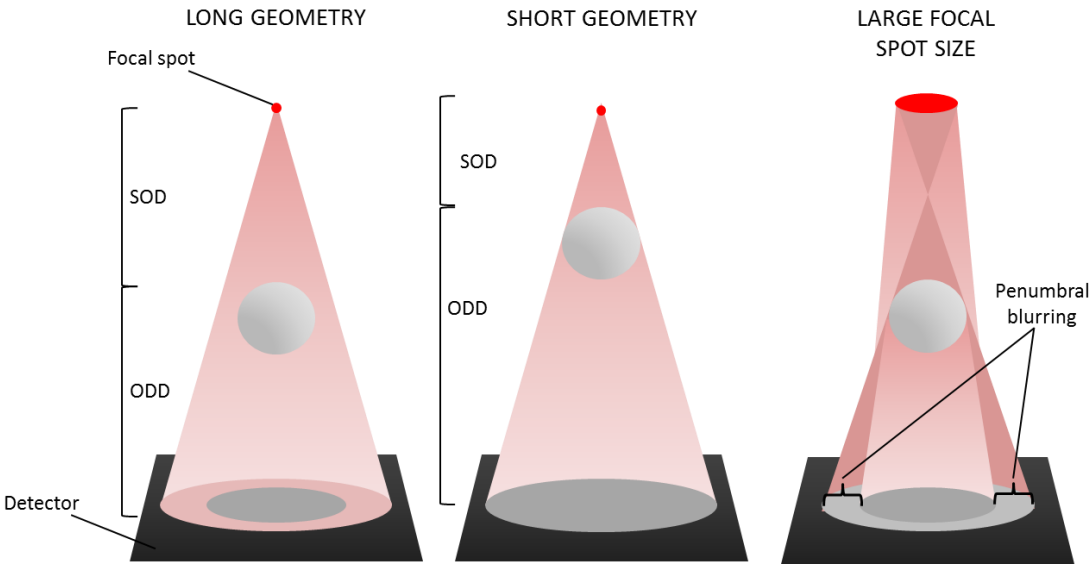

Figure 1.15 Diagrammatic representations of different micro-computed tomography scanning geometries. Showing the effects of long geometry (left) and short geometry (middle) on magnification, and the importance of a small focal spot size (right).

Rotating sample and rotating gantry systems

Micro-CT scanners can be classified as rotating sample or rotating gantry (Holdsworth and Thornton, 2002). Rotating gantry systems are usually used for *in vivo* studies as the animal can be scanned unsedated without the introduction of motion artefacts from rotating a live sample (not an issue *ex vivo*. However in these systems the geometry is often fixed so that image magnification and resolution cannot be manipulated. In rotating sample systems the source is fixed and precisely aligned with the detector and central axis of the system, the detector and gantry however can moved allowing fine manipulation of the scanner geometry. A rotating sample system was used in the present study.

X-ray source and target

An X-ray source for micro-CT should have a small focal spot size (figure 1.15), emit high photon flux, and X-ray energies should be selectable (Bartling et al., 2007). Focal spot size should be as small as possible to reduce blur, however focal spot size is roughly inversely proportional to flux. High flux is desirable for high temporal resolution and short scan times, and to allow good low-contrast spatial resolution and

reduce image noise (Badea et al., 2004, Bartling et al., 2007). But having the ability to select the tube current and voltage to suit your specific sample partly solves this issue. Micro focus X-ray tubes used for micro-CT have small focal spot sizes (2-50 μm) and have the advantage of permitting high isometric spatial resolutions of ~5-50 μm in a FOV of 30-50 mm (Bartling et al., 2007, Wang and Vannier, 2001). The X-ray spectrum (figure 1.17) produced by the tube is dependent on the energy of the incident electrons and also the atomic number of the target material (see below).

X-ray interactions with matter-the generation of X-rays

X-rays are electromagnetic radiation, and with γ-rays are the only forms of electromagnetic radiation that have the capability to liberate electrons from their atomic bonds . The energy of an X-ray is inversely proportionate to its wavelength, the wavelengths of X-rays range from a few picometers to nanometers (Hay and Hughes, 1983). X-rays with longer wavelengths are referred to as 'soft', and usually do not have sufficient energy to penetrate deep into tissues. Shorter wavelengths correspond to 'hard' X-rays which in some cases too easily penetrate the tissue and result in poor contrast resolution (Hay and Hughes, 1983). Therefore the use of a suitable X-ray energy and target for your sample is essential. The effect of different X-ray targets on soft tissue imaging is investigated in Chapter 3.

In micro-CT -rays are produced using an X-ray tube; a heated cathode filament and an anode target are placed at opposite ends of the tube which is under vacuum. When current passes through the filament it sputters electrons off its surface. Due to the high charge difference these electrons travel at high speeds down the tube to bombard the anode target (normally tungsten). From these interactions two major types of X-rays are produced- Bremsstrahlung radiation and Characteristic X-rays (figure 1.16).

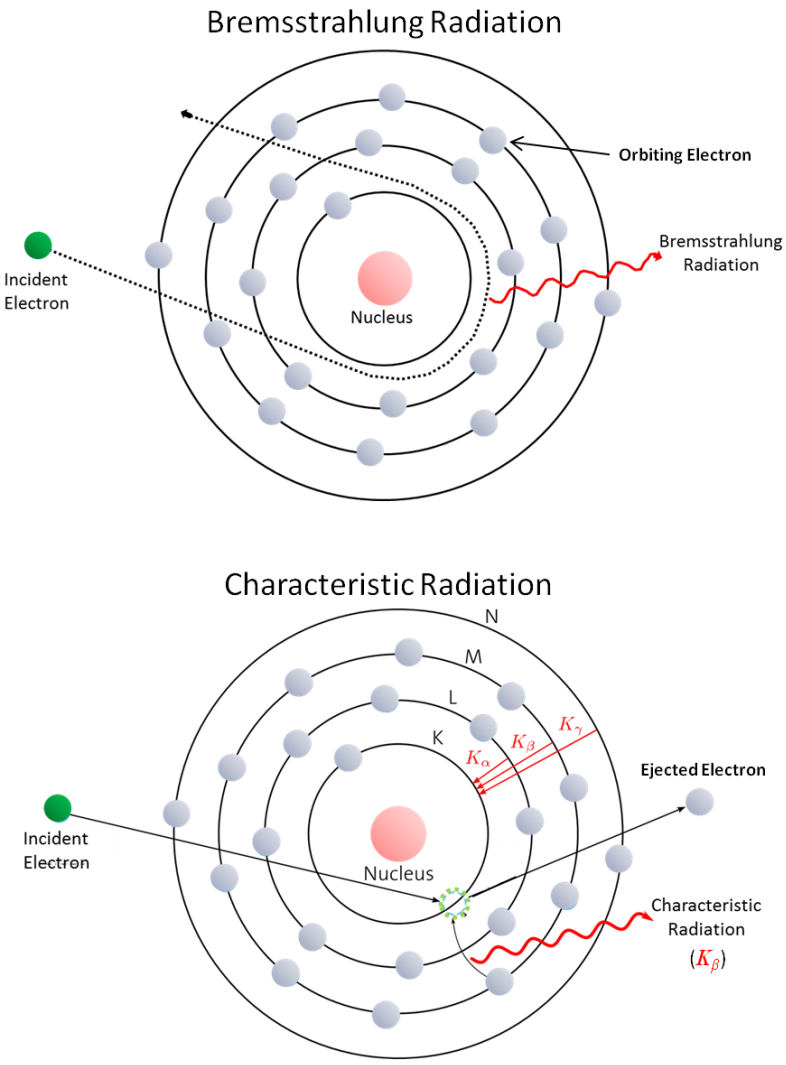

Figure 1.16 Diagrammatic representations of X-ray interactions with matter. Showing the two major processes for generation of X-rays, Bremsstrahlung radiation (top) and characteristic radiation (bottom).

Bremsstrahlung radiation

The interaction of an incident electron with the nuclei of an atom produces Bremsstrahlung radiation. When the incident electron passes near an atoms nucleus the difference in charge between the negatively charged electron and positively charged nucleus causes deceleration of the electron, and the energy lost produces radiation (figure 1.16). The level of radiation is dictated by how close the electron is to the nucleus and also by the atomic number of the anode target and the incidence electrons energy (Hay and Hughes, 1983, Yin et al., 1987, Beutel et al., 2000).

Secondly Bremsstrahlung radiation can be produced when the incident electron directly interacts with the nucleus, causing the entire energy of the electron to be converted into radiation. This interaction therefore produces more energy than the aforementioned interaction and is responsible for the upper end of the X-ray energy spectrum, however this occurs rarely (figure 1.17).

Characteristic X-rays

Characteristic X-ray production involves the displacement of electrons orbiting the target atom's nucleus by the incident electrons. Electrons occupy specific orbits (shells) around the nucleus of an atom, and the number of electrons and shells dictates the atom's atomic number (figure 1.16). The innermost shell, the K shell, has the highest binding energy. When interacting with the target some incident electrons will collide with the orbiting electrons. If the electron is knocked out of its orbit, the atom is ionised and an X-ray photon is produced (figure 1.16). This is followed by an electron with a higher potential energy (lower shell binding energy) from an outer shell taking the place of ejected electron, this energy transfer creates another X-ray photon called characteristic radiation (figure 1.16). This process is then repeated for all subsequent shells until equilibrium is reached (figure 1.16) (Hay and Hughes, 1983, Khandelwal, 1968).

Each element of the periodic table has its own 'characteristic' shell binding energies (greater the atomic number the greater the binding energies), and thus the X-ray photons produced by each element are unique and have a specific X-ray spectrum (figure1.17). This can be utilised in the imaging process by using different target materials to suit a specific sample. For example the higher energy rays produced by tungsten (atomic number 74) are suitable for analysing tissues with high electron density like bone, but would produce too harder rays to provide good image quality for imaging soft tissue (Hay and Hughes, 1983, Khandelwal, 1968). The use of different X-ray targets for soft tissue imaging is investigated in Chapter 3.

It should be noted excitation and ionization of outer shell electrons causes the incident electron to only lose a small amount of energy, as a result an X-ray photon is not produced, and the energy loss ultimately appears as heat (Hay and Hughes, 1983).

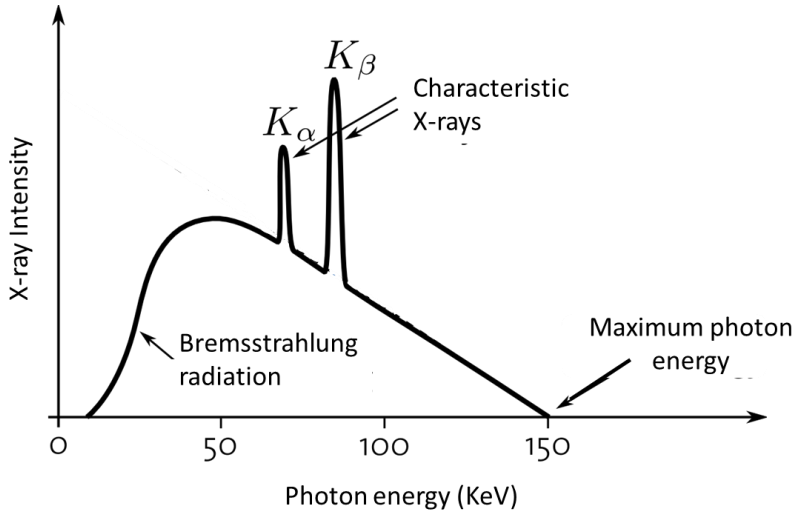

Figure 1.17 Typical X-ray spectrum. Showing the high frequency of the lower energy X-ray photons production by Bremsstrahlung radiation, the interaction of an incident electron with the target atoms nucleus corresponds to the point of maximum photon energy. The two spikes represent the characteristic X-rays generated from the transfer of electrons from outer shells to inner shells. The increased energy generated by K_β represents the movement of electrons with higher potential energies.

X-rays interaction with matter- Attenuation

The interactions of incident X-rays with a sample act to reduce the energy of the X-rays as they transverse the tissue, this attenuates the X-ray beam by removing photons. Attenuation is dependent on the energy of the X-ray beam, the atomic number/s of the tissue and the sample thickness. Physically, X-ray CT is the measurement of the samples X-ray absorption along many straight lines (projections used in micro-CT in 360°: 1400-3500). For incident X-rays ($I0$), the effect of sample thickness (d) and attenuation coefficient (μ) on the number of photons (quanta) reaching the detector (I) is given by the exponential attenuation law (KachelrieiB et al., 2008).

$$I = I0\, e^{-\mu d}.$$

It is the level of attenuation by the sample that is the basis of differential contrast in micro-CT imaging. An electron dense tissue (high atomic number), such as bone, will have regular interactions with the incident X-rays and thus highly ‘attenuate’ the

X-rays. This will result in less photons been detected by the detector and thus the structure appears as bright white in the resultant grayscale data. In contrast, X-rays readily pass through soft tissues which have low atomic numbers, and these structures appear greyish. Space has little or no attenuating affect and appears black.

X-ray interactions with matter-incident X-rays are absorbed or scattered by the sample

The way generated X-rays interact with matter is somewhat energy dependent. In micro-CT, energies for soft tissue imaging range from ~10 Kev to ~150Kev, within this energy range X-rays interact via the photoelectric effect, Rayleigh scatter or Compton scatter.

The photoelectric effect states: an electron can be ejected from its orbit if the energy of the incident electromagnetic radiation is equal or greater than the binding energy of the orbiting electron (Hay and Hughes, 1983, Yin et al., 1987). In this process the binding energy of the orbiting electron relates to the amount of energy absorbed or attenuated from the incident photon, but usually all of the photons energy is absorbed. As with the interaction of the incident electrons with the atoms of the target anode, the ejection of an electron will cause the movement of higher energy electrons from outer shells, thus creating characteristic X-rays. The probability of a photoelectric effect occurring is proportional to the cube of the atomic number, therefore small differences in atomic number can result in large differences in absorption of X-rays, and thus contribute to differential attenuation and inter tissue contrast.

Rayleigh scatter occurs at low energies, here the incident photon lacks the energy to enable the photoelectric effect. In this process the photons are scattered (change in trajectory) broadening the X-ray beam, this is not desirable, but Rayleigh scatter can be reduced by using higher X-ray energies (Beutel et al., 2000).

Compton scatter involves the interaction of incident photons with electrons on the outer shells of an atom, causing a decrease in the photons energy (increased wavelength) as it is scattered (Beutal et al., 2000). In these interactions, due to the relative low binding energy of the electron, the photon keeps a lot of its energy while the amount transferred to the electron is sufficient to eject it from its bond. The

scatter angle of the incident photon dictates the energy shift, with increased scatter causing an increase in wavelength and thus a decrease in energy. This process is repeated until all of the photon's energy is lost or until the photon transverses the entire sample. Therefore, in contrast to the photoelectric effect the probability of this interaction depends on electron density of the whole sample, and because electron density does not vary much within soft tissues, Compton scatter offers very little contrast differentiation. However the addition of contrast agents with high atomic numbers (higher binding energies) for soft tissue imaging means the photo electric effect dominates.

Spatial resolution

Spatial resolution is the smallest distance between two objects at which they are still distinguishable as separate entities. Spatial resolution is an important parameter in any morphological study. In micro-CT it is dependent on scanner geometry (magnification) and focal spot size (penumbral blurring), but detector technology is also crucial as display size and single detector element size ultimately dictate acquired resolution (Bartling et al., 2007).

Low contrast resolution

For soft tissue imaging high spatial resolution is wasted if the scanner is unable to resolve small differences between structures. Contrast is dependent on differences in attenuation coefficients of different tissues (Wang and Vannier, 2001). Low-contrast detectability has been defined as the capability to distinguish fine variations in electron density of an object compared to background/space (Gupta et al., 2006). This is largely dependent on the quantum efficiency (amount of photons needed to detect a signal) and dynamic range (the range of photon flux detectable) of the detector, but also on the use of suitable X-ray energies, as sufficient flux is needed so that the signal from the incident photons exceeds noise (Bartling et al., 2007).

Contrast agents

Low contrast resolution can be enhanced by the presence of contrast agents; heavy element solutions with K-shell binding energies ideal for X-ray interactions. Contrast agents are particularly useful for soft tissue imaging, as biological soft tissues are composed of elements with low atomic numbers/electron densities (e.g. carbon and

oxygen), and as a result produce poor X-ray contrast. Contrast agents increase the atomic number of the tissues they reside in, thus allowing visualisation of internal soft tissue structures (Faraj et al., 2009, Metscher, 2009a). An ideal contrast agent; 1) has an ideal k-shell binding energy; 2) readily penetrates soft tissue allowing imaging of large samples; 3) can be removed allowing for post scan analysis; 4) is differentially taken up by different tissue types, enhancing contrast resolution between tissues and 5) once stained it is stable, remaining localised differentially within tissues and does not bleed into adjacent structures. Studies into the proficiency of various contrast agents for soft tissue imaging using micro-CT have been reviewed previously (Faraj et al., 2009, Metscher, 2009a, Pauwels et al., 2013). In Chapters 3,4,5 and 6 we assess the proficiency of an iodine based contrast agent for imaging various soft tissue types.

There is also interest in targeted contrast enhancement, where antibodies labelled with radiopaque nanoparticles are targeted to specific aspects of cells. Such techniques have been applied to specifically detect lymph nodes, tumour cells, and different types of cancer cells (Bartlett et al., 2007, Bartling et al., 2007). Such approaches have great implication clinically and offer a basis for therapeutic approaches, in Chapter 6 we show a technique based on similar principles for targeted contrast enhancement of the CCS.

Radiation

Radiation dose should be considered even in *ex vivo* micro-CT, as one of the advantages of the technique is its non-invasive nature and thus the ability to post-process tissue. Therefore radiation damage should be avoided. X-ray exposure can cause disruption of chemical bonds and also cause super radical production which can damage nearby molecules including DNA (Ritman, 2011). In micro-CT, image quality is related to radiation exposure; increased exposure time increases the signal:noise ratio but in turn increases radiation dose, and reducing exposure times by increasing flux also contributes to increased radiation dose. Therefore such factors should be considered if post processing (e.g. histology) or repeat scans are to be performed. The effect of radiation on gross morphology is investigated in Chapter 3.

1.5.4 Non-invasive investigations of 3D fibre orientation

2D fibre orientation has previously been investigated using standard histology (Streeter et al., 1969), and more recently using micro-CT (Jeffery et al., 2011, Jorgensen et al., 1998b). Over recent years the diffusion tensor MRI (DT-MRI) has become the gold standard for the non-invasive analysis of 3D fibre orientation in biological tissues, including skeletal muscle (Damon et al., 2011, Lansdown et al., 2007), cardiac muscle (Rohmer et al., 2007), and in the brain (Wedeen et al., 2012a). However DT-MRI is not a morphological method, in that it does not resolve physical structures. Rather, the preferential diffusion direction for water is calculated for each voxel. Since water will be less constrained to move in the long axis than in the short axis of a fibre, an indication of fibre direction is achieved (Le Bihan et al., 2001). From the probability density function obtained from each voxel, DT-MRI can produce streamlines representing the distribution of the direction of diffusibility. This is not visualisation of true cellular structure, and as a result controversy is currently playing out concerning the proposed arrangement of nerve fibres in the brain based on similar analysis (Wedeen et al., 2012b, Wedeen et al., 2012a, Catani et al., 2012). The virtual streamline structures produced by DT-MRI are usually of the order of 400-1300 μm in diameter (Nielsen et al., 2009, Smerup et al., 2009). In order to derive sufficient signal to calculate diffusion vectors, MRI voxels are typically rectangles (non-isometric) rather than cubes, the longest axis of which can extend up to 1300 μm, and the acquisitions are repeated many times such that scan times can take several days (Gilbert et al., 2012).

Contrast enhanced Micro-CT is potentially capable of producing an accurate representation 3D fibre orientation in the heart, as resolutions fine enough to resolve single muscle fibres and their surrounding connective tissue network have been described (Jeffery et al., 2011, Stephenson et al., 2012). Such data is inevitably more complex given its finer resolution than the equivalent DT MRI data, although scanning electron microscopy and extended volume confocal microscopy will continue to provide the greatest resolution, such techniques have many limitations (discussed above). We (in collaboration with colleagues at the University of Manchester UK and the University of Auckland NZ) have recently begun to extract 3D fibre orientation maps from micro-CT scans by means of eigen analysis of the 3D structure tensor (Krause et al., 2010, Zhao et al., 2012). Such methods were

originally used to analyse the complex structure within sheets of paper or reconstituted wood products (Axelsson and Svensson, 2010), and have more recently been developed by our colleagues to extract fibre orientation of cardiac tissue from data generated by episcopic microscopy (Zhao et al., 2012) and micro-CT (Aslanidi et al., 2012). In this technique, an algorithm samples the space surrounding an individual voxel and searches for the direction in which the attenuation (gray values) changes the least. Therefore local fibre alignment is modelled as the orientation with the least signal variation, which corresponds to the eigenvector paired with the smallest eigenvalue. In this way each voxel of the original dataset is assigned a vector in 3D. These vectors are used to build up a representation of the direction of individual cardiomyocytes as they pass through the 3D matrix of voxels. While this technique is operating at the limit of resolution for whole hearts of small mammals, unlike DT-MRI it is based on attenuation data that is derived directly from the physical structure of the biological material. Extraction of 3D fibre orientation from micro-CT data using this method is validated in Chapter 4, and applied to the whole heart in Chapter 5, the CCS in Chapter 7, and the failing heart in Chapter 8.

1.6 Thesis aims

The aim of this thesis was to develop an imaging technique capable of producing high resolution data of large muscle tissue samples in which morphological and functional information could be obtained, specifically;

- Optimise contrast enhanced micro-CT for soft tissue imaging to allow the differentiation of multiple soft tissue types, for example; muscle, connective tissue and fat.

- Apply the micro-CT technique to fully intact mammalian hearts fixed in a naturally inflated state to allow detailed morphological analysis, and differentiation of the specialised tissues of the CCS.

- Investigate the longitudinal effects of experimental HF in rabbits, and subsequently, using micro-CT, assess changes to the working myocardium and CCS in HF.

- Assess the validity of applying a novel technique for analysis of the 3D fibre orientation to high resolution micro-CT data.

- Apply 3D fibre orientation analysis to the fully intact mammalian heart. Specifically investigate the detailed fibre orientation of the atria and the accompanying muscle bands, and investigate the incorporation of such data into biophysical mathematical models of the heart.

- Investigate changes in 3D fibre orientation in the ventricles and CCS of the failing heart.

CHAPTER 2

Materials and methods

2.1 Animal tissue preparation

2.1.1 Rat heart preparation

Adult wistar rats were terminated by exposure to increasing concentrations of CO_2 followed by cervical dislocation, as stated in Schedule 1 of the Animals (Scientific Procedures) Act 1986. The thoracic cavity was exposed and the hearts excised, keeping all major vessels intact, hearts were the transferred to vials and fixed in phosphate buffered formal saline (PBFS - formaldehyde dissolved as a 10% solution in phosphate buffered saline) for at least 48 hours. This allows storage and fixation with limited tissue shrinkage. The PBFS solution was changed as necessary to avoid acidic conditions.

2.1.2 Mouse tissue preparation

Adult mice were terminated by exposure to increasing concentrations of CO_2 followed by cervical dislocation, as stated in Schedule 1 of the Animals (Scientific Procedures) Act 1986. Whole mice were subsequently fixed by perfusion fixation, see section 2.2.4 for methodology. Heart, liver, brain and limb tissues were excised then transferred to vials and fixed in phosphate buffered formal saline (PBFS - formaldehyde dissolved as a 10% solution in phosphate buffered saline) for at least 48 hours.

2.1.3 Pig embryonic tissue

Fixed pig embryonic tissue with gestation ages ranging from ~10-120 days were obtained from Carolina Biological Supply, Wisconsin. Samples were stored in vials containing phosphate buffered formal saline (PBFS - formaldehyde dissolved as a 10% solution in phosphate buffered saline).

2.2 Experimental heart failure model in rabbit

Experimental heart failure was induced in rabbit by the means of aortic valve disruption and subsequent aortic banding, enabling investigation of both morphological and function changes in hearts exposed to both volume and pressure overload. In all studies experimental subjects were adult rabbits weighing 3.1±0.2kg (pre-procedure). Longitudinal echocardiography was undertaken weekly when

possible, ~12 weeks after the first intervention subjects were culled, their hearts perfusion fixed and excised for further analysis. In line with ethical guidelines any subjects that reached end-stage heart failure prior to the 12 week deadline were culled, but still included in analysis. Sham control subjects underwent invasive surgery at the same time points as the procedure group, but were not subjected to valve damage or aortic banding. Surgery was conducted by Dr Antonio Corno and Dr Xue Cai.

2.2.1 Aortic valve disruption

All rabbits were anesthetized with ketamine (50mg/kg) and maintained with 2% isofluorane, after tracheal intubation and with self-ventilation.Through a longitudinal incision in the right side of the neck, the right carotid artery was dissected free, distally ligated and proximally controlled with a tie.

Through a 1 mm incision on the anterior aspect of the right carotid artery, a sharp, bevel-tipped 1.22 mm catheter was introduced into the proximal right carotid artery, advanced retrogradely towards the ascending aorta, and connected to a pressure transducer whose output was monitored and recorded using ACODAS (Dataq Instruments, Akron, Ohio, USA).

Control group.

At this point for the animals in the Control group the catheter was removed from the right carotid artery, the proximal carotid artery was ligated, the tissues were closed in layers and the "sham" procedure terminated, with recovery of the animals from the general anesthesia.

Heart Failure group

In the animals in the Heart Failure group aortic valve regurgitation was obtained by disruption of ≥2 aortic leaflets by repeatedly moving the catheter across the aortic valve into the left ventricle, with continuous pressure recording. Fluoroscopy was not used. The degree of aortic valve regurgitation obtained was judged adequate when the on-line monitored pulse pressure (difference between systolic and diastolic pressure), measured through the same catheter when positioned in the ascending aorta, increased between 80 and 100% in comparison with the pre-procedure value. The maneuver was repeated until the desired degree of aortic valve regurgitation was

reached. At this point the catheter was withdrawn, the proximal carotid artery ligated, and the tissues were closed in layers. The animals were then allowed to recover from the general anesthesia.

2.2.2 Aortic banding

After an interval of 3 weeks, all animals underwent a second general anesthesia with tracheal intubation as described before. Through a longitudinal laparotomy the abdominal aorta and the renal arteries were identified, and the abdominal aorta was dissected free above the renal arteries.

Control group.

At this point for the animals in Control group the "sham" procedure was completed with the closure of the laparotomy incision in layers, and the animals were allowed to recover from the general anesthesia.

Heart Failure group.

In the Heart Failure group a pre-measured (2.44 mm) silver clip was positioned around the pre-renal abdominal aorta and occluded, inducing severe aortic narrowing with approximately 50% reduction of the aortic diameter. At this point the surgical procedure was completed with the closure of the laparotomy incision in layers, and these animals too were allowed to recover from the general anesthesia.

2.2.3 *In vivo* echocardiography

In vivo echocardiography was used to investigate longitudinal functional and morphological changes in procedure and sham control rabbit subjects. Transthoracic echocardiography was performed using a GE Vivid 3 ultrasound machine and a 5s transducer. Rabbits were held in a supine position and precordial fur was shaved, 2D images were obtained in the parasternal long axis view and Colour Doppler was used to assess aortic and mitral valve regurgitation. The M mode cursor was placed at the tip of the mitral valve leaflets, perpendicular to the IVS, images were stored and measurement of the left ventricular internal dimension and IVS and left ventricular posterior wall thickness were made in both diastole and systole. Left ventricular fractional shortening and ejection fraction was then calculated from these

measurements. Each measurement was recorded on 3 separate cardiac cycles and the mean taken.

2.2.4 Terminal procedure and perfusion fixation

Systemic heparin was administered prior to termination by intravenous injection under isoflurane aneshesia (2000 Units/kg). The rabbits were then terminated by overdose of sodium pentobarbitone. The thoracic cavity was exposed and the inferior vena cava and descending aorta cannulated. In order to clear the heart of blood the chambers were flushed *in situ* via the inferior vena cava and aorta with heparinised saline (5000 Units/ml) until the expelled solution ran clear. The heart was then fixed by a period of perfusion with PBFS by retrograde injection via the aorta. In specimens in which the aortic valve was intact, blanching of the coronary arteries was achieved with no further intervention. In samples from rabbits whose aortic valve was damaged to create an experimental model of left heart failure, it was necessary to divert the flow into the coronary arteries by pressure applied to the ventricles, and sometimes to the head and neck vessels. Samples were then fixed by a period of perfusion with PBFS (approx 10 minutes) via the aorta and, if necessary, via the venae cavae to naturally inflate all of the heart chambers with PBFS, and all major vessels (IVC,SVC, Aorta, PA, PVs) were clamped using surgical vessel clamps. The partially fixed hearts were then removed to separate vials containing PBFS for further long-term fixation. The inflated state of the hearts was maintained by gentle agitation, and if required further injection of PBFS via the cannulated vessels, until all chambers were full of fixative and the hearts were floating freely without contact with the vial walls; particular care was taken over the thin-walled atria. Samples were considered fully fixed after 48 hours fixation.

All procedures were carried out under the UK Home office regulations (Animal Scientific Procedures, Act 1986)

2.3 *Ex-vivo* Imaging techniques

2.3.1 Back scattered scanning electron microscopy

BSSEM was used to investigate the affinity and localisation of iodine in various biological soft tissues. Tissue samples were obtained from perfusion fixed (see above methodology) mouse, Rat and embryonic pig subjects. BSSEM was conducted in collaboration with Professor Alan Boyde (Queen Mary University of London).

2.3.1.1 Tissue embedding

Prior to scanning samples were embedded in polymethylmethacrylate (PMMA). In brief, fixed tissue samples were washed in 70% ethanol for 2 hours, and then stored in 100% ethanol for 24 hours, then transferred to Xylene for 24 hours, during which the xylene solution is changed twice, Samples are then added to the liquid monomer, Methylmethacrylate, for at least 24 hours, benzoyl peroxide is then added to catalyse cross linking and the formation of the polymer- PMMA. Samples are then baked at increasing temperatures (37, 45, 50°C) until a hard acrylic like state is achieved. PMMA blocks are then trimmed, and the block surfaces smoothed and diamond polished.

2.3.1.2 Iodine Contrast enhancement

A 7.5% solution of molecular iodine dissolved in potassium iodide (I_2KI) was applied neat by pipetting directly onto the prepared PMMA block surfaces, the solution was left in place for 2-3 minutes. The I_2KI was then washed off with distilled water and the block blotted dry.

2.3.1.3 Scanning procedure

Embedded and stained samples were imaged using 20 kV BSE in a Zeiss EVO MA10 SEM, uncoated, using a chamber vacuum of 49 Pa. Probe current ranged from 1.0-1.5 nA and working distance ranged from 8-12 mm.

2.3.2 Contrast enhanced micro computed tomography

Contrast enhanced Micro-CT was used to rapidly and non-invasively obtained high resolution (6-50µm) tomographic data sets of soft tissue samples. Data sets are 3D

matrices made up of isometric voxels, whose grayscale value represents the X-ray attenuation at a point in space (dark = low attenuating, light = high attenuating). data was subsequently used for detailed morphological analysis. Training in the use of Micro-CT scanner was conducted under the supervision of Dr Nathan Jeffery (The University of Liverpool).

2.3.2.1 Iodine Contrast enhancement and Imaging

Samples were removed from PBFS, drained and blotted dry. Samples were then fully immersed in a solution of I_2KI contrast agent (iodine crystals (I2), potassium iodide (KI), added to PBFS) at various concentration (1.87, 3.75, 7.5 or 15%), for various durations (2-7 days). Each sample was removed from the staining solution, rinsed with PBFS to remove excess stain and to prevent surface saturation, drained and blotted. Therefore, any spaces within samples (e.g. ventricular cavities) were thus filled only with air. The samples were then triple-bagged (in compliance with local regulations for the use of the micro-CT scanner) and securely supported centrally in a plastic (radiotranslucent) tube by placing additional thin polythene bags. This allowed alignment of the samples with the axes of the micro-CT scanner and to reduce the likelihood of rotational artefacts in the slice reconstructions. All specimens were micro-CT imaged with the Metris X-Tec custom 320 kV bay system at the EPSRC-funded Henry Moseley X-Ray imaging Facility, Manchester University. Imaging parameters were optimised for each specimen to maximise spatial and contrast resolution and to facilitate data handling. Scans were acquired using various targets (copper, silver, tungsten, or molybdenum) with X-ray energies ranging from 90-160 kV. 1440-3500 projections within the 360° rotation were recorded on a 2K x 2K Perkin Elmer 1621-16-bit amorphous silicon flat-panel detector with 200 μm pixel pitch, resulting in scan times of approximately 20-50 minutes. All scans were reconstructed using Nikon Metrolasis CT-Pro software (Metris XT 1.6) at 50% or 100% of the obtained resolution, with post processing and analysis taken into consideration. Isometric resolutions ranged from 6-50 μm.

2.3.3 Targeted contrast enhanced micro-CT

TCE uses the same principles as whole mount immunohistochemistry, were an antigen of interest is targeted with a primary antibody specific to it, the primary

antibody is then bound with a secondary antibody that facilitates visualisation of the level of antigen expression within the tissue. In TCE the secondary antibody is conjugated with a heavy metal which acts to attenuate X-rays, and thus allows non-invasive visualisation and quantification of a specific antigens expression within a tissue volume. In this case TCE was used to investigate the expression of neurofilament within full intact rabbit hearts.

2.3.3.1 Whole mount immunostaining

Samples are perfusion fixed at room temperature in glyoxal-based fixative (Shandon Glyo-Fixx, Thermo Scientific) (120-180 minutes) or in 10% PBFS (60 minutes), and then placed in 3% hydrogen peroxide in methanol (60 minutes), to purge any endogenous peroxidase activity. Samples were then washed in MABT (100mM maleic acid, 150mM Nacl, 1% Triton X-100) PH 7.4 (10 minutes), followed by MABT plus 0.5% saponin (10 minutes) to permeablise the tissue. Samples are then blocked in blocking solution (MABT, 0.5% saponin, 10% horse serum, 0.5% Roche Blocking Reagent (Roche applied sciences), 1% dimethylsulfoxide) (90 minutes), and incubated at room temperature overnight in mouse monoclonal anti-neurofilament middle primary antibody (NF-M) (Hybridoma Bank, USA) prepared at a concentration of 1:50 in blocking solution (MABT, 0.5% saponin, 10% horse serum, 0.5% Roche Blocking Reagent, 1% dimethylsulfoxide). The sample was washed three times in PBS (10 min each wash), before application of Donkey anti-mouse IgG HRP conjugated diluted 1:500 in blocking solution (MABT, 0.5% saponin, 10% horse serum, 0.5% Roche Blocking Reagent, 1% dimethylsulfoxide) (180 minutes). The sample was washed three times in PBS (Sigma) (10 minutes each wash), postfixed in 10% formalin in MABT (20 minutes), and washed three times in double distilled water (ddH_20) (10 minutes each wash).

2.3.3.2 Contrast molecular probes and Micro-CT imaging

The metal deposition scheme of an enzyme metallography kit (Nanoprobes EnzMet 6010, consisting of three proprietary solutions) from Nanoprobes, Inc. (Yaphank, NY) was used in place of a usual chromogen reaction. From the EnzMet kit, 7.5 ml of solution A was added to each sample and mixed gently (4 min), then 7.5 ml of Solution B was added and mixed gently (4 min), after which 7.5 ml of Solution C

was added and mixed. Samples were incubated at room temperature for 5–15 min and the staining monitored by eye. As the solution began to appear slightly gray (indicating nonspecific precipitation of silver), the samples were transferred to 1% sodium thiosulfate in 0.1% Triton (10 min**)** to stop the reaction and remove unreduced silver ions. For fixation and to allow long term storage, samples were washed in ddH_20 (5 minues), transferred to 75% methanol followed by 100% methanol. For scanning each sample was removed from methanol, drained and blotted. Therefore, any spaces within samples (e.g. ventricular cavities) were thus filled only with air. The samples were then triple-bagged (in compliance with local regulations for the use of the micro-CT scanner) and securely supported centrally in a plastic (radiotranslucent) tube by placing additional thin polythene bags. All samples were micro-CT imaged with the Metris X-Tec custom 320 kV bay system at the EPSRC-funded Henry Moseley X-Ray imaging Facility, Manchester University. Imaging parameters were optimised for each specimen to maximise spatial and contrast resolution and to facilitate data handling. Scans were acquired using a copper or silver target with X-ray energies ranging from 40-90 kV. 1440-3500 projections within the 360° rotation were recorded, resulting in scan times of approximately 20-50 minutes. All scans were reconstructed at 50% or 100% of the obtained resolution with post processing and analysis taken into consideration, isometric resolutions ranged from 18-50 μm.

2.4 Sample analysis: Image analysis

2.4.1 Image handling

Micro-CT and BSSEM and data was viewed, manipulated and analysed using ImageJ 1.45i (http://rsbweb.nih.gov/ij/). Regions of interest (ROI) within micro-CT data sets were reconstructed in 3D using volume rendering (VRT) and semi-automatic segmentation techniques in Amira 5.33 (see below). The resultant 3D meshes made up of the voxels attributed to the ROI could be manipulated and cropped in any orientation and their respective volumes, surface areas and dimensions quantified.

2.4.2 Data segmentation and visualisation

Using Amira 5.33 ROI within micro-CT data sets were segmented using 2 Semi-automatic segmentation techniques;

I) In this approach, pixel values representing X-ray attenuation within the anatomically defined ROI are recorded. A masking window is then created that identifies further structures of the region, on the basis that they will have similar pixel values, and thus discriminates the ROI from the surrounding tissue. The ‘magic wand’ tool is then used at the defined window settings to segment the structure slice by slice, that is to identify contiguous blocks of pixels that correspond to the defined window of pixel values. The 'magic wand' tool implements a recursive seed fill method of filling 2D graphic images; the selected seed is allowed to grow selecting adjacent pixels under the constraint of the masking window. The efficiency of the technique can be improved by the use of the interpolation function which anticipates the position of a structure over multiple slices between two reference planes. Where there was an overlap of pixel values between ROI and the surrounding tissues the limit line function was implemented, to make an objective identification of pixels near to boundaries between one level of attenuation and another.

II) This approach uses two stages: a primary segmentation based on inclusion of the ROI with its immediately surrounding air volume, and a secondary segmentation based on differential attenuation.

The regions of interest (ROI) are initially selected using an oversized 'brush' tool to incorporate both the ROI and a thin shell of empty space that just includes the outermost elements of the ROI. Using an large brush size that selects both ROI and surrounding regions of a significantly different set of pixel values (e.g space) allows for interpolations between large numbers of slices (10-200), and makes for a highly efficient method. The selection is then stored, and the range of pixel values within the anatomically defined ROI are recorded.Using the 'threshold' tool a masking window is then applied to the stored selection that identifies, and thus discriminates the ROI from the surrounding tissue or void space within the stored selection. The first selection is then removed leaving only the ROI pixels selected as the working volume. Segmented ROI are then smoothed and any small islands are removed, 3D

isosurfaces are then generated which can be quantified and viewed and cropped in any orientation.

Volume rendering:

Micro-CT data can also be visualised using volume rendering. In this rapid automatic technique, an opacity curve is windowed to include voxel values of interest and a 3D colour map selected. The resultant 3D volume is rendered using a VRT render mode in which voxels are assigned a level of opacity (0-100%) calculated from their CT attenuation value. The resultant 3D volume can be viewed and cropped in any orientation, but not quantified, thus both semi-automatic segmentation and volume rendering are used in data analysis.

3D segmentation:

In this method a 3D volume rendering is created, and ROI is then drawn around in 3D using the pencil tool (Amira 5.4.0). All pixels (space and myocardium) within the drawn boundary plane are selected, these pixels are then stored as a material, and unwanted tissue is removed using further 3D segmentation. Once segmented a window reflecting the ROI pixel values is applied to the material. This technique therefore allows rapid segmentation of complex structures, eliminating the need for laborious serial segmentation.

2.4.3 3D Filament analysis

3D filament analysis (Amira 5.4.0) was used to investigate and quantify the Purkinje fibre networks and coronary circulation of the heart. Originally developed for use in analysis of nerve dendrites the *Auto Skeleton* tool (Amira 5.4.0) traces connected regions according to a user-defined window level and converts the centerline of those regions into graphs composed of points, segments, nodes, and Loops. Individual and total segment length and widths can also be extracted. The *Interactive Tracer* tool enables semi-automatic tracing of specifc filaments based on their gray values using an innovative tracing algorithm developed by Visage Imaging. The user sets the starting and ending points of a segment and the *Interactive Tracer* finds the shortest line connecting the two points with respect to the user-defined data window.

2.4.4 Fibre orientation analysis

In Amira 5.33 ROI are segmented from micro-CT data using semi-automatic segmentation technique II, the selections are saved as a series of .TIFF files, creating a mask for each CT slice that only includes the ROI. Using Matlab (R2009b) the created mask is applied to the micro-CT data and structure tensor and fibre tracking analysis performed. Training using Matlab (R2009b) for fibre orientation was conducted under the supervision of Dr Jichao Zhao (The University of Auckland).

2.4.4.1 Structure tensor analysis

Grayscale intensity gradient information from micro-CT data can correspond to detailed internal structure, in this case the long axis of myocytes. Using Matlab (R2009b) the structure tensor method, representing gradient information for 3D imaging problems (Zhao et al., 2012, Krause et al., 2010), was implemented. The structure tensor contains gradient information at each voxel in the 3D volume in the form of a matrix. The tensor field is smoothed by convolving it with a Gaussian kernel before an eigenvalue decomposition solver is applied to obtain the eigenvalues and eigenvectors of the tensor field. Local fibre alignment is modelled as the orientation with the least signal variation, which corresponds to the eigenvector paired with the smallest eigenvalue. At the final stage, the fibre field is further smoothed by averaging fibre orientations in the neighbourhood of each voxel. Inclination and transverse fibre angles (figures 2.1, 2.2) at each voxel are then extracted for statistical analysis. The inclination angle, α, is the projection of this vector onto a vertical plane parallel to the epicardial boundary (yellow box figure 2.1). This angle is measured with respect to the horizontal and has values in the range from 0-1 (corresponding to 0°- 90°). The transverse angle, β, is the projection of the fibre vector onto the horizontal plane (blue box figure 2.1), with respect to the surface tangent plane defined as the epicardial boundary. The use of differing ranges for inclination and transverse angles allows simple differentiation between data sets during analysis. Conversion of extracted vectors to physical angles is possible during post processing.

2.4.4.2 Fibre tracking

State of the art reconstruction methods for fibre tracking using the structure tensor data have been developed previously (Zhao et al., 2012). We implemented a simple

line interpolation algorithm: the 3D trajectory propagates along a line starting from a seed point in a region of interest with a predefined sub-pixel size and varying vector orientation, and the vector orientation is continually updated by averaging eight neighbouring vectors in any new coordinate during propagation. Fibre tracks are then rendered in 3D using custom colour maps corresponding to either inclination or transverse angles.

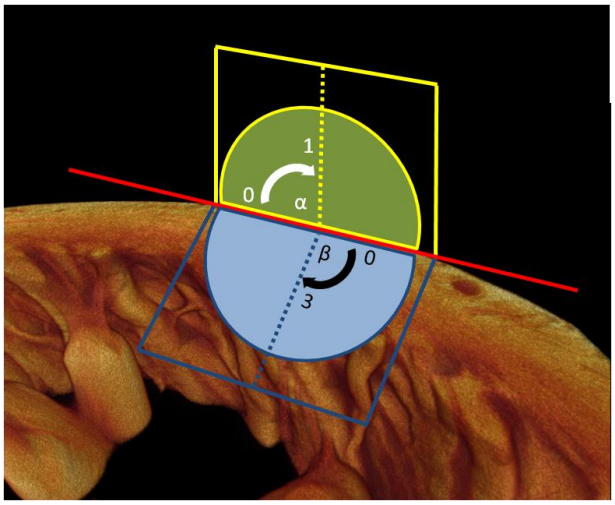

Figure 2.1 Schematic explanation of 3D fibre orientation: the inclination and transverse fibre angles. The inclination angle *α* is the projection of a fibre vector onto a vertical plane parallel to the epicardial boundary (yellow box). This angle is measured with respect to the horizontal (blue box) and has values in the range of 0-1 (0° to 90°). The transverse angle *β* is the projection of a fibre vector onto the horizontal plane (blue box), with respect to the surface tangent plane defined above (yellow box), values range from 0-3 (0° to 90°)**.**

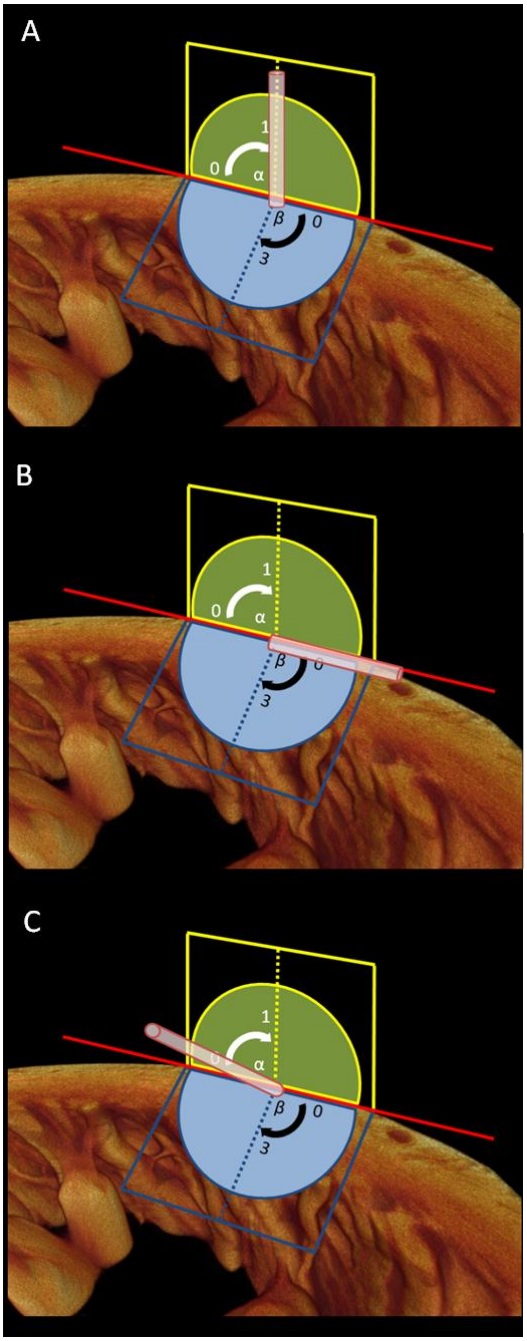

Figure 2.2 Schematic representations of the Inclination and transverse angles of examplelocal myofibre vectors. The pink fibre indicates the myofibre orientation at a point in the horizontal X-Y plane. A shows a vertically running fibre with high inclination angle of 1, and low transverse angle of 0. B shows a fibre running circumferentially with low inclination angle of 0, and low transverse angle of 0. C represents a fibre with a inclination angle of 0.5 and a transverse angle of 1.5.

2.5 Sample analysis: Histological analysis

To confirm morphology of structures identified in imaged data, contrast agent was leached out of previously scanned tissue by replacing the fixative with fresh PBFS at weekly intervals until yellow colouration in the fixative surrounding the sample ceased. Samples were then processed for histology using either frozen or paraffin sectioning techniques.

2.5.1 Frozen sections

Samples were mounted onto cork discs and immediately frozen in isopentane over liquid nitrogen, before being submerged in liquid nitrogen. Samples were then stored at -80°C for subsequent analysis. Serial sections, at 10µm were cut using a cryostat (Bright Instrument company, Ltd) and mounted onto subbed, glass slides. Slides of sectioned tissue were stored at -20°C for future analysis by histological staining.

2.5.2 Paraffin sections

Tissues were processed first through increasing grades of ethanol (70%, 90%, and 100% (x4) – 1hr in each) to dehydrate the tissue. Once dehydrated, tissues were cleared using two changes of xylene (45 minutes in each) before being passed through two changes of paraffin wax (1hr in each). Processing was performed using a Leica TP1020 tissue processor (Leica, Germany).

Following processing tissues were embedded in molten paraffin wax on a plastic chuck. Tissue blocks were then cooled until solidified, blocks were then sectioned using a Leica RM2245 semi-automated microtome (Leica, Germany). Sections were floated onto subbed glass slides and stored at room temperature.

2.5.3 Haemotoxylin and Eosin staining for gross morphology

Regressive haematoxylin and eosin staining was used to assess general morphology. With H & E staining muscle fibres appear pink and nuclei blue. Before staining, frozen sections were removed from the -20˚C freezer and left for 20-30 minutes to adjust to room temperature. Sections were then quickly dipped in tap water to

hydrate. Parrafin sections were deparaffinise in two changes of xylene (5 minutes) and hydrated through ethanol. In brief, the sections were stained with haematoxylin and eosin and then dehydrated through ascending grades of alcohol (50, 70, 90, 100%), cleared in xylene and finally mounted in Di-N-Butyle phthalate in xylene (DPX) (BHD, UK).

2.5.4 Sirius red staining for connective tissue distribution

Sirius red staining was used to asses connective tissue distribution. With Sirius red staining collagen appears red, muscle yellow and nuclei blue/black. Before staining, frozen sections were removed from the -20˚C freezer and left for 20-30 minutes to adjust to room temperature. Sections were then quickly dipped in tap water to hydrate. Parrafin sections were deparaffinise in two changes of xylene (5 minutes) and hydrated through ethanol In brief, the sections were stained with haematoxylin and Sirius red and then dehydrated through ascending grades of alcohol (50, 70, 90, 100%), cleared in xylene and finally mounted in Di-N-Butyle phthalate in xylene (DPX) (BHD, UK).

2.2.5 Masson's Trichrome for CCS confirmation and morphology

Masson's Trichrome staining was used to confirm the morphology of the CSS seen in micro-CT data. With Masson's trichrome staining muscle appears pink, CCS light pink, erthyrocytes red, collagen blue/green and nuclei blue/black. Before staining, frozen sections were removed from the -20˚C freezer and left for 20-30 minutes to adjust to room temperature. Sections were then quickly dipped in tap water to hydrate. Parrafin sections were deparaffinise in two changes of xylene (5 minutes) and hydrated through ethanol In brief, the sections were stained with haematoxylin, acid fuchsin, phosphomolybdic acid and methyl blue, and then dehydrated through ascending grades of alcohol (50, 70, 90, 100%), cleared in xylene and finally mounted in Di-N-Butyle phthalate in xylene (DPX) (BHD, UK).

2.6 Whole mount immunohistochemistry

Whole mount immunohistochmeistry was used to investigate the distribution of neurofilament throughout the right atrium in rabbit, and was carried out in collaboration with Dr Halina Dobrzynski (The University of Manchester). Whole rabbit hearts where dissected to expose the endocardium of the right atrium, first the apex of the heart and left atrial appendage (LAA) were removed. Next an incision was made up the left ventricular free wall running from the apical opening to the orifice left by removal of the LAA, and the papillary muscles of the left ventricle (LV) removed. The heart was then positioned with the RA and RV uppermost and pinned out by reflecting the LV 'flaps' created by the previous incision. An incision was then made up the RV free wall running from the apical opening to the right atrial appendage (RAA), a further incision was made running from the apex of the RAA round the lower border of the RA to the posterior wall, up the right hand side of the crista terminalis (CT) to the top of the superior vena cava (SVC). A final incision is made up the anterior border of the pulmonary artery (PA), the heart was then pinned out flat by reflecting the free running borders created, exposing the entire RA endocardial surface and the basal portion of the RV endocardial surface.

2.6.1 Whole mount immunostaining

An established protocol for the VECTASTAIN Elite ABC Kit (Vector Laboratories) was used and all solutions made up according to the manufacturer's instructions. The kit includes an appropriate normal serum, a biotinylated secondary antibody and a preformed avidin and biotinylated horseradish peroxidise macromolecular complex (ABC) reagent. Firstly the sample was fixed at room temperature in 10% PBFS (60 min), then washed three times in PBS (Sigma) (10 min each wash), and placed in 3% hydrogen peroxide in methanol (30 minutes), to purge any endogenous peroxidase activity. Following a brief wash with ddH_2O the sample was permeabilised by treatment with 0.5% Triton X-100 (in PBS) (30 min) followed by three PBS washes (10 min each wash). The sample was then blocked using the normal horse serum made up from the VECTASTAIN kit with PBS (60 min), then incubated with mouse monoclonal anti-neurofilament primary antibody (NF-M) (Hybridoma Bank, USA) prepared at a concentration of 1:50 in 1% bovine serum albumin (BSA) (Sigma) at room temperature overnight. The sample was then washed three times in PBS (10

min each wash) before application of the diluted biotinylated secondary antibody made up from the VECTASTAIN kit (120 min). The tissue was washed three times in PBS (10 min each wash). The ABC reagent from the kit was then applied (60 min) followed by three PBS washes (10 min each wash). To develop the signal, the DAB (3,3'-diaminobenzidine) Peroxidase Substrate Kit (Vector Laboratories) was applied until adequate development was achieved (1 to 3 min) and the reaction was stopped by immersion in ddH_2O for 10 min. The tissue was viewed and images recorded using a Zeiss SteREO Discovery.V8 microscope (Carl Zeiss Microscopy) with Axiovision v4.7 software (Carl Zeiss Microscopy).

2.7 Photomicrographs

Photomicrography was performed with a Leitz Diaplan microscope and images were captured using a digital Nikon 4500 cameara.

2.8 Statistical analysis

Statistical analysis was conducted in Microsoft Excel 2010 and Apple Numbers 2009 including; T-tests, F-tests, anovas and distribution and regression analysis.

CHAPTER 3

Principles, Development and Optimization of Contrast Enhanced Micro-computed Tomography

3.1 Introduction

The desire for true and accurate 3D representations of soft tissue structures has been ever present in the scientific community. Developmental, comparative and functional investigation of animal tissue morphology necessitates accurate visualisation and analysis of 3D tissue structure. In addition, modern genomic and mutational investigations into morphogenesis are equally dependent on 3D visualisation and interpretation of global morphological change. There are also many applications for 3D data in teaching, medical demonstration and surgical planning. These all require 3D images that accurately preserve 3D relationships within samples. Classical histology can offer high resolution images in a single plane, but is highly labour intensive and is plagued by registration issues (see below). Confocal microscopy provides suitable data, but is hampered by the fact that a sample depth of only a few hundred microns is viable. In block face techniques such as Episcopic microscopy, images are automatically aligned, but acquisition time is slow and the sample is destroyed in the process. Micro-CT imaging offers automatically aligned tomographic data sets with isometric resolutions of ~5μm attainable. The technique is non-invasive, fast, and economically viable for any laboratory. Micro-CT is based on X-ray interactions with the electrons of the sample (matter); therefore tissues with inherent high atomic numbers or electron-density can be easily visualised using micro-CT. As a result micro-CT has traditionally been used successfully for developmental and morphological analysis of calcified tissues.

Biological soft tissues are composed of elements with low atomic numbers/electron densities (e.g. carbon and oxygen), and as a result produce poor X-ray contrast. Therefore most soft tissues present similar X-ray attenuation coefficients between which no internal detail is resolved. The introduction of heavy elements in the form of contrast agents, with K-shell binding energies ideal for X-ray interactions, have allowed visualisation of internal soft tissue detail. Osmium tetroxide with its suitable k-shell energy of 73.9 KeV, has been successfully used as a micro-CT contrast agent for soft tissue contrast enhancement. However it has been shown to work poorly on tissue stored in alcohol, its soft tissue penetration is limited, and it is a toxic and volatile substance which is both expensive to purchase and dispose of. Iodine based contrast agents have proved effective in clinical practice. Here we assess the use of

an iodine based contrast agent (I_2KI) for mammalian soft tissue contrast enhancement. We investigate how concentration and incubation time of the contrast agent affects image quality, and investigate the mechanism behind differential uptake of iodine by different tissue types. We also examine how sample preparation affects soft tissue morphology, and investigate the most suitable X-ray targets for micro-CT imaging of soft tissue.

Some of the work in the following chapter has been published as:

Jeffery NS, Stephenson RS, Gallagher JA, Jarvis JC, Cox PG (2011) Micro-computed tomography with iodine staining resolves the arrangement of muscle fibres. Journal of Biomechanics 44: 503 189-192.

Jarvis J, Stephenson RS (2013) Studying the microanatomy of the heart in 3 dimensions: a practical update. Frontiers in Paediatric Cardiology, doi: 10.3389/fped.2013.00026.

The papers are appended.

New insights include; investigation of the mechanism of iodine uptake by soft tissue, the effects of sample preparation on tissue morphology and how X-ray targets affect image quality.

3.2 I_2KI as a contrast agent for micro-CT imaging

Molecular iodine is a 'heavy' molecule and therefore has a high atomic number (53), this means iodine has an ideal K-shell binding energy (33.2 KeV) for the X-ray spectrum produced by micro-CT X-ray tubes. Molecular Iodine (I_2) is insoluble in water but the addition of potassium iodide (KI) allows the formation of a soluble potassium tri-iodide molecule (I_2KI). To investigate the potential use of I_2KI as a contrast agent, I_2 was solubilised in KI and 10% phosphate buffered formal saline (PBFS). A 15% stock solution (10% I_2, 5% KI) was made up from which further dilutions were made. Figure 3.1 shows transverse micro-CT sections through a mouse head before and after iodine staining, and highlights the advantage of using a contrast agent for micro-CT scanning. Without the use of contrast agent non-

calcified tissue appeared as a homogenous structure, and no internal detail was resolved (figure 3.1A). However due to its inherent properties calcified tissue and its fine internal details were resolved (figure 3.1A). Figure 3.1B shows a mouse head stained by diffusion with 3.75% I_2KI for 7 days; iodine diffused into and was retained in the soft tissue structures, and thus increased their effective atomic number. The resulting differential attenuation is proportionate to the amount of iodine within a structure. Contrast enhancement allowed individual muscles and their complex internal detail to be resolved alongside the naturally high attenuating calcified tissue (figure 3.1B).

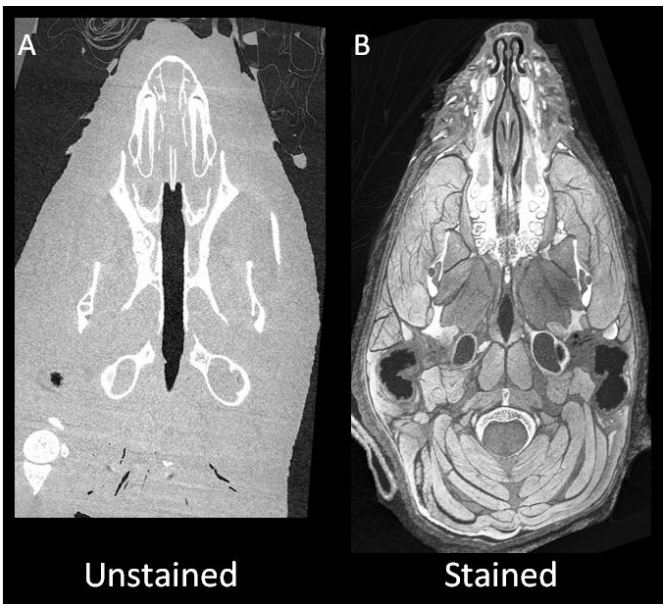

Figure 3.1 Transverse micro-CT images of unstained and I_2KI stained adult mouse heads. Showing the improved visualisation of internal soft tissue structures in a mouse head stained with 3.75% I_2KI solution for 7 days (B), compared with an unstained sample (A). Image acquisition by Dr Nathan Jeffery.

3.3 Optimisation of I_2KI contrast enhancement

I_2KI has been shown to be a suitable contrast agent for soft tissue contrast enhancement in micro-CT scanning (figure 3.1). To optimise the staining technique, variables affecting the quality of contrast enhancement were investigated. To assess the effect of I_2KI concentration, fixed rat hearts were chosen as a specimen tissue in which to investigate differential contrast in various tissue types and were stained with varying concentrations (15, 7.5, 3.75 and 1.89%) for the same incubation time

(2 days). Figure 3.2 shows longitudinal micro-CT sections through the hearts at a point where 4 major tissue types were present (fat, myocardium, nodal tissue and connective tissue). It was evident that concentration is an important variable in achieving the best image quality possible. At all concentrations fat appeared as the highest attenuating structure (figure 3.2). However, differentiation of the other tissue types was concentration dependent. Over staining was apparent in samples stained with 15% I_2KI (figure 3.2A,E): differentiation between myocardium and nodal tissue was achieved, but considerable overlapping of pixel values was evident, and connective tissue could not be clearly differentiated (figure 3.2 A,E). These results are probably due to saturation of the tissue. Under staining was seen in samples stained with 1.89% I_2KI: although differentiation of tissue types was achieved, internal detail was poorly resolved, and areas of the endocardium were unstained (figure 3.2 D,H). This suggests that effective diffusion of the contrast agent in a practical time frame is dependent on the presence of sufficient iodine molecules. Staining with 7.5% (figure 3.2B,F) and 3.75% (figure 3.2C,G) I_2KI yielded the best image quality. Connective tissue, nodal tissue, myocardium and fat (figure 3.2G 1-4) could be easily differentiated from one another, showing increasing levels of attenuation (pixel values) respectively.

To investigate the effect of both I_2KI concentration and incubation time on image quality, fixed mouse heads were stained with 7.5, 3.75 and 2.25% I_2KI for 1-7 days, and imaged using micro-CT (figure 3.3). Figure 3.3A shows a mouse head stained with 2.25% I_2KI for 7 days. Although this is long enough to although diffusion of the solution to the centre of the mouse head (~10mm), homogenous staining was not achieved. Figure 3.3B shows that increasing the concentration I_2KI to 3.75% provides consistent staining throughout the sample, and improved definition of internal structures. To show the staining process is not solely dependent on concentration, a sample was stained with a high concentration of I_2KI (7.5%) for 1 day (figure 3.3C); high contrast and fine detail was resolved at the posterior portion of the head, due to open access for the I_2KI via the exposed neck. However in other regions the stain had not diffused much below the epidermis, so the majority of the internal structures remained unstained. This highlights the need for a sufficient incubation period as well as a suitable concentration when using I_2KI as a contrast agent for micro-CT imaging of soft tissue.

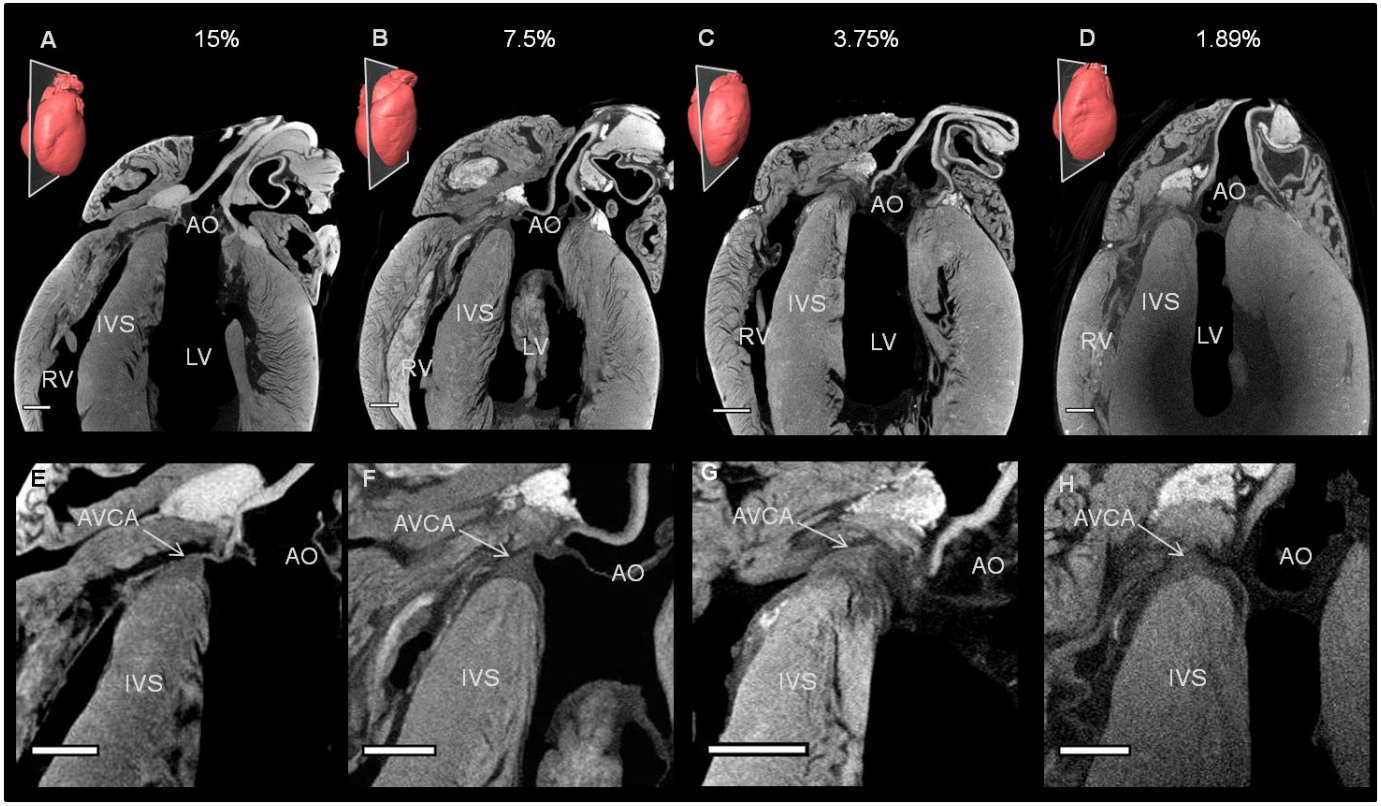

Figure 3.2 Longitudinal micro-CT images through 4 different rat hearts stained with different concentrations of I_2KI for 2 days. Hearts stained with 15, 7.5, 3.75 and 1.87% I_2KI concentrations respectively (A-D). Corresponding high power images focusing on the atrioventricular conduction axis (E-H). Inset 3D renderings of each heart show the associated planes of interest. AO- aorta, AVCA- atrioventricular conduction axis, IVS- inter-ventricular septum, LV- left ventricle, RV- right ventricle. (scale bar represents 1 mm)

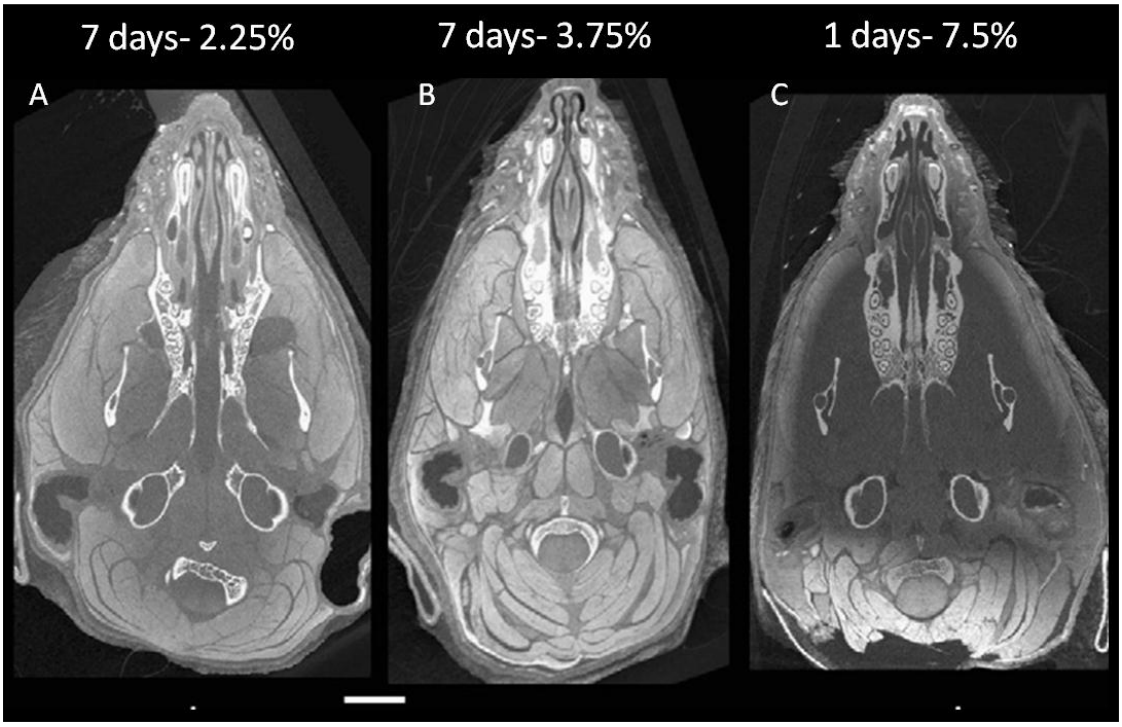

Figure 3.3 Transverse micro-CT images of adult mouse heads stained with I_2KI contrast agent. mouse heads stained with 2.25% I_2KI for 7 days (A), 3.75% I_2KI for 7 days (B) and 7.5% I_2KI for 1 day (C). (Scale bar represents approximately 3 mm). Image acquisition by Dr Nathan Jeffery.

3.4 Iodine interactions with soft tissue, and its affinity for glycogen and lipid complexes

Based on classical experiments of iodine interactions with glycogen and lipids, we tested whether the differential uptake of I_2KI by different tissue types was based on the amount of glycogen and or lipid within them. Fixed pig embryonic tissue (~45 days gestation) was stained with 3.75% I_2KI for 2 days and scanned using micro-CT. Figure 3.4A shows a sagittal section through the whole embryo. The liver, which is known to have a high glycogen content, appeared as a high attenuating (high pixel values) structure. This suggests iodine is preferentially residing in the organ over surrounding tissues. This was also clearly seen in transverse sections of the liver (figure 3.4C). The boundaries of organs appeared sharp, and there was little gradation at tissue edges, suggesting iodine accumulation is localised, and based on a tissues affinity for iodine. Areas where you would expect to see high attenuating

calcified tissue (eg vertebrae) appeared low attenuating structures. This is because at this stage of development endochondral ossification is yet to take place, indicating that cartilage does not readily take up iodine. Some nerve axons are sheathed by myelin, which acts to insulate axons, speeding up signal propagation and preventing electrical current from leaving the axon. The dry mass of myelin is ~80% lipid and ~20% protein, and therefore iodine should readily reside within the high lipid component. In transverse micro-CT sections through the embryo, high attenuating structures were evident inside and at the periphery of the vertebral column (figure 3.4B,C,D). Due to the lack of calcified vertebrae, it is likely that these structures represent the spinal cord and ventral root nerves respectively, with iodine preferentially residing in the lipid rich myelinated regions.

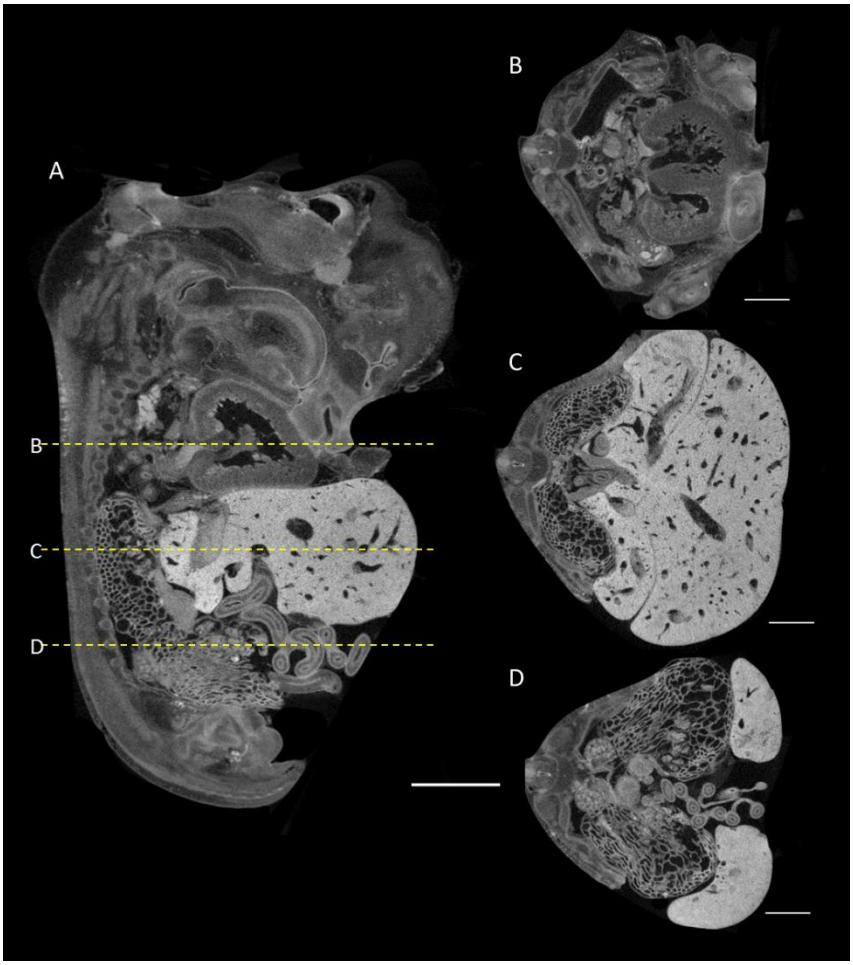

Figure 3.4 Micro-CT images of pig embryo stained with I_2KI contrast agent. Sagittal micro-CT image of pig embryo (~45 days gestation) stained with 3.75% I_2KI for 2 days, showing the position of transverse sections B,C and D (A). Transverse micro-CT images through heart (B), liver (C) and intestine (D). (Scale bars represent 1 mm and 0.5 mm)

Although images with spatial resolutions as low as 5µm are attainable from micro-CT, back scattered scanning electron microscopy (BSSEM) offers a spatial resolution of <1nm, and a depth of field of ~1000µm is achievable. To investigate the interaction of iodine with soft tissue at a sub µm level, various tissue types from mouse were processed for BSSEM (in collaboration with Professor Alan Boyde, Queen Mary University, London). This is a suitably comparative technique to micro-CT as the signal is based on interactions of incident electrons with the sample (matter). K-shell interactions are proportionate to atomic number, and therefore areas of high atomic number produce a bright signal. Skeletal muscle, cardiac, brain and liver tissue were dissected from a perfusion fixed whole mouse. Prior to scanning, samples were dehydrated and embedded in polymethylmethacrylate (PMMA) (methods 2.3.1). PMMA blocks were then trimmed and the block faces smoothed and diamond polished. A 7.5% I_2KI solution in methanol was applied by pipetting directly onto the prepared PMMA block surfaces, the solution was left in place for 2-3 minutes, then the I_2KI was washed off with distilled water and the block blotted dry. Embedded and stained samples were imaged using 20 kV BSE in a Zeiss EVO MA10 SEM, uncoated, using a chamber vacuum of 49 Pa. Probe current ranged from 1.0-1.5 nA and working distance ranged from 8-12 mm (Queen Mary, University of London). Figure 3.5 shows BSSEM images from the liver which further indicates iodine's affinity for glycogen. At low power, bright areas were evident around the portal regions, suggesting an increased level of iodine was residing in these regions (figure 3.5A). At high power iodine was seen residing in hepatocytes, and preferentially in hepatocytes surrounding the portal region (figure 3.5B). Portal regions are rich in glycogen as the portal veins carry blood rich in nutrients from the gastrointestinal tract to the liver to be processed.

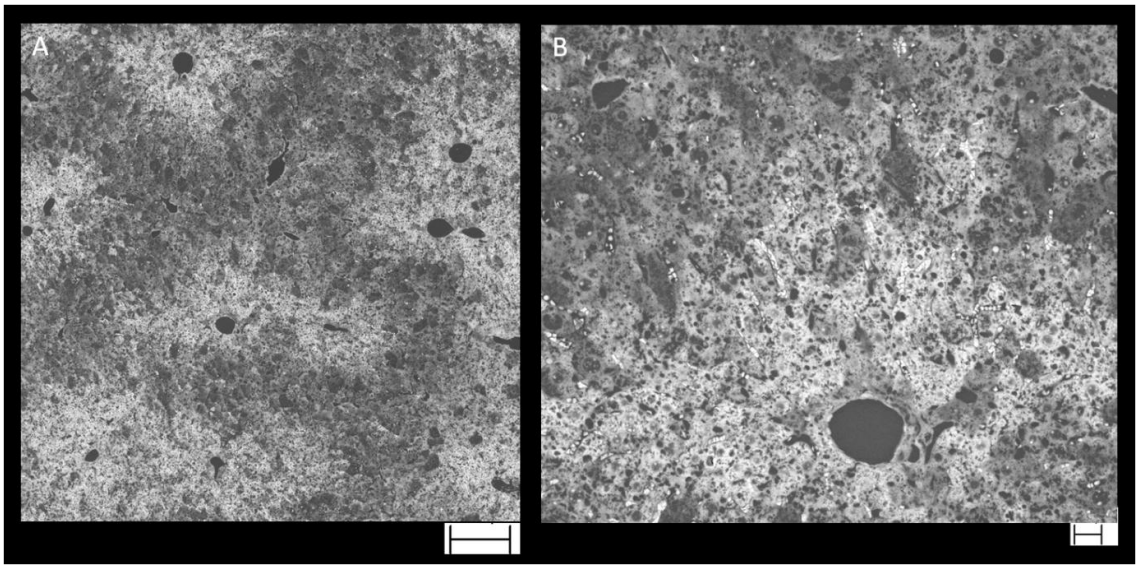

Figure 3.5 Transverse BSSEM images of a mouse liver stained with 7.5% I_2KI. showing iodine accumulation around hepatic portal regions at low (A) and high power (B). (Scale bars represent 100 µm and 20 µm respectively)

BSSEM images of skeletal muscle showed differential iodine uptake between (figure 3.6A) and within (figure 3.6B) single muscle fibres. Figure 3.6A shows a longitudinal image of tibialis anterior (TA), a skeletal muscle responsible for dorsiflexion of the foot. Iodine appeared to reside more readily in some fibres than others, the apparent banding created suggests the glycogen rich slow twitch muscle fibres have taken on more stain than the fast twitch fibres which contain reduced levels of glycogen. Figure 3.6B shows a high power image of the extensor digitorum muscle (EDL), which is involved in extension of the foot. The banding in this image represents individual sarcomeres, the functional subunits of a muscle fibre. It appeared iodine preferentially accumulated (bright bands) in regions where actin and myosin filaments overlap, the A band. The thick dark bands running either side of the A band are likely to represent the I band, this region is not infiltrated by thick myosin filaments, and includes the z disk where actin filaments of adjacent sarcomeres anchor themselves. Fine dark bands were observed running down the centre of the A bands, which corresponds to the H zone, the central region of the sarcomere where only the tails of myosin filaments are present. Figure 3.6A and B therefore strongly suggests iodine resides preferentially in areas of high glycogen content on a subcellular scale. Figure 3.6C shows a BSSEM image through a

coronary artery surrounded by ventricular myocardium. Within the vessel lumen red blood cells produced a very high signal, suggesting a high iodine uptake, however some cells with a low signal were observed. This suggests the iodine was differentiating between glycogen rich and glycogen starved red blood cells.

We have previously described the ability to differentiate between cardiac tissue and connective tissue using iodine contrast enhancement for micro-CT imaging (Stephenson et al., 2012). Using BSSEM this differentiation was seen at the level of a single Purkinje fibre (figure 3.6D); the Purkinje cells produced a considerably higher signal then the surrounding connective tissue.

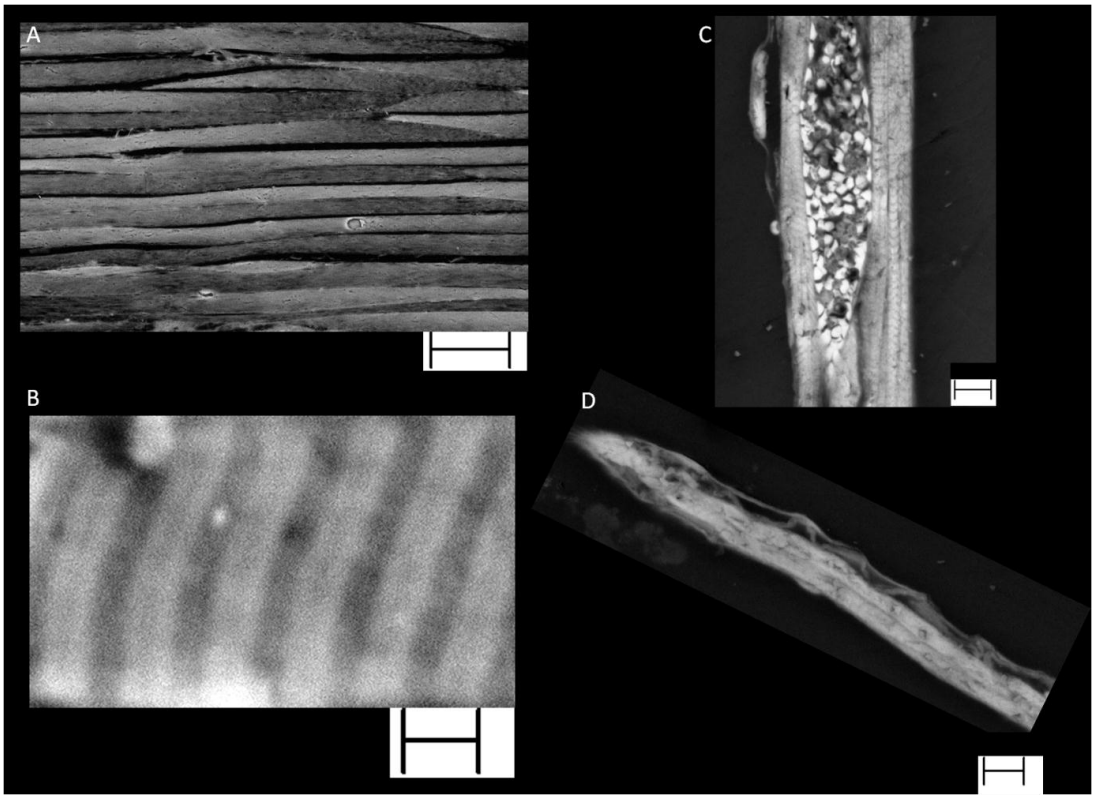

Figure 3.6 BSSEM images of a mouse soft tissue samples stained with 7.5% I_2KI. longitudinal BSSEM image of tibialis anterior muscle (scale bar represents 100 µm), showing multiple muscle fibres (A), high power longitudinal BSSEM image of extensor digitorum longus muscle (scale bar represents 2 µm), showing sarcomere arrangement within a single fibre (B). BSSEM image through a coronary artery embedded within the myocardium, showing the arrangement of blood cells within the vessel lumen (scale bar represents 10 µm) (C) and longitudinal BSSEM image through a free running Purkinje fibre (scale bar represents 10 µm) (D).

Samples of mouse cerebellum and cerebrum were processed for BSSEM to investigate the interaction of iodine with the lipid rich regions of the brain. White matter axons are insulated with lipid rich myelin, this gives it its pinkish white appearance in a freshly cut brain. Sagittal images through the cerebellum at increasing magnification are shown in figure 3.7A,B and C. The dashed yellow line in figure 3.7B corresponds to the plot profile of gray values in figure 3.8 (each voxel within the 3D volume is assigned a gray scale value based on its X-ray attenuation). The gray values (signal) of white matter (WM) were higher than those observed in the molecular layer (ML), which corresponds to grey matter (figures 3.7B and 3.8). Iodine is thus residing preferentially in the lipid rich white matter (figure 3.7). The highest gray values were seen in the granular layer (GL) and in the large Purkinje cells (PC) (figure 3.7 and 3.8). The granular layer is made up of densely packed granule cells and large golgi cells, in contrast the ML is more sparsely populated, and consists mostly of dendrites from PCs and parallel fibres from granule cells. PCs are some of the largest neurons in the brain, and have up to 200,000 parallel fibres running through them. The GL and PCs are an example of how high tissue density and large cell size can influence X-ray interactions. Another example of this effect is iodine's interaction with nodal tissue (figure 3.2). Although the nodal cells are glycogen rich, they are small (compared to working myocytes) and sparsely arranged compared to the dense working myocardium, and thus nodal tissue appears as a low attenuating region (figure 3.2) (for further detail see Chapter 6).

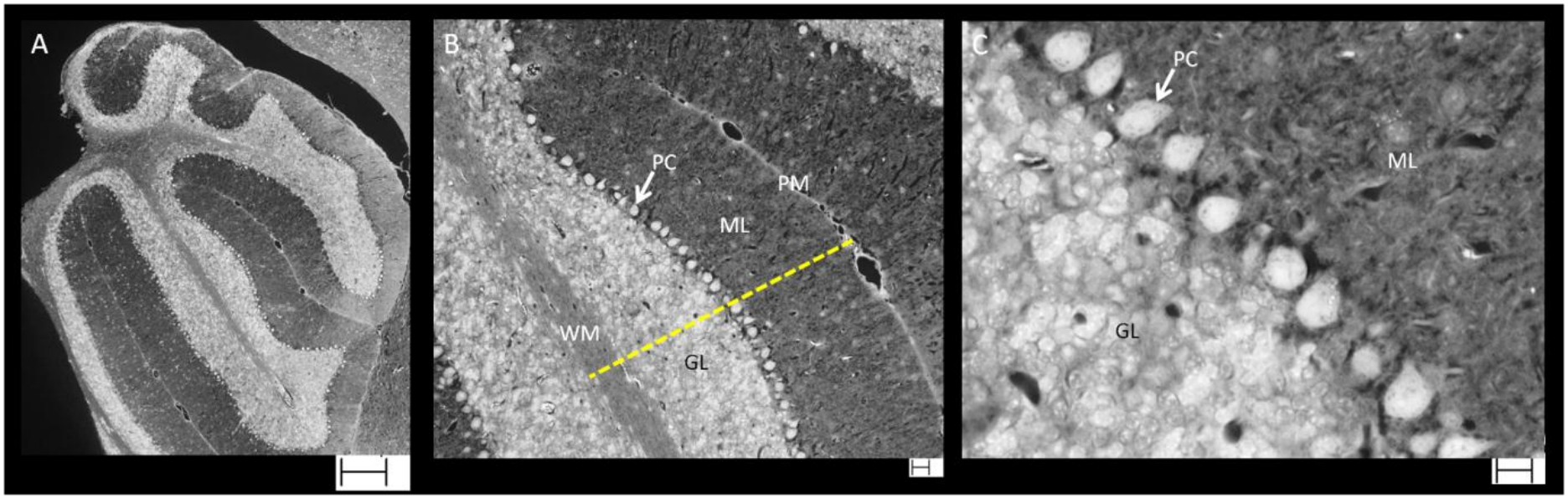

Figure 3.7 Sagittal BSSEM images through a mouse cerebellum stained with 7.5% I_2KI. Showing low (A), mid (B) and high power (C) images. Iodine can be seen to preferentialy reside in lipid rich regiosn. GL- granular layer, ML- molecular layer, PC- Purkinje cell, PM- pia mater, WM- white matter. Yellow dotted line represent plot profile plotted in figure 3.8. (scale bars represent 100 µm, 20 µm and 10 µm respectively)

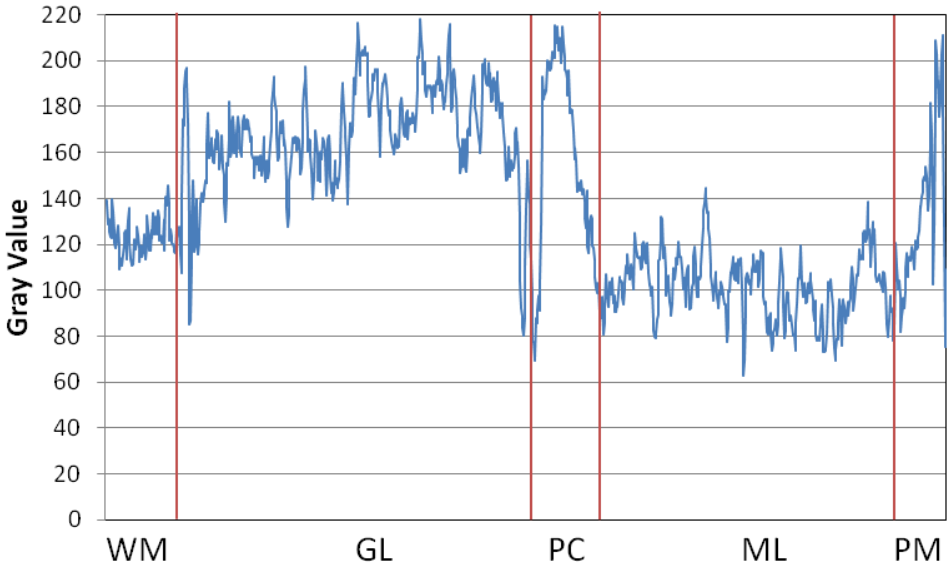

Figure 3.8 Plot profile of gray values across BSSEM image of mouse cerebellum stained with 7.5% I_2KI. Yellow dotted line shown in figure 3.7B indicates plane used for plot profile. Increased gray values indicates increased signal intensity in BSSEM image and hence iodine accumulation. GL- granular layer, ML- molecular layer, PC- Purkinje cell, PM- pia mater, WM- white matter.

3.5 The effects of perfusion fixation on the image quality of soft tissue imaged using contrast enhanced micro-CT

Previously we have noted the negative affect residing blood can have on micro-CT image quality (Stephenson et al., 2012, Jarvis and Stephenson, 2013). To investigate how tissue preparation can enhance the image quality of cardiac tissue, a perfusion fixation methodology was developed in rabbit (methods 2.2.4 (Stephenson et al., 2012, Jarvis and Stephenson, 2013)). Systemic heparin was administered prior to termination by intravenous injection under isoflurane aneshesia (2000 Units/kg). The rabbits were then terminated by overdose of sodium pentobarbitone. The thoracic cavity was exposed, the pericardium was removed, and the inferior vena cava and descending aorta cannulated. In order to clear the heart of blood, the chambers were flushed *in situ* via the inferior vena cava and aorta with heparinised saline (5000

Units/ml) until the expelled solution ran clear. The heart was then fixed by a period of perfusion with PBFS (approx. 10 mins) by retrograde injection via the aorta, allowing perfusion of the coronaries. If necessary, further PBFS was passed through the heart via the inferior vena cava. All major vessels (IVC,SVC, Aorta, PA, PVs) were clamped using surgical vessel clamps to allow inflation of the heart chambers with PBFS. The partially fixed hearts were then removed to separate vials containing PBFS for further long-term fixation. The inflated state of the hearts was maintained by gentle agitation, and if required further injection of PBFS via the cannulated vessels, until all chambers were full of fixative and the hearts were floating freely without contact with the vial walls. Particular care was taken over the thin-walled atria. *In situ* heparinisation followed by perfusion fixation, accompanied with careful monitoring, produced naturally inflated hearts with no residing blood in the atrial or ventricular cavities (figure 3.9B). The level of inflation was validated by cross reference with *in vivo* echocardiography (see Chapter 8.6). Heparinisation and flushing prevented visual impairment of internal structure by residing blood, which otherwise would readily take up the iodine (as shown previously in figure 3.6C) and appear as a high attenuating structure. Figure 3.10 shows image data and volume renderings from a sample that has been immersion fixed (figure 3.9A,C,E), and a sample that has undergone perfusion fixation (figure 3.9B,D,F). Perfusion fixation removed all residing blood from the ventricular and atrial cavities, and naturally inflated the heart chambers (figure 3.9B). Figure 3.10C,E show volume renderings of the atrial and ventricular cavities from a immersion fixed heart, it was not possible to visualise internal details of the cavities or endocardial surfaces. In contrast, corresponding volume renderings from a perfusion fixed heart revealed the striking fine detail micro-CT can resolve (figure 3.9D,F), detail which would otherwise be hidden by residing blood. Ridding the hearts of blood also aided analysis and quantification of the cavities and internal structures. The detailed cardiac anatomy revealed here is discussed and analysed further in chapters 5, 6, 7 and 8.

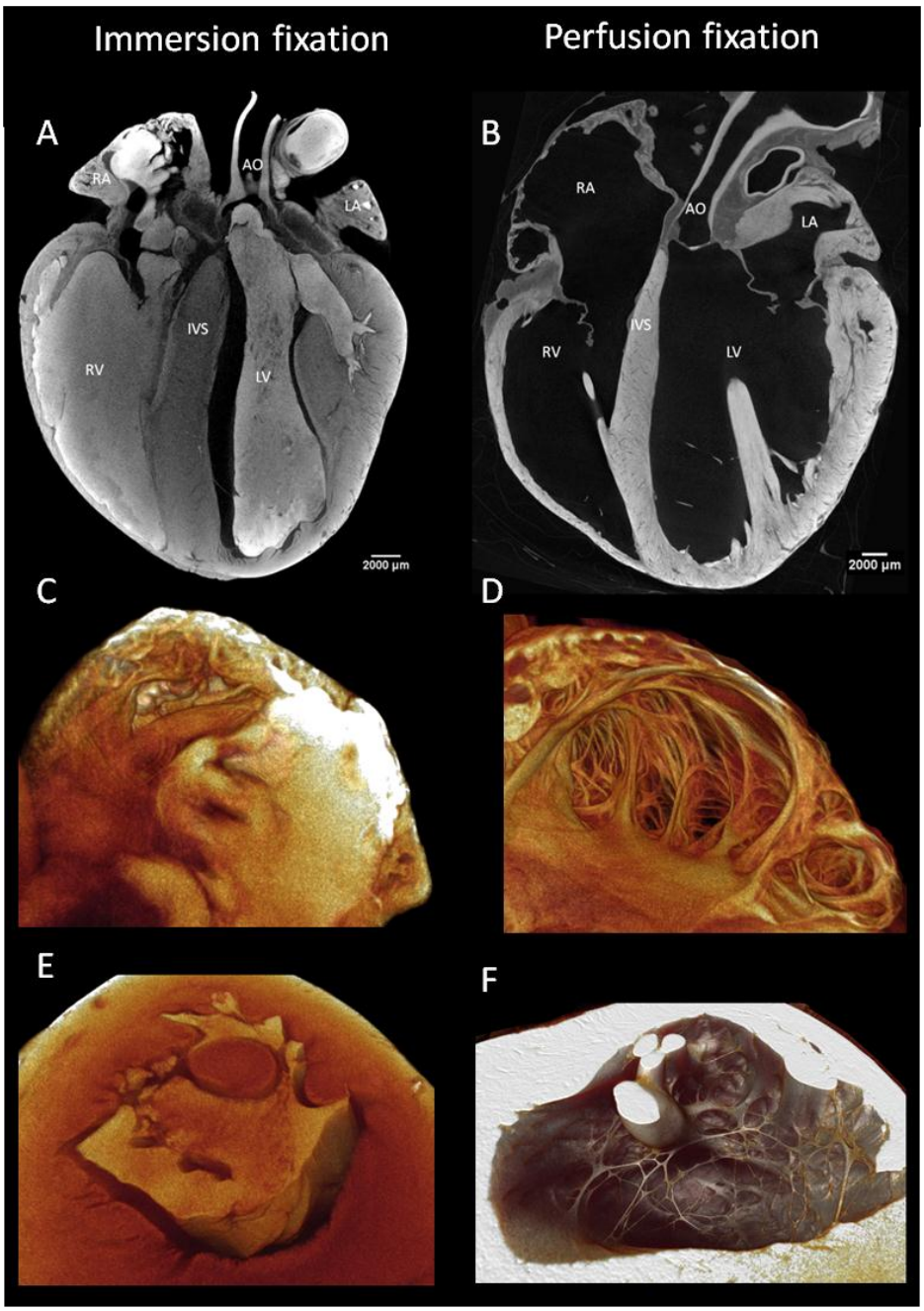

Figure 3.9 Micro-CT images and volume renderings of immersion fixed and perfusion fixed rabbit hearts. Longitudinal micro-CT images of hearts immersion fixed (A) and perfusion fixed (B). Volume renderings of right atrial and left ventricular cavities of immersion fixed (C,E) and perfusion fixed (D,F) hearts. (scale bars represent 2000 µm)

Perfusion fixation not only removed residing blood from the cavities, it also removed blood residing within blood vessels in the walls of the myocardium. Figure 3.11 shows transverse micro-CT images from the ventricle in a sample that has been

immersion fixed (figure 3.10A,B), and a sample that has undergone perfusion fixation (figure 3.10C,D). Although internal transmural detail was observed in both samples, perfusion fixation allowed the detailed laminar sheet formation to be resolved throughout the ventricles (figure 3.10C,D). Without perfusion fixation the epicardium and mid wall regions appeared as a homogenous mass of tissue (figure 3.10A,B). Perfusion fixation allowed for interpretation of the laminar sheet formation in 3D throughout the ventricles (see Chapter 5.8), and also allowed for novel analysis of 3D fibre orientation throughout the whole heart (see Chapter 5,6,7,8).

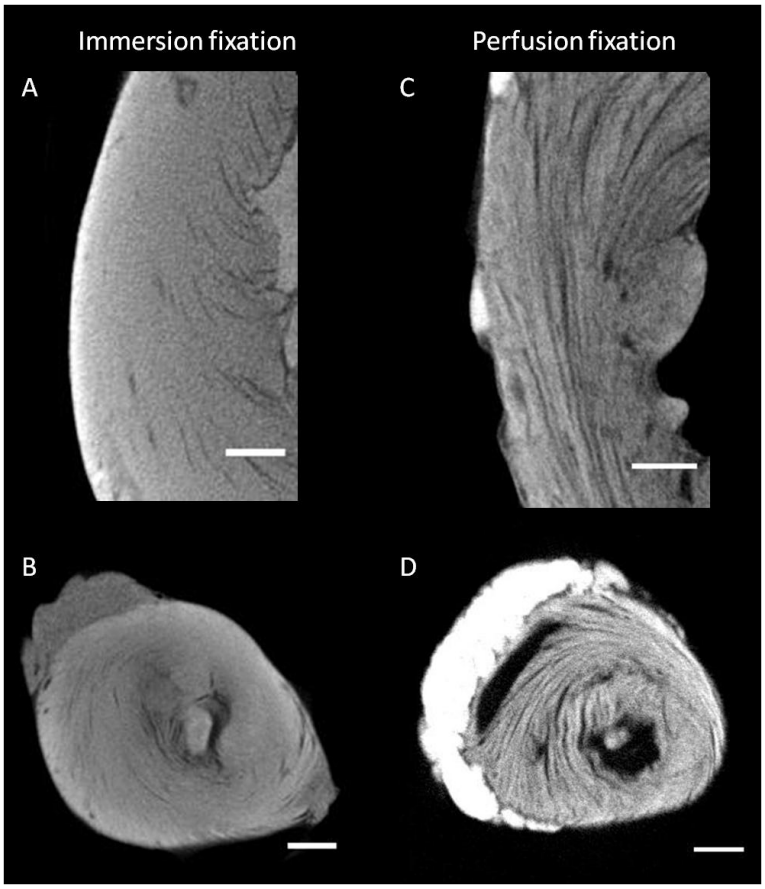

Figure 3.10 Transverse micro-CT images from immersion fixed and perfusion fixed rabbit hearts. Showing images of the posterior left ventricular wall at the basal region (A,C), and images from the apical region (B,D), from immersion fixed (A,B) and perfusion fixed (C,D) hearts. High attenuating regions indicate iodine-lipid interaction. (scale bars represent 1 mm)

3.6 The effects of X-ray targets used for contrast enhanced micro-CT imaging on soft tissue image quality

X-rays are produced by electron interactions with matter, and can be generated by an X-ray tube. Within the X-ray tube is a cathode, which under high voltages produces electrons that are accelerated through a vacuum at high velocity. The high velocity electrons collide with a metal target, the anode, which generates the X-rays. The target (anode) material within an X-ray tube determines the X-ray spectrum the tube produces. The X-ray spectrum of any particular target is made up of a continuous Bremsstrahlung spectrum with numerous spikes created by characteristic interactions (Introduction 1.5.3.2). The wavelength of the characteristic spikes is inversely proportional to the atomic number of the target material. This suggests when using I_2KI as a contrast agent a target with an atomic number close but greater than iodine should produce the most photons with a suitable k-shell binding energy, and thus provide the best image contrast. However the accumulative effect of tissue depth on attenuation also needs to be considered. The standard target used in micro-CT imaging is tungsten (W). However, the Metris X-Tec custom 320 kV bay system at the EPSRC-funded Henry Moseley X-Ray imaging Facility (Manchester University) allows the target material to be changed easily, a process that would require specialist technical support in standard scanners. To investigate the effects of different X-ray targets on image quality, a fixed rabbit heart stained with 3.75% I_2KI for 5 days was scanned using a copper (Cu) target, and the I_2KI was subsequently removed from the heart using multiple PBFS washes. The same heart was then restained with 3.75% I_2KI for 5 days and scanned with silver (Ag), molybdenum (Mo) and W targets. All scans were optimised for X-ray transmission and image quality. Acquired scan data was manipulated into the same orientation, and from transverse sections at the same plane (see figure 3.11) plot profiles of the gray values across the left ventricular wall were plotted (figure 3.11 yellow dotted line) for each data set (figure 3.11). Surprisingly, there was negligible difference in image contrast when comparing the different X-ray targets. All targets showed clear contrast between myocardium and space, and internal transmural detail was resolved (figure 3.11). With all targets the major tissue types; fat, myocardium, nodal tissue and connective tissue, could be differentiated with decreasing attenuation coefficients respectively. Of the targets used, the atomic number of Ag (47) was the closest to

that of iodine (53), yet there was no discernible improvement in image quality over the other targets. We did measure some subtle differences: the Mo target did provide the best transmural contrast, showing the biggest difference in gray values between laminar sheets and space (figure 3.11C). The Cu target provided the best transmural detail; the increased number of peaks within the plot profile suggests an increased number of laminar sheets have been resolved. Cu also produced the steepest curve at the myocardium-space boundary, suggesting a reduced signal averaging effect (figure 3.11A). To assess the effect of X-ray targets on the differentiation of different tissue types, plot profiles encompasses four different tissue types (fat, myocardium, nodal tissue and connective tissue) were plotted from image data of rabbit hearts scanned using Cu (figure 13.12A) and W (figure 13.12B) targets. The Cu target provided superior differential contrast between soft tissues, with larger differences in gray values observed between different tissue types (figure 13.12). Transitions at tissue boundaries were sharper in the Cu target images. In W target images smooth transitions, especially between nodal and myocardial tissue were observed, suggesting reduced contrast resolution (figure 13.12). These results influenced future scans, in that only Cu and Mo targets were used when imaging iodine stained soft tissue.

3.7 The effects of rescanning, restaining and radiation on fixed soft tissue.

During a micro-CT scan, samples are subjected to levels of electromagnetic radiation in the form of X-rays similar to those used in clinical imaging techniques. However, the increased exposure times used in micro-CT imaging mean samples are exposed to levels of radiation which would not be acceptable in a clinical setting. To assess the effects of radiation on gross soft tissue morphology a fixed rabbit heart stained with 3.75% I_2KI for 5 days was scanned as usual. The I_2KI was then removed from the heart using multiple PBFS washes. The same heart was then restained with 3.75% I_2KI for 5 days and scanned a further 3 times under optimal conditions with 3 different X-ray targets. All scan data was virtually manipulated into the same orientation and from four transverse planes, evenly spaced from based to apex, left ventricular free wall (LVFW) and left ventricular internal dimension (LVID) measurements were recorded (figure 3.11 yellow dotted lines). This also allowed

investigation of how restaining soft tissue affects morphology. ANOVA tests at each region showed, there was no difference in LVFW ($p=<0.99$) or LVID ($p=<0.99$) measurements (figure 3.13). This shows multi-scanning and hence radiation exposure during micro-CT scans does not affect gross tissue morphology of previously scanned tissue. This also suggests the removal of the I_2KI contrast agent and restaining of previously scanned samples is acceptable, as there was no significant change in tissue morphology after the first scan (Cu) (figure 3.13). To investigate the effects of micro-CT scanning on tissue morphology at a cellular level, contrast agent was removed from previously scanned tissue using multiple PBFS washes. Tissue preparations were then wax embedded and processed for histology. Inspection of cell structure and morphology from mounted histology sections showed cell structure and integrity was normal, and impressive correspondence with micro-CT data was achievable (figure 6.2). This confirms that both the gross and microscopic anatomy is preserved in micro-CT scanned soft tissue, thus validating any further experimental investigation of previously scanned tissue.

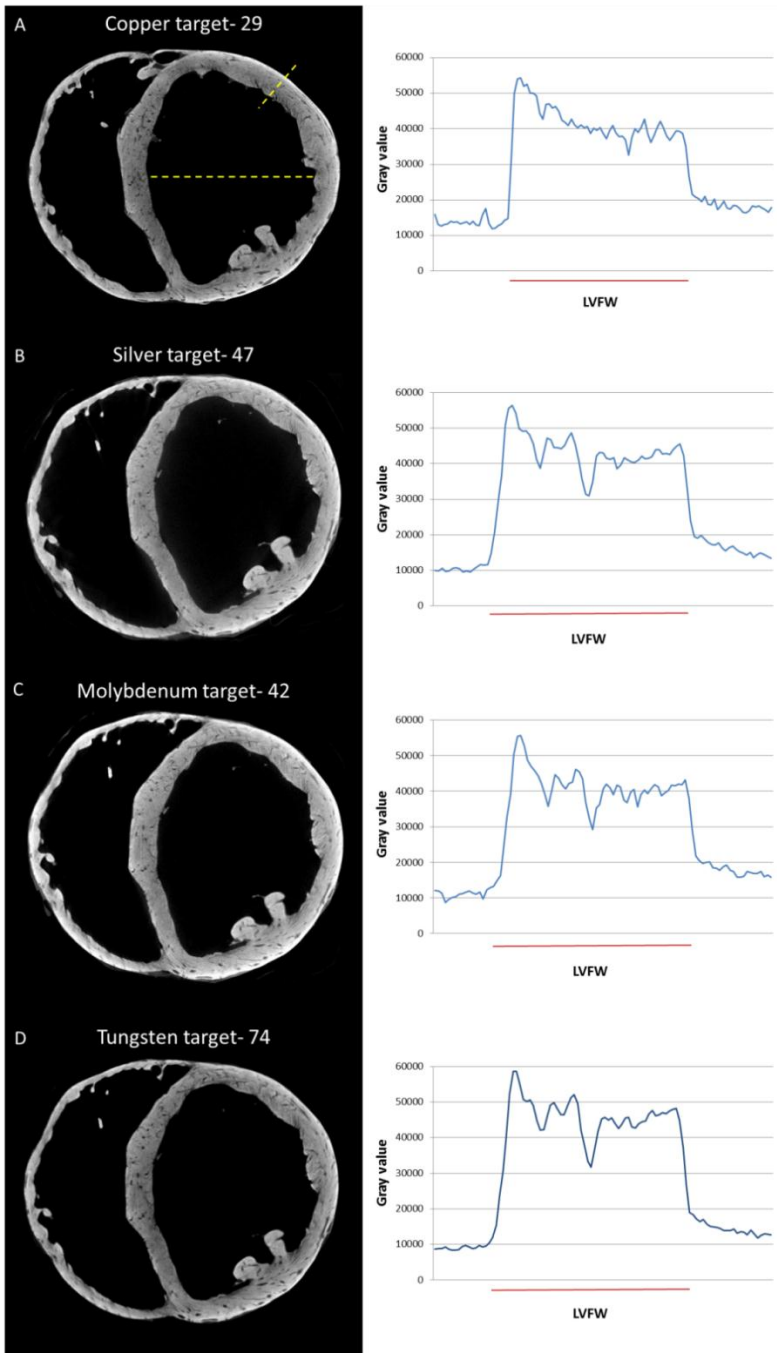

Figure 3.11 Micro-CT images and plot profiles of rabbit hearts scanned with different X-ray targets. Transverse micro-CT image (acquired with copper target) of rabbit heart stained with 3.75% I_2KI for 5 days with corresponding plot profile of gray values across left ventricular free wall (LVFW) (small yellow dotted line) (A). B-D shows the same sample as shown in A, bled of iodine, restained (3.75% I_2KI for 5 days) and rescanned with silver, molybdenum and tungsten targets respectively, corresponding plot profiles are shown. Target values represent atomic number. Small yellow dotted line represents plane for plot profiles. Red line indicates values for myocardium, extremities represent space. Large yellow dotted line indicates example LVID measurement.

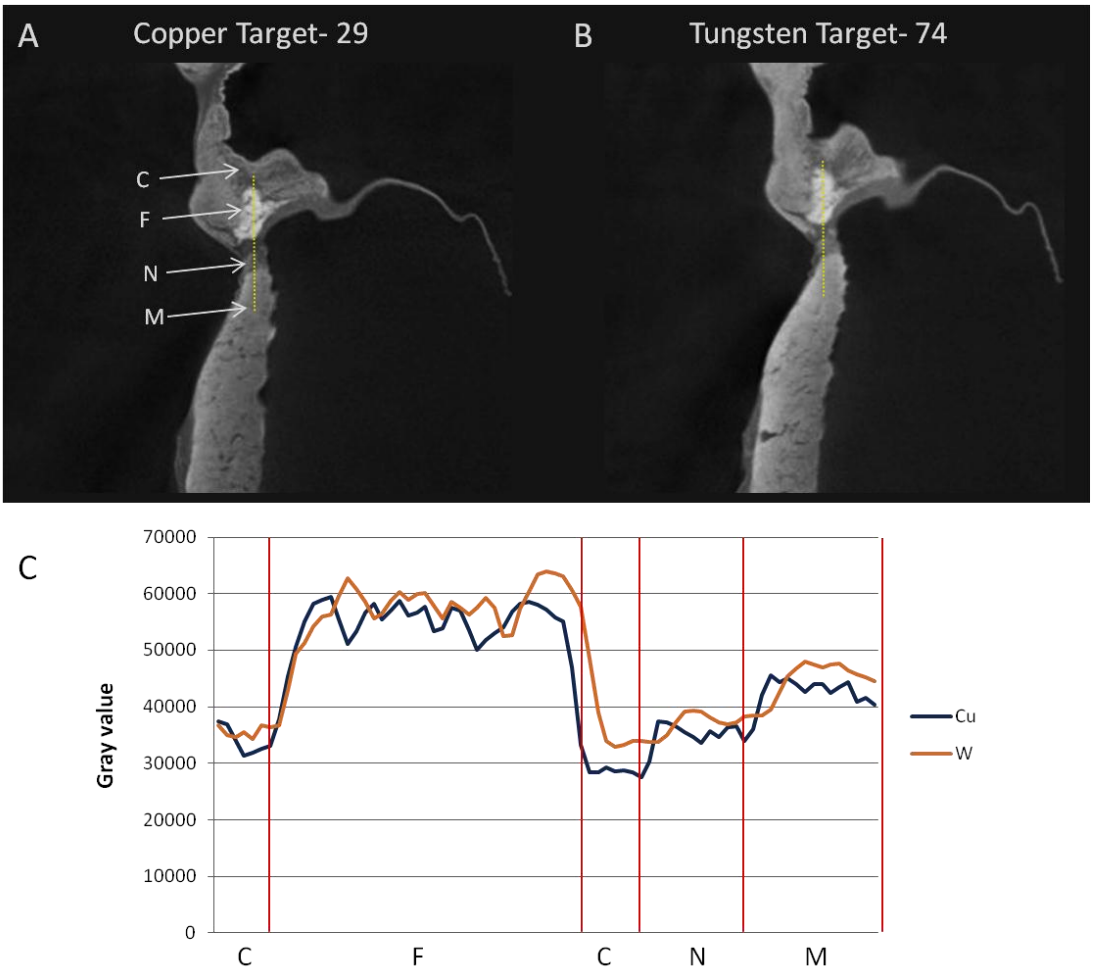

Figure 3.12 Comparison of different X-ray targets for micro-CT imaging of different tissue types. Longitudinal micro-CT images of rabbit intervetricular and interatrial septa stained with 3.75% I_2KI for 5 days, acquired with copper target (A), and Tungsten target (B). Corresponding plot profile of gray values across four major tissue types (yellow dotted line in A and B) using copper (Cu) and tungsten (W) targets (C). Target values represent atomic number. C- connective tissue, F- fat, M- working myocardium, N- nodal tissue.

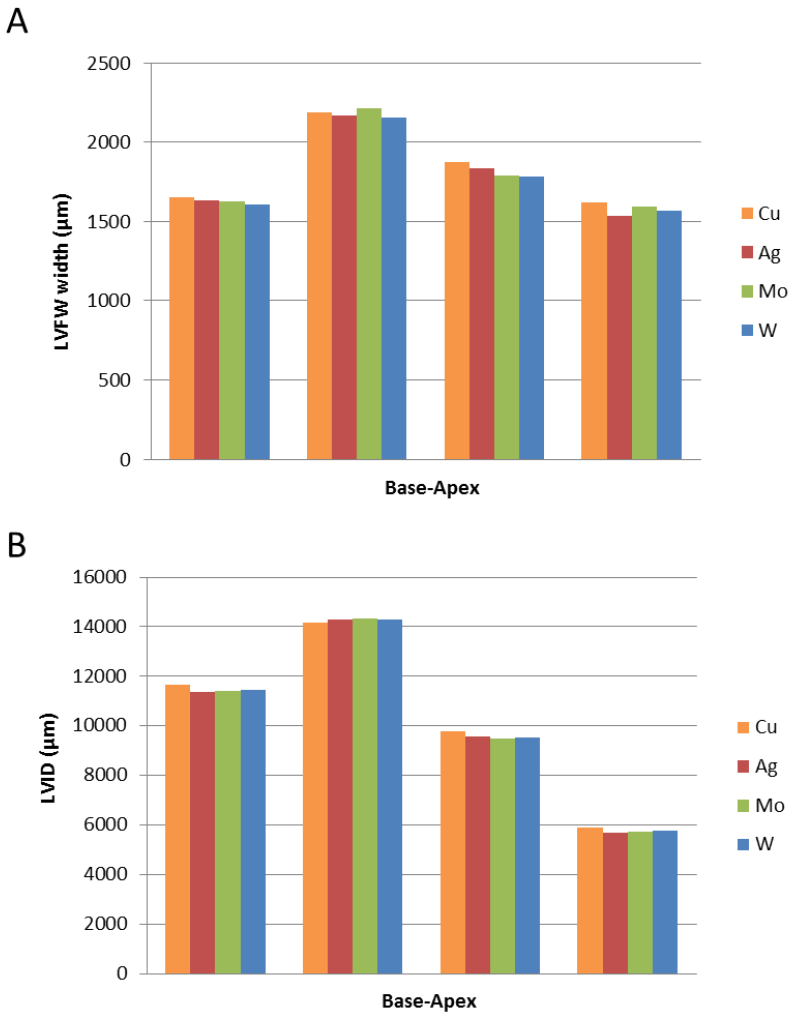

Figure 3.13 Measurements of left ventricular dimensions in rabbit hearts restained and rescanned by micro-CT. LVFW width (A) and LVID measurements (B) recorded from transverse micro-CT sections at 4 evenly spaced intervals from base to apex. For scan using Cu target rabbit heart stained with 3.75% I_2KI for 5 days. For Ag, Mo, W targets the same rabbit heart was bled of iodine and restained with 3.75% I_2KI for 5 days. ANOVA tests showed there was no significant difference in LVFW (p=<0.99) or LVID (p=<0.99) measurements at the different sites. Cu- copper, Ag- silver, Mo- molybdenum, W- tungsten.

3.8 Discussion

Here a methodology to implement micro-CT for soft tissue imaging has been successfully developed. We show the necessity for perfusion fixation of samples, the utility of I_2KI as a contrast agent, and the most suitable X-ray targets for contrast enhanced micro-CT. Data presented here will inform future applications of micro-CT for soft tissue imaging, and reveals the ability of the technique to non-invasively produce accurately aligned, high resolution, tomographic data sets in a time and cost effective manner. This chapter shows the suitability of micro-CT for a wide range of scientific applications including; developmental, comparative and functional investigation of animal tissue morphology.

3.8.1 Traditional techniques for analysis of soft tissue

Classical histology offers high resolution images in a single plane, but serial sectioning is highly labour intensive and 3D reconstructions are plagued with registration issues. Confocal microscopy provides high resolution 3D data, but is hampered by the fact that a sample depth of only a few hundred microns is viable (Semwogerere and Weeks, 2005). In block face techniques such as Episcopic microscopy (Mohun and Weninger, 2011) or extended volume confocal microscopy (Sands et al., 2005) images are automatically aligned, but acquisition time is slow and the sample is destroyed in the process. Micro MRI produces high resolution images non-invasively which are automatically aligned, and has been used in the imaging of soft tissue (Driehuys et al., 2008, Johnson et al., 2002, Li et al., 2005). However MRI does have drawbacks; a) acquisition times are often several hours (Li et al., 2005), with comparable scans achievable in ~20 minutes using micro-CT (Jeffery et al., 2011, Stephenson et al., 2012), b) spatial resolutions are almost an order of magnitude lower than that achievable with micro-CT, c) at high resolutions signal to noise diminishes more rapidly in MRI, and voxels are typically rectangles (non-isometric), with the longest axis extending up to 1000 µm. Micro-CT voxels are fully isometric cubes, thus image data has superior fidelity over micro-MRI (Jeffery et al., 2011). Recently phase-contrast X-ray micro tomography has been used for high resolution non-invasive soft tissue imaging (Hoshino et al., 2012). Although soft tissue contrast is achieved without the need for a contrast agent, the best results

have been achieved with a synchrotron source (Hoshino et al., 2012), which makes the technique logistically and economically difficult.

3.8.2 Previous applications of micro-CT

Tissues with inherent high atomic numbers or electron-density can be easily visualised using micro-CT. As a result, micro-CT has traditionally been used for developmental and morphological analysis of calcified tissues (Kinney et al., 1998, Wise et al., 2013). Micro-CT has also been used in multimodal imaging (Mouchess et al., 2006), in which the morphology of calcified tissues is acquired using micro-CT, while soft tissue image data is acquired by other imaging modalities. Here we show iodine contrast enhancement allows calcified and soft tissue to be imaged simultaneously, allowing appreciation of the true 3D relationships between muscle and bone. We also show its ability to resolve and differentiate cartilaginous tissues, a principle which allowed us to develop a new surface staining methodology for BSSEM (Boyde, 2012). Recently the addition of X-ray contrast agents has allowed micro-CT imaging of soft tissues in embryos (Metscher, 2009b, Metscher, 2009a), muscle (Jeffery et al., 2011) and biomaterials (Faraj et al., 2009). Also 'low' resolution (~100- μm) *in vivo* images of soft tissues have been acquired in small animals (Almajdub et al., 2008, Badea et al., 2005, Badea et al., 2008). Here we have extended the application of micro-CT for soft tissue imaging to large samples, and shown the capability of the technique to allow differentiation of various tissue types. This is a desirable characteristic for any soft tissue visualisation and analysis, and is the major benefit attributed to traditional histology.

3.8.3 The necessity for perfusion fixation in soft tissue imaging

Here we show the influence tissue preparation has on soft tissue imaging. Image quality of micro-CT scan data was vastly improved by heparinisation and perfusion fixation of samples. Blood residing within cavities, lumens and the tissue itself reduces image quality. This is because iodine readily and preferentially resides in blood over soft tissue (figure 3.6C, 3.10), and hence blood appears as a highly attenuating structure. This prevents visualisation of blood contact surfaces, and

impairs image quality within soft tissue structures (figures 3.10 and 3.9). Perfusion fixation also preserves the true 3D relationships of adjacent structures, which for morphological studies is of great importance. Too many morphological studies are based on tissue fixed in a way that does not reflect the true *in vivo* state, this makes interpretation and dissemination of results difficult. However, soft tissue is plastic so care must be taken not to distort samples by over inflation or high pressure when using perfusion fixation. The use physiological isotonic fixatives, for example PBFS, is imperative to prevent cell damage.

The relationship between sample preparation and image quality is well documented for traditional morphological analysis techniques such as histology or electron microscopy (Boyde, 2012, Wisse et al., 2010). However its influence on image quality in micro-CT has been overlooked. Rather emphasis has been placed on suitable contrast agents (Faraj et al., 2009, Metscher, 2009b, Pauwels et al., 2013). We show here how a seemingly 'good' contrast agent for soft tissue imaging can be made excellent by correct sample preparation. As a result initial studies into the effectiveness of contrast agents for micro-CT (Faraj et al., 2009, Metscher, 2009b, Pauwels et al., 2013), need to be repeated in larger perfusion fixed samples before contrast agents are disregarded or stated unsuitable.

3.8.4 The principles of iodine contrast enhancement

Here we introduce the principles of iodine contrast enhancement for micro-CT imaging, which will aid successful application of the technique in the future. I_2KI is an ideal contrast agent; a) it has an ideal k-shell binding energy, b) it readily penetrates soft tissue allowing imaging of large samples, c) it can be removed allowing for post scan analysis (e.g. histology), d) it is differentially taken up by different tissue types, e) and once stained iodine is stable. I_2KI remains localised differentially within tissues and does not bleed into adjacent structures; this reduces image artefacts and blurring at tissue boundaries. The proficiency of other heavy molecules to provide soft tissue contrast has been extensively explored (Metscher, 2009b, Pauwels et al., 2013), but none match up to the numerous advantages we have found using I_2KI. Osmium tetroxide has a suitable k-shell energy and offers good soft tissue contrast. However it has been shown to work poorly on tissue stored in

alcohol, and like phosphotungstic acid its soft tissue penetration is limited (Metscher, 2009b). I_2KI also benefits from low toxicity and is inexpensive. In contrast, Osmium tetroxide and Uranyl acetate are highly toxic and radioactive respectively, and are both volatile substances which are expensive to purchase and dispose of (Faraj et al., 2009, Hayat, 1970). Drying has been shown to improve soft tissue contrast but this causes tissue shrinkage and inevitably leads to structural changes. Freeze drying and critical-point freezing can reduce such artefacts (Leroux et al., 2009, Zysk et al., 2012), but these methods are time consuming and require devices to monitor sample temperature and pressure. In contrast, I_2KI staining is straight forward, and we have shown staining, scanning, restaining and rescanning does not distort the morphology of large soft tissue samples. In small samples however, there is evidence that high concentrations of iodine coupled with long incubation times can cause considerable tissue shrinkage and care needs to be taken in this context (Vickerton et al., 2013).

Investigations into optimisation of contrast enhancement revealed staining with I_2KI is dependent on 3 factors; concentration, incubation time, and sample size. It was revealed that the correct combination of these factors is essential for the differentiation of different tissue types (fat, myocardium, nodal tissue and connective tissue), and the visualisation of soft tissue internal detail. The principles behind the differential uptake of iodine was assessed using micro-CT and BSSEM. It was clear that iodine preferentially resides in areas rich in glycogen such as skeletal muscle, red blood cells, hepatocytes and astrocytes. It is hypothesised that iodine ions becomes aligned and immobilised within the cavities of helical coils formed by glycogen complexes (Lecker et al., 1997, Saenger, 1984)- the basis of simple tests for polysaccharides. Iodine also showed a high affinity for lipid rich regions such as pericardial fat, and myelinated neurons. Iodine has been shown to readily bind with the hydrophilic groups of lipid complexes, which is attributed to charge-transfer complex formation (Bhowmik and Jendrasiak, 1967, Szundi, 1978). Yohe et al. showed iodine readily interacts with gangliosides (Yohe and Rosenberg, 1972), a type of glyolipid which is abundantly found in nervous tissues.

Iodine accumulation and thus X-ray attenuation of soft tissues was also shown to be dependent on tissue density, with areas of tightly packed cells appearing as high

attenuating regions. This was to be expected as the relationship between iodine accumulation and optical density has long been established (Szundi, 1978).

3.8.5 The effects of X-ray targets on soft tissue image quality

The wavelength of the characteristic X-rays generated is inversely proportional to the target's atomic number. This suggests a target with an atomic number close to iodine (53) should provide the best contrast for micro-CT using our I_2KI contrast agent. Therefore, of the targets tested. silver (Ag) target with an atomic number of 47 should in theory produce the best contrast resolution. Analysis of the effects of different X-ray targets (Cu, Ag, Mo, W) on image quality revealed that targets with vastly different k-shell energies and thus X-ray spectra, still produce satisfactory results for imaging of soft tissue. With all targets the major tissue types; fat, myocardium, nodal tissue and connective tissue, could be differentiated. This is due to the fact that for all targets, the X-ray spectrum produced has a wide range of energies, some of which will be complimentary to the K-shell binding energy of iodine. However we conclude Cu and Mo are most suitable for imaging of soft tissue using micro-CT. The Mo target provided the best transmural contrast, showing the biggest difference in gray values between laminar sheets and space. The Cu target provided the best internal detail, and produced the steepest curve at the myocardium-space boundary, suggesting a reduced signal averaging effect. This can be explained by the relationship between the k-shell binding energy of iodine and atomic numbers of Cu and Mo; the k-shell binding energy of iodine (33.2 KeV) does not correspond to its atomic number (53), therefore the atomic numbers of Cu (29) and Mo (42) means, as a target, they produce characteristic X-rays with an ideal energy for successful displacement of iodine electrons (Bearden and Burr, 1967). This also explains the observed superior contrast resolution when using a Cu target, as the spectrum produced will be sensitive to small differences in iodine concentrations between tissue types. Higher energy X-ray spectra, like those produced by W, which is often the default target for micro-CT systems, were not as sensitive to changes in iodine concentrations. This is because W has a high atomic number (74), and thus produces X-rays that readily generate photon events regardless of iodine concentration.

3.9 Summary

A methodology to implement micro-CT for soft tissue imaging was developed. We show the necessity for perfusion fixation of samples, the utility of I_2KI as a contrast agent and the most suitable X-ray targets for contrast enhanced micro-CT.

Investigations into optimisation of contrast enhancement revealed staining with I_2KI is dependent on 3 factors; concentration, incubation time, and sample size. It was revealed that the correct combination of these factors is essential for the differentiation of different tissue types and the visualisation of a tissues internal detail.

The principles of differential uptake of iodine by different tissue types were assessed in various tissues using micro-CT and BSSEM. It was clear that iodine preferentially resides in areas rich in glycogen and lipids. Iodine accumulation was localised allowing clear discrimination of cell and tissue boundaries especially with BSSEM. Iodine accumulation and the attenuation of soft tissue was also shown to be dependent on tissue density, with areas of tightly packed cells appearing as high attenuating regions.

Tissue preparation was shown to be vitally important in achieving the best image quality possible. Our perfusion fixation method ridded samples of residing blood which improved visualisation and analysis of sample cavities and internal tissue detail. We also showed that tissue preparation, staining and the scanning process itself does not negatively affect tissue morphology. Analysis of effects of different X-ray targets, and thus different X-ray spectra on image quality revealed most that X-ray targets produce satisfactory results, but we conclude that Cu and Mo are most suitable for imaging of soft tissue using micro-CT.

The data presented here will inform future applications of micro-CT for soft tissue imaging, and reveals the ability of contrast enhanced micro-CT to non-invasively produce accurately aligned, high resolution, tomographic data sets in a time, and cost-effective manner. Micro-CT is therefore suitable for application in developmental, comparative and functional investigation of tissue morphology, as well as in genomic and mutational investigations were visualisation of global effects are desirable.

CHAPTER 4

Detailed Morphology of Skeletal Muscle Revealed by Micro-computed Tomography

4.1 Introduction

The morphology of skeletal muscle and its associated connective tissue network is changed in response to a number of factors, including physical activity and disease. There has been a vast amount of research conducted to investigate the modification of muscle during and after; training, electrical stimulation and genetic modification. As well as biomechanical modelling of musculoskeletal function using techniques such as finite elements analysis. Therefore, information on the morphology and internal structure of muscle and connective tissue is important for numerous applications in basic and clinical research. The established methods for visualising and collecting morphological data from skeletal muscle are dissection and histological sectioning, which are both destructive and laborious. Low X-ray attenuation has formerly ruled out micro-CT as a modality to resolve internal structures of soft tissue. Incorporation of iodine, which has a high molecular weight, into soft tissues enhances the differential attenuation of X-rays, and has allowed visualisation of fine detail in embryos and skeletal muscle. Here we investigate the potential of iodine staining to generate high resolution micro-CT images of skeletal muscle tissue, and assess whether muscle and connective tissue can be discriminated. We show the ability of micro-CT to resolve single muscle fibres, and validate a novel method of extracting fibre orientation from micro-CT data.

Some of the work in the following chapter has been published as:

Jeffery NS, Stephenson RS, Gallagher JA, Jarvis JC, Cox PG (2011) Micro-computed tomography with iodine staining resolves the arrangement of muscle fibres. Journal of Biomechanics 44: 503 189-192.

The paper is appended

New insights include; the visualisation of muscle bundle structure in whole intact samples, and the validation of 3D fibre orientation, extracted from micro-CT data using a novel methodology developed by our collaborator Dr Jichao Zhao (The University of Auckland).

4.2 Discrimination of skeletal muscle from connective tissue

To assess the potential contrast enhancement of I_2KI staining for micro-CT imaging of skeletal muscle, samples of extensor digitorum longus (EDL) muscle were taken from commercially available fixed foetal pig material (110-115 days gestation age) (Carolina Biological Supply, Wisconsin). An 8mm x 8mm x 8mm block of tissue from the distal part of EDL was chosen because in this area tendons make their connections with skeletal muscle fibres, and so differentiation between muscle and connective tissue could be studied. Samples were stained with I_2KI (15 %, 2 days), micro-CT scanned, and subsequently processed for histology. Mouse heads were taken from adult WMT mice that had been previously fixed in PBFS, stained with I_2KI (7.5%, 7 days), and micro-CT scanned. Contrast enhanced micro-CT images of pig EDL indicate that muscle appears as a highly attenuating structure (bright grayscale values), and the accompanying connective tissue appears as low attenuating structures (dark grayscale values). Perimysial, and even endomysial connective tissue can be resolved and discriminated from tendinous connective tissue (figure 4.1). These findings were validated by processing the same sample for histology and staining with Sirius red, however, fine connective tissue tracts (red) are less defined than in micro-CT data, and tissue shrinkage is evident (figure 4.1).

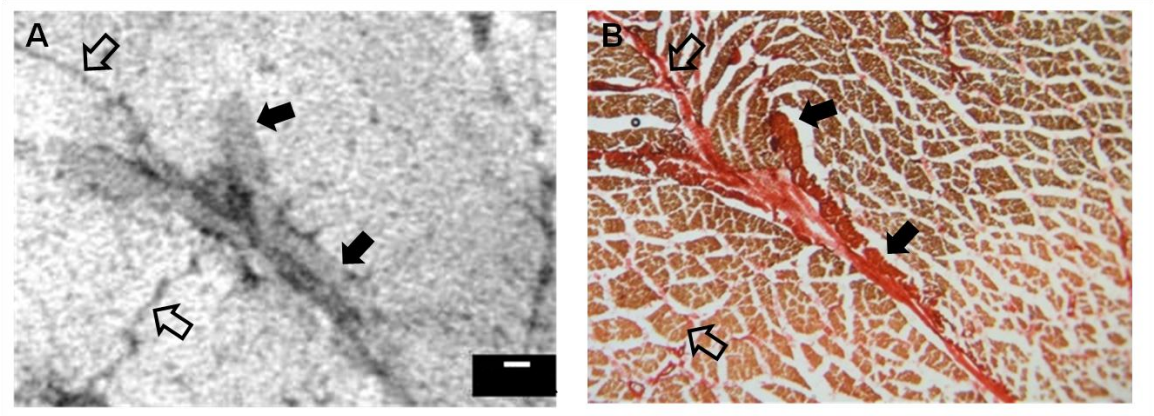

Figure 4.1 Discrimination of skeletal muscle and connective tissue using micro-CT and histology. Transverse micro-CT image of extensor digitorum longus muscle stained with 15% I_2KI for 2 days showing low attenuating connective tissue tracts (A). Corresponding histological section stained with Sirius red. Clear arrows indicate perimysium, filled arrows indicate tendinous connective tissue. (Scale bar represents 0.1 mm)

We have shown that the I_2KI contrast agent is preferentially taken up by different tissue types (Chapter 3), here more iodine resides in muscle than connective tissue (figure 4.1). This was also seen to be the case when an intact mouse head was stained with I_2KI. Even with physical barriers such as fur, epidermis, subcutaneous fat and calcified tissue, iodine diffuses into and more readily resides in muscle than the surrounding connective tissue (figure 4.2). The mouse masseter muscle, for example, showed clear definition of low attenuating connective tissue septa, whose configuration suggested that the iodine stain was differentiating between muscle fibres and the epimysial connective tissue separating muscle components (e.g. deep and superficial layers of the masseter) and the perimysial connective tissue that delineates fascicles or parallel bundles of muscle fibres (figure 4.2). Bone due to its high atomic number and density appeared as the highest attenuating structure (figure 4.2).

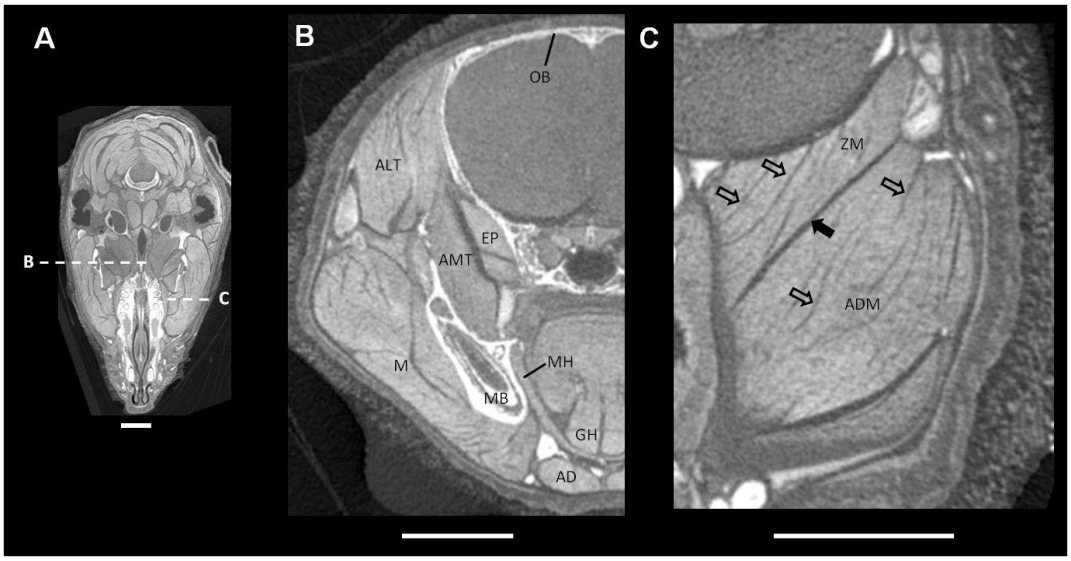

Figure 4.2 Micro-CT images of adult mouse head stained with 3.75% I_2KI solution for 7 days. (A) transverse image at 0.033 mm showing position of resliced images B and C; (B) coronal image at 0.033 mm showing various muscles; (C) coronal image at 0.010 mm resolution showing thick dark bands of epimysium (black arrow) separating the muscles and the narrower dark bands representing perimysium (clear arrows). AD, anterior digastric; ADM, deep masseter; ALT, anterior lateral temporal; AMT, anterior medial temporal; OB, occipital bone; EP, external pterygoid; GH, geniohyoid; M, masseter; MH, mylohyoid; MB, mandibular bone; ZM, zygomatico-mandibular muscle. Scan data acquired from and interpreted with Dr Nathan S. Jeffery. (Scale bars represent 3 mm)

4.3 Contrast enhanced micro-CT resolves the arrangement of single muscle fibres

Muscle fibre architecture was investigated using high resolution scans of a intact fixed adult grey squirrel head, adult WMT mouse head and fixed foetal pig EDL muscle (110-115 days gestation age) (Carolina Biological Supply, Wisconsin). Scan data confirmed that the arrangement of muscle fibre bundles (figure 4.4, 4.5) and single muscle fibres within these bundles (figure 4.3, 4.6, 4.7) can be resolved using contrast enhancement micro-CT. In scans of the EDL, it was clear that the delineation of connective tissue and skeletal muscle tissue extended to the endomysial level. The endomysium is the fine layer of connective tissue which surrounds individual muscle cells. Fig.4.3 shows that structures of approximately 30-40 microns in width can be resolved, and these are individual muscle fibres. The CT scan is compared with the microscopic appearance of an unstained section in Figure 4.3C. In this case, the iodine staining of the individual muscle fibres can be seen as a yellow/orange colour, validating structures seen in the micro-CT data.

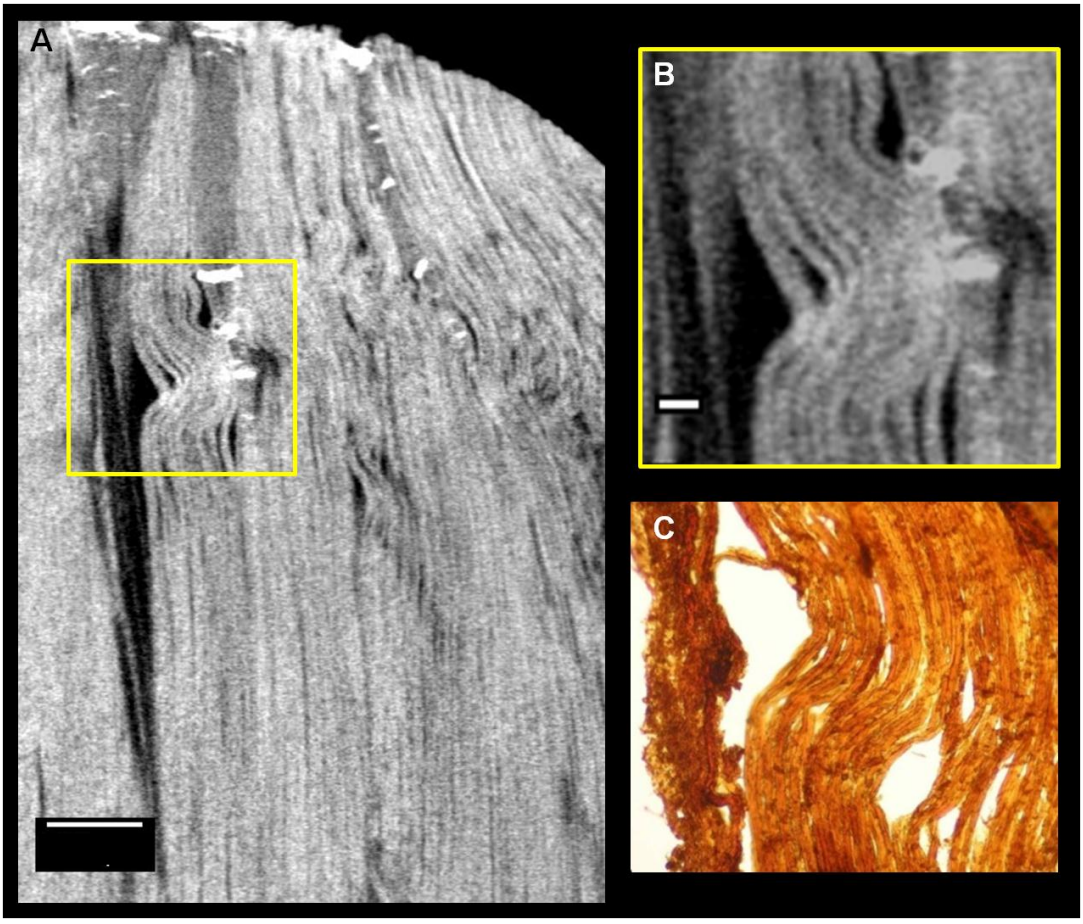

Figure 4.3 Longitudinal micro-CT images of extensor digitorum longus with corresponding histology. Extensor digitorum longus micro-CT image (resolution 0.006 mm) stained with 15% I_2KI for 2 days (A), and high power image (B). Corresponding histological section stained by residing iodine (C), validating micro-CT findings. (Scale bars represent 0.5 mm and 0.1 mm)

Muscle bundle arrangement was resolved in whole intact mouse and squirrel heads (figure 4.4, 4.5). The best visualisation of muscle fibre direction was achieved by virtually reslicing the scan data to match the longitudinal axis of muscle fibres (figure 4.4B,C,E,F), in this plane discrete changes in muscle bundle orientation across a muscle are easily visualised. The inability to clearly visualise individual muscle fibres in larger samples, is due to both the inverse relationship between sample size and attainable resolution and down sampling of the data, but is not due to a limitation of the staining technique. Whole muscles (figure 4.5B) and their muscle bundles (figure 4.5C) can be segmented and quantified. In figure 4.5 the anterior

deep masseter of an adult squirrel has been segmented (by Dr Philip G. Cox) and its major muscle fibre bundles presented in 3D; volume, surface area, and 3D length can be calculated using Amira 5.4 tool kit.

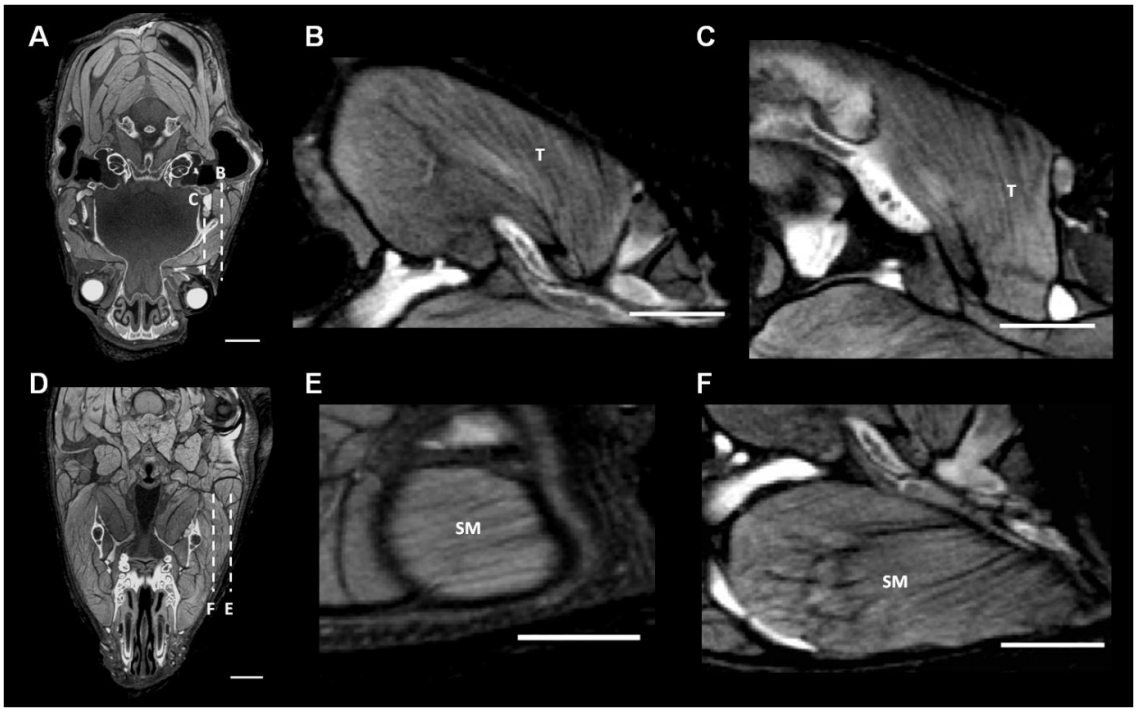

Figure 4.4 Micro-CT images of adult mouse head stained with 3.75% I_2KI solution for 7 days. (A) transverse image showing position of resliced images B and C; sagittal images showing fibre orientation in temporalis muscle. (D) transverse image showing position of resliced images E and F; sagittal images showing fibre orientation in superior masseter muscle. SM- superior masseter, T- temporalis. Image resolution 0.033 mm, scan data acquired from Dr Nathan S. Jeffery. (scale bars represent 3 mm)

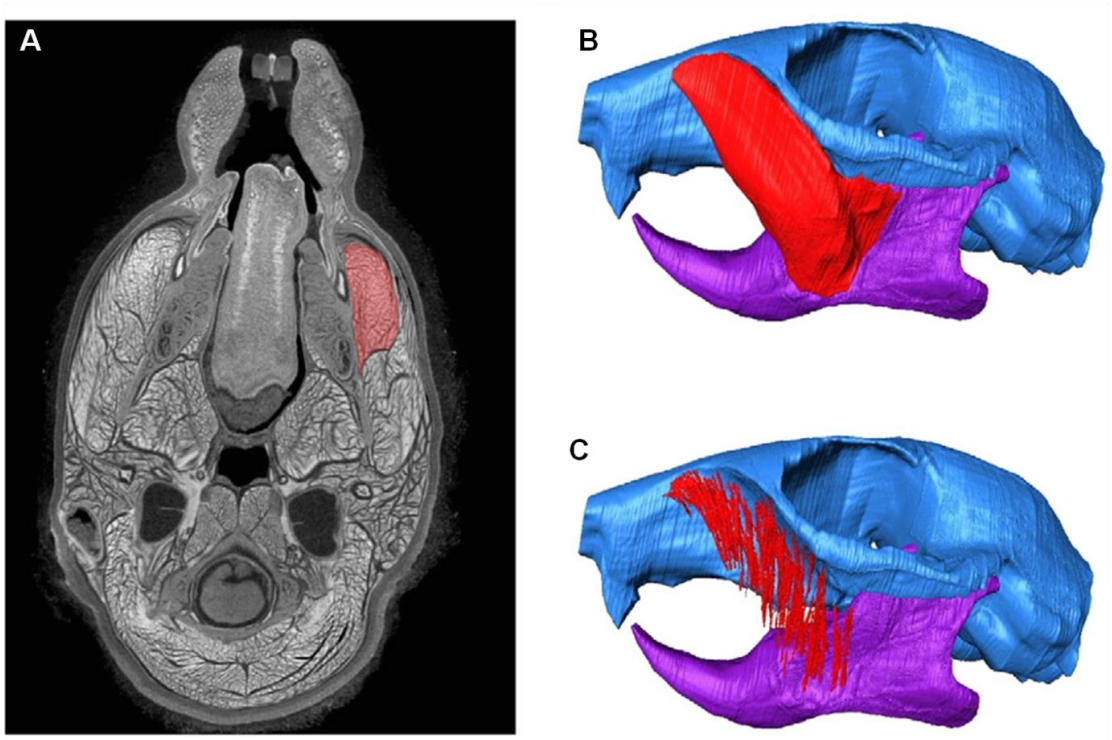

Figure 4.5 Transverse micro-CT image of squirrel head with corresponding volume renderings of anterior deep masseter muscle. Images illustrating how the geometry and internal architecture of a muscle, in this instance the anterior deep masseter muscle in the squirrel, could be defined: (A) transverse enhanced micro-CT image showing the outline and internal features of the muscle; (B) 3D reconstruction of the skull showing the external geometry of the muscle (red); (C) 3D reconstruction of the skull demonstrating the arrangement and length of fibre bundles in the muscle. Volumes, areas as well as fascicle length and orientation can be measured, using the Amira toolkit. Image resolution 0.040 mm, scan data acquired from and analysed by Dr Phillip G. Cox.

4.4 3D fibre orientation of skeletal muscle

We have shown contrast enhanced micro-CT can non-invasively resolve the arrangement of single muscle fibres (figure 4.3). However, the nature of tomographic image data means the 3D morphology of fibres is not easily interpreted. Consequently, novel structure tensor and fibre tracking analysis was carried out on micro-CT data of foetal pig EDL muscle to visualise and quantify muscle fibre orientation in 3D. Using segmentation tools in Amira 5.4, a tissue mask was created that only encompassed the muscle tissue and excluded the connective tissue. Then

using Matlab (R2009b) a structure tensor method representing gradient information for 3D imaging problems (Krause et al., 2010; Zhao et al., 2012) was implemented on the micro-CT data using the previously created mask. The structure tensor contains gradient information at each voxel in the 3D volume. Eigen analysis of the 3D structure tensor is then carried out. Local fibre alignment is modelled as the orientation with the least signal variation, which corresponds to the eigenvector paired with the smallest eigenvalue. Fibre angles at each voxel are then extracted for statistical analysis. State of the art reconstruction methods for fibre tracking using the structure tensor data have been developed previously (Zhao et al., 2012). We then implemented a simple line interpolation algorithm; the 3D trajectory propagates along a line starting from a seed point in a region of interest with a predefined pixel size (in this case 1) and varying vector orientation. The vector orientation is continually updated by averaging eight neighbouring vectors in any new coordinate during propagation. Fibre tracks are then rendered in 3D using custom colour maps corresponding to either inclination or transverse angles. 3D fibre angles, including both inclination and transverse angles (See methods 2.4.4 and figures 2.1 and 2.2) were successfully extracted from the micro-CT data, allowing visualisation of 3D fibre orientation in the muscle.

To validate fibre orientation analysis a sub-region of the muscle (1.1 mm^3; 6 µm isometric resolution) containing predominantly vertical fibres was analysed (figure 4.6A,B), figure 4.6C,D shows the result of the fibre orientation analysis for the region. It was evident that the algorithm could successfully extract muscle fibre information from the micro-CT data, inclination angles confirmed, as expected, a predominant vertical fibre orientation across the tissue block. Fibre tracking clearly showed overlapping of fibres and branching between fibres in 3D, characteristics that cannot be easily identified when viewing the data in a tomographic format (figure 4.6A). The large spaces evident within 3D fibre plots (figure 4.6C,D) correspond to the connective tissue tracts removed in the segmentation process. With the method validated for a regular muscle fibre pattern, the ability of the technique to plot areas of irregular fibre orientation was investigated. Figure 4.7A,B shows a longitudinal micro-CT slice taken from a sub-volume (1.6 mm^3; 6 µm isometric resolution) of a foetal pig EDL data set, the region contains a 'kink' of muscle fibres likely to be an artefact of the fixation process. Fibre orientation analysis of the volume (figure

4.7C,D) clearly depicts the 'kink', and provides detailed quantification of the inclination angle of the individual fibres as they transverse the 'kink' region. A fibre with a complex orientation was observed (figure 4.7D- white arrow), the fibre appeared to turn back on itself and coil, not characteristic of muscle fibres. However, the structure is present in the micro-CT data and may represent an area of micro damage.

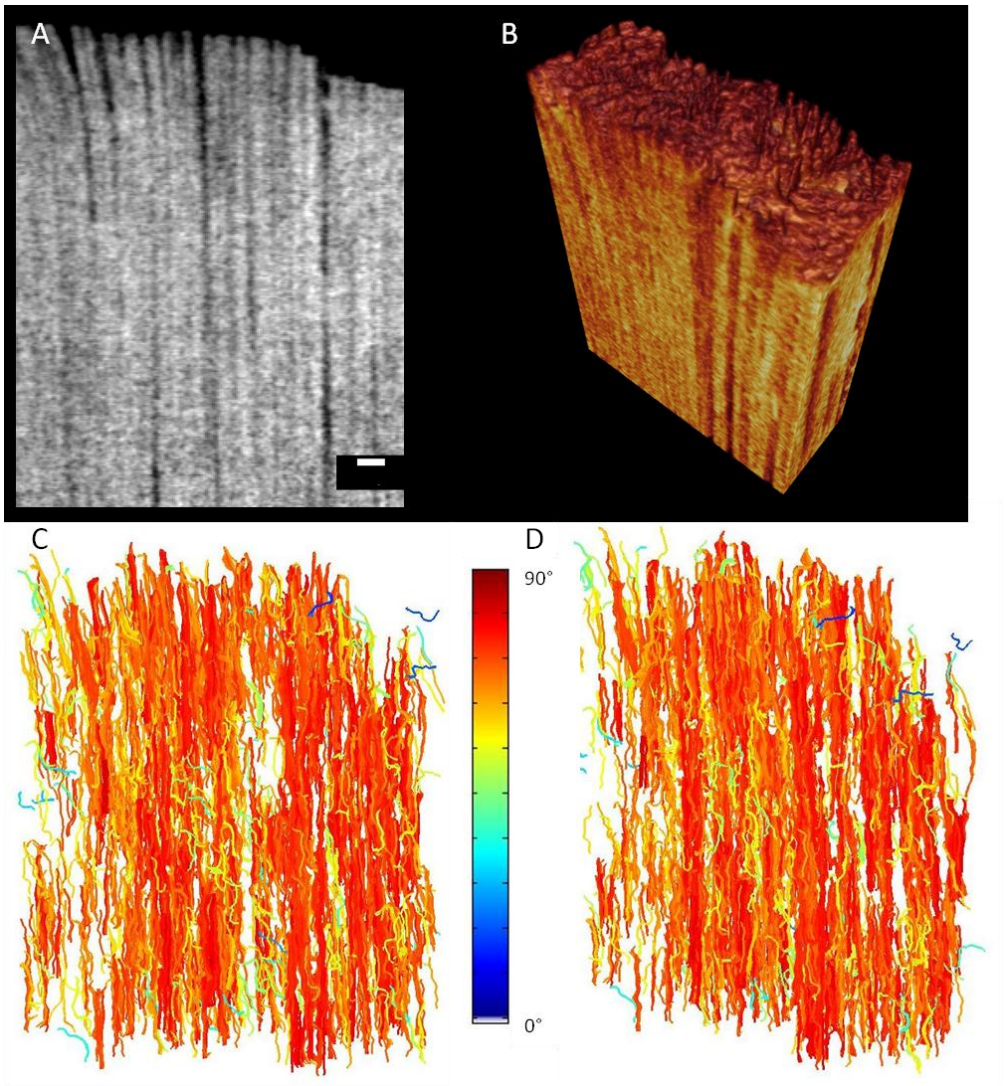

Figure 4.6 Longitudinal micro-CT image of pig extensor digitorum longus muscle with corresponding volume rendering and 3D fibre orientation. Extensor digitorum longus micro-CT image (resolution 0.006 mm) stained with 15% I_2KI for 2 days (A), with corresponding volume rendering (B). C and D show 3D muscle fibre tracks extracted from micro-CT data shown in A and B. Anterior view (C) and laterally rotated view (D), showing predominantly vertical fibres and branches between fibres. Colour bar represents inclination angle. (Scale bar represents 0.1 mm)

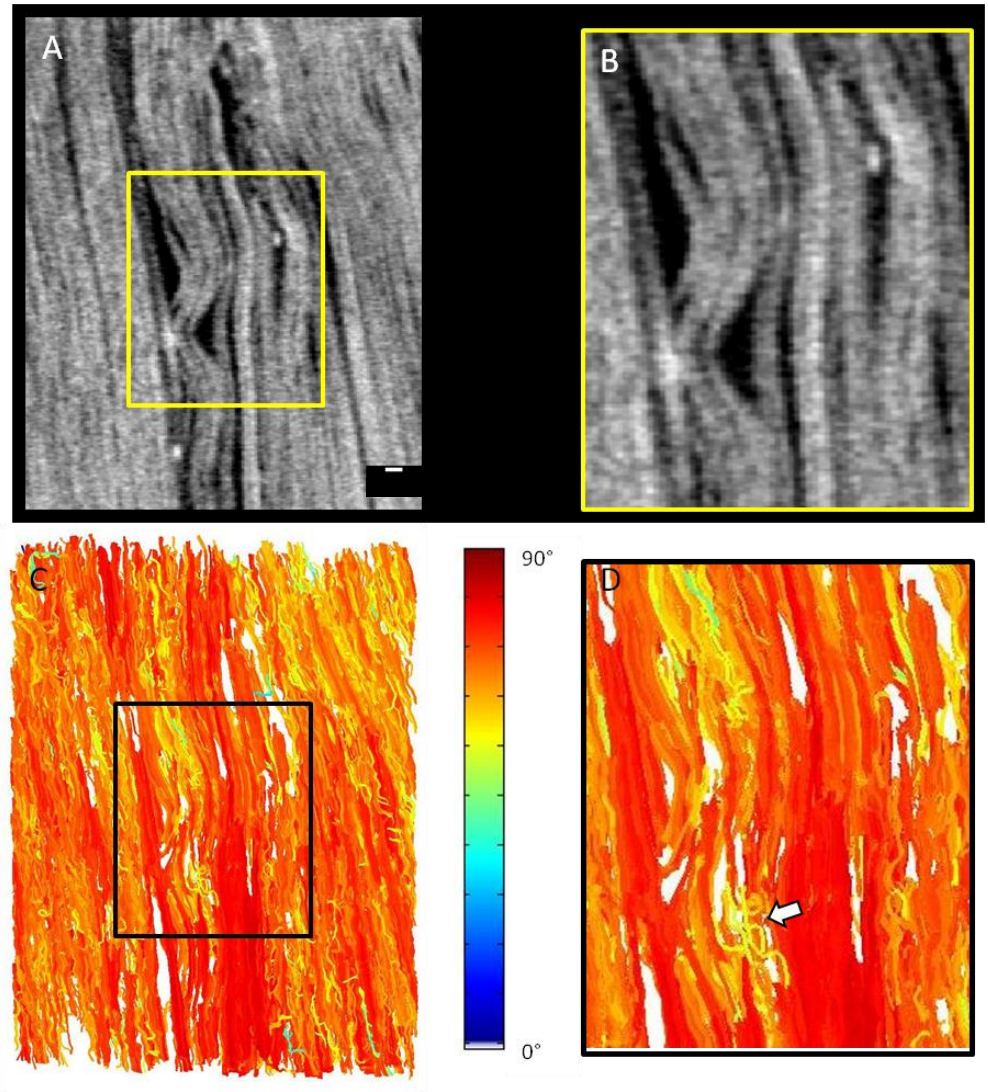

Figure 4.7 Longitudinal micro-CT images of pig extensor digitorum longus muscle with corresponding 3D fibre orientation. Extensor digitorum longus micro-CT images (resolution 0.006 mm) stained with 15% I_2KI for 2 days (A), high power image of complex 'kink' region (B). C and D show 3D muscle fibre tracks plotted from micro-CT data shown in A and B. Anterior view (C) and high power view of 'kink' region (D), showing predominately vertical fibres and accurate tracing of areas of complex fibre orientation. Arrow indicates area of fibre disarray. Colour bar represents inclination angle. (Scale bar represents 0.1 mm)

4.5 Discussion

The potential use of contrast enhanced micro-CT to investigate the detailed morphology of skeletal muscle and the accompanying connective tissue networks was assessed. Our findings confirm that muscle structures down to the level of single muscle fibres can be resolved with contrast enhanced micro-CT. Various skeletal muscle samples including dissected preparations and whole intact animal heads were stained with an iodine based contrast agent (I_2KI) and subsequently scanned using micro-CT. Diffusion of iodine, which has a high molecular weight, into skeletal muscle enhances the differential attenuation of X-rays. This allowed visualisation of fine internal detail, and differentiation between muscle and the surrounding connective tissue. Further analysis using novel structure tensor and fibre tracking methods, allowed extraction of 3D fibre orientation from skeletal muscle. The methods and data presented here will help improve our understanding of the internal architecture muscles, and could have implications in a wide range of basic and clinical research fields.

4.5.1 Skeletal muscle contrast enhancement

The use I_2KI as a contrast agent allowed differentiation of muscle and connective tissue, single fibres were resolved along with the epimysium, perimysium and endomysium. Iodine preferentially resided in muscle over connective tissue, and thus muscle appeared as a high attenuating structure (brighter pixel values). The exact mechanism for the observed differential contrast enhancement is unknown. The attenuation of X-rays is dependent on the thickness, atomic density and the number of electrons per atom (atomic number, Z). Iodine has an atomic number of 53 compared with ~7 for muscle (Spiers, 1946), it is soluble in water when mixed with potassium iodide forming the compound iodine potassium iodide (I_2KI). Once in aqueous solution, the iodine can passively diffuse into the tissues. Why the iodine then binds more readily to the muscle fibres than the connective tissues is unclear. It is hypothesised iodine becomes trapped within the complex double helical structure of glycogen and other polysaccharides (Lecker et al., 1997, Saenger, 1984, Yu et al., 1996). It is thought that the I_2KI anion is attracted to the positively charged core of the glycogen helixes, the core is also hydrophobic which is complementary to iodine

accumulation (Immel, 1995). Glycogen is used for energy storage and is most abundant as granules in the cytoplasm of liver and muscle cells (Kerem et al., 1973), and is not found in connective tissues. Collagen is the major constituent of the connective tissue associated with muscle, and like glycogen, has a helical structure, albeit triple and right handed. Connective tissue is also a cation, and therefore carries a positive net charge that will act to attract I_2KI, which itself is a negatively charged anion. Both these characteristics could contribute to the observed uptake of iodine by connective tissue. However, collagen has a high water content and the core of its triple helix is hydrophilic, conditions which are not complementary to iodine and will reduce iodine uptake. In addition connective tissue is structurally less dense than muscle, previously we have shown increased tissue density corresponds to an increased X-ray attenuation and I_2KI uptake (Jeffery et al., 2011) (Chapter 3).

Metscher's (Metscher, 2009a, Metscher, 2009b) earlier work on micro-CT imaging of embryos showed excellent penetration and stable contrast enhancement with 10% I_2KI solutions. Improved contrast was most obvious for the cranial nerves as well as the developing otic and optic regions. In contrast to our findings the author reports that the staining was not specific to any one type of tissue (Metscher, 2009b). Metscher (2009a) also demonstrates that vertebrate and invertebrate muscle can be visualised with phosphotungstic acid (PTA). This is a highly acidic substance which can cause decalcification of skeletal tissue, and been a much larger molecule takes longer to penetrate soft tissue, requiring approximately 12hrs for specimens 2-3mm thick. PTA would not be practical for the size or type (muscle and bone present) of specimens imaged in the present study. Indeed, findings for the squirrel head indicated that we have almost reached the size limit for passive diffusion of iodine. Larger specimens would require active perfusion of contrast agents to ensure homogenous staining throughout the sample and avoid surface saturation. In large excised samples or organs (e.g. heart) that lack physical barriers to diffusion, such as fur, epidermis and bone, means iodine penetration is not an issue. Nevertheless, we anticipate that there is a surface area to volume ratio below which passive perfusion can no longer be relied upon, and active perfusion of the contrast agent would become a necessity.

4.5.2 Existing techniques for analysis of muscle morphology

Traditional techniques

Traditionally knowledge on the gross morphology of muscle came from careful dissection (Vesalius, 1544), with fine morphological knowledge coming from histological studies (Harman and Gwinn, 1949, Hoagland et al., 1944). Both techniques are still frequently implemented, although we show the scope for a single micro-CT scan to provide sufficient detail for both gross and fine morphological analysis. Histology is notoriously labour intensive and only permits analysis of small sample preparations, meaning analysis of gross morphological changes in suitable n number is impractical. Dissection suffers from similar limitations. Non-invasive imaging techniques such as micro-CT and micro-MRI do not suffer from such limitations. High resolution global analysis of multiple muscle samples is not only possible but also time efficient, especially with the fast acquisition times attributed to micro-CT (Jeffery et al., 2011, Stephenson et al., 2012). These imaging techniques also produced automatically aligned tomographic data sets, allowing for detailed 3D analysis of muscle structure and function (Buckberg et al., 2006, Cox and Jeffery, 2011, Galban et al., 2007, Gilbert et al., 2012, Jeffery et al., 2011). In contrast histology suffers from registration issues of serial sections and poor z-plane resolution, as a result segmentation is painstakingly slow. Additionally the cutting plane is fixed, meaning structures of interest can be 'hidden' by overlying structures, and this is also a common issue when using dissection. In contrast Micro-CT data is made up of a 3D matrix that can be virtually sectioned rapidly in multiple planes simultaneously. Histology does allow for staining of specific structures, for example muscle fibre types (Tunell and Hart, 1977) and connective tissue networks (Dolber and Spach, 1987). However we have recently shown the scope for differentiation of muscle fibre types using I_2KI staining (Chapter 3- figure 3.6), and revealed micro-CT can differentiate connective tissue networks in 3D. I_2KI can also be removed from soft tissue post scan, and samples subsequently processed for histology with excellent correspondence and no apparent tissue damage is observed (Stephenson et al., 2012).

Modern techniques

To address some of the issues which hamper traditional histology, techniques such as episcopic microscopy (Mohun and Weninger, 2011, Weninger et al., 2006), extended volume confocal (Pope et al., 2008, Sands et al., 2006) and surface imaging microscopy (Gerneke et al., 2007) have been developed. These techniques address the issue of registration of sections in the z-plane, and allow specific staining, although staining access is an issue as samples are embedded. Further drawbacks include; long acquisition times, currently only small samples can be processed, and the destructive nature of the techniques means tissue damage is unavoidable.

Fibre orientation analysis

Here we have shown a novel method for extraction of 3D fibre orientation from micro-CT image data. 2D fibre orientation has previously been investigated using standard histology (Streeter et al., 1969), and more recently using micro-CT (Jorgensen et al., 1998a, Jeffery et al., 2011). Over recent years the diffusion tensor MRI (DT-MRI) has become the gold standard for analysis of 3D fibre orientation in biological soft tissues, including skeletal muscle (Damon et al., 2011, Lansdown et al., 2007), cardiac muscle (Rohmer et al., 2007), and in the brain (Wedeen et al., 2012a). The method presented here uses structure tensor analysis to extract 3D fibre orientation from Micro-CT data. Structure tensor analysis has features in common with DT-MRI and has previously been used to characterize fibre orientation from scan data of composite materials (Axelsson and Svensson, 2010). Micro-CT is superior to DT-MRI in terms of the fidelity of morphological information it produces. Unlike micro-CT which distinguishes individual muscle fibres based on their structural differences to surrounding tissues. DT-MRI is not a morphological method, in that it does not resolve physical structures. Rather, the preferential diffusion direction for water is calculated for each voxel. Since water will be less constrained to move in the long axis than in the short axis of a fibre, then an indication of fibre direction is achieved (Le Bihan et al., 2001). From the probability density function obtained from each voxel, DT-MRI can produce streamlines representing the distribution of direction of diffusibility. This is still not the same as visualising the cellular structure, and as a result controversy is currently playing out concerning the proposed arrangement of nerve fibres in the brain based on similar

analysis (Wedeen et al., 2012b, Wedeen et al., 2012a, Catani et al., 2012). Spatial resolutions attainable using Micro-CT are almost an order of magnitude greater than that achievable with MRI, the virtual fibre structures achieved by DT-MRI are usually of the order of 400-1500 μm in diameter (Nielsen et al., 2009). Also, In order to derive sufficient signal to calculate diffusion vectors, MRI voxels are typically rectangles rather than cubes, the longest axis of which can extend up to 1500 μm, and the acquisitions are repeated many times such that scan times can take many hours (72 hours- Gilbert et al., 2012). By comparison, micro-CT can generate isometric voxels in a matter of minutes, with vertices well within the size range of mammalian muscle fibres diameters; ~10-20 μm x 50-100 μm (Levick, 2003, Drake et al., 2005). We were able to achieve resolutions of 6 μm in 20-30 minute scans, whilst maintaining sufficient image quality to visualise individual muscle fibres. Surface imaging microscopy (Gerneke et al., 2007) and optical coherence tomography (Ambrosi et al., 2012, Fleming et al., 2008) have been used for analysis of fibre orientation in muscle. Both techniques have the advantage over DT-MRI that they map actual physical structures, but suffer from poor z-plane resolution and z-plane depth respectively.

There are some potential limitations of structure tensor analysis of micro-CT data; a) connective tissue boundaries on the surface of blood vessels and within muscle may generate fibre artefacts. However segmentation to remove such regions is feasible. b) For analysis of large muscle samples, the inevitable increase in spatial resolution would mean myo-bundles rather than single muscle fibres would be resolved. However muscle fascicles do give an accurate representation of global fibre orientation in skeletal muscle. c) Possible limitations of the imaging method described here and by Metscher (2009a,b) for *in vivo* work are related to the exposure to high levels of ionising radiation. However, we have shown previously that this does not affect tissue morphology (chapter 3.7), and for work on *ex vivo* samples the method has several advantages over other non-invasive techniques, as mentioned above.

4.6 Summary

The potential use of contrast enhanced micro-CT to investigate the detailed morphology of skeletal muscle and accompanying connective tissue network was assessed. Various skeletal muscle samples including dissected preparations and whole intact animal heads were stained with an iodine based contrast agent (I_2KI), and subsequently scanned using micro-CT. Diffusion of iodine, which has a high molecular weight, into skeletal muscle tissue enhances the differential attenuation of X-rays and allows visualisation of fine detail. The results showed that iodine diffuses differentially into different tissue types. In this case, iodine more readily accumulates in muscle tissue than surrounding connective tissue, thus muscle has a more attenuating affect to X-rays, and can be easily distinguished from the lower attenuating connective tissue.

The high spatial resolution provided by micro-CT, and the delineation of connective tissue and skeletal muscle at a perimysial and endomysial level, allows visualisation of muscle fibre bundles and even single muscle fibres. A novel structure tensor and fibre tracking method for extraction of fibre orientation from micro-CT data was validated. This method provides an accurate representation of muscle fibres in 3D, quantification of fibre angulations at a µm scale, and shows scope for analysis/identification of muscle micro damage.

Data obtained in this chapter confirms contrast enhanced micro-CT as an effective and efficient method for analysis of muscle morphology at a gross and cellular scale. It provides non-destructive, non-invasive and high resolution data rivalling any existing technique, and presents a novel method for fibre orientation extraction and quantification which will be useful and applicable in a wide range of scientific disciplines.

CHAPTER 5

Detailed Anatomy of the Heart Revealed by Micro-computed Tomography

5.1 Introduction

The normal structure and function of the heart, the common pathological changes that cause abnormal function, and the interventions proposed to improve or restore its function are fundamentally based on structure. Therefore in all these areas a detailed and accurate understanding of 3D cardiac anatomy is essential. Traditional understanding of cardiac anatomy from histological studies requires the interpretation of many serial 2D sections of a small tissue sample sectioned in a single plane. As a result histological sections are difficult to interpret for non-specialists, and suffer from many drawbacks when concatenated into 3D. Contrast enhanced micro-CT offers a rapid, non-invasive, high resolution method to investigate cardiac anatomy in normal and pathological hearts. Here we present high resolution (19-40μm) scans of whole hearts, which reveal the detailed anatomy of the atria, ventricles, valves and cardiac vessels, unrivalled by traditional methods. These scans demonstrate the potential of micro-CT to reveal new anatomical detail, advance existing anatomical understanding and teaching, and improve the fidelity of morphological and developmental studies of the heart. With single myocyte resolution attainable, we assess the extraction of fibre orientation within the atria and ventricles. This will aid the characterisation of fibre orientation in normal and diseased hearts, and inform the development of 'virtual hearts'- anatomically and biophysically-detailed mathematical models, which map the wave of depolarisation and/or contraction across the heart. In this chapter emphasis is placed on the detailed anatomy of the atria in rabbit, including novel insight into the 3D morphology and fibre orientation of the pectinate muscles and the so-called muscular bands. The atria are particularly prone to arrhythmogenesis, and their complex microstructure has been shown to provide a morphological substrate for electrical dysfunction. The detailed microstructure revealed here potentiates a step wise change to the understanding of atrial anatomy and function.

Some of the work in this chapter on fibre orientation in the atria has been published as:

Robert S. Stephenson, Jichao Zhao, George Hart, Mark R. Boyett, Antonio F. Corno, Prem S. Venugopal, Ram Dhannapuneni, Xue Cai, Philip J. Withers, Henggui Zhang, Bruce H. Smaill, Jonathan C. Jarvis. Detailed Study of 3D Atrial Myostructure using Contrast Enhanced Micro-CT. Featured section, Heart Rhythm Society conference, Denver, CO, USA, 2013

Sample preparation and segmentation methodology has been published as:

Jarvis J, Stephenson RS (2013) Studying the microanatomy of the heart in 3 dimensions: a practical update. Frontiers in Paediatric Cardiology, doi: 10.3389/fped.2013.00026.

Papers are appended.

5.2 Detailed anatomy of the four chambered mammalian heart

To assess the potential of micro-CT imaging with iodine staining to resolve the detailed anatomy of cardiac tissue, perfusion fixed (methods 2.2.4) whole intact adult rabbit hearts (n= 8) were stained with I_2KI and micro-CT scanned. Isometric resolution of samples ranged from 18-24 μm. *In situ* heparinisation followed by perfusion fixation, accompanied with careful monitoring, produced naturally inflated hearts, with no residing blood in atrial or ventricular cavities (figure 5.1). The level of inflation was validated by cross reference with *in vivo* echocardiography (see Chapter 8.6). Heparinisation and flushing prevented visual impairment of internal structure by residing blood, which otherwise would readily take up the iodine and appear as a high attenuating structure. This facilitated visualisation and analysis of internal anatomy (figures 5.1-5.15).

In human, the heart is orientated so that on exposure of the thoracic cavity the major portion of the right atrium (RA) free wall is facing anteriorly, as a result anatomists refer to this region as the anterior wall of the RA. In contrast the rabbit heart is orientated so that all four chambers of the heart are visible (figure 5.1A,E), therefore

in this chapter anatomical descriptions will refer to the heart as though the rabbit is stood in the anatomical position (on hind legs). All figures presented in this chapter are from rabbit unless otherwise stated.

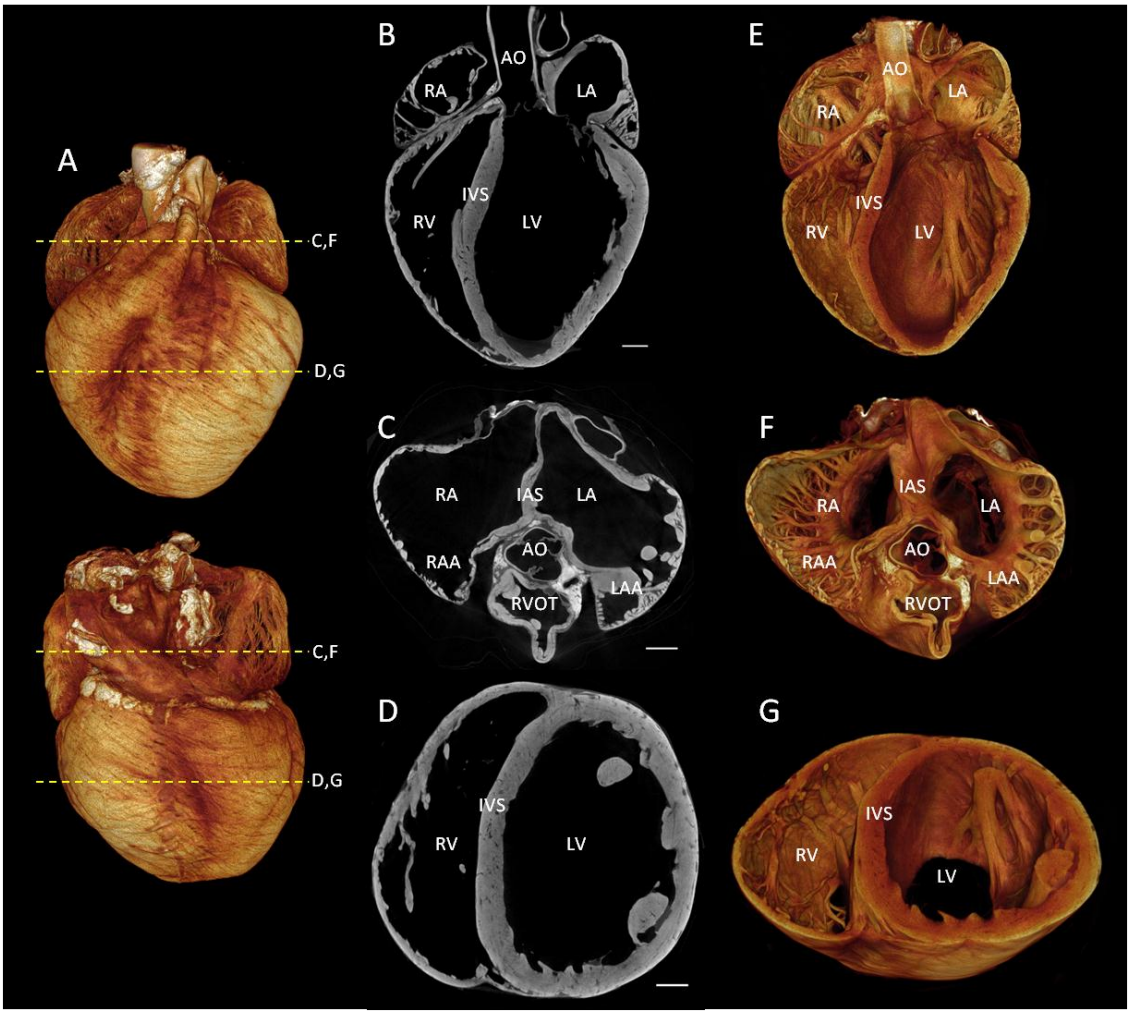

Figure 5.1 Gross anatomy of the rabbit heart shown by micro-CT. Volume rendering of whole rabbit heart stained with 7.5% I_2KI for 3 days, anterior view (above), posterior view (below) (Panel A), showing position of resliced images C,F and D,G. Central column; longitudinal, transverse atrial and transverse ventricular micro-CT images (B,C,D respectively), volume renderings at corresponding planes (E,F,G). AO- aorta, IAS- interatrial septum, IVS- interventricular septum, LA- left atrium, LAA- left atrial appendage, LV- left ventricle, RVOT- right ventricular outflow tract, RA- right atrium, RAA- right atrial appendage, RV- right ventricle. (Scale bars represent 3 mm)

5.3 The detailed 3D anatomy of the Atria

There are anatomical features characteristic of both atria, each has an appendage, venous component and a vestibule, and the respective atria are separated by an interatrial septum (IAS). The appendages, which are pouch-like extensions of the atria, could be differentiated based on morphological differences. The right atrial appendage (RAA) appeared more triangular than the left, and extended anteriorly and superiorly, coursing medially to lie on the aortic root (figure 5.1A). The left atrial appendage (LAA) was positioned more superiorly then the RAA. The larger and more pronounced LAA, projected anteriorly in the transverse plane to lie in relation with the right ventricular outflow tract (RVOT) (figure 5.1A,E).

The appendages formed the anterior walls and majority of the lateral walls of both atria. Pectinate muscles (PcMs), and thus the appendages, ran all around the lateral borders of the vestibules until they met with the venous regions. This is best shown in figure 5.1C and F. The atria were seen to have extremely thin walls supported by a complex scaffold of strut-like PcMs. When inflated during perfusion, the wall spanning between PcMs appeared semi-transparent (Figure 5.1). The PcMs, which can be seen clearly in volume renderings such as in figure 5.2D,G, figure 5.3 and figure 5.15G,I, emerge from their respective vestibules, run superiorly up the atrial free wall, before arcing medially, forming the roof of the atrium. In most cases, superiorly PcMs branched like the primary branching of a tree, giving off both medial and lateral branches (figure 5.3), with the most complex branching observed in the left atrium (LA) (figure 5.3B). Differences in PcM size and morphology were evident when comparing right and left atria; in the RA PcMs are thinner and as a result are structurally weaker, however they do show increased periodicity (figure 5.1 F, 5.2D, 5.3A). PcMs in the LA are much broader, and although are fewer in number, show increased branching superiorly (figure 5.1F, 5.2G, 5.3B). The complexity and differences are highlighted by 3D volume renderings of the endocardium and virtual casts of the cavity volumes (figure 5.2). It was clear that PcMs did not simply follow the contours of their respective atrial free walls, both atria showed PcMs with free running aspects. The PcMs were a 3D networks, with PcMs lying over one another, 4-5 muscles deep in places, analogous to a forest of trees with roots spanning the atrial floor and branches running in the roof (figure 5.3). The thickness of the atrial walls varied regionally, but on the whole the left atrial wall was significantly thicker

than the right (see Chapter 8.3). The walls of both atria were thickest inferiorly, with the thinnest regions mid-way up the free walls.

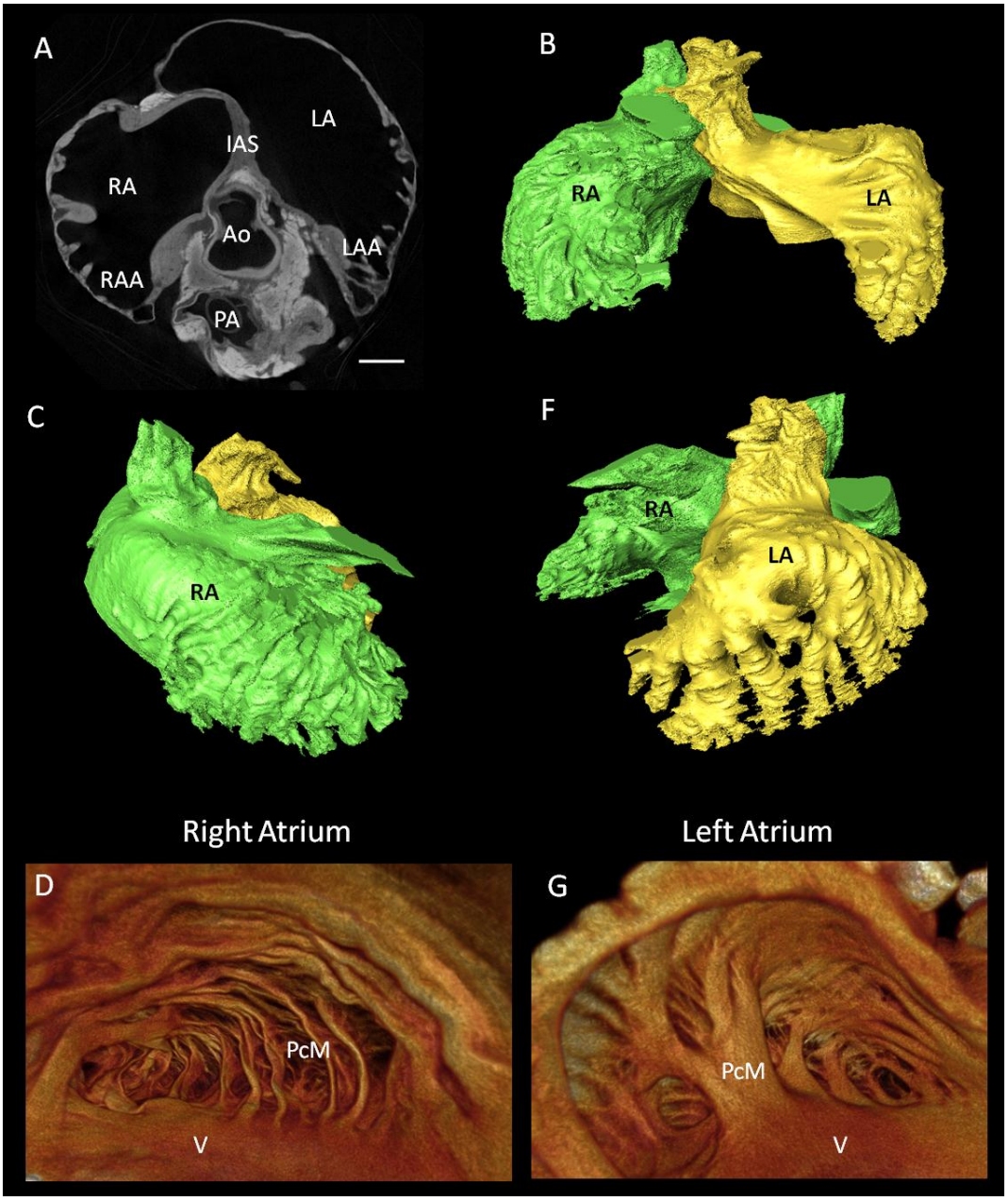

Figure 5.2 The detailed internal anatomy of the atria shown by micro-CT. Transverse Micro-CT image at the level of the atria in rabbit heart stained with 7.5% I_2KI for 3 days. 3D Isosurface of atrial cavities; anterior view (B), lateral view of right (C) and left atria (F). Internal volume renderings of right and left atrial appendages (D and G respectively), showing the detailed architecture of the pectinate muscles. Ao- aorta, PA- pulmonary artery, IAS- interatrial septum, LA- left atrium, LAA- left atrial appendage, PcM- pectinate muscle, RA- right atrium, RAA- right atrial appendage, V- vestibule. (Scale bar represents 3 mm)

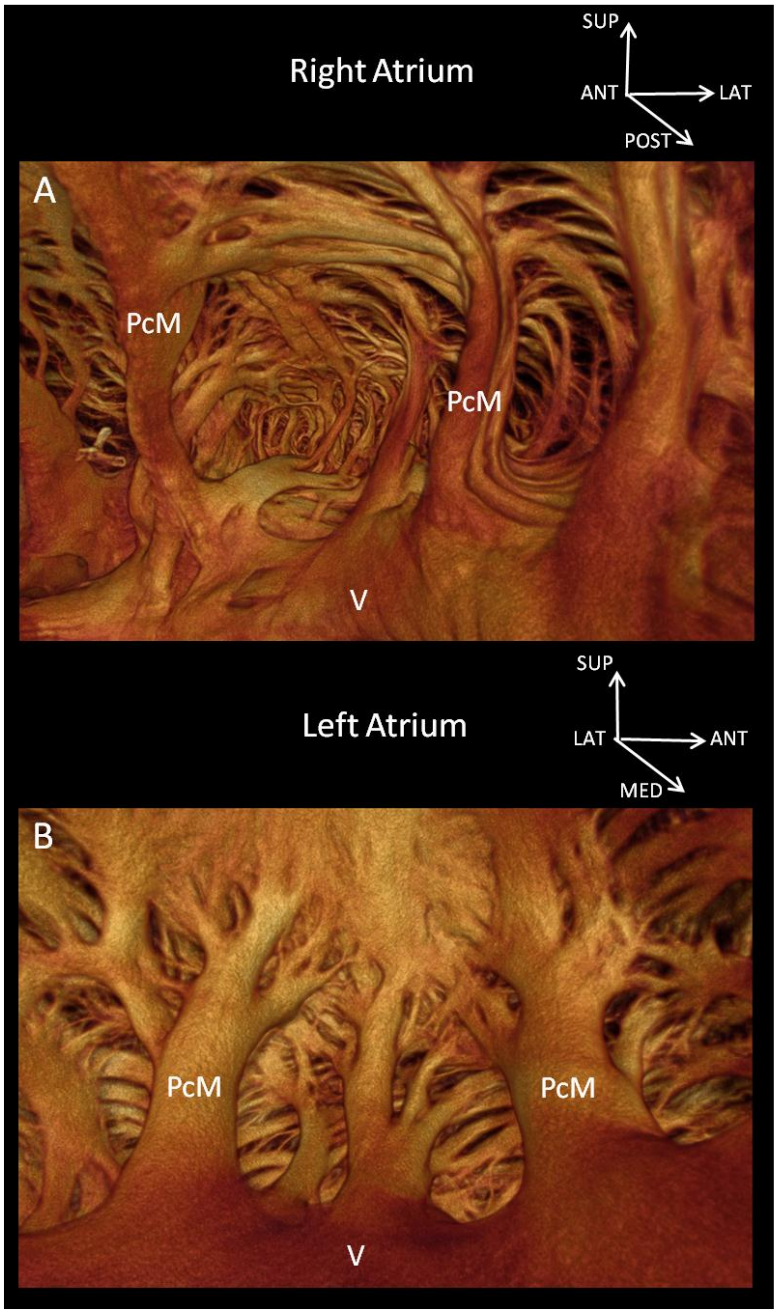

Figure 5.3 Endocardial volume renderings of right and left atrial appendages. Showing the detailed architecture of the pectinate muscles in the right (A) and left (B) atrial appendages, note their complex superior branching. Images derived from micro-CT data. PcM- pectinate muscle, V- vestibule.

Volume renderings of the posterior wall of the RA show the transition from trabeculation of the PcMs to the smooth walled venous component (intercaval region) (figure 5.4A). The transition is demarcated on the endocardium by the crista terminalis (CT); a thick band of muscle running lateral to the opening of the superior vena cava, obliquely down, like a twisted 'C', to the opening of the inferior vena cava (figure 5.4A, 5.14B). The smooth wall of the intercaval region continues medially where it becomes continuous with the IAS (figure 5.4A). On the epicardial surface the CT, referred to as the sulcus terminalis, appears as a clear ridge of muscle, and was often an area of fat accumulation. Excess fat can be removed virtually using segmentation due to its high attenuation in comparison other tissues (as shown previously in Chapter 3). Posteriorly PcMs were primarily seen to originate from the CT, with their orientation appearing as a continuation of the CT curvature (figure 5.5A,B), although in some samples the CT also gave off PcMs perpendicular to its longitudinal axis. Generally most of the PcMs took their origin from the more anteriorly lying septum spurium, a finer muscle bundle which runs anterior to the CT. In most samples numerous PcMs projected at right angles from this muscle bundle (figure 5.5A,B). Further anteriorly, accessory bundles were evident giving rise to highly complex PcMs networks (figure 5.5A,B). In the LA the majority of PcMs originated from the superior and inferior branches of Bachmann's bundle (BB), a thick muscular band which is continuous with the CT and forms the major interatrial connection anteriorly. The major free running PcMs come from the inferior branch as it circles the vestibule, while the superior branch gives rise to numerous finer and highly branching PcMs (figure 5.5C). PcMs were also seen to radiate from the septopulmonary bundle in a circumferential fashion (figure 5.5C).

In the RA, the distal ramification of the CT with the coronary sinus is often referred to as the 'flutter isthmus', because of its arrhythmogenic properties. In this region complex, interlacing muscle bundles were observed (figure 5.6). Fibres of the right vestibule were continuous with the region. Highly anisotropic muscle bundles were observed in the sub-Thebesian pouch; figure 5.6 shows this region giving branches to the IAS, Eustachian ridge and the inferior border of the atrium continuous with the triangle of Koch. The landmarks making up the triangle of Koch were resolved within the RA. In attitudinal orientation the Eustachian ridge which is continuous with the tendon of Todaro formed the medial border and the hinge line of the

tricuspid valve the lateral border. The apex is formed at the point where these borders meet anteriorly, and the base is formed by the orifice of the coronary sinus (figure 5.4A). The fossa ovalis (FO) was found superior to the triangle (figure 5.4A, 5.7, 5.14D). The ridges associated with the FO are mainly formed by infolding of the muscular atrial wall, and are believed to play an important role in cardiac conduction. In the RA the ridges were numerous and continuous with the vestibule anteriorly, and the CT and septum spurium superiorly (figure 5.7). Fibre orientation analysis of this region, in the same sample (figure 5.14D,I), reveals fibre orientation corresponds well with the folds identified in figure 5.7, meaning folds could be identified objectively from fibre orientation plots. Fibres within the folds predominantly ran in the longitudinal axis of the folds (figure 5.14I).

The pulmonary vein sleeves are located in the posterior wall or venous component of the LA (Which is larger than in RA). These are short tubes of circumferentially running myofibres, which anchor the 2-4 pulmonary veins to the LA. Figure 5.4B shows the two inferior PV sleeves, and reveals a complex relationship between the PV sleeves and the posterior LA. At the superior and inferior borders, the circumferential fibres of the PV sleeves become continuous with the vertical fibres of the LA, initially appearing as defined ridges, before embedding into the myocardium. Fine connections exist between the superior and inferior regions of the two sleeves respectively, which run perpendicular to myocardium dividing the sleeves. The extracted fibre orientation of the right inferior PV sleeve is shown in figure 5.14E,J.

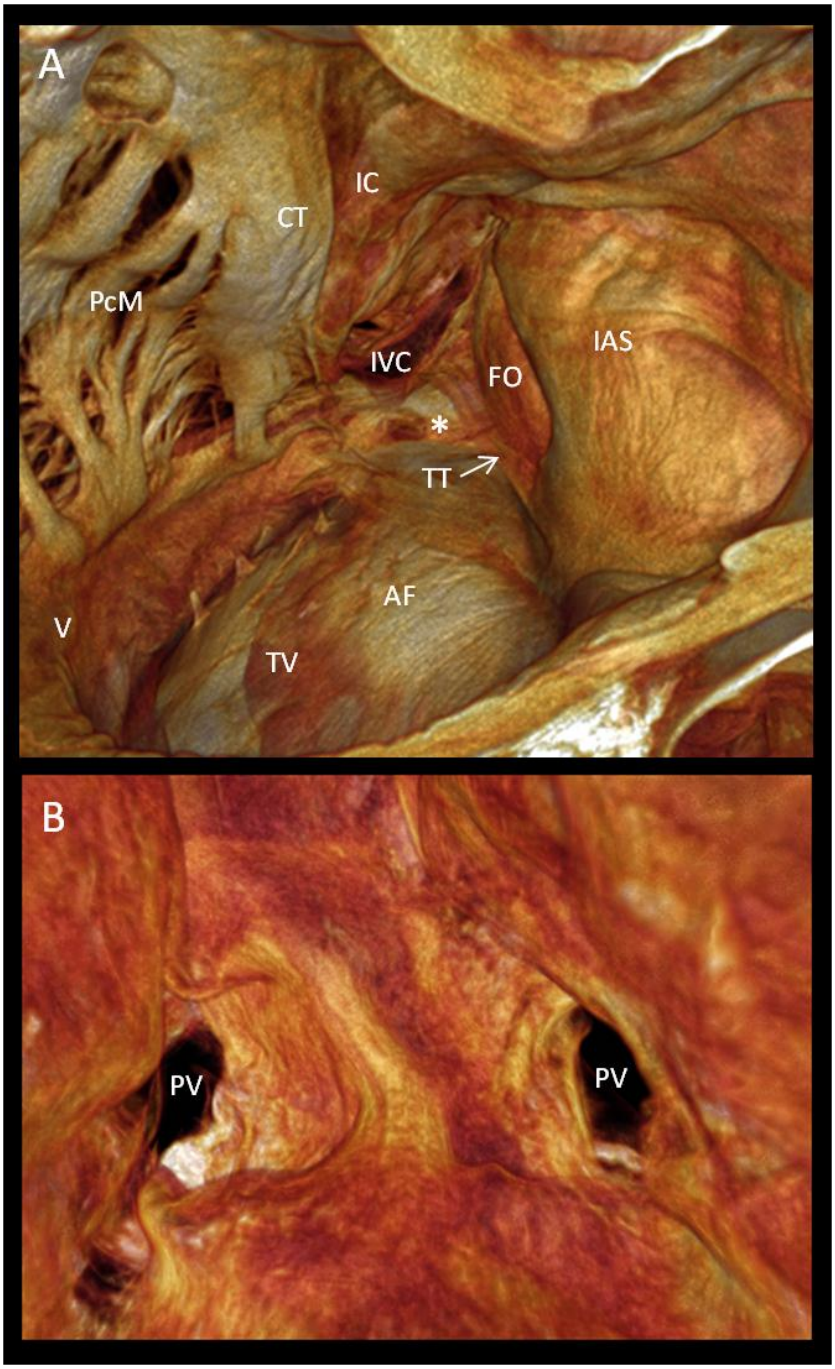

Figure 5.4 Endocardial volume renderings in the venous regions of the atria. The right atrial cavity (A): showing the transition from the PcMs of the right atrial appendage to the smooth venous region, and the anatomical landmarks for the triangle of Koch. The venous region of the left atrium (B); showing the complex relationship between the working myocardium and pulmonary sleeves (B). Images derived from micro-CT data. CT- crista terminalis, FO- Fossa ovalis, IAS- interatrial septum, IC- intercaval region, IVC- inferior vena cava, PcM- pectinate muscle, RIPV,LIPV- right and left inferior pulmonary vein, TT- tendon of Todaro, TV- Hinge of tricuspid valve, V- vestibule, *- opening of coronary sinus.

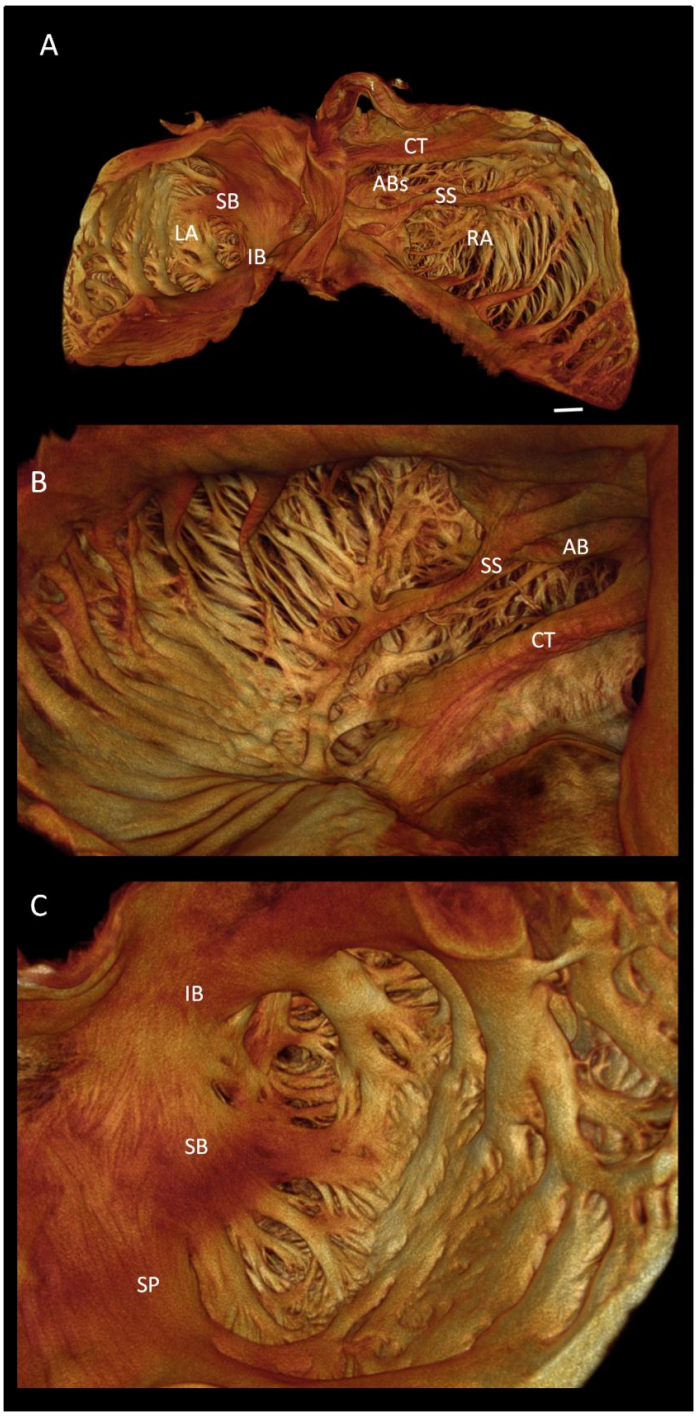

Figure 5.5 Volume renderings of the atrial cavities showing the origin of the pectinate muscles. Internal volume rendering of the atria, longitudinally resliced and viewed posteriorly (A), showing the major muscle bands (CT, SS, ABs) that give rise to the pectinate muscles (Scale bar represents 2mm). High power internal volume renderings viewed from inferior/posterior aspect of the right and left atria (B and C respectively). Images derived from micro-CT data. AB- accessory bundle, CT- crista terminalis, IB and SB- inferior and superior branches of Bachmann's bundle, LA- left atrium, RA- right atrium, SP- septopulmonary bundle, ss-septum spurium.

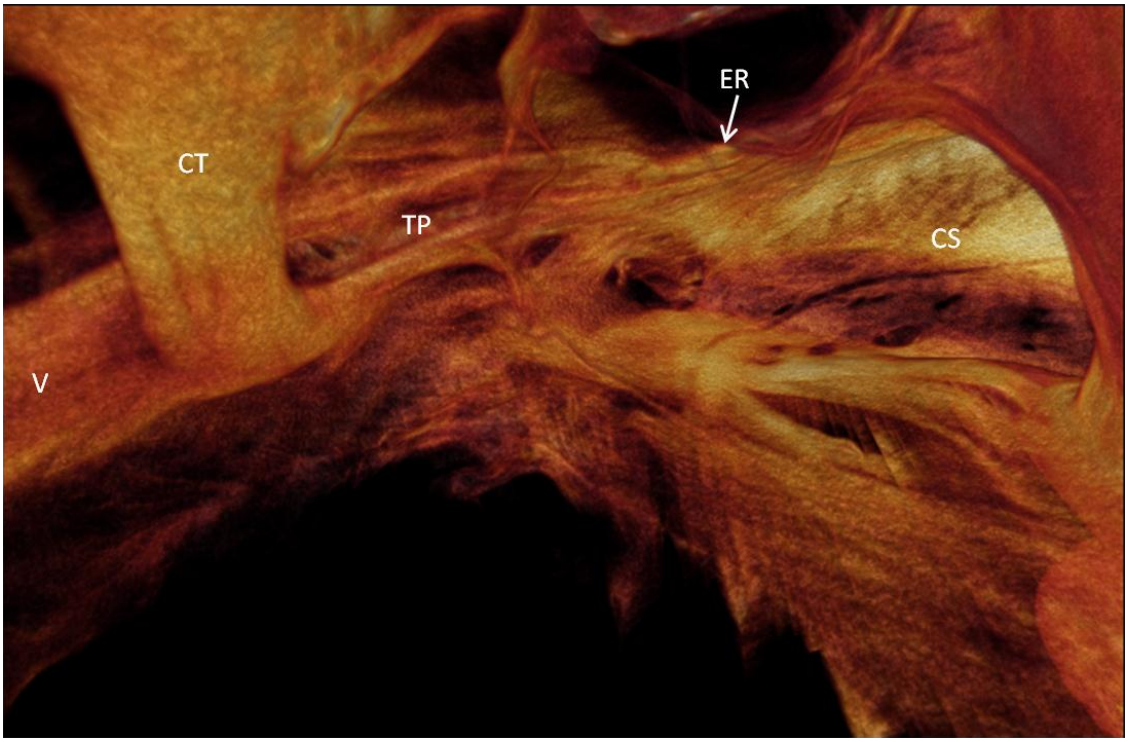

Figure 5.6 Volume rendering of the 'flutter isthmus'. Endocardial view in the region of the 'flutter isthmus' of the right atrium. Image derived from micro-CT data. CT- crista terminalis, CS- coronary sinus, ER- eustachian ridge, TP- sub Thebesian pouch, V- vestibule.

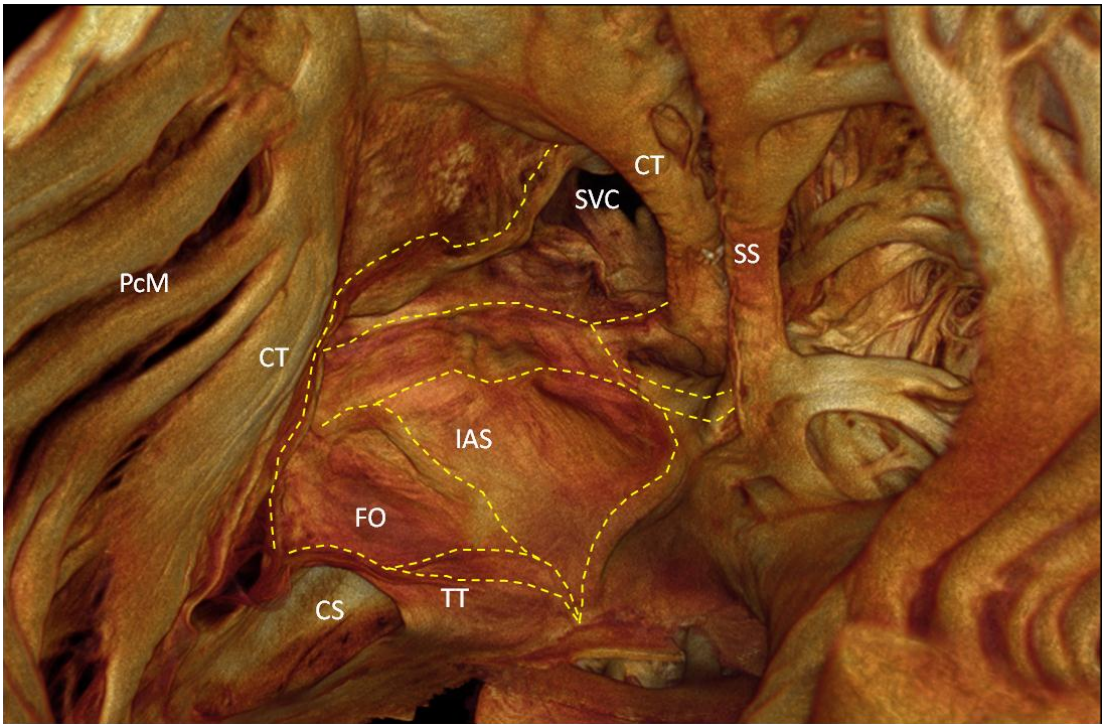

Figure 5.7 Volume rendering of interatrial septum from inside the right atrium. showing the anatomical ridges (yellow dotted lines) associated with the fossa ovalis and their relationship with surrounding structures. Image derived from micro-CT data. CT- crista terminalis, CS- coronary, FO- fossa ovalis, IAS- interatrial septum, PcM- pectinate muscle, SS- septum spurium, TT- tendon of Todaro.

3.4 Anatomy of the Ventricles

Similar differences were evident when analysing the internal anatomy of the ventricles, differences have been noted previously however surfaces generated here from micro-CT data offer a new visual appreciation. In mature hearts the RV had a thinner wall and smaller myocardial volume than the LV (602±63 mm^3 vs. 1514±177 mm^3, mean±SE, n=7), but the RV cavity had a larger volume (1905±322 mm^3 vs. 1426±343 mm^3, n=7) and surface area. The trabeculae carneae on the endocardial surface of the RV (figure 5.8B,C) appeared fine and complex, with many interconnecting elements. This is in contrast to the thick trabeculae carneae of the LV, which appeared more organised with few interconnections (figure 5.8F). Septomarginal trabeculae were resolved connecting the RV free wall to IVS, the most prominent being the moderator band (figure 5.8B). In contrast to the ventricular

free walls the IVS was smooth with very few trabeculae. The fibres of the IVS can be seen to radiate from the superoanterior region (figure 5.8E), where the bundle branches of the cardiac conduction system would be expected to arise as they course inferiorly from the branching bundle.

In the LV papillary muscles, (PM) appeared as thick free running muscle bundles, strongly anchored inferiorly in the apical region, and thus spanned the majority of the LV cavity longitudinally (figure 5.8F). In contrast PMs of the RV appeared as short, fine muscle bundles, originating from mid-way down the IVS. PMs in the RV varied in number, with 2-4 muscles observed across samples. In contrast, there was no variation evident in the LV, with 2 PMs present in every sample. In micro-CT data the membranous septum was resolved as a low attenuating structure, and as a result could be differentiated from the muscular IVS (figure 5.8A). The 3D morphology of the membranous septum, and its division into atrioventricular and interventricular components could be appreciated (figure 5.12) .

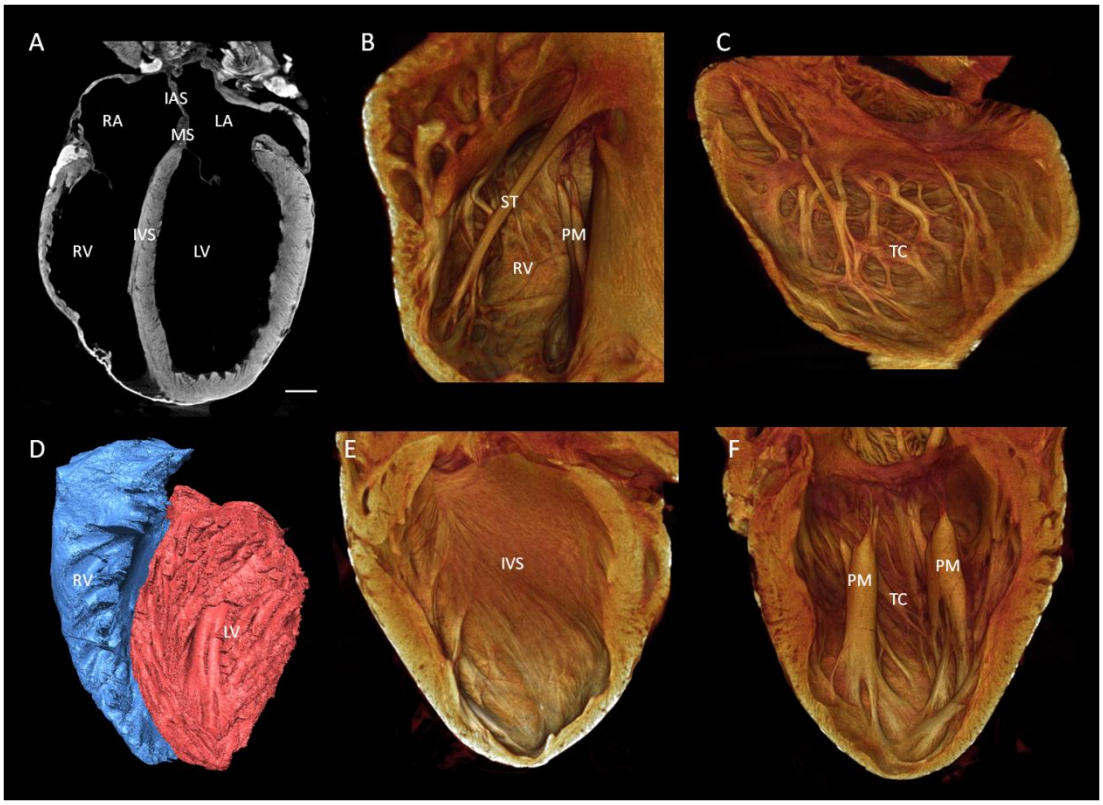

Figure 5.8 The internal anatomy of the ventricles revealed by micro-CT. Longitudinal Micro-CT image of rabbit heart stained with 7.5% I_2KI for 3 days (A), corresponding isosurface of right and left ventricular cavities (D). Volume renderings from the right ventricular cavity; anterior view (B) and right ventricular free wall (C). Volume renderings from left ventricular cavity; septal view (E) and left ventricular free wall (F). IAS- interatrial septum, IVS- interventricular septum, LA- left atrium, LV- left ventricle, MS- membranous septum, PM- papillary muscle, RA- right atrium, RV- right ventricle, ST- septomarginal trabeculae (moderator band), TC- trabeculae carneae. (Scale bars represent 3 mm)

High resolution coupled with high signal: noise ratio allows imaging of very small samples while maintaining impressive image quality. This facilitates the investigation of embryonic development of the heart. Here images are presented from fixed embryonic pig samples of varying gestation age (~30-100 days), stained with I_2KI and micro-CT scanned. Vast morphological changes were evident; initially hearts appeared symmetrical with even wall thickness and two distinct ventricles, resulting in a heart with two apices (figure 5.9B,C). As development proceeds the RV wraps itself around the elongating LV (figure 5.9E,F), and a single apex is

formed. Close to full term the heart takes on an elongated appearance, the LV wall thickens and the dilatation of the RV cavity is coupled with thinning of the RV free wall (figure 5.9H,I). Analysis of the ventricular cavities revealed a morphological shift throughout the course of development, early in development the LV cavity volume is larger than the RV (figure 5.9B,C), and this relationship is maintained up until ~. 50 days gestation (figure 5.9E,F), after this point LV elongation and wall thickening causes the LV cavity to considerable decrease in relation to the dilating RV (figure 5.9H,I). The trabeculation on endocardial surface appears complex and disordered early in development (figure 5.9C), as development proceeds the trabeculae gradually become more ordered, and at term appear as well defined tracts (figure 5.9I).

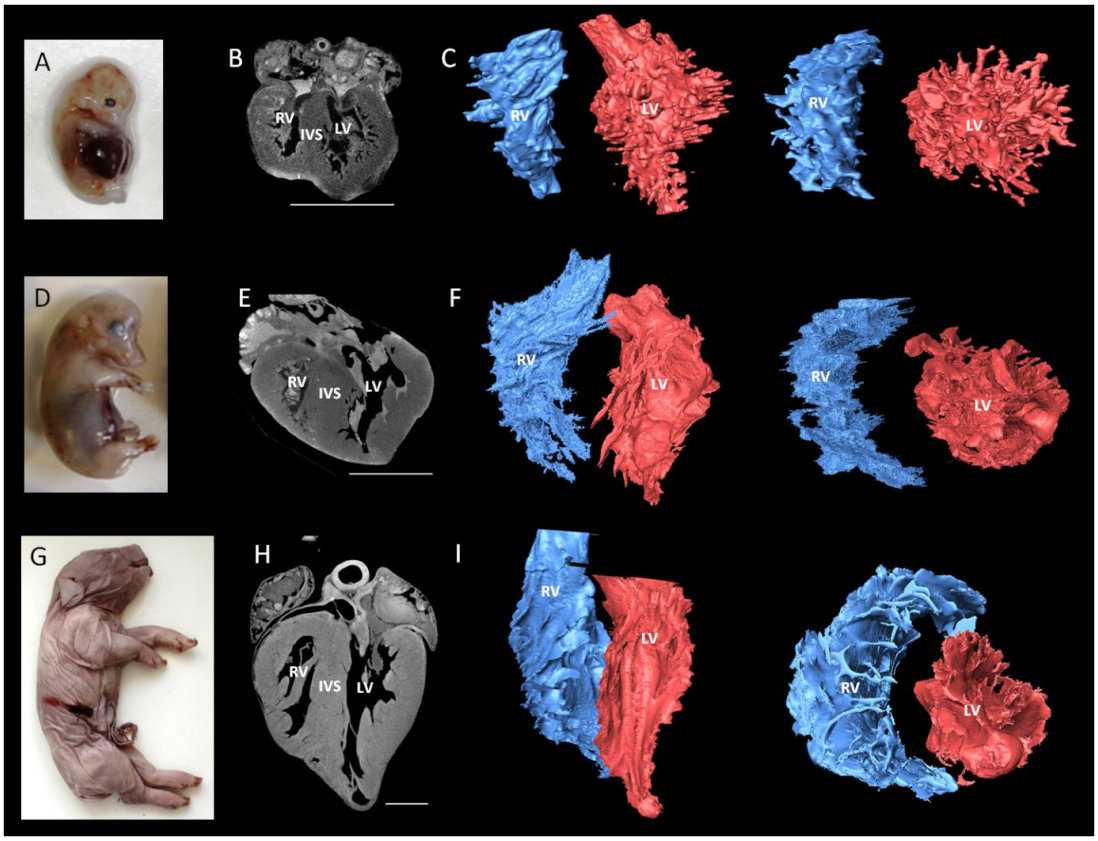

Figure 5.9 Micro-CT images of the developing pig heart with corresponding isosurfaces of the ventricular cavities. Pig embryonic specimens at various stages of gestation (~30, 50, 100 days respectively), rostral-caudal length (22, 49, 310mm respectively) (A,D,G). Longitudinal micro-CT sections from the corresponding hearts (B,E,H). Isosurfaces of ventricular cavities in longitudinal and transverse (apex-base) orientation (C,F,I). RV volumes- 0.64, 1.39, 65.49mm³ respectively, LV volumes- 1.01, 2.68, 40.42mm³ respectively. IVS- interventricular septum, LV- left ventricle, RV- right ventricle. (Scale bar represents 3 mm)

5.5 The 3D anatomy of the cardiac valves

Here the detailed anatomy and fine structure of the cardiac valves are revealed by contrast enhanced micro-CT. Valve leaflets are made up of fibrous tissue, and thus do not readily take up the iodine contrast (see Chapter 4.2). Therefore leaflets appear as low attenuating structures in comparison to the high attenuating myocardium and surrounding vessel walls. The atrioventricular valves permit flow of blood from the atria to the ventricles, and prevent regurgitation. The atrioventricular valvar complex

is made up of an annulus, valve leaflets, tendinous cords and papillary muscles. The annulus is part of the fibrous skeleton of the heart, and is where the valve leaflets hinge from. The attachments at the annuli appeared more substantial in the mitral valve (MV) (figure 5.10C,D) than in the tricuspid (TV) (figure 5.10A,B). The TV has two leaflets (lateral and septal) in rabbit and hence should be defined as bicuspid (figure 5.10B). The leaflets of the TV are seen to hang from their respective annuli, with the lateral cusp attaching to two-thirds of the annular circumference, while the septal leaflet attaches to the remaining one-third (figure 5.10B). The leaflets of the MV appeared to occupy even amounts of the annulus, and volume renderings allowed detailed appreciation of the relationship between the aortic leaflet of the MV and the leaflets of the aortic valve (figure 5.10D). The papillary muscles and chordae tendineae make up the sub-valvar apparatus, which functions to prevent prolapse back into the atria, aid ventricular ejections and moderate mural tensions in diastole. The papillary muscles morphology and there attachments were variable. The papillary muscles associated with TV were shorter, finer and less substantial than those in the LV, and their number ranged from 2-4. The MV consistently had two muscles supporting its leaflets. 3D volume renderings reveal the chordae tendineae run from the superior aspect of the papillary muscles to form extensive connections which run deep into the complex fibrous tissue mesh of the valve leaflets (figure 5.10B,D). All categories of chordae tendineae; strut, basal and fan, were observed in both TVs and MVs, as shown in figure 5.5B,D. Strut cords can be distinguished by their size, and attach to the rough zones- the regions of leaflets between the free edge and annulus. Basal cords attach to the ventricular surface of the leaflets at the annulus, while fan cords support the free edges of the leaflets. So, all components of the atrioventricular valves are resolved in impressive detail using contrast enhanced micro-CT (figure 5.10).

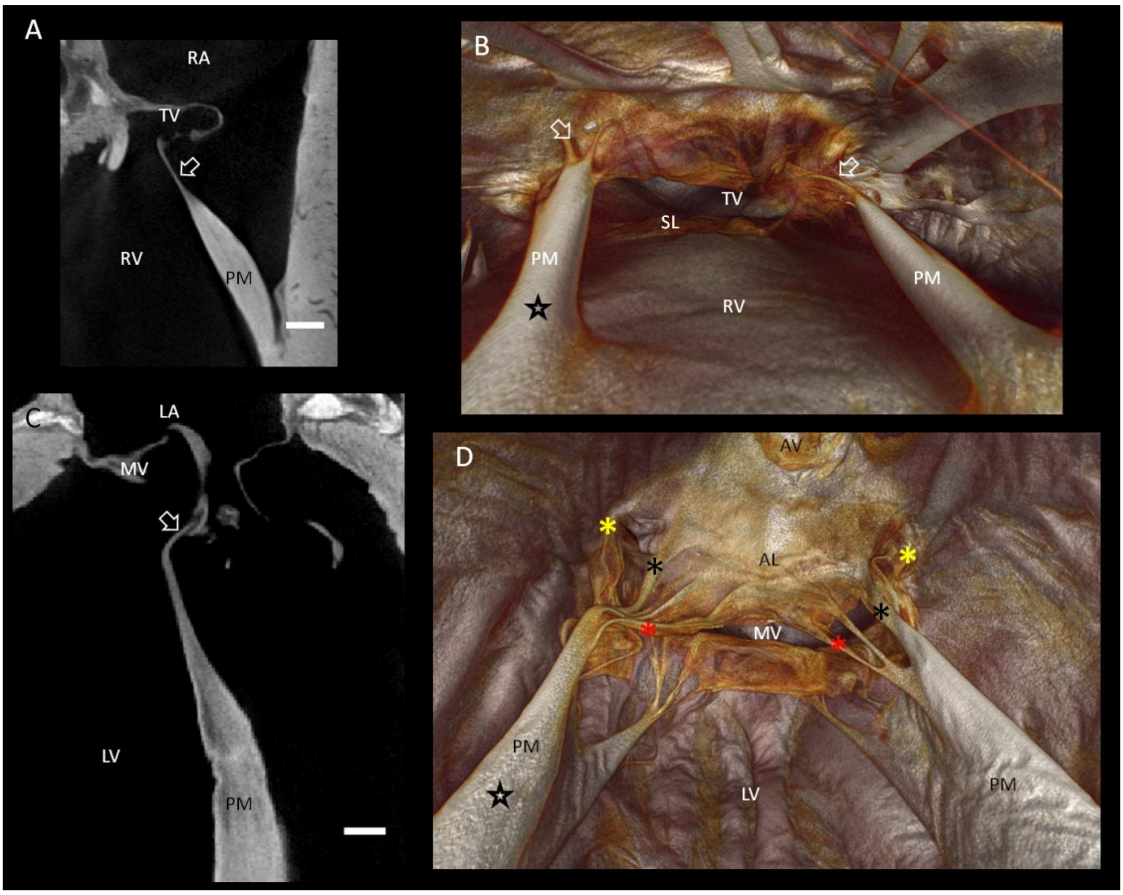

Figure 5.10 Longitudinal micro-CT images of the atrioventricular valves with corresponding volume renderings. Tricuspid and mitral valve micro-CT images (A,C respectively), showing the valve leaflets' fine connections with the papillary muscles. Volume renderings looking from apex to base of tricuspid (B) and mitral valves (D), showing their 3D morphology. Arrows indicate chordae tendineae, stars indicate posterior papillary muscle, *- Strut cord, *- Basal cord, *- Fan cord. AL- aortic leaflet, AV- aortic valve, LV- left ventricle, MV- mitral valve, PM- papillary muscle, RV- right ventricle, SL- septal leaflet, TV- tricuspid valve. (Scale bar represents 1 mm)

The semilunar valves are positioned at the base of both the pulmonary artery and the aorta, and function to prevent backflow of blood into the heart. Figure 5.11A,B,C show the 3 low attenuating valve cusps of the aortic valve are easily distinguished from the high attenuating walls of the aorta, longitudinal micro-CT images reveal the aortic sinus and nodule of each cusp (figure 5.11A). The left (LCC) and right (RCC) coronary cusps were identified as the two cusps from which the left and right coronaries could be seen emerging, you can see the right coronary artery emerging

from the RCC in figure 5.11B. The non-coronary cusp (NCC) lies posterior to the two anterior cusps (figure 5.11). The valve leaflets can be segmented and presented as 3D quantifiable isosurfaces (figure5.11D,E,F). The apposed state of the leaflets, as seen in figure 5.11, was not achieved in all samples, but this appearance shows that our perfusion fixation technique preserves the structural integrity of the valves. In this the apposed state the commissures of the valves can be appreciated, as they run from the periphery to the centre of the valve orifice at the point where adjacent cusps meet (figure 5.11C,D). The extension of the superior attachments high up the aortic root was evident in all samples (figure 5.11B,E,F and figure 5.12). The differential attenuation achieved between the myocardium, membranous septum, nodal tissue and the valve cusps allowed visualisation of the attachments of the cusps to the so-called 'aortic annulus' and their 3D relationship with surrounding structures. Visualisation of relationships was aided by virtual removal and addition of the valve leaflets in real time based on their pixel values. The attachment of the cusps to both the fibrous skeleton and muscular IVS was clarified; The RCC and NCC took attachment at the central fibrous body, laterally the RCC anchored to the membranous septum (figure 5.12A), and posteriorly the NCC was seen to attach in the region of the right fibrous trigone, and had a fibrous attachment to the MV (figure 5.12A). Figure 5.12A nicely shows the 3D relationship of the RCC and NCC with the inferiorly lying atrioventricular conduction axis (see Chapter 6 for detailed description), which originates at the apex of the triangle of Koch in the RA, before snaking anteriorly on top of the IVS embedded within the central fibrous body. The LCC was shown to have attachments to both the IVS and atrial myocardium (figure 5.12B), and like the NCC was seen to have a fibrous continuity with the MV (figure 5.12B). Volume renderings revealed low attenuating regions extending below the apex of the commissures, these areas correspond to regions of thin fibrous tissue, the interleaflet triangles, which form the anatomic ventriculoaortic junction.

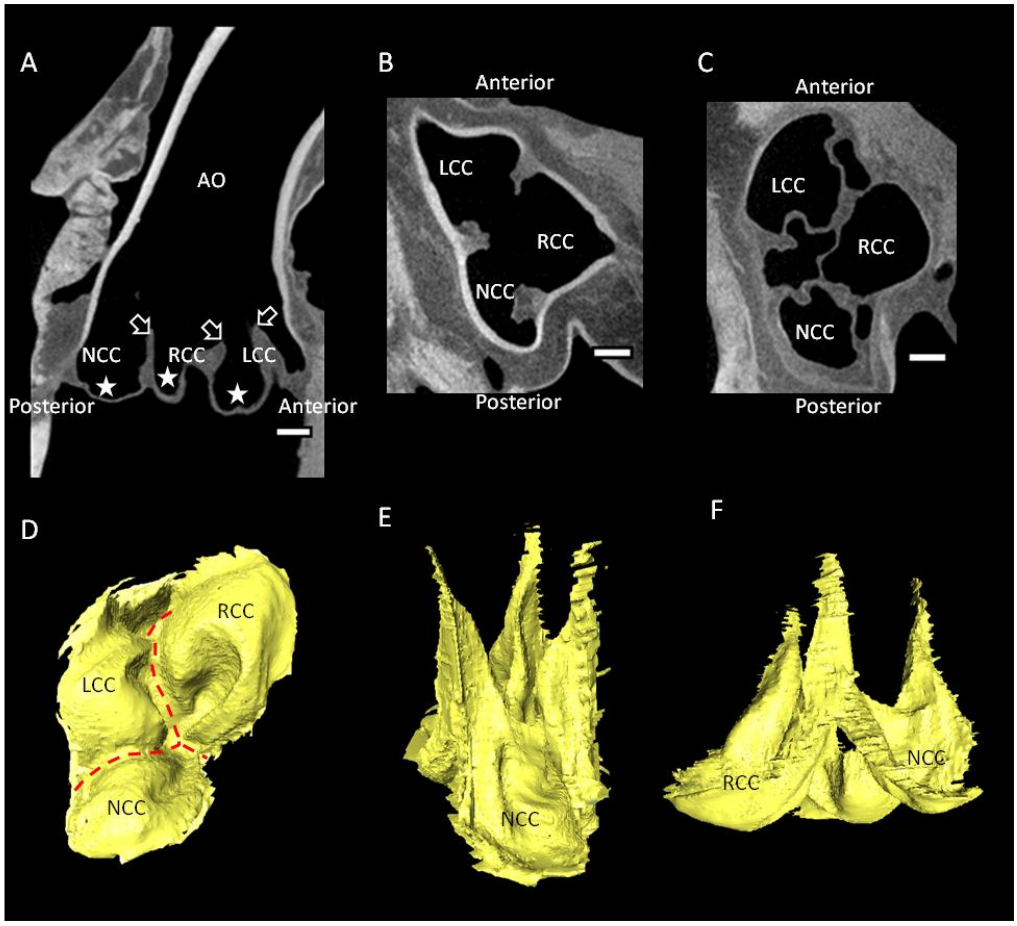

Figure 5.11 Micro-CT images of the aortic valve with corresponding isosurfaces of the valve leaflets. Micro-CT images through the aorta showing the three cusps of the aortic valve; mid longitudinal plane (A), superior transverse plane (B) and inferior transverse plane (C). Open arrows represent nodules, stars represent aortic sinuses. Isosurface of segmented aortic valve, inferior view (D), posterior view (E) and lateral view (F). Aortic valve volume- 12.8 mm^3. Red dotted line represents valve commissures. Ao- aorta, LCC- left coronary cusp, NCC- non coronary cusp, RCC- right coronary cusp. (Scale bar represents 1 mm)

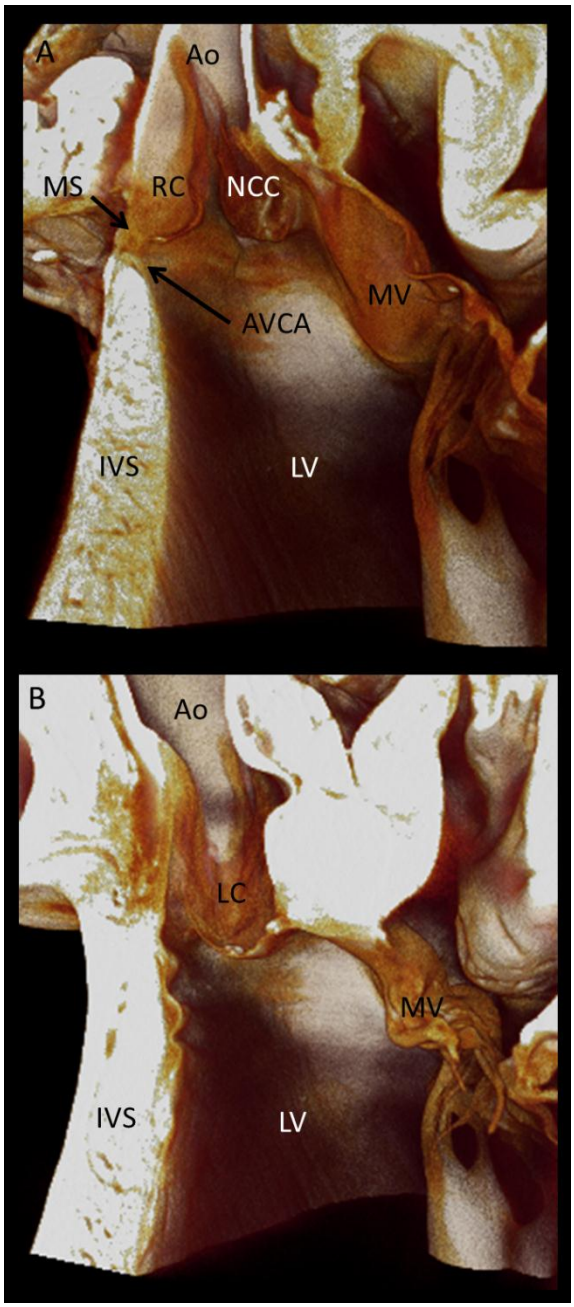

Figure 5.12 Volume renderings of the aortic valve and surrounding structures. Volume renderings longitudinally resliced and viewed anteriorly, showing the posteriorly lying non-coronary cusp and the adjacent right coronary cusp (A), and the more anteriorly lying left coronary cusp of the aortic valve (B). Images derived from micro-CT data. Ao- aorta, AVCA- atrioventricular conduction axis, IVS- interventricular septum, LC- left coronary cusp, LV- left ventricles, MS- membranous septum, MV- mitral valve, NCC- non-coronary cusp, RC- right coronary cusp.

5.6 Morphology of the cardiac vessels

Perfusion fixation blanches the myocardium by washing the residing blood from the coronary and venous circulation, this allows mapping of their complex course throughout the myocardium. The thick wall of the aorta appears as a high attenuating structure (figure 5.13A,B), however as the left and right coronary arteries (which emerge from the aorta) run into the ventricles their walls become low attenuating in comparison to the surrounding myocardium (figure 5.13A,B). In figure 5.13C,D the lumen of the left coronary artery has been semi-automatically segmented and presented in 3D and overlaid with semi-transparent myocardium of the whole heart. This allows appreciation of the vessels' branching pattern, thickness and transmural position in 3D. Using filament analysis (methods 2.4.3) this data can then be quantified to show the vessels' volume, length, and width variations; the number of segments, nodes and branching points can also be extracted (figure 5.13).

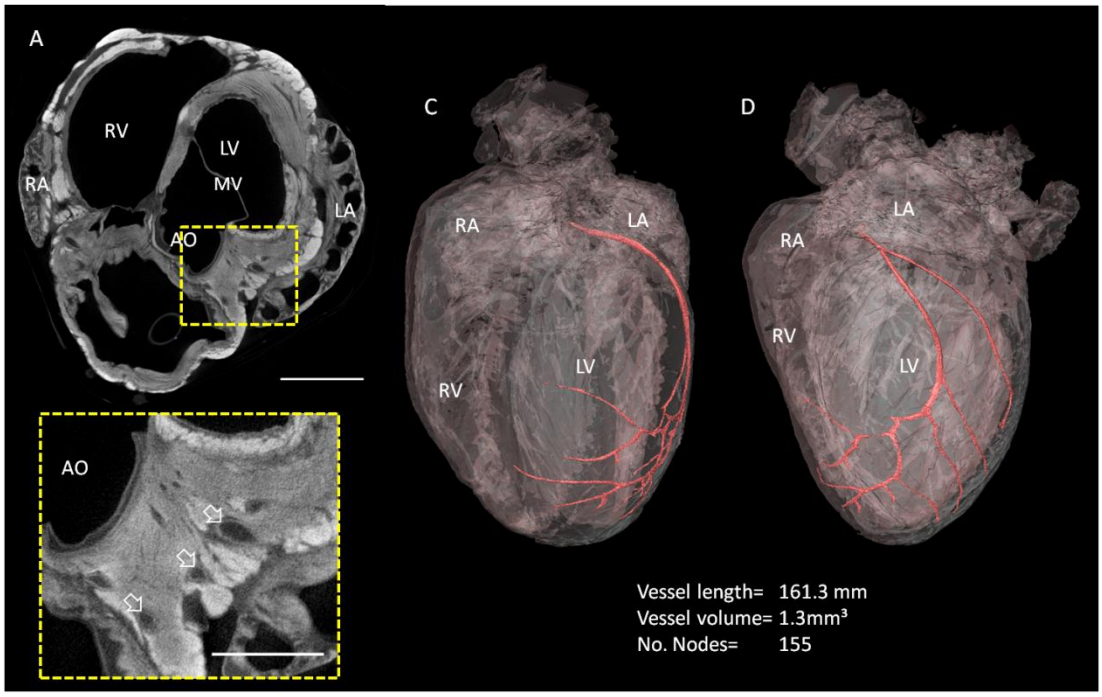

Figure 5.13 The left coronary artery segmented from micro-CT data. Transverse micro-CT image of rabbit heart showing the early course of the left coronary artery (A), high power image (B). Arrows indicate artery walls. Segmented isosurface showing the 3D course of the left coronary artery (red), overlaid with semi-transparent cardiac mass (pink). LA- left atrium, LV- left ventricle, RA- right atrium, RV- right ventricle, MV- Mitral valve. (Scale bar represents 3 mm)

5.7 Fibre orientation in the atria and the associated muscle bands

Contrast enhanced micro-CT has been shown to non-invasively resolve the arrangement of single muscle fibres (Chapter 4.3). Consequently novel structure tensor and fibre tracking analysis was carried out on micro-CT data of 5 adult rabbit hearts, to visualise and quantify 3D myofibre orientation of the atria and ventricles. Methods for fibre orientation extraction are the same as those described in Chapter 4 when the fibre orientation of skeletal muscle blocks was extracted. For full methods see methods 2.4.4 and Figures 2.1 and 2.2.

The atria

Fibre orientation in the atria was complex with dramatic shifts in fibre orientation transmurally and at structural junctions. Considerable regional heterogeneity was evident; sub regions such as CT, PcMs, Bachmann's bundle (BB) appeared ordered (figure 5.14 A,B,F,G), whereas the intercaval region, IAS and LAA showed striking complex myofibre architectures (figure 5.14 C,D,H,I). In the PV sleeve (figure 5.14E, J), fibres ran circumferentially at the point where the PV anchors into the posterior LA. However as the fibres become continuous with the surrounding myocardium of the LA, complex arrangements were observed, and in some regions fibre ran orthogonal to one another.

The fibre orientation in the RA free wall was shown predominantly to consist of vertical fibres running parallel to the scores of slender PcMs (figure 5.15B,C,D,G.H). In contrast the LA free wall showed an abrupt transmural transition, from predominantly transverse fibres at the epicardium (figure 5.15B,E,F), to vertical fibres at the endocardium dictated by the large PcMs (figure 5.15I,J). The fibre orientation analysis reveals that inferiorly the PcMs of the RA and LA are strongly anchored into the lateral aspect of the tricuspid and bicuspid vestibules respectively, with many fibres radiating from the majority of the circumference of the PcMs base (Figure 5.15H, J). At this junction there is an abrupt change from vertical fibres to transverse circumferential fibres, and in some areas there was evidence of orthogonally running fibres (figure 5.14G,H,I,J). Superiorly their relationship with atrial wall is more disordered, with complex networks of overlying fibres branching into the atrial wall. The most complex relationships were observed in the LA (figure 5.15I,J), this is partly due to the complex branching as discussed previously (figure

5.2.1). In the LA a complex intermingling of circumferential and longitudinal fibres in between PcMs was evident (figure 5.15J), this was in contrast to the predominantly vertical arrangement of fibres between PcMs in the thin RA wall (figure 5.15H). In both the RA and LA the atrial roof consisted of mostly transverse fibres, appearing as a continuation of the curvature of the PcMs fibres (figure 5.14B,D,F).

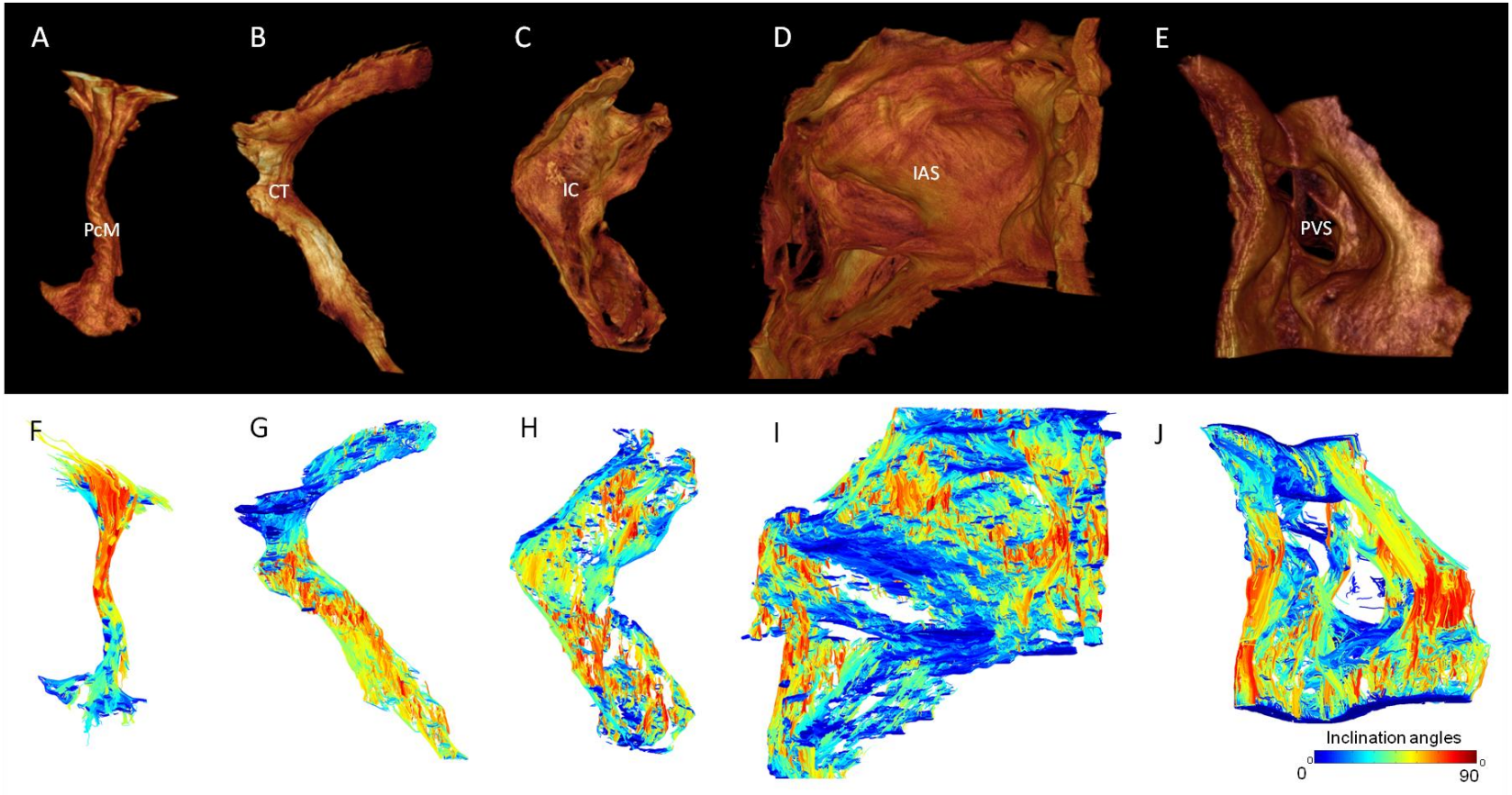

Figure 5.14 Volume renderings of segmented atrial structures with corresponding fibre orientation extracted from micro-CT data. Volume rendering of pectinate muscle (A), crtista terminalis (B), inter caval region (C), interatrial septum (D) and right inferior pulmonary vein sleeve (E). Corresponding fibre orientations extracted from micro-CT data (F,G,H,I,J). Isometric resolution of micro-CT data ~20 µm. Colour bar represents inclination angle. PcM- pectinate muscle. CT- crist terminalis, IC-intercaval region, IAS- interatrial septum, PVS- pulmonary vein sleeve. Fibre orientation extracted in collaboration with Dr Jichao Zhao, The University of Auckland, NZ.

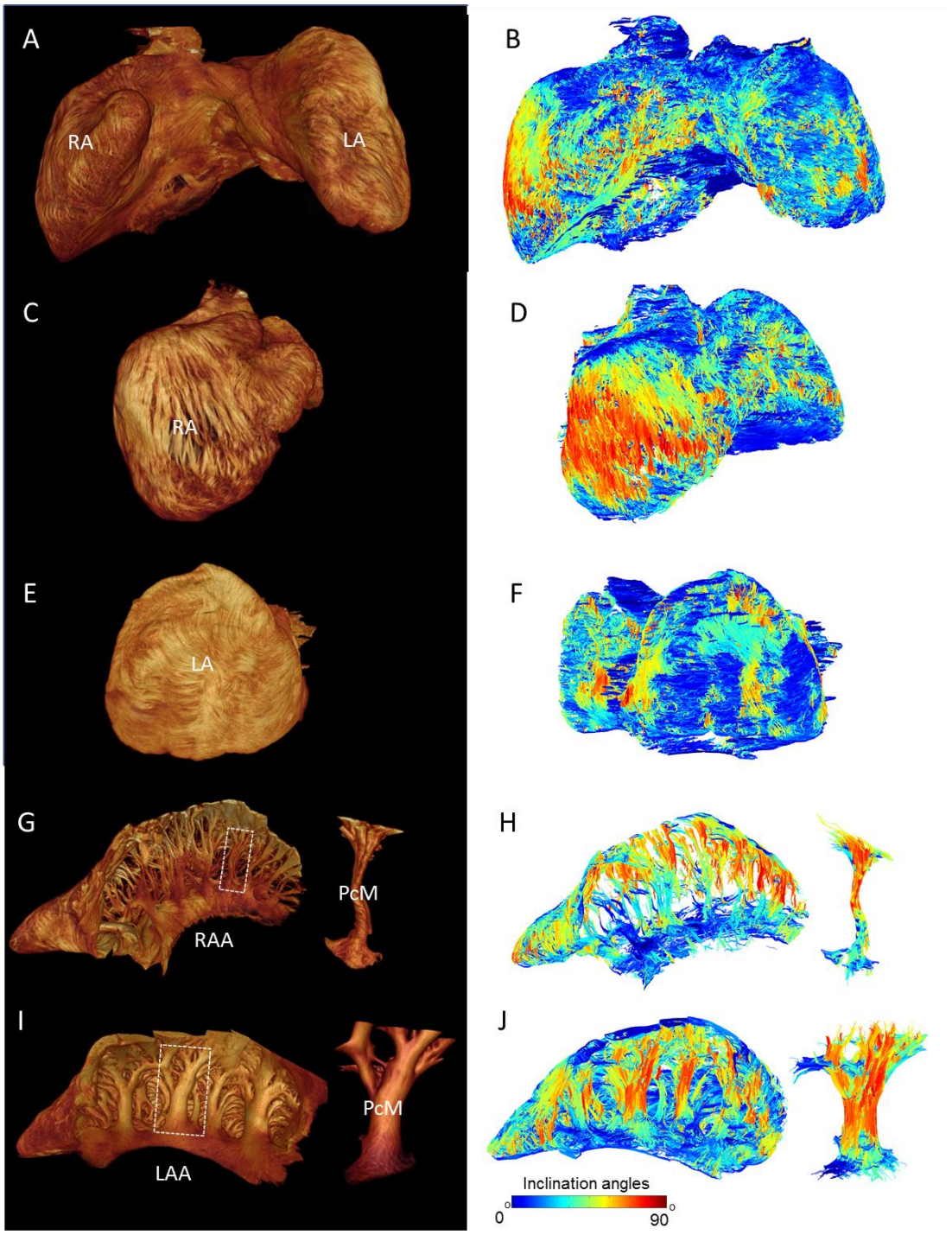

Figure 5.15 Atrial volume renderings with corresponding fibre orientations extracted from micro-CT data. Volume renderings of the whole atria (A), right (C) and left (E) atria (lateral aspects), and right and left atrial appendages with isolated pectinate muscles (G and I respectively). Corresponding fibre orientations maps (B,D,F,H,J). Isometric resolution of micro-CT data ~20 µm. Colour bar represents inclination angle. LA- left atrium, LAA- left atrial appendage, PcM- pectinate muscle, RA- right atrium, RAA- right atrial appendage. Fibre orientation extracted in collaboration with Dr Jichao Zhao, The University of Auckland, NZ.

The muscle bands

Muscular bands and sleeves exist within the atria which are thought to play a vital role in the preferential propagation of action potentials and effective muscular contraction of the atria. 3D fibre orientation was conducted to reveal and clarify the arrangement of muscle fibres within these structures. These bands vary in size, shape and prominence, and include: the CT (figure 5.14B,G) and septum spurium, the Eustachian ridge and rims of the fossa ovalis (figure 5.14D,I), the PcMs and their associated vestibules (all discussed above) (figure 5.14A,F and 5.15I,J), and the circumferential muscle bands. Generally the fibre orientation in these structures was ordered and followed their longitudinal axis, which will assist in both fast propagation and efficient contraction in their long axis. An example of a sleeve structure is the muscular extensions of the PVs (figure 5.14E,J), the fibres of these sleeves were predominantly circumferential, but extremely complex interlacing fibres were observed at its integration with the venous region of the LA.

The circumferential muscle bands of the RA are often categorised into internal and external bands. The internal circumferential bundle is made up of fibres running around the contour of the tricuspid vestibule (partly shown in figure 5.15G, H). The external bundle was identified running around the inferior aspect of the RAA (figure 5.15 B,D), extending round posteriorly towards the interatrial groove- Waterson's groove (figure 5.16C,D). Posteriorly the external circumferential bundle is almost continuous with the posterior interatrial bundle, which runs from the region of the coronary sinus across to embed into the venous component of the LA (figure 5.16C,D). Superior to the origin of the posterior interatrial bundle, the transverse running fibres of the intercaval bundle could be appreciated as distinctive bands of circumferential running fibres (figure 5.16C,D). Running below the epicardium, the intercaval fibres originate from the rims of the fossa ovalis, and run laterally, coursing the venous region, to merge with the PcMs of the RA free wall. The circumferential bundles of the LA are stronger and more pronounced, the principal bundle was identified as a continuation of the anterior interatrial bundle, also known as Bachmann's bundle (figure 5.16A,B). It forms superior and inferior bundles (figure 5.5A,C), both of which give branches to the PcMs. The lower bundle also gives a branch to the mitral vestibule (figure 5.5), eventually coursing round to Waterson's groove posteriorly (figure 5.15J). The septopulmonary bundle was also

identified, originating posteriorly in Waterson's groove, it coursed vertically to the superior anterior LA as a broad and ordered bundle (figure 5.16 C,D), before connecting with BB anteriorly and giving off branches to the anterior LA free wall (figures 5.16B and 5.15B).

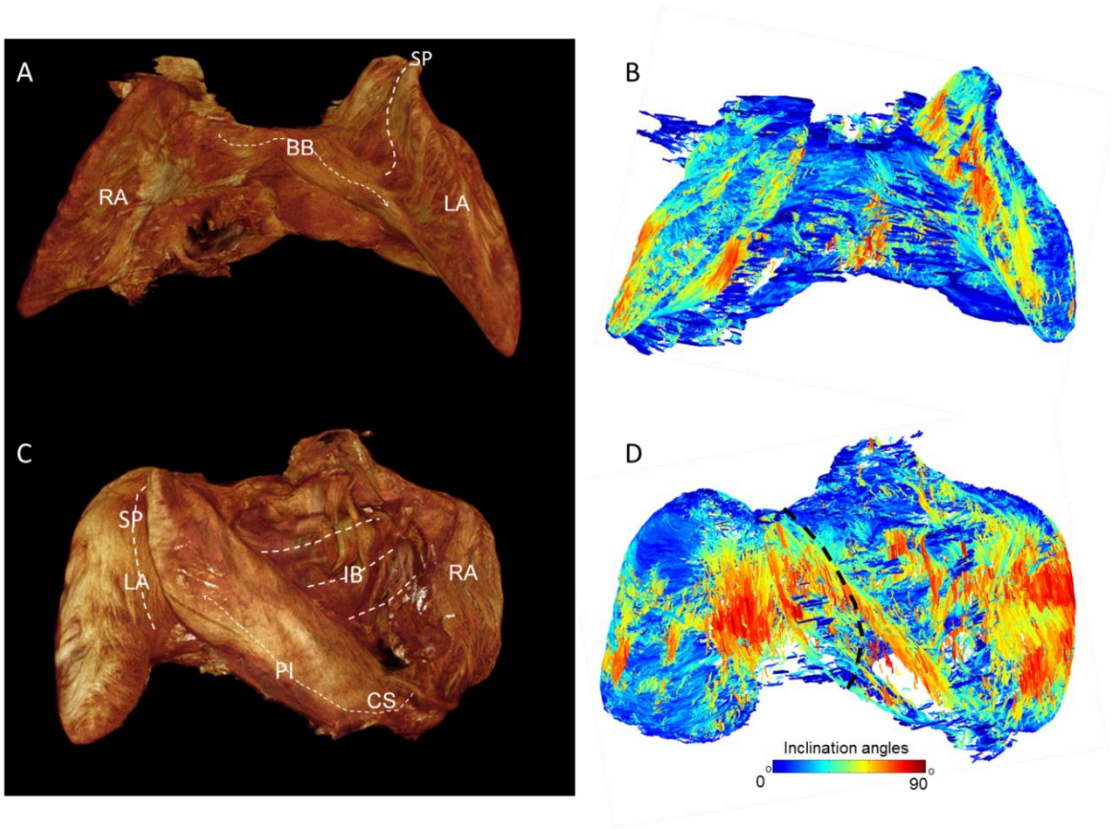

Figure 5.16 Volume renderings of the atrial muscle bands with corresponding fibre orientations extracted from micro-CT data. Volume renderings of the atria; anterior view (A), posterior view (B). fibre orientation maps (B,D) showing the fibre architecture of the atrial muscle bands. Colour bar represents inclination angle. White dotted lines indicate muscle bands, black dotted line indicates interatrial groove (Waterson's groove). BB- Bachmann's bundle, CS- coronary sinus, IB- intercaval bundle, LA- left atrium, PI- posterior interatrial bundle, RA- right atrium, SP- septopulmonary bundle. Isometric resolution of micro-CT data ~20 µm. Fibre orientation extracted in collaboration with Dr Jichao Zhao, The University of Auckland, NZ.

5.8 Fibre orientation in the ventricles and the associated laminar sheets.

The fibre orientation seen in the ventricles is less variable than in the atria, and this is in part due to the laminar sheet architecture seen in the ventricles. The laminae are

formed by blocks of myocytes (4-6 cells thick) arranged end to end on their long axis, although transmurally they show branching and abrupt changes in organisation (figure 5.18). It is thought these structures play functional roles in both contraction and electrical propagation (LeGrice et al., 1995, Smaill et al., 2013, Hooks et al., 2007). Backscattered scanning electron microscopy (BSSEM) with iodine contrast enhancement (7.5% I_2KI) of PMMA embedded ventricular tissue (methods 2.3.1) allowed visualisation of the micro structure of the laminar sheets (figure 5.17). Transverse BSSEM images clearly showed how muscle fibres are arranged within a single sheet (figure 5.17 yellow dotted lines), and allowed appreciation of how the connective tissue (low signal) surrounds individual fibres and forms branches between fibres (yellow arrows figure 5.17). A less dense connective tissue network was seen between laminar sheets. Laminar sheet 3D structure was resolved in rabbit, pig, rat and mouse hearts using micro-CT, figure 5.18 shows the laminar sheet organisation in the adult rabbit LV. The laminae are well defined in the subendocardium, divided by low attenuating cleavage planes, but are not present in much of the epicardium. Laminar sheet organisation within the trabeculae carneae is highly variable, sheets can be seen running within and even forming divisions of trabeculae (figure 5.18G,H), but in some cases laminae are absent entirely (figure 5.18F). Visualisation of serial transverse micro-CT images shows the 3D laminar sheet organisation creates concentric spiralling masses of tissue at the epicardium and endocardium which run in opposite directions. This arrangement is most obvious in the LV and IVS, and seems to anatomically distinguish them from the RV, which appears as an accessory structure wrapping around the LV. Analysis of transverse micro-CT images shows that laminar sheet organisation changes from base to apex; in basal regions laminae predominantly match the curvature of the LV wall (run circumferentially) and there is little evidence of orthotropy (figure 5.18B,F). Midway down the LV, laminae remain ordered in the mid-wall, but at the endocardium and subendocardium laminae run almost perpendicular to the epicardial surface and complex orthotropy and 'zig-zagging' of sheets is visible (figure 5.18C,G). The non-uniform wall thickness of the apical region results in a complex spiralling laminae sheet arrangement, in some regions the laminae run parallel to the wall curvature (figure 5.18C,G), and in other regions perpendicular, with many orthogonal and ‘zig-zagging’ sheets visible. (figure 5.18D,H,E).

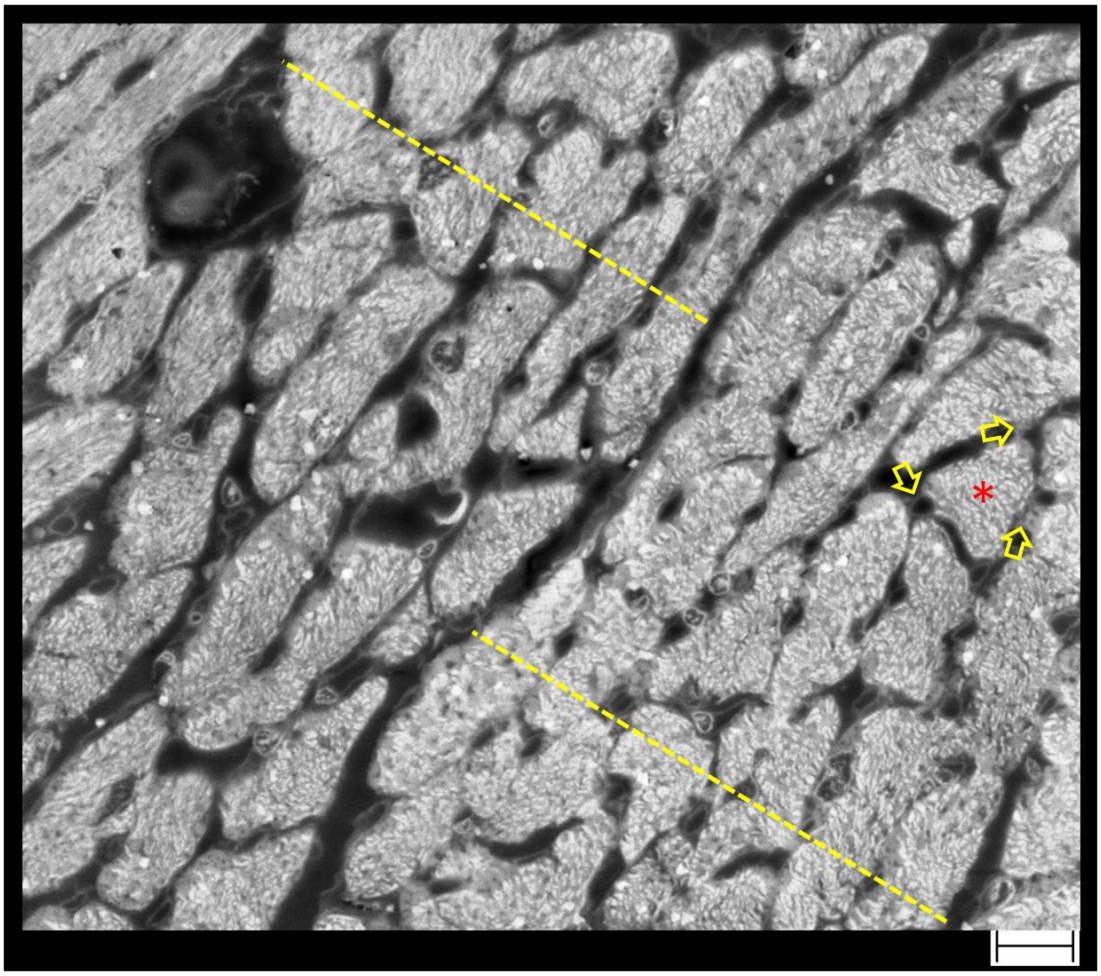

Figure 5.17 Transverse BSSEM image of Laminar sheet organisation in the endocardium of mouse left ventricle. Showing the 4-6 cell stacked arrangement and connective tissue network of the laminar sheets. Tissue block stained with 7.5% I_2KI. Red asterix- myocyte, yellow arrows- connective tissue. Yellow dotted line indicates single laminar sheet. (Scale bar represents 10µm)

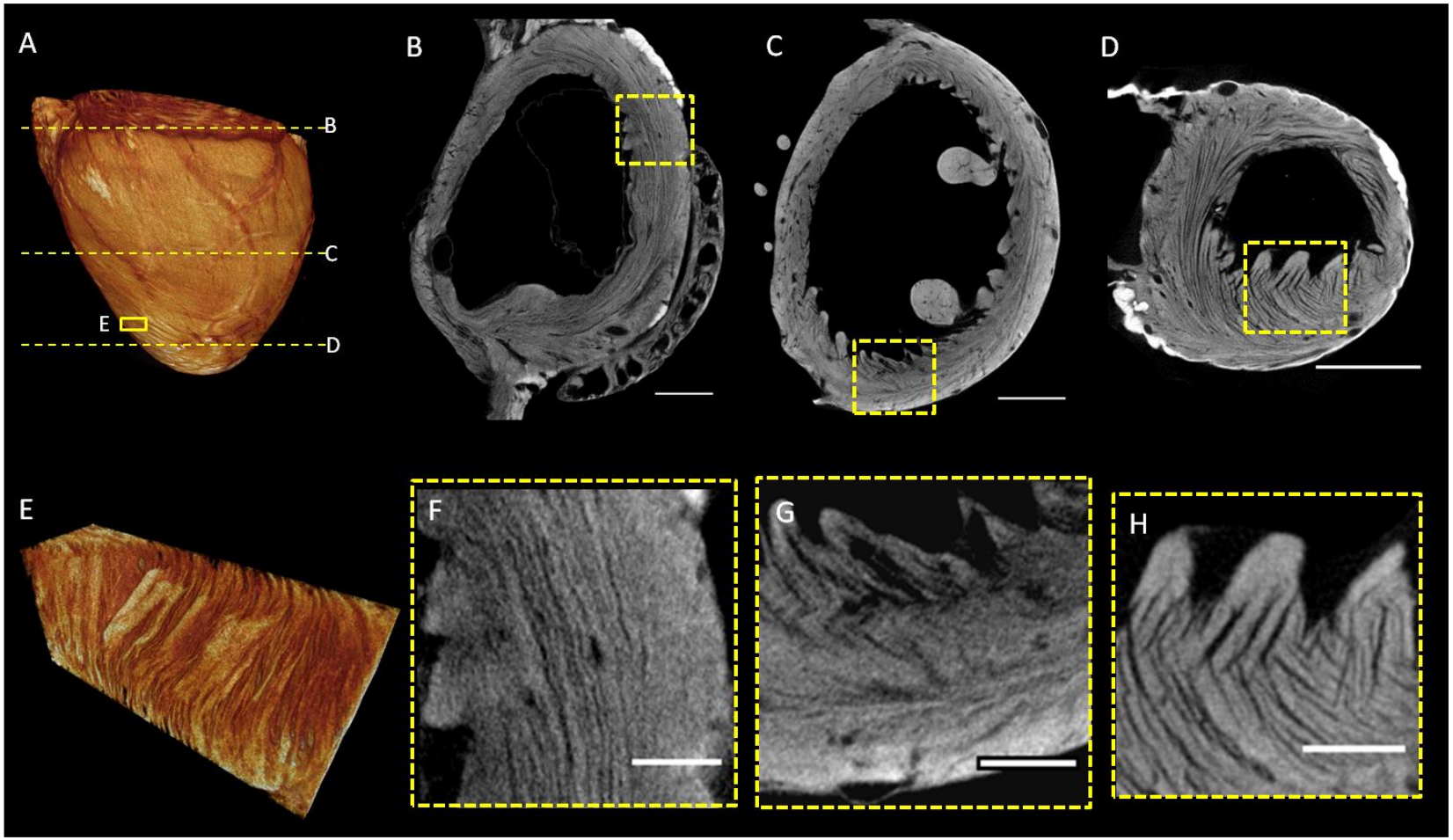

Figure 5.18 Laminar sheet organisation of the left ventricle revealed by micro-CT. Volume rendering of rabbit ventricles (A), showing position of resliced images B,C ,D and volume rendering E. Transverse micro-CT images (B,C,D), with high power images (F,G,H). Volume rendering of endocardial laminae sheet organisation (E). (Scale bar represents 3 mm-B,C,D and 1 mm-F,G,H)

In figure 5.19 fibre orientation has been extracted from a sample (4mm x 3mm x 5mm) of LV posterior wall at the level of the equator. Fibre orientation was then analysed by plotting transmural inclination and transverse fibre angles (figures 5.19A) from a 1 voxel wide track from endocardium to epicardium through the centre of the volume (figure 5.19D,E). The data was then combined and presented as a 3D plot (figure 5.19F). All angle values are referenced to the epicardial surface which was used as the surface tangent plane (yellow box figure 5.19A). Myocytes generally had a helical organization, rotating through ~160° transmurally from endocardium to epicardium (figure 5.19C,D,E,F). There was a proportional relationship between inclination angle and transverse angle transmurally; as fibres became more vertically oriented their transverse angle increased (figure 5.19D,E,F).

Although the traditional helical transmural organization was identified, abrupt changes in fibre orientation were evident. In some regions the epicardium, mid-wall and endocardium appeared as 3 distinct regions (figure 5.19C,D,E), however within these regions small bundles of orthogonal fibres were evident (figure 5.19C,D,E). Suggesting fibres within the ventricular wall form a complex, anisotropic mesh. The blocks of vertical fibres seen at the lateral extremes of the tissue volume (figure 5.19B,C), are due to an artefact generated by sub-pixel cropping. This can be avoided by creating a tissue mask that excludes the extreme boundaries of the cropping plane. The artefact is not generated at the pixel boundaries between tissue and space.

Figure 5.19F shows a 3D plot which incorporates both inclination and transverse fibre angles, giving an accurate quantification and representation of the transmural fibre orientation in 3D. At the epicardial surface there was a small area of vertically orientated fibres running parallel to the long-axis of the heart (figure 5.19F). In the mid-wall fibres had low inclination and transverse angles, this constitutes circumferential running fibres (figure 5.19F). At the endocardium and subendocardium fibres are predominantly vertical with considerable intrusion (transverse angle), these are fibres that run almost perpendicular to the epicardial surface (surface tangent plane). It should be noted that the endocardial surface does present complex fibre orientation in areas of trabeculation; fibres predominantly run in the longitudinal axis of the trabeculae carnae (figure 5.19B,F). More detailed analysis of fibre orientation across the whole of the LV in normal and failing hearts can be found in Chapter 8.5.

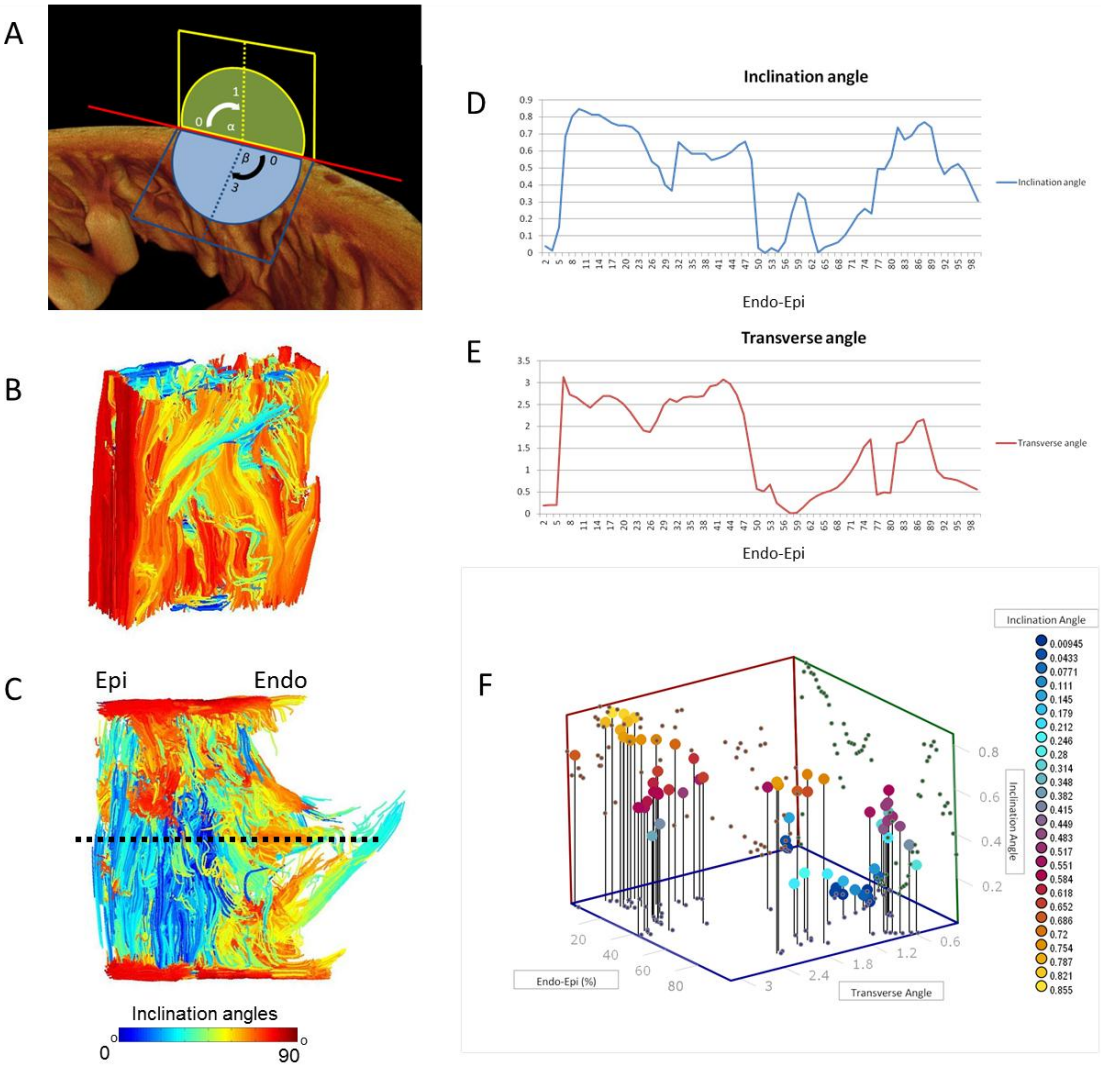

Figure 5.19 3D transmural fibre orientation in the left ventricle extracted from micro-CT data. Possible range of Inclination angle and transverse angle of local myofibre vector- The inclination angle α is the projection of a fibre vector onto a vertical plane parallel to the epicardial boundary (yellow box). This angle is measured with respect to the horizontal (blue box) and has values in the range of 0-1 (0° to 90°). The transverse angle θ is the projection of a fibre vector onto the horizontal plane (blue box), with respect to the surface tangent plane defined above (yellow box) (A). Fibre orientation extracted from micro-CT data of left ventricular segment, showing endocardial surface (B) and transverse surface (C). Plotted transmural inclination angle (D) and transverse angle (E), combined as a 3D plot (F). Isometric resolution of micro-CT data ~40 µm. Colour bars represent inclination angle.

5.9 The important role of fibre orientation in cardiac propagation

Fibre orientation has long been shown to play an important role in the preferential propagation of electrical stimulus through the heart. The extraction of high resolution 3D fibre orientation from micro-CT data can provide powerful functional information when incorporated into mathematical models of cardiac function. Here using structure tensor and fibre tracking analysis (methods 2.4.4 figure 2.1, 2.2), we extracted the 3D fibre orientation from a micro-CT data set of the rabbit atria (resolution ~22 μm). From this data the monodomain version of the reaction-diffusion equation was solved on a voxel-based finite difference grid (as described in Zhao et al., 2013a). Electrical properties were assumed either to be isotropic (fibre orientation not considered) (figure 5.20C) or axially anisotropic (following fibre orientation) (figure 5.20D). For anisotropic modelling conductivity was set at 9.0 mS in the myofibre direction and 0.9 mS transverse to it, therefore preferential to fibre orientation. For isotropic modelling, conductivity was assumed equal in all directions. The seed point of electrical stimulation was from the centre of the sinoatrial node, which in life is the primary pacemaker of the heart. Modelling of propagation was conducted by Dr Jichao Zhao, The University of Auckland. Figure 5.20 shows that incorporating fibre orientation into models of electrical propagation provides improved fidelity of results. When isotropy was assumed (figure 5.20C), conduction across the atria was predominantly uniform in all directions, this was particularly the case for the LA. However the high spatial resolution of the micro-CT data did provide some sources of preferential propagation in the RA, most obviously in the CT.

In contrast, when anisotropy was assumed propagation preferentially ran in the muscle bands of the atria (described above). Conduction was faster across the CT (figure 5.20D- white asterix) and could be seen to follow Bachmann's bundle as a preferential course for interatrial conduction (figure 5.20D- red arrowhead). Once propagation reached the LA via Bachmann's bundle, propagation was fastest down the inferior branch, travelling anteriorly and towards the vestibule. Propagation could also be seen running across the roof of the LA to stimulate the PcMs (figure 5.20- black arrow head). Conduction through the septum spurium was evident (figure 5.20- black asterix), and its origin to many of the anteriorly lying PcMs could be appreciated. Interestingly when anisotropy was assumed conduction towards the

inferior border of the RA was slowed (figure 5.20- open arrow head), and more closely matched the activation time of the corresponding regions in the LA. This suggests the complex network of PcMs and their fibre orientation may play an important role in maintaining synchronous contraction of the atria.

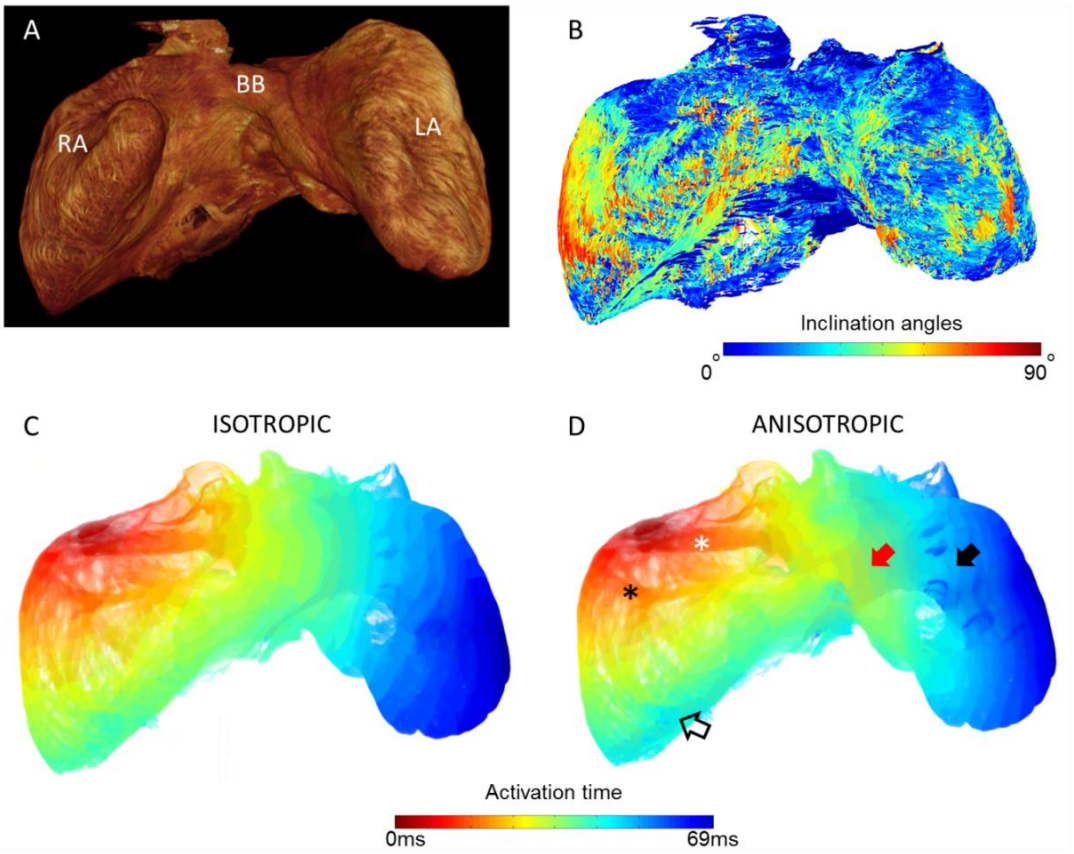

Figure 5.20 The role of fibre orientation on electrical propagation in the atria. Volume rendering of rabbit atria produced from micro-CT data (A), used as geometry for isotropic simulation (C). Fibre orientation plot extracted from micro-CT data (B), and used for anisotropic simulation (D). Isometric resolution of micro-CT data ~22 µm. For simulations the monodomain version of reaction-diffusion equation was solved on a voxel-based finite difference grid (Zhao et al., 2013a). For anisotropic modelling, conductivity was set at 9.0 mS in the myofibre direction and 0.9 mS transverse. For isotropic modelling, conductivity was assumed equal in all directions. The seed point of electrical stimulation was from the centre of the sinoatrial node. Modelling was conducted by Dr Jichao Zhao, The University of Auckland. BB- Bachmann's bundle, LA- left atrium, RA- right atrium. White asterix- cristae terminalis, Black asterix- septum spurium, Open arrowhead- anterior right atrium, Red arrow head- Bachmann's bundle, Black arrowhead- pectinate muscles of left atrium.

5.10 Discussion

The normal structure and function of the heart, common pathological changes that affect function, and the interventions proposed to improve or restore cardiac function, are all fundamentally based on structure. Therefore in all these areas a detailed and accurate understanding of 3D cardiac anatomy is essential. Here the potential of contrast enhanced micro-CT to resolve the detailed anatomy of the heart was assessed. Whole hearts from rabbit, rat, mouse and pig were prepared and stained with an iodine based contrast agent (I_2KI), and scanned using micro-CT. The high spatial resolution provided by micro-CT, and the delineation of various tissue types, allows detailed visualisation of cardiac anatomy. Fat, myocardium, nodal tissue, connective tissue, valves and vasculature can be differentiated from one another and resolved in impressive detail. 3D Fibre orientation throughout the entire heart can be plotted and quantified, allowing comprehensive analysis of the true 3D arrangement of myofibres. This holds great promise for a step change in the ability to model the precise progression of electrical depolarisation within the myocardium, and underpin the mechanics of cardiac contraction.

5.10.1 The advantages of non-invasive 3D imaging

Traditionally, knowledge on the gross anatomy of the heart came from careful dissection (Pettigrew, 1864), with fine anatomical knowledge coming from histological studies (Streeter et al., 1969). Both techniques are still frequently implemented, although here we show that a single micro-CT scan provides sufficient detail for both gross and fine morphological analysis. Dissection, like histology, suffers from been destructive and is intensely time consuming. Due to its destructive nature, advanced anatomical knowledge is required to avoid damage to structures of interest. Gross dissection makes differentiation of different tissue types difficult, especially specialised tissues, this is why dissection and histology are often used in combination for studies of anatomy (Anderson et al., 2011, Sanchez-Quintana et al., 2013). Histology of the heart requires the interpretation of many serial 2D sections through small tissue samples sectioned in a single plane. As a result histological sections are difficult to interpret for non-specialists, and global anatomy cannot be appreciated. Drawbacks of traditional techniques are discussed in detail in chapters 3 and 4. Contrast enhanced micro-CT offers a rapid, non-invasive, high resolution

imaging method, in which the resultant 3D tomographic data is automatically aligned. With the addition of I_2KI, we have shown its capability to allow differentiation of multiple tissue types, including specialised tissues (Jeffery et al., 2011, Stephenson et al., 2012). Due to the development of high performance desktop computing and image analysis software (eg. Amira and ImageJ), visualisation of large 3D image data sets (like micro-CT data) has become feasible in the standard laboratory setting. Discussions of cardiac microanatomy are greatly facilitated by access to 3D views using software in which the virtual structure can be rotated, sliced and manipulated in any orientation instantaneously. Landmarks can be pinpointed within a few microns, and viewed in 2D orthogonal planes and in 3D volumes simultaneously. In addition using volume rendering techniques (VRT), overlapping structures can be viewed by making overlying structures appear semi-transparent. This reveals anatomical detail and relationships which cannot be appreciated using traditional techniques (Jarvis and Stephenson, 2013). Furthermore, when working with datasets that are fundamentally 3D, the information deriving from layers above or below a point of interest often give visual context. This enables the observer to detect structures difficult to recognise in a series of 2D histological slices from small sample preparations, or 2D schematics. We show here how high resolution, non-invasive imaging can allow appreciation of the 'true' anatomy. Simplifications in most medical textbooks give inferior or even misleading representations of anatomical structure (Jarvis and Stephenson, 2013). In the case of the cardiac conduction system, for example, micro-CT reveals that traditional representations, which have gained credence by repetition in successive generations of text books, are inaccurate (Stephenson et al., 2012 and Chapter 6).

Virtual data, such as micro-CT data is easy to disseminate. This is especially useful for investigations of human tissue; sending tissue across the world is confronted with numerous ethical issues, and concerns over safe transit of the sample. In contrast, a high resolution micro-CT scan can be sent to colleagues across the world via the internet within minutes of acquisition.

5.10.2 Do we need 'new' anatomy?

One interpretation is that ‘all is known about gross anatomy’. Such an interpretation is far from true, much is still to be learnt about the anatomy in growth, development and disease of the heart, and its roles in cardiac function are still contested (Anderson et al., 2008, Buckberg et al., 2008, Torrent-Guasp et al., 2005). Today debates still exist over the anatomy of the heart (discussed below), and research continues to reveal ‘new’ anatomical detail (Ambrosi et al., 2012, Stephenson et al., 2012, Smerup et al., 2013a), and clarify areas of ambiguity related to structure, function and nomenclature.

Improving and clarifying existing knowledge

Micro-CT provides data which can clarify areas of anatomical ambiguity, and reveal new anatomical detail. Although the rabbit is used in many investigation of the heart (Dobrzynski et al., 2005, Gilson et al., 1990, Pogwizd, 1995, Gilbert et al., 2012), not a great deal of information exists in the literature on the detailed anatomy of the rabbit heart. This is not the case for other experimental species, with the pig, dog, sheep and human well represented (Hill and Iaizzo, 2009). It is wrong to assume that human anatomy can be simply applied to investigation in rabbit and vice versa (as stated by Nikolaidou et al., 2012).

From our current investigations of rabbit cardiac anatomy we can highlight some major differences from the human heart. The wall of the LA in human is described to be relatively featureless and smooth, with heterogeneous muscle formation (Ho et al., 2002), and PcMs less pronounced than those in the RA (Wang et al., 1995). This is not the case in rabbit, the LAA makes up the majority of the LA and is populated by large broad free running PcMs which have ordered fibre orientation, but complex branching superiorly makes the atrial wall highly trabeculated. In human, the PcMs of the RA have been described as lining the atrial wall, with a comb like arrangement (Ho et al., 2002). In rabbit, micro-CT reveals a forest-like hierarchy of PcMs (4-5 deep in places), many of which are free running with complex integration into the superior aspect of the RA. The origin and branching of the PcMs in the atria seems to require clarification; it has long been stated that the PcMs of the RA take origin from the CT or terminal crest (Anderson and Cook, 2007). However, our data suggests, in most cases, the majority of PcMs originate from septum spurium. Although this

could be attributed to species variation, in descriptions of atrial anatomy in human the role of the septum spurium and the origin it gives to the PcMs is often ignored (Wang et al., 1995). The septum spurium, which is also known as the sagittal bundle or tenia sagittalis by arrhytmologists, is a muscle bundle that originates from the CT, running anterosuperiorly it is often described as the most prominant PcM (Loukas et al., 2008, Ueda et al., 2013). The existence of the septum spurium is appreciated by Loukas et al., 2008 using gross dissection of human hearts, they produced a 6 type classification system based on observed morphological variations of the bundle. Recently Ueda et al., 2013 described the variation in the distal ramifications of the septum spurium, again using gross dissection. However detailed investigations of the 3D morphology, using techniques such as micro-CT, are required to reveal the true extent and possible functional implications of the septum spurium and its distal ramifications.

Wang et al. 1995 also describe how the LA vestibule is not associated with the PcMs in human, this not the case in rabbit, the majority of PcMs branch superiorly from the inferiorly lying vestibule. Furthermore the morphology of the trabeculae carneae in rabbit appeared considerable different to the descriptions derived from dissections of human hearts. Trabeculation in the LV in human has been described as finer, with more criss cossing bundles than the in RV (Anderson et al., 2011). The opposite was observed in rabbit, with very complex and fine trabeculation observed in the RV, in comparison to the more ordered and substantial trabeculation seen in the LV. These findings highlight the difficulty to appreciate the 'true' anatomy using traditional techniques, and shows the advantages 3D imaging of hearts in a naturally inflated state (achieved by perfusion fixation) has on the study of 3D cardiac anatomy (Jarvis and Stephenson, 2013, Stephenson et al., 2012). The data also raises questions over the validity of current views on human cardiac anatomy, and highlights the need for high resolution 3D imaging of human hearts using the present technique.

Conflicting anatomical descriptions

Conflicts exist in relation to anatomical structures and their correct nomenclature. In traditional descriptions of rabbit anatomy there are discrepancies over the PVs, with some studies describing 3 PVs- 1 left and 2 right (Rowlatt, 1990), and others stating only two, a right and a left (McCracken et al., 2008), and in some cases just 1 PV is

described. Our study suggests the morphology of the PVs is variable in rabbit with 2-4 PVs observed across samples. Rowlatt et al. 1990, also states the lack of a moderator band in the rabbit, this is conflicting with data presented here, and highlights the need for an appreciation of variation in certain regions of the heart. An extensive study by Loukas et al. 2010, highlights the variability and on some occasions absence of the moderator band in humans.

Similar conflicts exist in human cardiac anatomy; the atrial appendages are regularly wrongly described as only encompassing the tip of the atrium, when in fact, in both atria, the appendages extend round the atrial wall and are continuous with the venous component. Another example is the idea of what constitutes the IAS, with Ho et al. 1999 and Sweeney and Rosenquist 1979 (Sweeney and Rosenquist, 1979) presenting conflicting anatomical descriptions. Such debates and conflicts highlight the need for attititudinally appropriate nomenclature, as proposed by Anderson et al. 2007. But despite various consensus statements from the Cardiac Nomenclature Study Group (Anderson et al., 2000, Cosio et al., 1999, Racker, 2000), still incorrect and inappropriate terms are adopted in studies of the heart. One example is the LV portioning proposed by Cerqueirs et al. 2002, although recommended by the American Heart Association, it did not comply with anatomical rules, and did not refer to the heart in the correct anatomical position (Partridge and Anderson, 2009). Poor anatomical consensus also has clear implications in 'bench to bedside' success. Therefore the use of the same anatomical language is essential, be it for consensus of nomenclature for surgical intervention, or continuity in the interpretation of image data (Bateman et al., 2013, Partridge and Anderson, 2009). However, it can be argued that specialist nomenclature and complex anatomical terminology can alienate some researchers or non-specialists. We propose micro-CT data can improve the understanding of complex anatomies, and thus aid translational research. We have shown its potential to clarify existing ambiguities, and challenge commonly accepted anatomy. It also reveals new anatomical detail, and potentiates new insight into areas of variability in health and disease. Points discussed above strongly suggest detailed anatomical atlases of human and animal cardiac anatomies should be developed from high resolution isometric 3D image data, to gain consensus on anatomical structures and nomenclature.

5.10.3 Myocardial architecture revealed by micro-CT

Muscular contraction and electrical conduction within the myocardium is strongly dictated by myocardial architecture (Irisawa, 1987, Roberts et al., 1979, Spach et al., 1982). Here using micro-CT imaging we have resolved key myocardial structures in high resolution, presented them in 3D, and extracted their 3D fibre orientation. This data coupled with computer modelling promises to provide new insight into cardiac function.

Fibre orientation in the atria

The methodology used here for fibre orientation extraction has been validated by us (Chapter 4.4) and colleagues (Varela et al., 2013, Zhao et al., 2013a, Zhao et al., 2012). The fibre orientation within the atria is not well understood, but multiple muscle bands within the atria have been described in studies using gross dissection (Ho et al., 2002, Wang et al., 1995). These bands dictate fibre orientation within the atria as fibres run predominantly in the longitudinal axis of these structures, and it is postulated they play important roles in preferential propagation and contraction in the atria (figure 5.20) (Ho et al., 2002, Wang et al., 1995). To our knowledge we are the first to map the global 3D fibre orientation of atria at high resolution from non-invasive image data. Globally fibre orientation in the atria appeared complex with dramatic shifts in fibre orientation transmurally and at structural junctions. Considerable regional heterogeneity was evident within the atria; the CT, PcMs and BB appeared ordered with smooth connections between one another, which our modelling data suggests forms pathways for fast preferential propagation. In contrast some regions had heterogeneous and 'disordered' fibre orientation. For example the intercaval region, which houses the sinoatrial node (the pacemaker of the heart), appeared complex with a high degree of anisotropy, it is postulated this will contribute to the sinoatrial nodes characteristic slow conduction velocity (Dobrzynski et al., 2013). The fibre orientation in this region of normal and failed hearts is investigated in Chapter 7.

The fibre orientation in the RA free wall predominantly consisted of vertical fibres running parallel to the PcMs. In contrast the thick LA free wall showed an abrupt

transmural transition, from predominantly circumferential fibres at the epicardium to vertical fibres at the endocardium, this is consistent with previous dissection studies (Ho et al., 2002, Wang et al., 1995). In the LA a complex intermingling of circumferential and longitudinal fibres in between PcMs was evident, this was in contrast to the predominantly vertical arrangement of fibres between PcMs in the thin RA wall. This suggest the two atria contract quiet differently, it is expected the RA will contract predominantly in the longitudinal axis, with the numerous PcMs pulling the atrial roof down towards the vestibule. The LAs transmurual arrangement and increased heterogeneity of muscle fibres suggests contraction would occur in several planes and appear as a 'scrunching' motion with both circumferential and longitudinal strains. It is expected that the LA contraction would be more effective at pumping large volumes of blood into its underlying ventricle than the RA, thus facilitating a briefly increased cardiac output when required. However, increased muscle fibre complexity and heterogeneity have been shown to increase the risk of electrical dysfunction (Hocini et al., 2002, Narayan et al., 2012, Zhao et al., 2012), and this probably contributes to the increased incidence of arrhythmias in LA compared to RA (Letsas et al., 2011, Hanna et al., 2004, Yamazaki et al., 2012).

The muscle bands and sleeves of the atria

3D fibre orientation was conducted to reveal and clarify the muscle fibres arrangement within the muscle bands of the atria. Our findings are consistent with previous investigations of the bands using dissection (Ho et al., 2002, Ho and Sánchez-Quintana, 2009). However Wang et al. 1995 describe how some less prominent and weakly developed muscle bands cannot be identified with certainty using dissection. This is not the case for micro-CT data; fibre orientation patterns are easily appreciated and thus muscle bundle can be identified regardless of their prominence. Because these structures have previously been investigated using dissection (Ho et al., 2002, Ho and Sánchez-Quintana, 2009, Wang et al., 1995) the 3D relationship of their fibres with the atrial wall and other structures was difficult to interpret. Here using micro-CT we show these junctions are often disordered, with complex networks of overlying fibres branching into the atrial wall. Fibre orientation analysis revealed inferiorly the PcMs of the RA and LA are strongly anchored into

the lateral aspect of their respective vestibules, with many fibres radiating from the majority of the circumference of the PcMs base. At these junctions abrupt changes from vertical to transverse circumferential fibres were seen, and in some areas there was evidence of orthogonally running fibres. Superiorly their relationship with atrial wall is more disordered, with complex networks of overlying fibres branching into the atrial wall. The most complex relationships were observed in the LA. We postulate these junctions and abrupt changes in fibre orientation will contribute to increased vulnerability of the region to electrical dysfunction (Smaill et al., 2013, Zhao et al., 2012). In addition fibres of the PV sleeves were predominantly circumferential, but extremely complex interlacing fibres were observed at their integration with the venous region of the LA. Using computer modelling based on high resolution fibre orientation, Zhao et al. 2012 showed the complex fibre orientations found in the region of the PV sleeves contribute to the regions vulnerability to arrhythmia (Zhao et al., 2012).

The laminar sheets of the ventricles

The existence of laminar sheet structures within the ventricles has been debated for some time (Anderson et al., 2008, LeGrice et al., 1995), however 3D investigations using SEM, histology and MRI has confirmed their existence (Gilbert et al., 2012, LeGrice et al., 1995, Hooks et al., 2007). Using micro-CT and contrast enhanced BSSEM we provide data on the anatomy of the laminar sheets consistent with previous studies, and provide new insight into their regional variability. The laminae were formed by blocks of myocytes (4-6 cells thick) arranged end to end on their long axis, and transmurally they showed branching and abrupt changes in organisation. Within sheets connective tissue was seen surrounding individual fibres, and forming branches between fibres. A less dense network was seen between laminar sheets, it is thought this arrangement aids shearing during contraction (LeGrice et al., 1995). The laminae were well defined in the subendocardium, divided by low attenuating cleavage planes, but were not visible in much of the epicardium.

Micro-CT images showed laminar sheet organisation creates masses of tissue which spiral in opposite directions; the functional role of this morphologly is yet to be

elucidated, it is postulated they play important roles in producing shearing forces and mural thickening (LeGrice et al., 1995, Costa et al., 1999). Here laminar sheet organisation was shown to be regionally variable; in basal regions laminae predominatley matched the curvature of the LV wall and ran circumferentially. Midway down the LV, laminae remain ordered in the mid-wall, but at the endocardium and subendocardium laminae ran almost perpendicular to the epicardial surface and complex orthotropy of sheets was visible. At the apical region the laminae sheets had a complex spiralling arrangement, in some regions the laminae ran circumferential, and in other regions ran perpendicular to the epicardium with many orthogonal and 'zig-zagging' sheets. It is anticipated that these regional differences will have impact on mechanical and electrical function of the LV. In terms of conduction, it has been postulated that they function to increase the safety factor of the myocardium by constraining passive current load locally (Smaill et al., 2013). This suggests the apex is less 'safe' than the base. With many 'zig-zagging' laminae and sheets intersecting and running orthogonal to one another, many abrupt changes in fibre orientation will exist. As a result in the apical region, laminae will be less proficient at constraining current locally and will be more prone to source-sink mismatch, re-entry circuits and conduction block (Hocini et al., 2002, Klos et al., 2008, Smaill et al., 2013).

The 3D fibre orientation of the ventricles

Here we have shown a method for extracting 3D fibre orientation from micro-CT image data of the heart. 2D fibre orientation in the ventricles has previously been investigated using standard histology (Streeter et al., 1969), and more recently using micro-CT (Jorgensen et al., 1998a). Over recent years diffusion tensor MRI (DT-MRI) has become the gold standard for analysis of 3D fibre orientation in the ventricles (Rohmer et al., 2007, Smerup et al., 2009). The method presented here uses structure tensor analysis to extract 3D fibre orientation from Micro-CT data (methods 2.4.4), advantages of the current method over traditional techniques, including DT-MRI, are discussed in Chapter 3 and 4.

Our analysis showed myocytes generally had a helical organization; rotating through ~160° transmurally from endocardium to epicardium, consistent with traditional

descriptions (Streeter et al., 1969). Our analysis extracts both the inclination angle, often referred to as the helical angle, and the transverse angle also called the intrusion angle. Comparing the two angles revealed a proportional relationship transmurally; as fibres became more vertically oriented, generally their transverse angle increased. 3D plots which incorporate both inclination and transverse fibre angles, give a more accurate quantification and representation of fibre orientation. As pointed out by Anderson et al. 2008 many studies of contractile function (eg. Sallin 1969) erroneously ignore the transvere angle of fibres. This is severely reduces the fidelity of computer models as it has been postulated these transverse angled fibres play important roles in; equalisation of wall strains, shape maintenance, cardiac contraction and dilation, and possibly antagonistic forces towards contriction (Anderson et al., 2006, Lunkenheimer et al., 2004, Smerup et al., 2013b). As described previously (Cryer et al., 1997, Lunkenheimer et al., 1997a), we found the highest transverse angles exist at the endocardium and sub-endocardium.

3D plots revealed that although the traditional helical transmural organization was identified, abrupt changes in fibre orientation exist, and fibres within the ventricular wall form a complex, anisotropic mesh. This is consistent with previous anatomical descriptions derived from histological study (Anderson et al., 2005, Lunkenheimer et al., 2006a). However this highlights the need to sample larger regions rather than a single 2D line (as done here) when comparing hearts. As the inherent anisotropy of the myocardium could give erroneous results if the sampled region is not representative. This is taken into consideration when the 3D fibre angles of normal and failed hearts are compared in Chapter 8.5.

Improving the morphological fidelity of functional mathematical models of the heart

At a cellular level there has been considerable focus on both transmembrane ion channels and their role in cellular excitability (Nattel et al., 2007), and the role of gap junctions in electrical transmission between cardiomyocytes (Severs et al., 2008). Wang 1995 highlighted the lack of attention paid to atrial musculature by cardiac morphologists since the studies of Keith and Flack 1907 and Papez 1920. But recently there has been an effort to gain high resolution 3D data of the heart using MRI (Helm et al., 2005b, Gilbert et al., 2012) and micro-CT (Aslanidi et al., 2012,

Stephenson et al., 2012-Papers appended). Computer models allow incorporation of experimental data from cellular investigations to be combined with 3D anatomy, offering a means of simulating cardiac function (Trayanova, 2011). However, typically electrical properties are assumed continuous (isotropic), morphology assumed homogenous, and the influences of fibre orientation and fibrosis are often ignored (Harrild and Henriquez, 2000). This makes many existing models of cardiac function inaccurate as myocardial morphology, fibre orientation and fibrosis have all been shown to be involved in cardiac function and dysfunction (Zhao et al., 2013b, Zhao et al., 2012, Rohr, 2012, Smaill et al., 2013, Spach and Kootsey, 1983).

Recently detailed 3D fibre orientation and myocardial geometry obtained from a surface imaging technique have been incorporated into functional models (Zhao et al., 2012), and we have been involved in extracting 3D fibre orientation from high resolution micro-CT data (Aslanidi et al., 2012). Using micro-CT to extract this level of anatomical detail (morphology and fibre orientation), as we have here, in a time effective manner is a considerable step forward. Modelling studies normally concentrate on a single data set, however the method presented here makes the modelling of multiple samples feasible. This has obvious implications in the modelling of heart function and dysfunction in disease. The important role of both high resolution geometry and fibre orientation on electrical propagation is highlighted in figure 5.20. The incorporation of both high resolution geometry and fibre orientation gives a much more accurate representation of conduction in the heart than when morphology is assumed homogenous and conduction isotropic. The data highlights the potential use of micro-CT to provide high resolution myocardial geometry and 3D fibre orientation, missing from many current models (Harrild and Henriquez, 2000, Trayanova, 2011), which will hugely improve the fidelity of future models.

Although fibrosis is not investigated in the current study, its influence of cardiac function and dysfunction is well described (Rohr, 2012, Schotten et al., 2011, Smaill et al., 2013), and its 3D distribution should be considered in cardiac models. The effects of fibrosis have been modelled from low resolution image data and using seeding methods (Zhao et al., 2013b- paper appended). However, accurate high resolution images of the 3D distribution are desirable to improve model fidelity. We have developed a technique for targeted contrast enhancement (TCE micro-CT)

(methods 2.3.3), which we have used to selectively image regions of the cardiac conduction system (see Chapter 6). It is anticipated that this technique could be adapted to obtain high resolution 3D images of fibrotic tissue in the heart.

5.11 Summary

The potential of contrast enhanced micro-CT to resolve the detailed anatomy of the heart was assessed. Whole hearts from rabbit and pig were prepared and stained with an iodine based contrast agent (I_2KI), and scanned using micro-CT. Diffusion of iodine into cardiac tissue enhances the differential attenuation of X-rays, allowing visualisation of fine detail.

The high spatial resolution provided by micro-CT, and the delineation of various tissue types allowed detailed visualisation of cardiac anatomy. Data provided gives novel insight into the 3D morphology of the heart, and both clarifies and challenges existing anatomical ideologies. We show fibre orientation throughout the entire heart can be plotted and quantified from micro-CT data, allowing comprehensive analysis of the true 3D arrangement of myofibres. We also show the promise of this data to provide a stepwise change in the ability to model the precise progression of electrical depolarisation within the myocardium.

Data presented confirms the capacity of micro-CT to reveal a detail of cardiac anatomy unrivalled by traditional methods, and to provide new insights into cardiac morphology. Such data can: 1) aid anatomical understanding, teaching and surgical guidance and planning; 2) Improve fidelity of morphological and developmental studies; 3) aid the characterisation of fibre orientation in specific disease states; 4) and inform the development of ‘virtual hearts’- anatomically and biophysically-detailed mathematical models, which map the wave of depolarisation and or contraction across the heart.

CHAPTER 6

Contrast Enhanced Micro-Computed Tomography Resolves the 3-Dimensional Morphology of the Cardiac Conduction System

6.1 Introduction

The cardiac conduction system (CCS) is a collection of specialised cells within the heart, responsible for the initiation and coordination of the heart beat: the CCS initiates the cardiac action potential and conducts it throughout the heart. Although the general anatomy of the CCS has been known for over 100 years, its complex and irregular 3D geometry is not so well understood. This is largely because the conducting tissue is not distinct from the surrounding tissue by dissection. The best descriptions of its anatomy come from studies based on serial sectioning of samples taken from the appropriate areas of the heart; the CCS can be distinguished histologically using both morphological stains and immunohistochemistry. Low X-ray attenuation has formerly ruled out micro-CT as a modality to resolve internal structures of soft tissue, but incorporation of iodine, which has a high molecular weight, into those tissues enhances the differential attenuation of X-rays and allows visualisation of fine detail in soft tissue. Recently, high resolution micro-computed tomography (micro-CT) imaging using iodine as a contrast agent has been introduced for *in vivo* and *ex vivo* anatomical studies. Here, with the use of an iodine based contrast agent (I_2KI), we show that contrast enhanced micro-CT can reveal the detailed 3D morphology of the CCS in rat and rabbit. We attempt to resolve the three major subdivisions of the CCS from the surrounding contractile myocardium, including; the sinoatrial node (SAN); the atrioventricular conduction axis (AVCA): the inferior nodal extension, penetrating bundle and non branching and branching bundle; and the bundle branches and Purkinje network. We also investigate the morphology of preferential conducting pathways in the right atrium, whose existence and significance have been the subject of considerable controversy. Micro-CT findings are validated using traditional histology, whole mount immunohistochemistry and targeted contrast enhancement (TCE).

Most of the work in this chapter has been published as:

Stephenson RS, Boyett MR, Hart G, Nikolaidou T, Cai X, Corno AF, Alphonso N, Jeffery N, Jarvis JC. Contrast enhanced micro-computed tomography resolves the 3-dimensional morphology of the cardiac conduction system in mammalian hearts. *PLoS One*. 2012; 7: e35299. The paper is appended.

New insights include; the development and use of a targeted contrast enhancement technique to investigate the distribution of specialised cells involved in electrical propagation non-invasively in 3D. Structures analysed include; the Purkinje network and internodal pathways. The relationship between the structure of morphologically identified pathways for conduction and fibre orientation is also investigated within the RA.

6.2 Optimization for micro-CT imaging of the CCS

The technique for contrast enhanced micro-CT imaging of the heart was refined using the rat heart. Longitudinal micro-CT Images from rat hearts stained for 48 hours with a range of I_2KI concentrations are shown in figure 6.1. For all concentrations tested, there was differential X-ray attenuation between the contractile myocardium (high attenuation) and the CCS tissue (low attenuation). We were able to identify the AVCA including the penetrating bundle, non-branching and branching bundle, the bundle branches themselves, and the Purkinje network. The lowest I_2KI concentration that allowed for high quality contrast enhancement was 3.75% (figure 6.1C,G). It was possible to identify the CCS in a heart stained with 1.87% I_2KI, but the ventricular endocardium was not stained homogeneously (figure 6.1D,H). Data could then be segmented using semi-automatic segmentation techniques I and II and presented as 3D isosurfaces (methods 2.4.2), or analysed using volume rendering techniques (VRT) (methods 2.4.2)

Figure 6.1 Longitudinal micro-CT images through 4 rat hearts stained with different concentrations of I_2KI for 2 days. Hearts stained with 15, 7.5, 3.75 and 1.87% I_2KI concentrations respectively (A-D). Corresponding high power images focusing on the atrioventricular conduction axis (E-H). Inset 3D renderings of each heart show the associated planes of interest. AO- aorta, IVS- inter-ventricular septum, BrB- branching bundle, LV- left ventricle, RV- right ventricle. (scale bar represents 1 mm)

6.2 Visualisation and validation of CCS in rat

To confirm the identity of the specialised structures, we attempted to make sections from frozen and paraffin-embedded blocks of the I_2KI stained tissue, but found that if I_2KI was not removed after micro-CT scanning, the tissue was brittle and it was not possible to obtain satisfactory tissue sections. Therefore, the I_2KI was leached from the hearts by immersion in PBFS for 2-5 weeks with weekly changes of PBFS. The time taken for complete leaching of I_2KI was dependent on I_2KI concentration, incubation time and specimen size. Leaching times ranged from two weeks for the lower concentrations to five weeks for the higher concentrations. Leaching was noted to be much quicker from dissected heart tissue, in which cut myocardial surfaces were exposed to the leaching solution. Figure 6.2A,B shows two micro-CT images virtually sectioned from the micro-CT data to match figure 6.2D,E showing sections from wax-embedded blocks, stained with Masson's trichrome- there is excellent correspondence, and the images demonstrate that the penetrating bundle, branching bundle and the bundle branches are distinguishable from the surrounding structures in the micro-CT images. Differential attenuation is also observed between the surrounding connective tissue and contractile myocardium. By thresholding the differential attenuation between contractile myocardium and the CCS tissue, it was possible to 'segment' the CCS tissue, isolating it from the surrounding tissues, and generate a 3D representation of the CCS tissue. 3D images of the AVCA in a normal rat heart are shown in anterior and lateral orientations in figure 6.2C,F. In figure 6.2F, the penetrating bundle is identified (separate from the surrounding central fibrous body), it connects to the inferior nodal extension posteriorly (not shown), and to the non-branching bundle anteriorly . The evident arching of the AVCA at its inferior border and the course of the bundle branches represents its close relationship with the IVS (figure 6.2).

Preparation of the rat hearts (immersion fixation) was such that collapsing of the atrial walls and blood residing in the chambers was unavoidable (figure 6.1), making identification of the SAN and Purkinje network difficult. The remainder of the results presented here are from rabbit hearts prepared with an improved method (perfusion fixation) detailed in the methods section (methods 2.2.4).

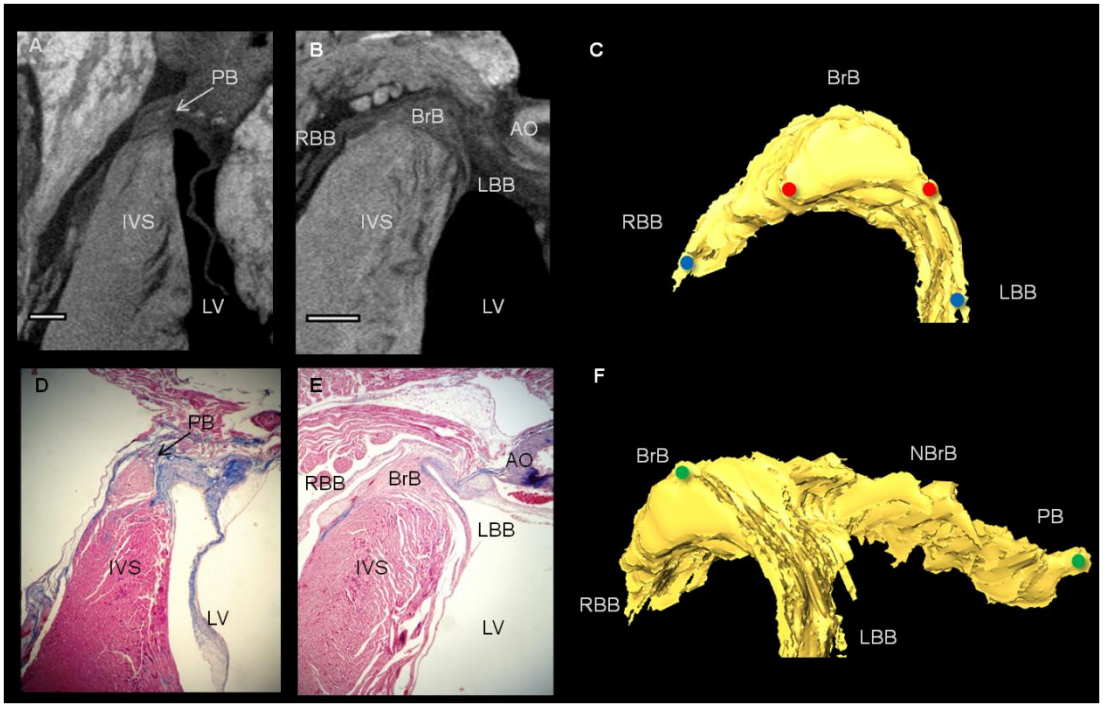

Figure 6.2. Longitudinal micro-CT images of atrioventricular conduction axis in rat with corresponiding histology and 3D isosurfaces. Micro-CT images of the penetrating bundle and branching bundle in rat hearts stained with 7.5% (A) and 3.75% (B) I_2KI for 2 days. Corresponding histological sections stained with Masson Trichrome (D,E). Segmented 3D isosurfaces of atrioventricular conduction axis (C,F), showing the anteriorly positioned branching bundle (C) and its lateral aspect showing the penetrating bundle, and non-branching and branching bundles (F). Distance between red dots- 0.6 mm, blue dots- 1.3 mm, green dots- 2.4 mm. AO- aorta, BrB- branching bundle, IVS- interventricular septum, LBB- left bundle branch, LV- Left ventricle, NBrB- non-branching bundle, PB-penetrating bundle, RBB-right bundle branch. (Scale bar represents 0.5 mm)

6.3 Sinoatrial node of the rabbit heart

Analysis of the SAN confirms that it is not so much a localised compact node but an extended thin layer of conducting cells (figure 6.3, figure 6.4B,D). In the micro-CT images, the SAN was easily differentiated from the surrounding atrial myocardium as shown in figure. 6.3A. It was a region of low attenuation (appears darker, figure 6.3A,B, figure 6.4B,D) in the intercaval region (between the superior and inferior venae cavae) in the posterior wall of the right atrium. It extends along the lateral aspect of the crista terminalis, which demarcates the boundary between the smooth

intercaval region and the pectinate muscles of the right atrial appendage (figure 6.3B, figure 6.4B,D). At the boundary of the intercaval region and crista terminalis, there was evidence of interdigitation of the SAN into the atrial muscle- the SAN tissue forks around the endocardial and epicardial surfaces of the crista terminalis (figure 6.3A). All of these features of the rabbit SAN are consistent with those identified by immunolabelling of marker proteins in physical sections (figure 6.4 and Dobrzynki et al. 2005). Figure 6.3B and figure 6.4D shows the extent of the rendered SAN as viewed from the endocardial surface of the right atrium. Figure 6.3C shows the rendered SAN running alongside the sinus node artery. The volume of the rendered SAN was 1.01 mm^3 in the rabbit heart shown. The attenuation data also contains evidence of a progressive increase in attenuation from the centre of the SAN towards its periphery, and continuing to increase towards the surrounding atrial myocardium. This suggests the change in morphology related to the paranodal or transitional region is distinguishable using micro-CT (see discussion).

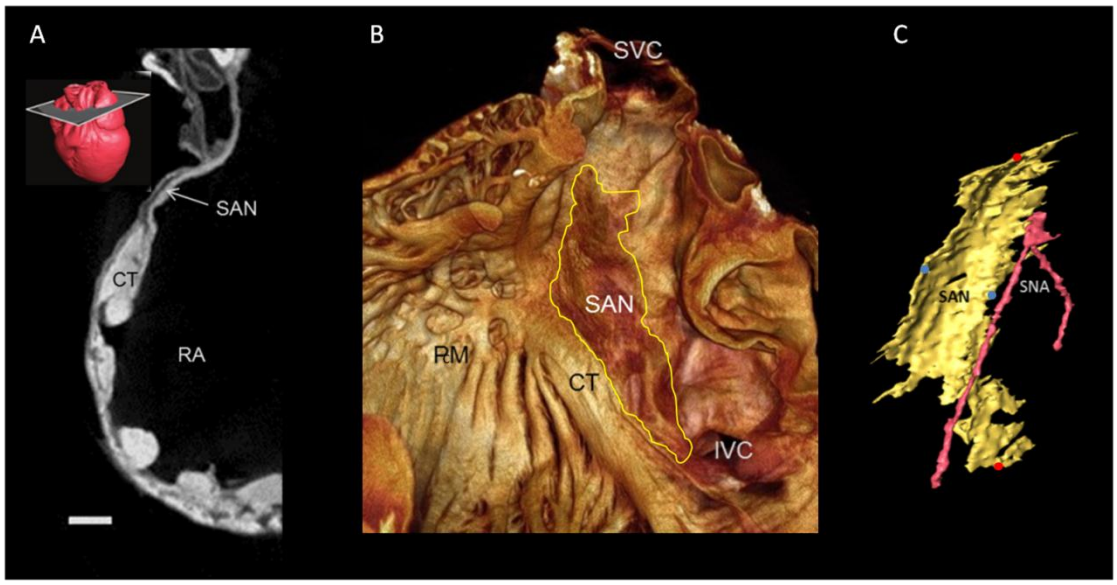

Figure 6.3 Transverse micro-CT image of posterior right atrium with corresponding volume rendering and segmentation of sinoatrial node. micro-CT image showing the sinoatrial node in a rabbit heart stained with 7.5% I_2KI for 3 days, with 3D rendering of the whole heart showing the associated plane of interest (A). Corresponding volume rendering (B) and Segmented 3D isosurface of sinoatrial node (C). Distance between red dots- 4.9 mm, blue dots- 2.5 mm. CT- crista terminalis, IVC- inferior vena cava, PM- pectinate muscle, RA- right atrium, SAN- sinoatrial node, SNA- sinus node artery, SVC- superior vena cava. (Scale bar represents 1 mm)

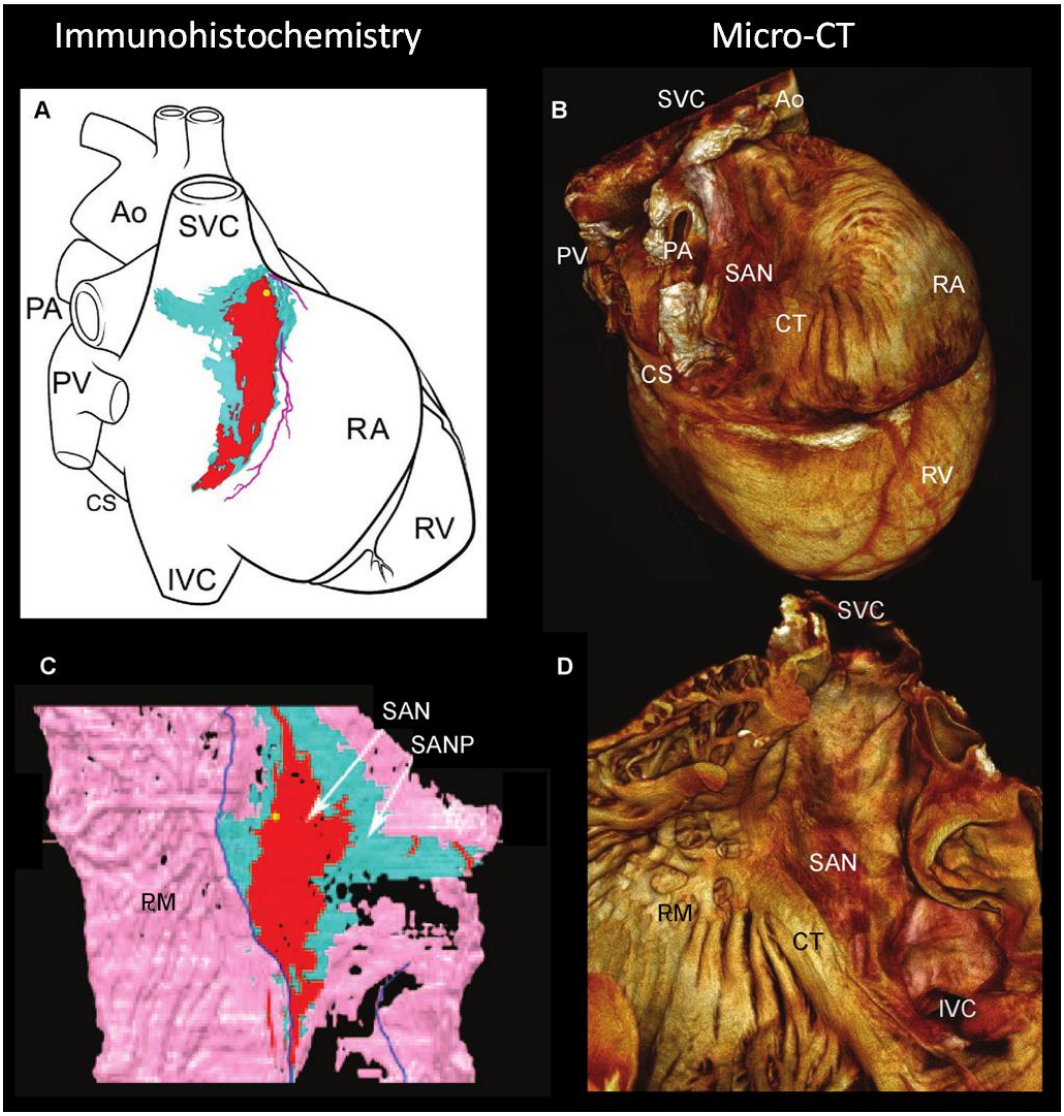

Figure 6.4 Comparison of existing and current 3D representations of the sinoatrial node. Existing model of the SAN in rabbit (modified from Dobrzynski et al. 2005) constructed from immunohistochemically stained sections (A,C), superimposed onto a schematic representation of the heart showing the SAN epicardial position (A), and its relationship with the myocardium on the endocardial surface (C). Volume rendering of the current model in rabbit of the SAN, showing its true position on the epicardial (B) and endocardial (D) surfaces. Ao- Aorta, CS- coronary sinus, CT- crista terminalis, IVC- inferior vena cava, PA- pulmonary artery, PM- pectinate muscle, PV- pulmonary veins, RA- right atrium, SAN- sinoatrial node, SANP- sinoatrial node periphery, SVC- superior vena cava.

6.4 Internodal pathways of the rabbit right atrium

Here the anatomy and possible function of the sinoatrial ring bundles in the rabbit right atrium is assessed. The right and left sinoatrial ring bundles (RSARB, LSARB) were identified and analysed using whole mount immunohistochemistry, contrast enhanced micro-CT, and targeted contrast enhanced (TCE) micro-CT. The ring bundles appeared as fine protrusions/tracts of neuro-filament positive tissue running along the lateral and medial borders of the SAN on the endocardial surface (figure 6.5B,C). The following findings are validated by whole mount immunohistochemistry and TCE micro-CT for specific expression of neurofilament middle (NF-M).

Inferiorly the RSARB and LSARB run towards the floor of the atrium and become continuous with the INE (figure 6.5B,C). Here, the right and left SARBs run inferior and superior to the opening of the CS respectively, both bundles can be seen to fan out into a network of numerous NF-M+ fibres prior to entering the INE. As they enter the INE the larger fan of the RSARB overlaps with the smaller LSARB fan forming a complex mesh of NF-M+ fibres. Superiorly the LSARB runs across the superior aspect of the IAS in a posterior-anterior fashion, with free running aspects evident. On reaching the anterior of the IAS, the LSARB runs inferiorly towards the atrial floor, anterior to the fossa ovale, and runs into the anterior aspect of the INE, in the region of the CN (figure 6.5B). Superiorly the RSARB arcs towards the RA free wall, forming branches which run on the endocardial surface of PcMs, and between PcMs as free running fibres (figure 6.6). Figure 6.6C,D shows images from TCE micro-CT scans, and clearly shows the SARBs are free running, NF-M positive (bright signal), but also insulated with a NF-M negative connective tissue sheath. The path and position of the SARBs corresponds with schematics of the fast and slow pathways (see introduction) produced from electrophysiological and channel protein data (figure 6.5A)(Mazgalev et al., 2001). The slow and fast pathways can be identified structurally in the micro-CT data, which for the most part appear as low attenuating regions (figure 6.5C). Figure 6.5D shows the corresponding fibre orientation plot for figure 6.5C. In this case, the fast and slow pathways can be distinguished by their fibre orientation, which matches the path of propagation postulated from electrophysiological studies.

Whole mount immunohistochemistry for NF-M confirmed other areas specialized for electrical propagation within the right atrium, including; the SAN, INE and BB (figure 6.5B). Superiorly the SAN can be seen to give off a network of NF-M+ fibres which run medially into BB (figure 6.5B), eventually becoming continuous with the LSARB at the superior aspect of the IAS. Directly inferior to this network is a region more or less void of NF-M+ fibres, this region may correspond to the block zone. This region has been previously described in functional studies of activation spread from the SAN (reviewed in Boyett et al., 2000). The SAN also gives of branches of NF-M+ fibres to the RSARB. Fibres in the SAN periphery run in parallel with the RSARB as it runs down the SAN lateral border, with some fibres appearing to enter the ring bundle in this region. As the SAN narrows inferiorly some of its fibres appear coalesce with the RSARB, possibly contributing to the network of multiple fibres seen when the RSARB fans out prior to entering the INE.

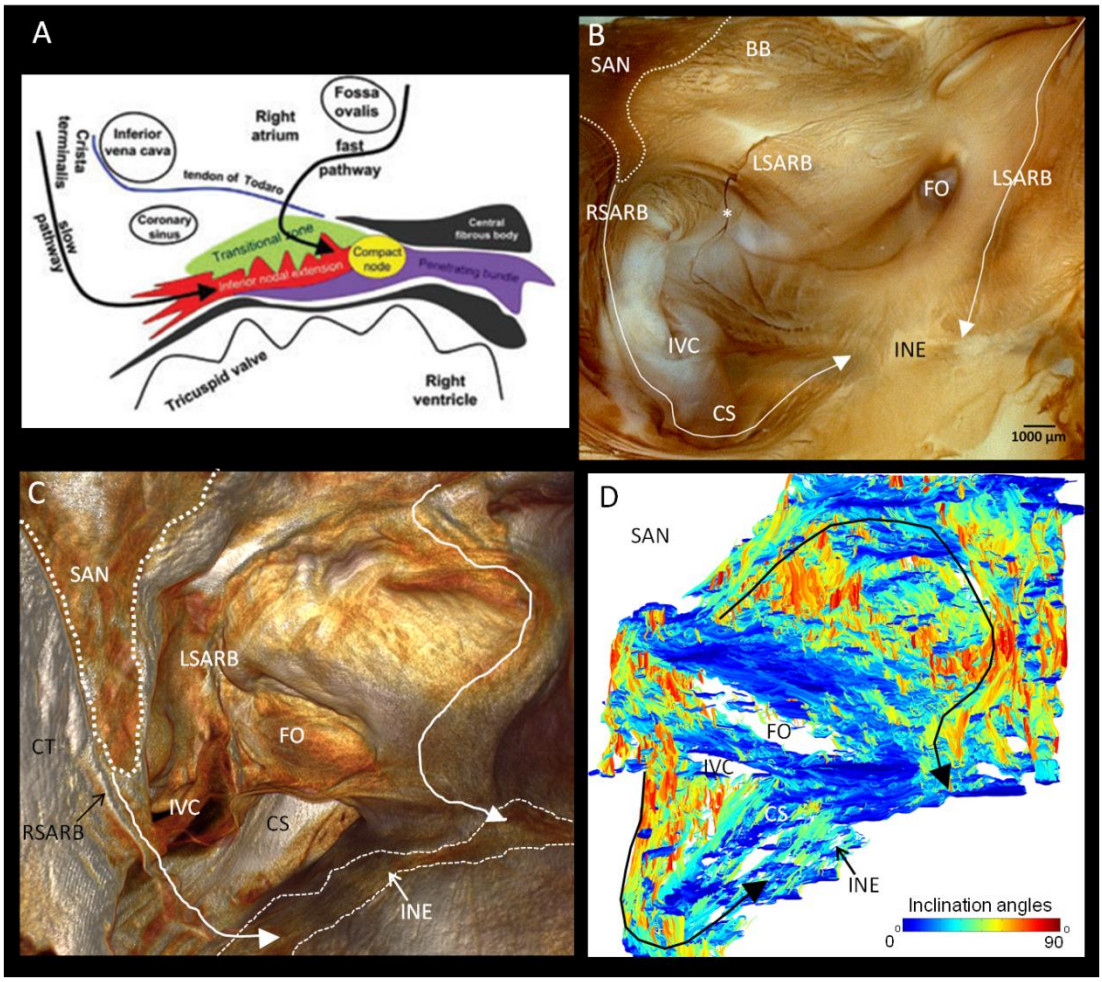

Figure 6.5 Anatomy of the internodal pathways in the rabbit right atrium investigated by immunohistochemistry, micro-CT and fibre orientation analysis. Schematic produced from electrophysiological and channel protein data (modified from Mazgalev et al., 2001), showing location of the fast and slow conduction pathways and their association with AV conduction axis (A). Whole mount immunohistochemistry for NF-M (brown indicates NF-M+ tissue) (B), and volume rendering (C) of regions corresponding to A, white arrows depict slow and fast pathways. Fibre orientation extracted from micro-CT data used in C (minus SAN) showing the fibre orientation of the conduction pathways (black arrows). Colour bar represents inclination angle. *- represents free running aspect. CS-coronary sinus, CT- crista terminalis, FO- fossa ovale, INE- inferior nodal extension, IVC- inferior vena cava, LSARB- left sinoatrial ring bundle, RSARB- right sinoatrial ring bundle, SAN- sinoatrial node. Fibre orientation analysis conducted together with Dr Jichao Zhao, whole mount Immunohistochemistry conducted together with Dr Halina Dobrzynski. (Scale bar represents 1 mm)

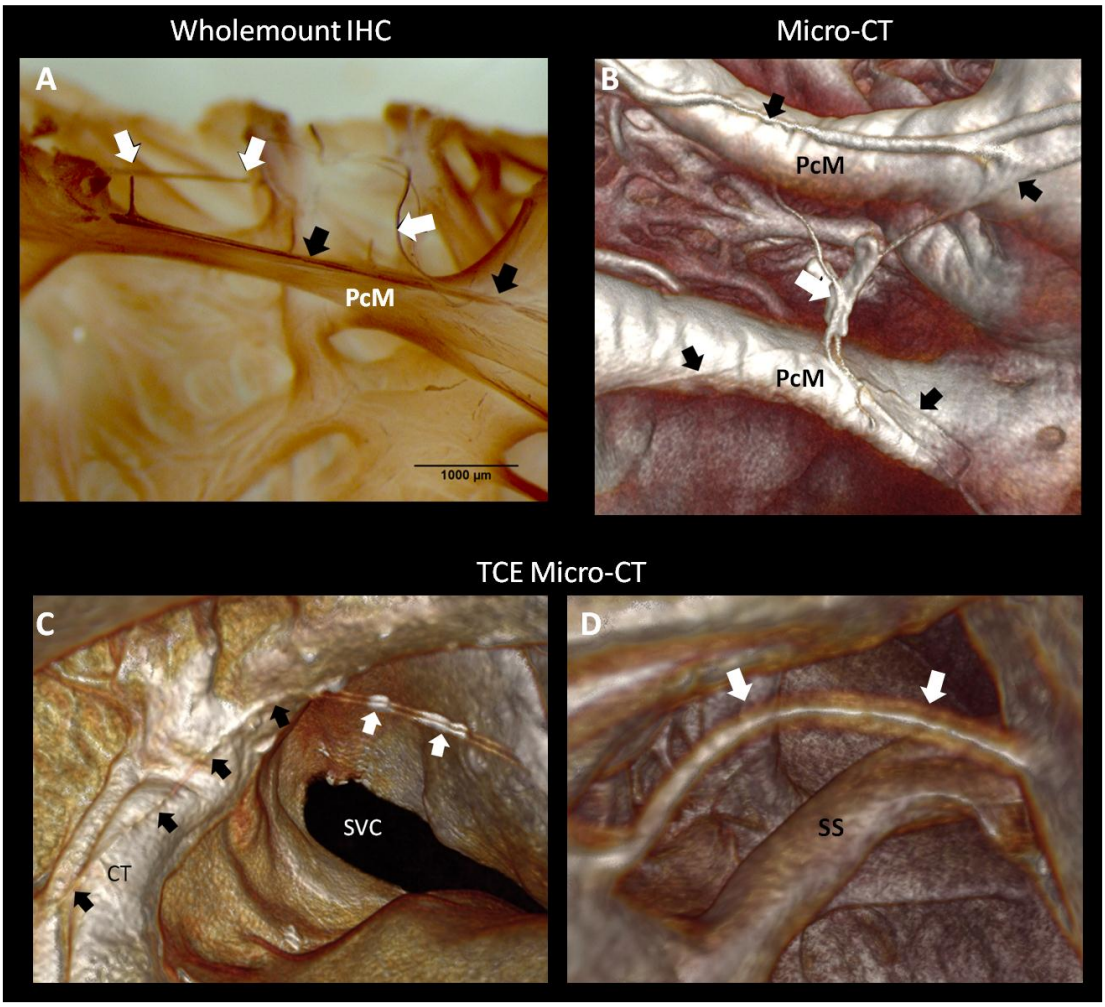

Figure 6.6 The anatomy of the right sinoatrial ring bundle in rabbit investigated by immunohistochemistry, micro-CT and TCE micro-CT. Whole mount immunohistochemistry for NF-M (A), Volume rendering (B) and targeted contrast enhanced micro-CT for NF-M (C,D), showing the 3D morphology of the right sinoatrial ring bundles (surface running bundles- black arrows, free running bundles- white arrows) in the roof of the right atrium (A,B), intercaval region (C) and the anterior portion of the right atrial appendage (D). CT- crista terminalis, PcM- pectinate muscle, SS- septum spurium, SVC- superior vena cava. Whole mount immunohistochemistry conducted together with Dr Halina Dobrzynski. (Scale bar represents 1 mm)

6.4 The Atrioventricular conduction axis of the rabbit heart

From the micro-CT data it was possible to identify the inferior nodal extension, penetrating bundle, non-branching and branching bundles, and the bundle branches. Furthermore these tissues could be differentiated from the associated contractile myocardium and connective tissue (which have higher and lower attenuation coefficients respectively) (figure 6.7A,B,D,E, figure 6.8). When viewed in longitudinal sections of the IVS, the posteriorly lying inferior nodal extension appeared as a thin smear of cells lying on the right lateral aspect of the IVS within the RA cavity (figure 6.8C,F). The penetrating bundle was identified as a oval mass of nodal cells surrounded by a layer of low attenuating connective tissue (figure 6.7A,D, figure 6.8B,E); this indicates the path of the AVCA through the central fibrous body. Anteriorly the branching bundle appeared as a triangle shaped structure, with its base arching over the underlying IVS (figure 6.7B,E, figure 6.8A,D). The 3D representation of the AVCA in the rabbit (figure 6.7C,F, figure 6.8G,H) shows it to be similar to that in the rat (figure 6.2C,F). The arching of the structure represents its position on the IVS (figure 6.7C,F, figure 6.11,6.12). The 3D relationship of the AVCA with surrounding structures can be appreciated in the volume rendering shown in figure 6.8G,H. As the bundle branches are traced along the IVS it is evident that at their origin they appear as ribbon like structures (figure 6.7F), which become thinner and more 'cord-like' as they give branches to the purkinje network (figures 6.11,6.12). When viewed in a transverse section, the AVCA can be seen to take origin in the expected location between the coronary sinus and the membranous septum at the base of the triangle of Koch and can be followed around the circumference of the aortic valve annulus (figure 6.8).

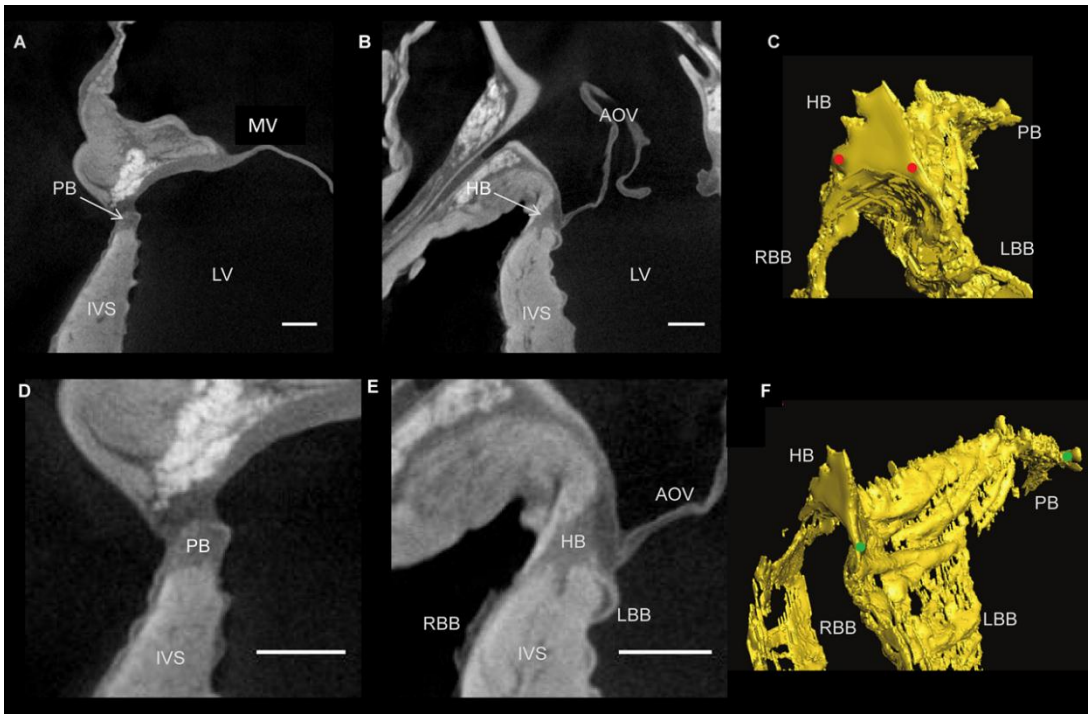

Figure 6.7 Longitudinal micro-CT images of atrioventricular conduction axis in rabbit with corresponding 3D isosurfaces. Showing the penetrating bundle (A,D) and branching bundle (B,E) in a rabbit heart stained with 7.5% I_2KI for 3 days. Segmented 3D isosurfaces of atrioventricular conduction axis, showing the anteriorly positioned branching bundle (C) and its lateral aspect showing the penetrating bundle, and non-branching and branching bundles (F). Distance between red dots- 1.1 mm, green dots- 7.8 mm. AOV- aortic valve, BrB- branching bundle, IVS- interventricular septum, LBB- left bundle branch, LV- left ventricle, MV- mitral valve, NBrB- non-branching bundle, PB- penetrating bundle, RBB- right bundle branch. (Scale bar represents 1 mm)

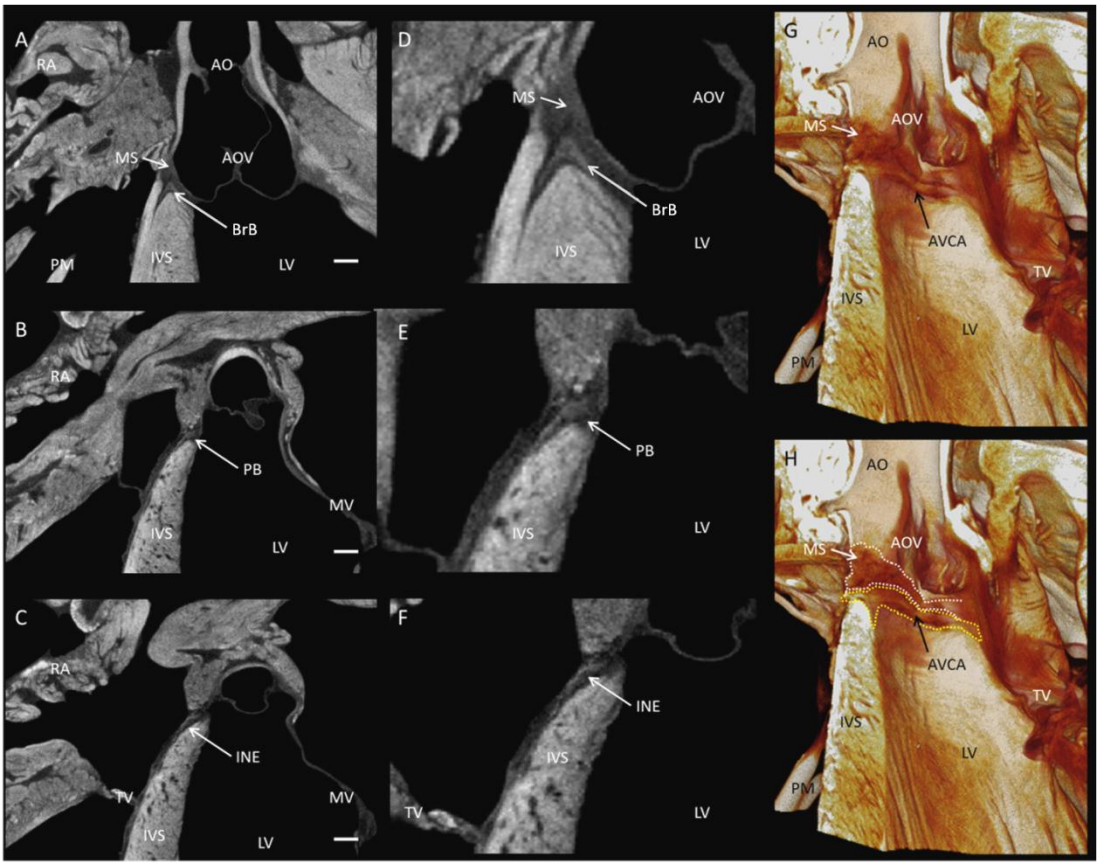

Figure 6.8 Longitudinal micro-CT images of atrioventricular conduction axis in rabbit with corresponding volume renderings. micro-CT images of the branching bundle (A,B), penetrating bundle (C,D) and inferior nodal extension (E,F) in a rabbit heart stained with 3.75% I_2KI for 5 days. Volume renderings showing the atrioventricular conduction axis and its relationship with surrounding structures (G,H). AO- aorta, AOV- aortic valve, AVCA- atrioventricular conduction axis, BrB- branching bundle, INE- inferior nodal extension, IVS- interventricular septum, LV- left ventricle, MS- membranous septum, MV- mitral valve, PB- penetrating bundle, PM- papillary muscle, RA- right atrium, TV- tricuspid valve. (Scale bar represents 1 mm)

6.5 Purkinje system of the rabbit heart

Free running Purkinje fibres are difficult to interpret in any destructive sectioning technique because they are easily lost or damaged and are challenging to follow in thin serial sections. In contrast, they were easily identified in micro-CT images, because in the image data they were running in air, and thus appeared clearly as high attenuating structures against the low attenuating ventricular cavity (space). As a

result free running aspects were segmented using semi-automatic method II (methods 2.4.2). However, fibres running on the endocardial surface of the ventricles were more difficult to discriminate from the contractile myocardium. It was possible to segment some fibres running on the endocardial surface, because they appeared as protrusions which were continuous with the free-running fibres. Because these protrusions are small structures with a relatively small differential attenuation to the myocardium, this aspect of the segmentation was largely a semi-automatic process (methods 2.4.2- semi-automatic segmentation I) and unlikely to be complete. However, in agreement with whole mount immunohistochemical studies, the rabbit does not seem to have a sub-endocardial Purkinje network (Atkinson et al., 2011). The ventricular Purkinje network is presented in three hearts from normal rabbits (figure 6.9). The least differentiated components of the Purkinje system are the right and left bundle branches (RBB, LBB) as they descend the IVS. This is because, in this area, the differential contrast between the (lower attenuating) conducting tissue and the (higher attenuating) working myocardium is smaller than in other areas of the CCS. Indeed, in some parts of the bundle branches, the conducting tissue had a higher attenuation than the surrounding working myocardium.

In figures 6.11 and 6.12, the rendered AVCA and Purkinje system is shown with its relationship to the surrounding myocardium. This shows that the LBB emerged as a ribbon-like structure (~2 mm wide) that draped over the IVS, at its widest point spanning ~4.5 mm (e.g. figure 6.11, figure 6.7C,F). In contrast, the RBB emerged as a thin structure (~0.75 mm wide), but still with a ribbon-like appearance (e.g. figure 6.12, figure 6.7C,F). The main branches can be traced down the IVS, with the LBB running vertically in the same plane as the branching bundle; in contrast, the RBB projects anteriorly before taking a more vertical route down the IVS (figure 6.7F, figures 6.11,6.12). Figures 6.11, 6.12 and 6.9 show that the Purkinje network occupies the luminal cavity, with large portions of the network running from one side of the lumen to the other and, therefore, in life, running within the flowing blood. The networks have a web-like appearance, with many interconnecting segments, which in places form loops. The data suggests that the Purkinje network in the left ventricle is more extensive than that in the right ventricle (figures 6.11,6.12). Finally, figure 6.9 shows that there is substantial variation in the Purkinje system between control hearts. There are surprising differences in fibre branching and thickness, and

in overall network volume (4.2mm³, 5.5mm³, 15.8mm³; figure 6.9). However, there are similarities in terms of connections in all three samples (figure 6.9). For example, there are common branchings from the IVS to the ventricular free wall and from the IVS directly to the papillary muscles (PMs), branches to the PMs were extensive in most samples (figure 6.9).

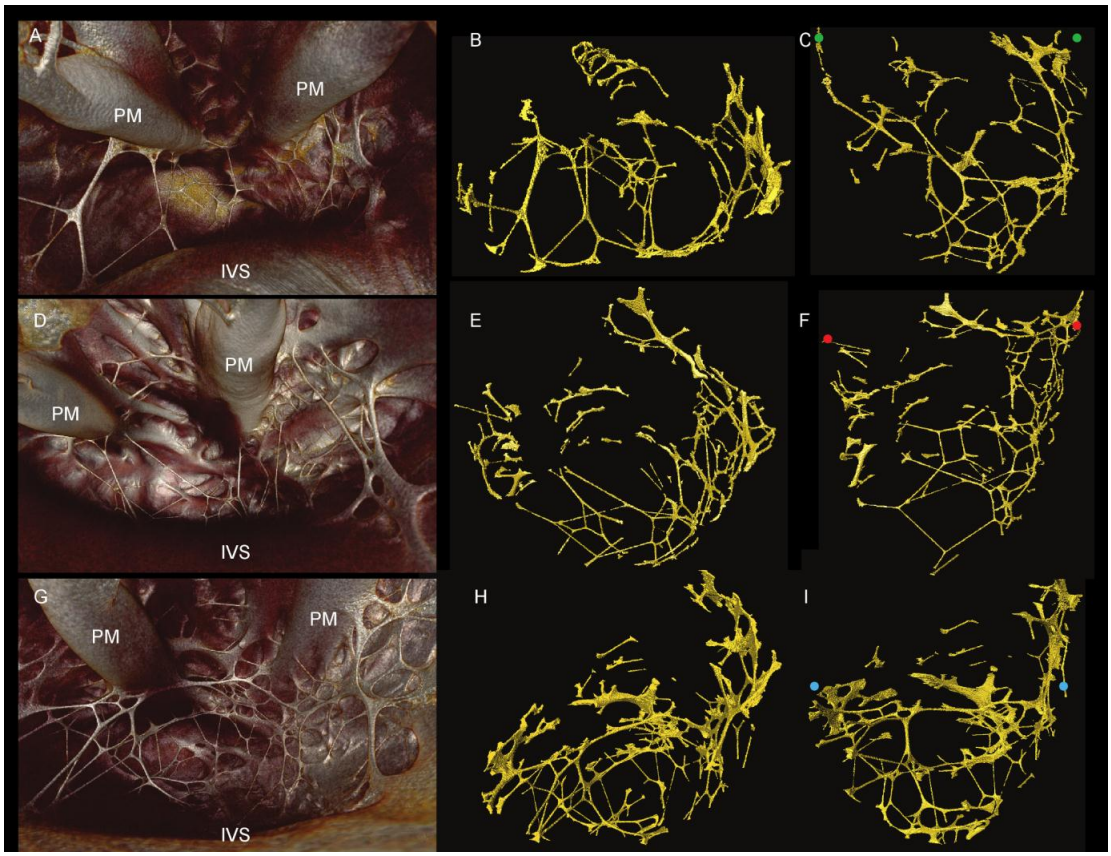

Figure 6.9 Volume renderings and corresponding 3D isosurfaces of Rabbit left ventricular Purkinje networks. 3 seperate rabbit hearts were stained with 7.5% I_2KI for 3 days (A-C) or 3.75% I_2KI for 5 days (D-F and G-I) and micro-CT scanned. Volume renderings viewed from base to apex (A,D,G), with corresponding segmented 3D isosurfaces in transverse (B,E,H) and longitudinal orientation (C,F,I). Volumes of segmented data- 4.2 mm³, 5.5 mm³, 15.8 mm³ respectively. Number of vertices in segmented data- 454, 370, 569 respectively. Coloured dots represent Purkinje network maximum widths- distance between green dots- 13.5 mm, red dots- 17.1 mm, blue dots- 14.4 mm. IVS- interventricular septum, PM- papillary muscle.

Figure 6.10 validates micro-CT findings which showed the Purkinje fibres as a complex network of many free running aspects. Whole mount immunohistochemistry and TCE micro-CT showed the Purkinje fibres to be NF-M positive confirming the networks potential to propagate the wave of depolarisation to the ventricular myocardium. TCE allowed for non-invasive visualisation of NF-M positive tissue in 3D, although the method suffered from background staining, this did not affect the free running Purkinje fibres, and allowed discrimination between the conducting tissue (high attenuation) and the surrounding connective tissue sheaths (low attenuating). The level of connective tissue surrounding individual fibres varied, with some regions heavily bound in connective tissue (figure 6.10). Quantification of the network in figure 6.10 revealed a mean segment radius of 47μm, corresponding closely with values described previously in histological studies (Stankovicová et al., 2003).

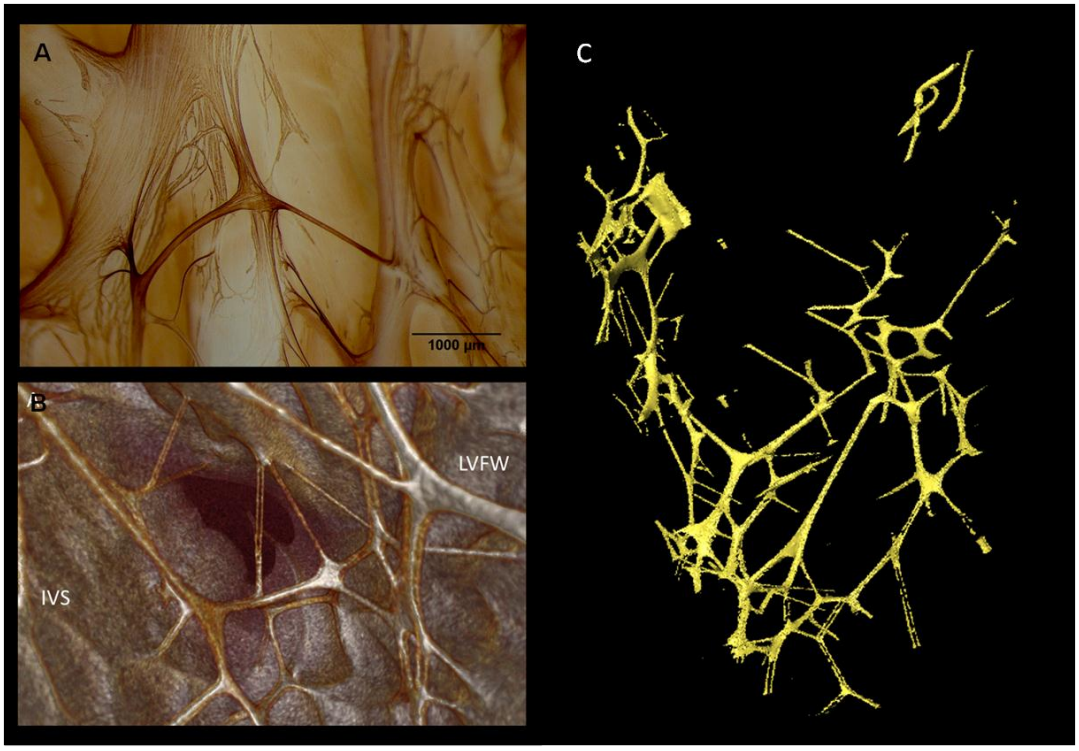

Figure 6.10 The 3D morphology of the rabbit left ventricular Purkinje network investigated by immunohistochemistry and TCE micro-CT. Whole mount immunohistochemistry for NF-M (brown indicates NF-M+ tissue) (A), and targeted contrast enhanced (TCE) micro-CT for NF-M (high attenuation represents NF-M+ tissue) (B). Segmented 3D surface of Purkinje network (network volume= 5.2mm³, network length= 238mm, mean segment radius 47µm) (C). IVS- interventricular septum, LVFW- left ventricle free wall. Whole mount immunohistochemistry conducted together with Dr Halina Dobrzynski. (Scale bar represents 1 mm)

6.6 Variations of the CCS in rat and rabbit

Although the major components of the CCS are associated with the same anatomical landmarks in both rat and rabbit, there is evident variation in their morphology. The branching bundle of the rat appears flattened and broader (figure 6.2) in comparison to the more narrow and elongated structure seen in rabbit (figure 6.7). The bundle branches and accompanying Purkinje networks are different in the two species; both bundle branches in the rat appear as uniform ribbon-like structure with widths of ~0.5 mm (figure 6.2C,F), in rabbit the morphology of the LBB is quite different; the LBB emerges as a ribbon-like structure (~2 mm wide) that drapes over the IVS, at its

widest point spanning ~4.5 mm (figure 6.7C,F, figures 6.11, 6.12) The RBB emerges as a thin structure (~0.75mm wide), but still has a ribbon like appearance (figure 6.7C,F, figures 6.11, 6.12). The main branches can be traced down the IVS, with the LBB continuing distally in the same plane as the more proximal branching bundle. In contrast, the RBB projects anteriorly before taken a more vertical route down the IVS. The left ventricular Purkinje network in rat is localised to the apical region, creating a scoop-like appearance, with evidence of trans-luminal fibres. Towards the base branches run on the endocardial surface with no cross luminal branching. In contrast the left ventricular Purkinje network of the rabbit appears as a web-like structure spanning the entire luminal cavity, with numerous branches traversing the cavity (figures 6.8, 6.10, 6.11,6.12).

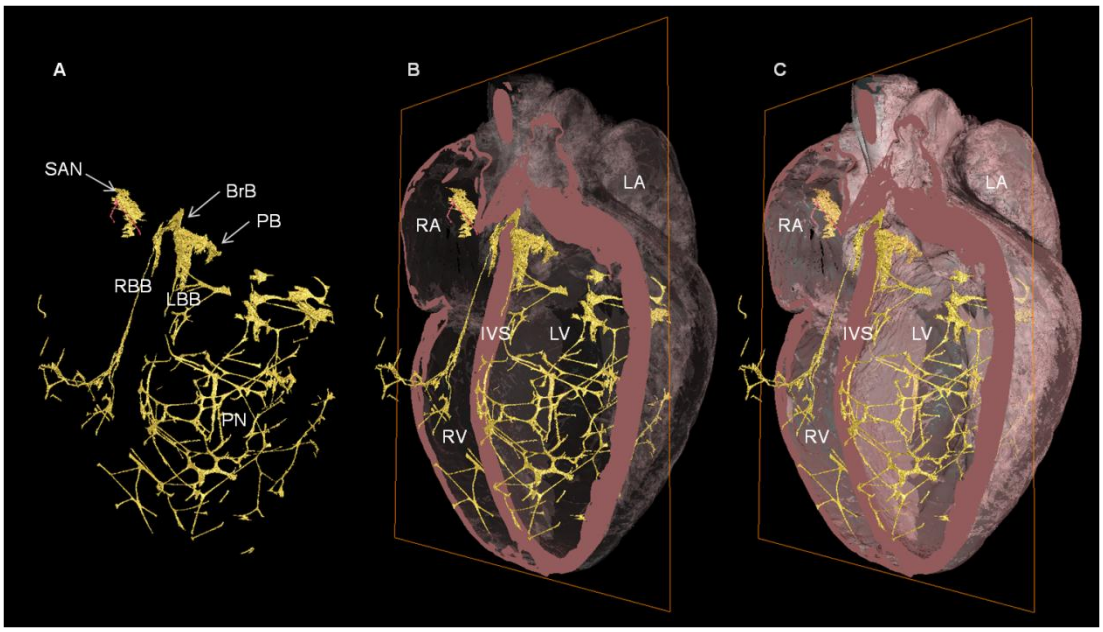

Figure 6.11 Segmented 3D surface of the three major components of the CCS in a failed rabbit heart. Showing the CCS isosurface (yellow) overlaid with the longitudinally cropped cardiac mass (pink). Decreasing levels of cardiac mass transparency (A-C) show the true in situ position of the CSS. BrB- branching bundle, IVS- interventricular septum, LA- left atrium, LBB- left bundle branch, LV- left ventricle, PB- penetrating bundle, PN- Purkinje network, RA- right atrium, RBB- right bundle branch, RV- right ventricle, SAN- sinoatrial node.

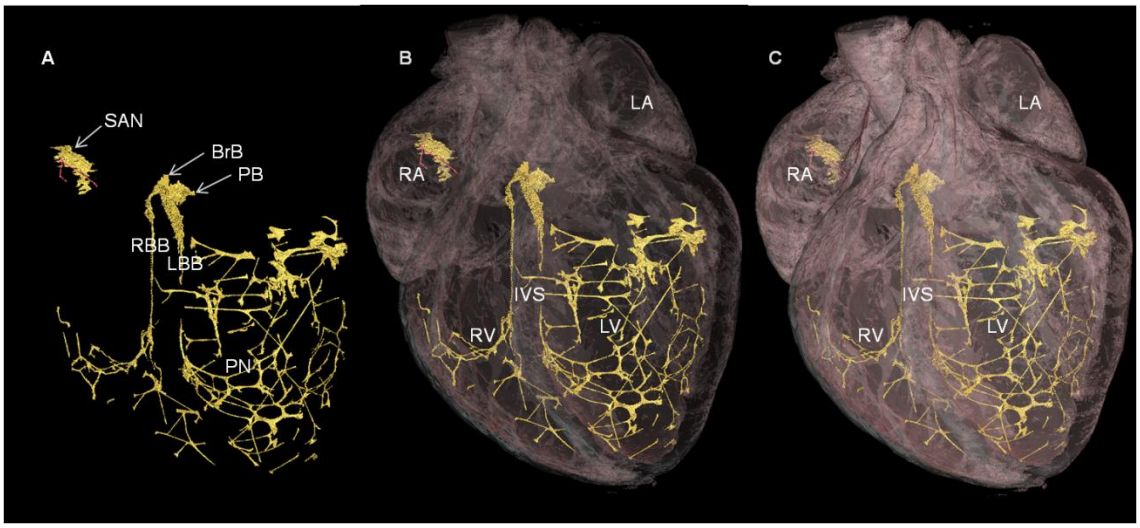

Figure 6.12 3D surface of the three major components of the CCS segemented in a failed rabbit heart. The CCS isosurface (yellow) (A) overlaid with cardiac mass (pink) at decreasing levels of transparency (B,C), showing the penetrating bundle emerging from the right atrium and transversing the IVS as non-branching bundle to become the branching bundle anteriorly (in true in situ position). BrB- branching bundle, LA- left atrium, LBB- left bundle branch, LV- left ventricle, PB- penetrating bundle, PN- Purkinje network, RA- right atrium, RBB- right bundle branch, RV- right ventricle, SAN- sinoatrial node, IVS- interventricular septum.

6.7 Discussion

This study has shown that contrast enhanced micro-CT offers a non-destructive method to obtain a high-resolution map of the 3D disposition of the CCS. High resolution, non-invasive imaging of the 3D morphology of the CCS will have several important benefits. It will: a) improve the understanding of CCS anatomy and function; b) inform the development of 'virtual hearts'- anatomically and biophysically-detailed mathematical models of the heart for education, research, planning surgical treatments and drug discovery; c) provide information on 3D fibre orientation in regions known to be involved in the pathway of conduction; d) inform cardiac ablation procedures; e) provide better guidance for implantation of prosthetic aortic valves to avoid LBB block; and f) guide the planning of reconstructive surgery for congenital heart defects, to avoid damage to the CCS and reduce the need for pacemakers. The figures presented here provide confirmation of many previous

studies (Chandler et al., 2011, Dobrzynski et al., 2005, Ko et al., 2004, Li et al., 2008), but are the first intrinsic 3D representations of the relationships between the conducting tissues and the surrounding cardiac anatomy, and are the first to show the three major components of the CCS within datasets captured from single intact hearts.

6.7.1 Comparison of Micro-CT to other Techniques for CCS analysis

During this study, hearts were carefully prepared by in situ perfusion to avoid the contrast degradation caused by the presence of luminal blood, and to provide uniform arterial fixation. During fixation, application of the contrast agent, and during preparation for scanning, care was taken to maintain the heart in an 'inflated' state. Without such care the atria are prone to collapse, and views from the inside of the atrial chambers are not possible (see 3.9 and 3.10 for images of a heart which has not undergone perfusion fixation). The micro-CT technique used in this study to identify and visualise the CCS has numerous advantages over alternative methods: (i) the technique is non-destructive and there is no distortion of the heart caused by dissection, embedding, freezing or cutting. (ii) The staining by the contrast agent is reversible, so that samples are preserved for any future studies such as light microscopy. (iii) The technique achieves automatically registered, high resolution, tomographic data sets which results in a more accurate representation of the CSS. In this study, the resolution was ~20 μm. In studies involving serial sectioning, the resolution is often 60–340 μm (Dobrzynski et al., 2005, Li et al., 2008). To achieve a similar level of a resolution by a sectioning-based technique would require a high level of technical expertise and resources. Furthermore, to obtain such a set of sections from a small mammalian heart in its natural blood-filled disposition would require fixation and embedding, and therefore filling, of a whole intact heart with wax or plastic. With atrial walls as thin as 0.2 mm, this would be a severe technical challenge. Although the resolution in this study is comparable to the resolution in a previous study involving high resolution MRI (Li et al., 2005), micro-CT offers inherent isometric resolutions while avoiding the issue of diminishing signal:noise ratio experienced with MRI at high resolutions. (iv) The technique is fast; in this study imaging of one sample ranged between ~20–50 minutes. In contrast, comparable serial sectioning work will take many weeks, and in the study of Li et al.

MRI was stated to have taken many hours (Li et al., 2005), but to obtain image quality comparable to micro-CT, scans as long as 72 hours are required (Gilbert et al., 2012). For a more comprehensive review of micro-CT advantage over MRI see Chapters 3 and 4. (V) Furthermore, existing techniques use small sample preparations removed from whole hearts by dissection, and therefore do not allow simple visualisation of the relationship between the CCS and the surrounding working myocardium and fibrous skeleton. Resultant 3D renderings from such preparations must subsequently be placed onto schematic diagrams of the whole heart somewhat subjectively (Dobrzynski et al., 2005, Li et al., 2008). This potential source of error is not a limitation of the current study.

Contrast enhanced Micro-CT as a technique does have a disadvantage: the ability to discriminate between different tissues is limited compared to traditional sectioning and staining (although perhaps better than that of MRI). Traditional immunohistochemical techniques allow discrimination of specialised tissues based on their specific ion channel and connexin expression (Dobrzynski et al., 2013). However based on similar principles as immunohistochemistry, and on work conducted by Metscher and Muller (Metscher and Müller, 2011) on embryonic tissue, we have developed a technique called TCE micro-CT. This allows specific tagging of proteins of interest with a heavy metal, hence increasing X-ray attenuation in these regions. We have developed the technique for use on whole hearts, and although further optimization is required to reduce background and to resolve access issues, this technique has the potential to become the gold standard for non-invasive 3D visualisation of the CCS.

6.7.2 Contrast Enhancement

The mode of contrast enhancement by iodine staining remains incompletely understood. Differential uptake of iodine by different tissue types allowed discrimination between; fat, myocardium, nodal tissue and connective tissue, with decreasing attenuation coefficients respectively (differences quantified in Chapter 3). One hypothesis is that the molecular iodine becomes immobilised within the structure of glycogen- the basis of simple tests for polysaccharides (Lecker et al., 1997, Saenger, 1984). For more details on the principles of differential uptake of

iodine see Chapters 3 and 4. While this provides a rational basis for the greater attenuation of myocardium compared to fibrous tissue, it does not so obviously explain the lower attenuation that we have found generally for tissues of the CCS. The specialised myocytes of the CCS are reported to have high glycogen content, and the classic histological stain for glycogen known as Periodic Acid Schiff (PAS) is used to provide discrimination between the CCS and surrounding tissue (Airey et al., 2004, Myers and Fishman, 2003). This apparent anomaly may be explained by the presence of glycogen-rich compartments in myocytes of the CCS, but a lower average density over the sectional area encompassed by a group of voxels. Myocyte density and cell size can be lower in the CCS (especially in parts of the sinoatrial and atrioventricular nodes (Boyett et al., 2000, Christoffels et al., 2010) than in the tightly-packed contractile myocardium. We have shown previously low tissue density coincides with lower attenuation (Chapter 3). In addition we have also shown previously the low attenuating properties of connective tissue (Jeffery et al., 2011). Therefore, with the connective tissue network more extensive, but less dense in nodal tissue than working myocardium (Dobrzynski et al., 2013), this will also contribute to overall lower attenuation coefficients in the CCS.

There is obvious potential for the current technique to be applied to the reconstruction of the CCS in larger hearts, including human hearts. Contrast enhancement of the CCS is achieved by the differential uptake of the contrast agent by different tissue types. In the present method the contrast agent is taken up by the tissue through the process of diffusion therefore this may be a limitation when preparing larger samples because contrast may be lost in more superficial areas (too much iodine), before sufficient contrast is obtained in deeper parts of the tissue. It may therefore be necessary to develop a perfusion-based technique in which the iodine contrast is delivered via the arterial system.

6.7.3 Segmentation of the CCS

The delineation of the CCS required use of various image analysis techniques. For the intra-ventricular Purkinje network, in which the structures run in air, an instantaneous volume rendering technique (VRT) can be used by windowing an opacity curve to include voxel values of interest and selecting a 3D colour map. The

resultant 3D volume is rendered using a VRT render mode in which voxels are assigned a level of opacity (0–100%) and colour calculated from their CT attenuation value. This complex procedure is versatile and time efficient and can easily combine characteristics of surface rendering and maximum intensity projection techniques, and offers improved definition of contours and semi-transparent displays over those techniques. For the SAN, a volume rendering that provided an image of the endocardial surface of the right atrium was most informative; use of VRT allowed an area to be identified that matched well with the landmarks of the crista terminalis and caval vein openings. Previously we described the difficulty to visualise the AVCA using VRT (Stephenson et al., 2012), subsequent optimisation has permitted visualisation of the AVCA using this technique, and allowed an appreciation of the AVCA's relationship with surrounding structures, and especially it course through the central fibrous body. Semi-automatic segmentation II (methods 2.4.2) was shown to be an ideal technique for segmentation of free running structures such as the LVFW or IVS (see chapter 8), and was used here to effectively and efficiently segment and quantify the Purkinje fibre networks. In the samples presented here, the attenuation differences between the CCS and the surrounding myocardium were higher in the rat than in the rabbit. Although the resolution attainable in rat is finer due to the smaller sample size, this may represent a real difference between the species at the cellular level.

6.7.4 Variations of the Ventricular Conduction System in the Rat and Rabbit

The branching bundle of the rat is flattened and broader than the more narrow and elongated structure seen in the rabbit. The bundle branches and accompanying Purkinje networks are also different in the two species. Both bundle branches in the rat are uniform ribbon-like structures with a width of ~0.5 mm. In the rabbit, the LBB was a ribbon-like structure ~2 mm wide that draped over the IVS, at its widest point spanning ~4.5 mm. However, the RBB was a relatively thin ribbon-like structure ~0.75 mm wide; this asymmetry between the bundle branches is consistent with the work of Miquerol et al. (Miquerol et al., 2004) and Atkinson et al. (Atkinson et al., 2011). The left ventricular Purkinje network in the rat was localised to the apical region, creating a scoop-like appearance, with the majority of branches running on the endocardial surface towards the base with few cross luminal branches.

In contrast, the left ventricular Purkinje network in the rabbit was a web-like structure spanning the entire luminal cavity, with numerous branches traversing the cavity. In addition there was clear variation between individuals in contrast to the conclusions of Atkinson et al. 2011.

6.7.5 Comparison to Previous Studies

The specialised AV ring tissues (Yanni et al., 2009a) and right ventricular outflow tract (Dobrzynski et al., 2013) were not analysed in the presented study. However results presented here suggest contrast enhanced micro-CT and/or TCE micro-CT will be capable of resolving these structures.

The Sinoatrial node

The shape and volume of the rendered SAN of the rabbit heart in this study are similar to those reported by Dobrzynski et al. 2005, who used a more time consuming and labour intensive serial sectioning technique. Whereas the volume of the rendered SAN was 1.01 mm^3 in this study, it was 1.4 mm^3 in the study of Dobrzynski et al. 2005. Analysis here shows the SAN in the rabbit heart to be an extensive structure, unlike the 'textbook view' of the SAN, which is normally portrayed as a small nodule at the junction of the superior vena cava and the right atrium (Boyett, 2009). In fact the leading pacemaker site in the rabbit can be located at any site along the length of the crista terminalis from the superior to the inferior vena cava (Boyett, 2009), and the extent of the SAN in the current study is consistent with this. The smear like appearence observed here in rabbit is consistent with histological studies of the SAN in rat (Atkinson et al., 2013), dog (Glukhov et al., 2013) and human (Fedorov et al., 2010, Matsuyama et al., 2004). In some of our samples regions corresponding to the paranodal region, as described by Boyett et al. (2000) and Fedorov et al. (2009), were observed. Furthermore indigitations of the SAN into the surrounding working myocardium were evident, these were first described by Liu et al. 2007(Liu et al., 2007), and their function is still debated (Fedorov et al., 2009, Boyett et al., 2006).

The Internodal pathways

Another controversial debate is the existence of distinct pathways responsible for internodal conduction within the RA. Data presented here and by collaborators is consistent with previous studies of the SARBs (Paes De Carvaho et al., 1953, Bojsen-Moller and Tranum-Jensen, 1972, Bojsen-Moller and Tranum-Jensen, 1971). They confirm that such pathways exist in the rabbit, although they have yet to be shown to extend directly from the sinus to the atrioventricular nodes. Whole mount immunohistochemistry and TCE micro-CT confirm the SARBs, which like the nodal cells have a primary myocardial lineage, are insulated from the myocardium and are NF-M positive; a cytoskeleton protein which is abundant in all regions of the CCS (Atkinson et al., 2011). In addition immunohistochemistry of serial sections confirms these tracts are also connexin 43 (Cx43) positive (Dobrzynski et al., 2005); Cx43 is fast conducting (60-100 picoseconds) and is strongly expressed in the fast conducting Purkinje network and working myocardium (Gourdie et al., 1993). Therefore these bundles are histologically discrete and are insulated from surrounding myocardium by connective tissue sheaths. In addition they are traceable from section to section (Dobrzynski et al., 2005). Thus the SARBs meet all the criteria set by the German Pathological Society (1910) for defining conducting tracts of the CCS, although as yet they have not been shown to extend directly from the sinus node to the atrioventricular node.

These NF-M+ tracts create a network which we have shown follow the latter routes of both the fast and slow pathways, as well as giving branches which run on and between the PcMs. Fibre orientation analysis shows that fibres in the vicinity of the SARBs run longitudinally with the tracts, which is known to contribute to fast conduction (anisotropic conduction) (Spach and Kootsey, 1983). Studies of the SARBs electrophysiology in rabbit using micro electrodes suggest, like Purkinje cells, they have slow diastolic depolarisation (pacemaker potential) and a fast upstroke (Hiraoka and Sano, 1976, Paes De Carvalho et al., 1953). Paes de Carvalho et al., 1953 suggested the SARBs are the first to be excited by the SAN and offer the fastest route for internodal conduction. However more recent studies have discredited the role of the SARBs, showing the CT is the first to be excited and offers the route

for preferential conduction due to its superior conduction velocity (Masuda and Paes de Carvalho, 1975, Hiraoka and Sano, 1976).

The suggested slow conduction velocity of the SARBs (Masuda and Paes de Carvalho) and their insulation from the myocardium suggests we cannot claim direct connections exist between the SARBs and the SAN, and thus cannot claim the SARBs are true internodal pathways. Further histological and electrophysiological evidence is required if the SARBs are to be accepted as the preferential pathways for internodal conduction in the rabbit.

The atrioventricular conduction axis

Consistent with Tawara's original histological description of the AVCA (Tawara, 2000), our 3D representation confirms that the AVCA originates in the expected location between the coronary sinus and the membranous septum at the base of the triangle of Koch and the axis can be followed around the circumference of the aortic valve annulus. The 3D rendering of the AVCA of the rabbit heart as shown here is qualitatively and quantitatively similar to the 3D rendering of the AVCA of the rabbit heart obtained from serial sectioning (Li et al., 2008). The 3D rendering in this study is superior in that it is higher resolution and shows the connections to the bundle branches (whereas that from Li et al., 2008 for example does not). However, the 3D rendering in this study fails to accurately differentiate the various sub-compartments (inferior nodal extension, transitional zone, compact node, upper and lower tracts of the penetrating bundle) within the AVCA that are identified by Li et al. 2008 by appropriate staining and immunolabelling of marker proteins.

ThePurkinje network

The Purkinje network identified in this study is qualitatively similar to that described in previous studies (Atkinson et al., 2011, Bordas et al., 2011, Tawara, 2000). Although the Purkinje network identified here appears more complete than in studies using MRI (Bordas et al., 2011), it is not as complete as the Purkinje network identified by 2D immunolabelling (Atkinson et al., 2011). However it is revealed in its true 3D relationship with the intact cardiac chambers and the true extent of its free

running aspect can be appreciated. TCE micro-CT allowed the connective tissue sheaths surrounding individual Purkinje fibres to be resolved in 3D; the density of the sheaths varied throughout the network. Previously, Indian ink staining of Purkinje fibres in dissected ventricles suggested connective tissue sheath distribution may play a key role in coordinated contraction of the ventricles (Ansari et al., 1999, Tranum-Jensen et al., 1991). Using functional mathematical models (Berenfeld and Jalife, 1998, Vigmond and Clements, 2007, Bordas et al., 2011) incorporated with the data presented here using TCE micro-CT, there is a good prospect that the true functional relationship between the Purkinje network and working myocardium will be resolved.

Here we present a technique by which the major regions of the CCS can be rapidly imaged non-invasively using reversible contrast enhancement for micro-CT in small mammalian hearts. Secondly we present a technique for targeted contrast enhancement, TCE micro-CT, which has great potential to provide morphological and functional information about the CCS in health and disease. The clear advantage over traditional methods of gross dissection, light microscopy and immunofluorescence staining for investigating the CCS is that high-resolution (μm) representations can be obtained with a non-destructive method while preserving 3D geometry and spatial relationships.

There is a worldwide effort to develop a 'virtual heart', an anatomically and biophysically-detailed model that can be used to describe normal function and predict dysfunction and arrhythmogenesis with pathology or malformation (Boyett et al., 2005). Although there are excellent models of the working myocardium (Trayanova, 2011, Nielsen et al., 1991, Boyett et al., 2005), predictive models of the whole heart must include the CCS. Contrast-enhanced micro-CT offers an effective and efficient method to generate an accurate anatomical model of the heart including the CCS, which can be incorporated into functional models, and thus help answer disputes over conduction throughout the heart.

6.8 Summary

Here we show contrast enhanced micro-CT can be used to non-invasively image the CCS efficiently (~20-50minutes) at high resolution (18-42μm). In figures 6.11 and 6.12, the whole of the CCS is rendered in one intact rabbit heart and is shown superimposed on different views of the heart. This is the first time that such views have been shown for any species.

The differential uptake of iodine by soft tissues, and the high spatial resolution provided by micro-CT allowed the three major tissue types; working myocardium, nodal tissue and connective tissue, to be delineated with decreasing levels of attenuation respectively. The SAN, AVCA and Purkinje system could be objectively identified, visualised in 3D and quantified. Internodal pathways were resolved, and controversially we revealed structures within right atrium continuous with the RSARB and LSARB analogous to the Purkinje fibres of the ventricles, these NF-M positive fibres are free running in part and could shed new light on the complex depolarisation of the atria. All findings were validated by histology, immunohistochemistry and TCE micro-CT.

We present a technique by which the major regions of the CCS can be rapidly imaged non-invasively using reversible contrast enhancement for micro-CT in small mammalian hearts. The clear advantage over traditional methods of gross dissection, light microscopy and immunofluorescence staining for investigating the CCS is that high-resolution (μm) representations can be obtained with a non-destructive method while preserving 3D geometry and spatial relationships. There is a worldwide effort to develop a ‘virtual heart’ model. Contrast-enhanced micro-CT offers an efficient method to generate an accurate anatomical geometry of the heart including the CCS, which can be incorporated into such models.

CHAPTER 7

The Effects of Volume and Pressure Overload on the 3D Morphology of the Cardiac Conduction System in the Rabbit Heart

7.1 Introduction

Heart failure (HF) is associated with structural and electrical remodelling of the working myocardium and cardiac conduction system (CCS). Such remodelling of the heart is a substrate for arrhythmogenic disorders such as atrial fibrillation, re-entry circuits and ventricular tachycardia (VT). Experimental studies have shown that structural remodelling is characterised by heterogeneous expression and down-regulation of connexins (Cx), the proteins that form intercellular gap junctions and allow action potential propagation. Other structural changes include increased fibrosis and muscle fibre disorganisation. Electrical remodelling is often characterised by changes to regional action potential morphology, and changes in expression and function of ion channel and Calcium handling proteins. Although experimental data exists on the remodelling of the CCS in HF at a cellular and protein level, little is known on how the 3D morphology of these specialised tissues is affected. This deficit is well illustrated by current mathematical models of the cardiac function; multi cell models of electrical propagation offer highly detailed functional modelling, but model fidelity is confounded by low-resolution and often inaccurate morphological data. This is due to the fact that, until recently, knowledge regarding the true 3D anatomy of the CCS was poor. Using contrast enhanced micro-CT we were the first to non-invasively image the major aspects of the CCS in a fully intact heart, and present their true relationship with the surrounding working myocardium. This is especially the case for the Purkinje fibre network, an appreciation of the extent of its free running aspect has only been achieved using non-invasive imaging such as micro-CT. Traditional histological analysis based on serial sections are hugely laborious and suffer from difficulties with resolution and registration, making analysis of groups large enough for statistical analysis unrealistic. Micro-CT is a fast, non-destructive and non-invasive imaging method, in which high resolution data (~5 μm attainable) is automatically aligned in 3D. Together with the recent advances in image analysis tools, the investigation of suitable n numbers to allow statistical comparison has become possible. In this chapter morphological changes to the sinoatrial node (SAN), atrioventricular conduction axis (AVCA) and the Purkinje fibre network are investigated in rabbits that have been subjected to experimental HF (volume and pressure overload) (methods 2.2). The effects of HF on fibre orientation in the SAN are assessed, and

filament analysis (methods 2.4.3) is conducted to investigate changes in complexity of the free running aspects of the Purkinje network. This data provides novel insights into morphological changes across all major regions of the CCS in HF, which in turn will improve the fidelity of mathematical models of cardiac function. Since 3D morphology is so closely related to the characteristics of electrical transmission, the data will allow inferences to be made regarding electrical dysfunction associated with HF.

7.2 Morphological changes to the sinoatrial node in experimental heart failure

Experimental HF was induced in adult rabbits by means of aortic valve disruption and subsequent aortic banding (2 weeks later), enabling investigation of morphological and functional changes in hearts exposed to both volume and pressure overload (see methods 2.2 for detailed method and see Chapter 8 for effects to the working myocardium). To assess morphological changes in control and HF animals, whole intact rabbit hearts were stained with I_2KI and scanned by micro-CT in optimal conditions. *In situ* heparinisation followed by perfusion fixation, accompanied with careful monitoring during the fixation process, produced naturally inflated hearts, with no residing blood in the atrial or ventricular cavities (methods 2.2.4). Particular attention was paid to the thin walled atria (RA ~250 μm, LA ~350 μm), however in some samples the intercaval region became folded during initial fixation (figure 7.3C), possibly due to the weight of the thick muscular crista terminalis. From whole heart scans atria and ventricles were reconstructed separately at 100% resolution, allowing fine details to be resolved in computationally manageable data sets. This section will concentrate on changes seen in the SAN in HF.

7.2.1 Volumetric changes to the sinoatrial node in heart failure

The SAN is the primary pacemaker of the heart and can be found in the intercaval region of the right atrium. To investigate morphological changes in the SAN, the right atrium (control n=4, HF n=5) was segmented from surrounding fat and fascia. Further segmentation was carried out to isolate the SAN from the posterior right atrium (see section 7.3.2 for segmentation details), then tissue volumes and surface

areas were calculated (Amira 5.4.0). Previous analysis of the SAN confirmed that it is not so much a localised compact node, but an extended thin layer of conducting cells (Chapter 6- figure 6.3, figure 6.4B,D and Stephenson et al., 2012). In the micro-CT images, the SAN was easily differentiated from the surrounding high attenuating atrial myocardium (Chapter 6- Figure. 6.3A). It appeared as a region of very low attenuation (dark) within the intercaval region of the posterior wall of the right atrium. It extends along the lateral aspect of the crista terminalis, which demarcates the boundary between the smooth intercaval region and the pectinate muscles of the right atrial appendage. Analysis using volume rendering techniques (VRT) showed the SAN was surrounded by a slightly higher attenuating region; distinct from the working myocardium this region corresponds to the paranodal tissue. This region is included in analysis here. The mean volume of the SAN was increased by 85% in HF (7.29±0.49 mm^3 vs 13.51±3.60 mm^3) (p=0.081) (figure 7.1A), this was coupled with a significant 51% increase in surface area (120.27±4.65 mm^2 vs 181.52±28.18 mm^2) (p=<0.05) (figure 7.1B). These results are consistent with the global morphological changes observed in the atria in HF (see Chapter 8.4).

To investigate morphological changes to the SAN at a cellular level, SAN preparations from control and HF samples were processed for histology, and cell diameters were measured and means taken. Analysis showed an increase in cell diameter in HF (7.7± 0.4 µm vs 8.7± 0.3 µm). Histology was conducted by Dr Xue Cai, The University of Manchester.

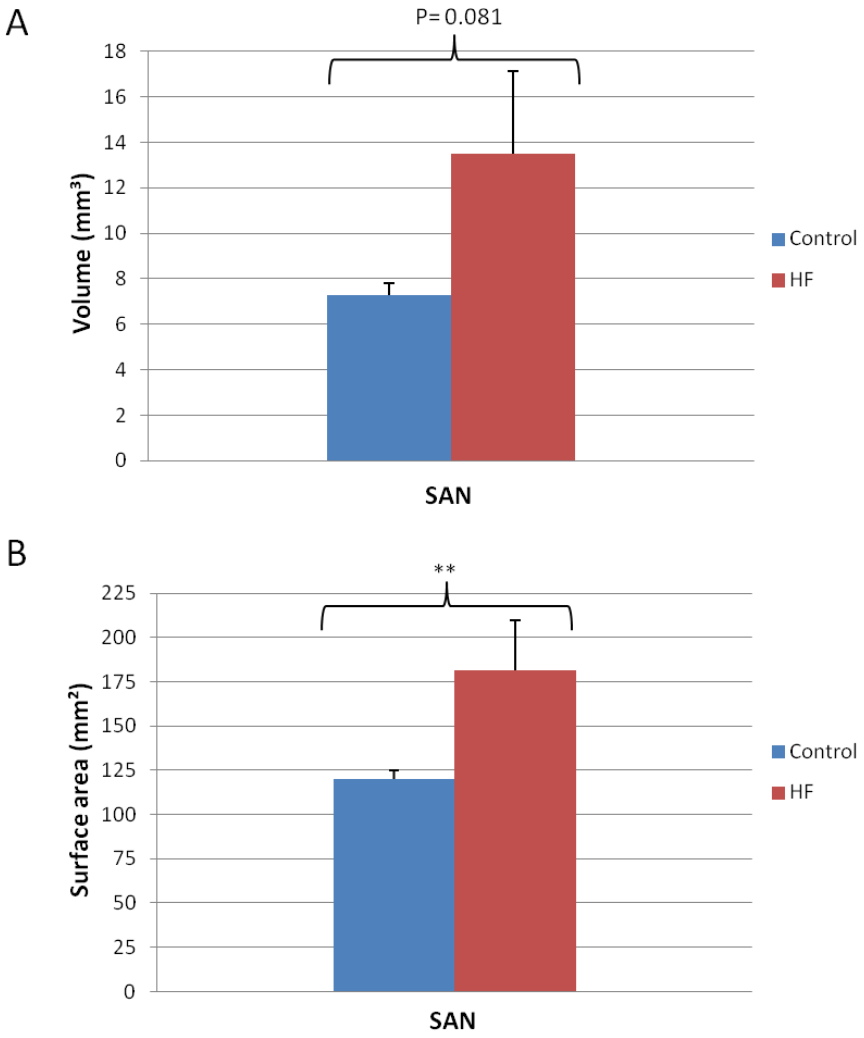

Figure 7.1 Tissue volume and surface area of the sinoatrial node segmented from micro-CT data of control and heart failure samples. Mean tissue volume (A) and mean surface area (B). (Control n=4, HF n= 5, **p=<0.05). Error bars indicate standard error of the mean (SEM). (HF-heart failure)

7.2.2 Fibre orientation in the sinoatrial node in control and heart failure

Contrast enhanced micro-CT has been shown to non-invasively indicate the arrangement of single muscle fibres in skeletal muscle (Chapter 4.3). Consequently novel structure tensor and fibre tracking analysis was carried out on micro-CT data of adult rabbit hearts (methods 2.4.4), to visualise and quantify the 3D fibre orientation of the SAN in control (n=4) and HF (n=5). Using a simple selection cropping method (ImageJ), the atrial data sets were segmented into subsets which

encompassed the posterior right atrium. The subsets were manipulated so that the crista terminalis was orientated vertically, and the SAN was then segmented using 3D segmentation (see methods 2.4.2). In this method a 3D volume rendering of the endocardial surface is created. The low attenuating area within the intercaval region (in this case corresponding to the SAN, periphery and paranodal region) is then drawn around in 3D using the pencil tool (Amira 5.4.0), and all pixels (space and myocardium) within the drawn boundary plane are selected. The selected pixels are then stored as a material, and unwanted tissue is removed using further 3D segmentation. Once segmented a window reflecting the SAN pixel values is applied to the material. This technique therefore allows rapid segmentation of subsets, eliminating the need for laborious serial segmentation. 3D segmentation was effective here because the SAN is not confounded by overlying structures, in addition the SAN is very thin and heterogeneous, and is therefore difficult to accurately segment using semi-automatic segmentation techniques.

Inclination and transverse fibre angles (figures 2.1,2.2) within the SAN were extracted from 6 transverse sections at evenly spaced intervals (superior-inferior). At each interval, all values across the corresponding transverse section were used for analysis. The mean fibre angle was calculated at each transverse section, and standard deviation of the fibre angle was used as an estimation of fibre organization, with high values representing fibre disarray. Figure 7.2A shows the standard deviation was reduced at all intervals in HF, suggesting more organised running fibres. However, statistical analysis using f-tests showed differences were not statistically significant. Across all intervals the trend for standard deviation was similar in both control and HF (figure 7.2A). The peaks seen at interval 5 correspond to a region of complex fibre orientation: here the fibres run around the coronary sinus and inferior vena cava, and begin to radiate out towards the IAS (figure 7.2A). This region corresponds to the flutter isthmus (figure 5.6), so-called because of its arrhythmogenic properties. Mean inclination angle was generally increased in HF (figure 7.2B), however significant differences were only seen at intervals 2 and 5. The SAN morphology was very variable, and also dependent on the fixation of the atria, this is illustrated by the volume renderings in figure 7.3. This variability makes comparative analysis of the SAN difficult. Analysis revealed a very complex and regionally variable fibre orientation in the SAN (figure 7.3). However, there were

fibre patterns that repeated in all samples; (1) the lateral border which is adjacent to the crista terminalis was predominantly made up of vertically running fibres; (2) Superiorly the SAN had fibres running into and following the curvature of the superior vena cava; (3) and fibres radiating from the central region running transversely towards the IAS were observed (figure 7.3).

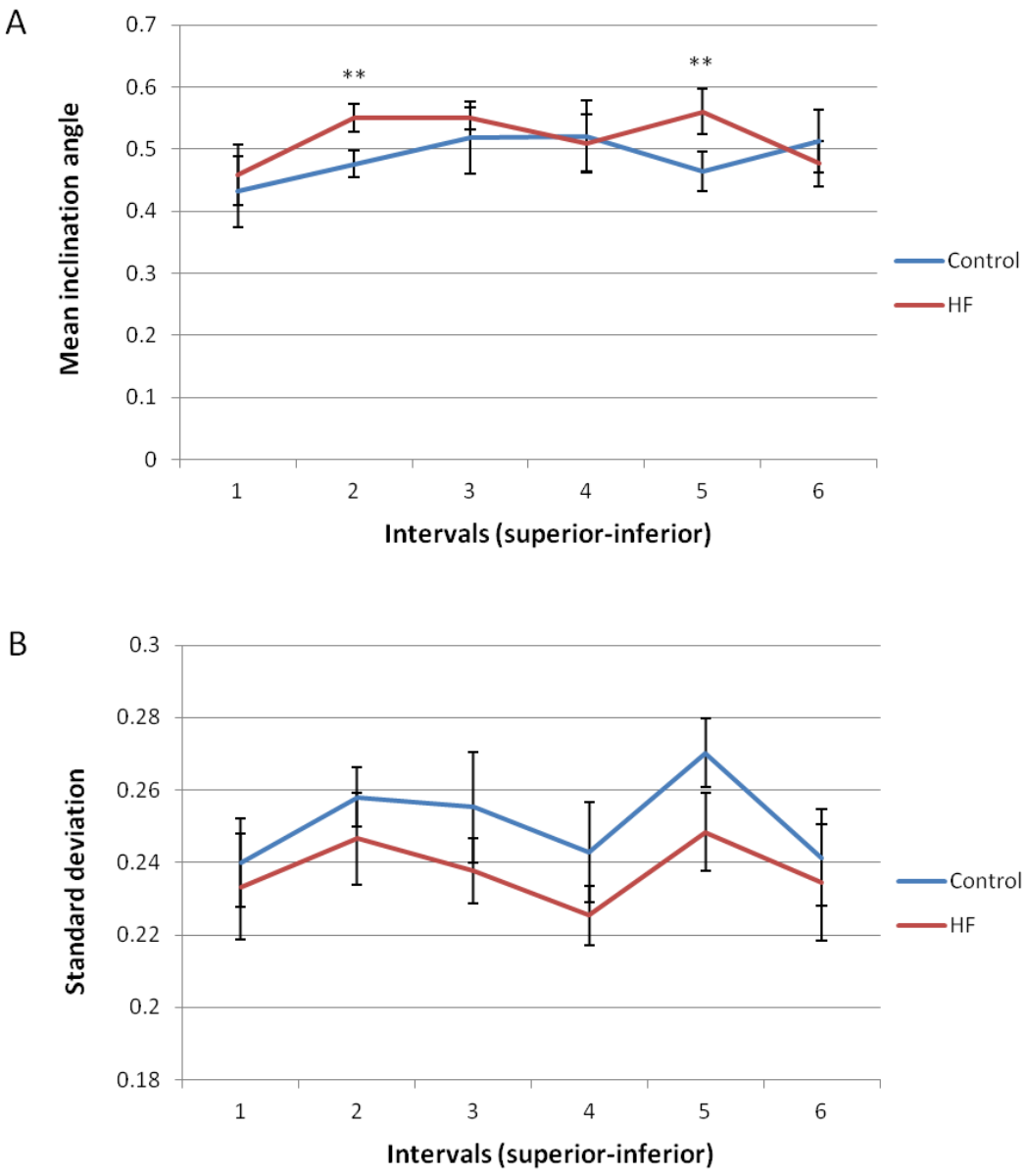

Figure 7.2 Fibre orientation analysis of the sinoatrial nodes segmented from micro-CT data of control and heart failure samples. Mean inclination angle of fibres (A) and the corresponding standard deviations (B) plotted at 6 transverse intervals through the node. (Control n=4, HF n= 5, **p=<0.05). HF-heart failure. Error bars indicate standard error of the mean (SEM).

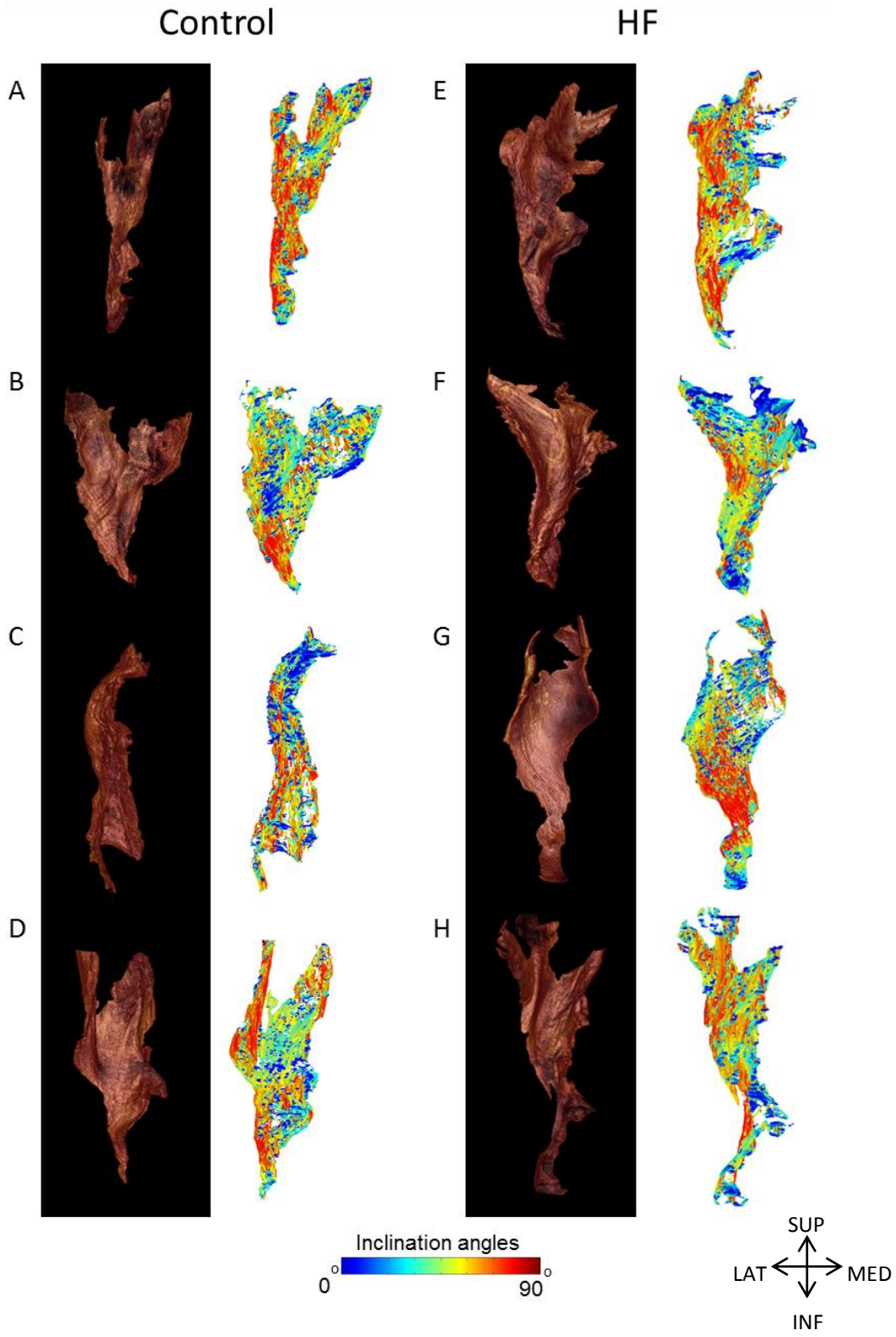

Figure 7.3 Volume renderings and fibre orientation of the sinoatrial node in control and heart failure samples. Volume renderings from endocardial view of the node segmented from micro-CT data with corresponding fibre orientation plots from control (A-D) and HF (E-H) animals. Isometric resolution of micro-CT data 18-24 µm. HF-heart failure. (Colour bar indicates inclination angles) Not to scale.

7.3 Morphological changes to the atrioventricular conduction axis in heart failure

The AVCA forms a structural connection between the atria and ventricles and is responsible for synchronised atrioventricular electrical conduction. To investigate morphological changes in the AVCA, image data was segmented in control (n=5) and HF (n=5) samples to isolate the AVCA (as previously described Stephenson et al., 2012). Selections included nodal cells and their surrounding extracellular matrix. Tissue volumes and 3D lengths were then calculated. 3D Lengths were calculated using the 3D measure tool (Amira 5.4.0). In this method, multiple line measurements following the length and curvature of a 3D isosurface representing the AVCA were recorded. This therefore offers an accurate 3D length, unlike multiplying the slice thickness by the number of slices in the z plane as done in histological studies. From micro-CT data it was possible to identify all major regions of the AVCA; the inferior nodal extension, penetrating bundle, and the non-branching and branching bundles, and differentiate them from the associated contractile myocardium and connective tissue (Chapter 6- Figures 6.7 and 6.8). The working myocardium, nodal tissue and connective tissue showed decreasing levels of attenuation respectively (differences quantified in Chapter 3). When viewed in longitudinal micro-CT slices and 3D segmentations, the AVCA can be seen to take origin in the expected location; between the coronary sinus and the membranous septum at the apex of the triangle of Koch. The AVCA can be traced anteriorly to where it penetrates the central fibrous body, it then runs around the circumference of the aortic valve annulus, and culminates as the branching bundle where the bundle branches are given off. In the results presented here the bundle branches have been excluded from analysis. In HF the AVCA was seen to significantly increase in both volume (60% increase: 0.90±0.16 mm^3 vs 1.44±0.28 mm^3) ($p=<0.05$), and 3D length (14% increase: 7134±404 μm vs 8141±327 μm) ($p=<0.05$) (figure 7.4). Figure 7.5 shows scaled 3D isosurfaces from representative control and HF samples, with their corresponding volume and 3D length. The increase in both volume and 3D length can be visually appreciated, however, the figure also highlights the variation of the morphological changes observed in HF (figure 7.5D,E,F).

7.3.1 Do global changes to the heart in heart failure affect atrioventricular conduction axis morphology?

Coefficient of determination (R^2) analysis was conducted to investigate the relationship between 3D length and volume (figure 7.6A). Analysis showed a strong correlation in control samples (R^2= 0.935), with increased 3D length proportional to an increase in volume (figure 7.6A). In HF samples a weak correlation was observed, it was apparent the volume increase was greater than the length increase, however change in morphology was varied; with some samples showing hypertrophy, some stretch and others a combined effect (figure 7.6A). To assess the effects of LV dilatation on AVCA length, 3D length was plotted against LV cavity volume (figure 7.6B). In control samples coefficient of determination (R^2) analysis showed there was a weak positive correlation between 3D length and LV cavity volume (figure 7.6B). In HF samples a stronger correlation was observed; increased 3D length was more closely correlated with increased LV cavity volume, and the data suggests the AVCA is stretched in HF samples (figure 7.6B). To determine whether the increase in volume and 3D length observed in HF was due to Hypertrophy of cells, increased deposition of extracellular matrix (fibrosis) or simply stretching of the conduction axis due to the drastic morphological changes to the surrounding working myocardium (see Chapter 8). Control and HF AVCA preparations (compacted node to left branching bundle) were processed for histology, and cell diameters were measured and means taken. Analysis showed no significant increase in cell size, however cell length was not investigated and a significant increase in total AVCA length was observed. Histology was conducted by Dr Theodora Nikolaidou, The University of Manchester.

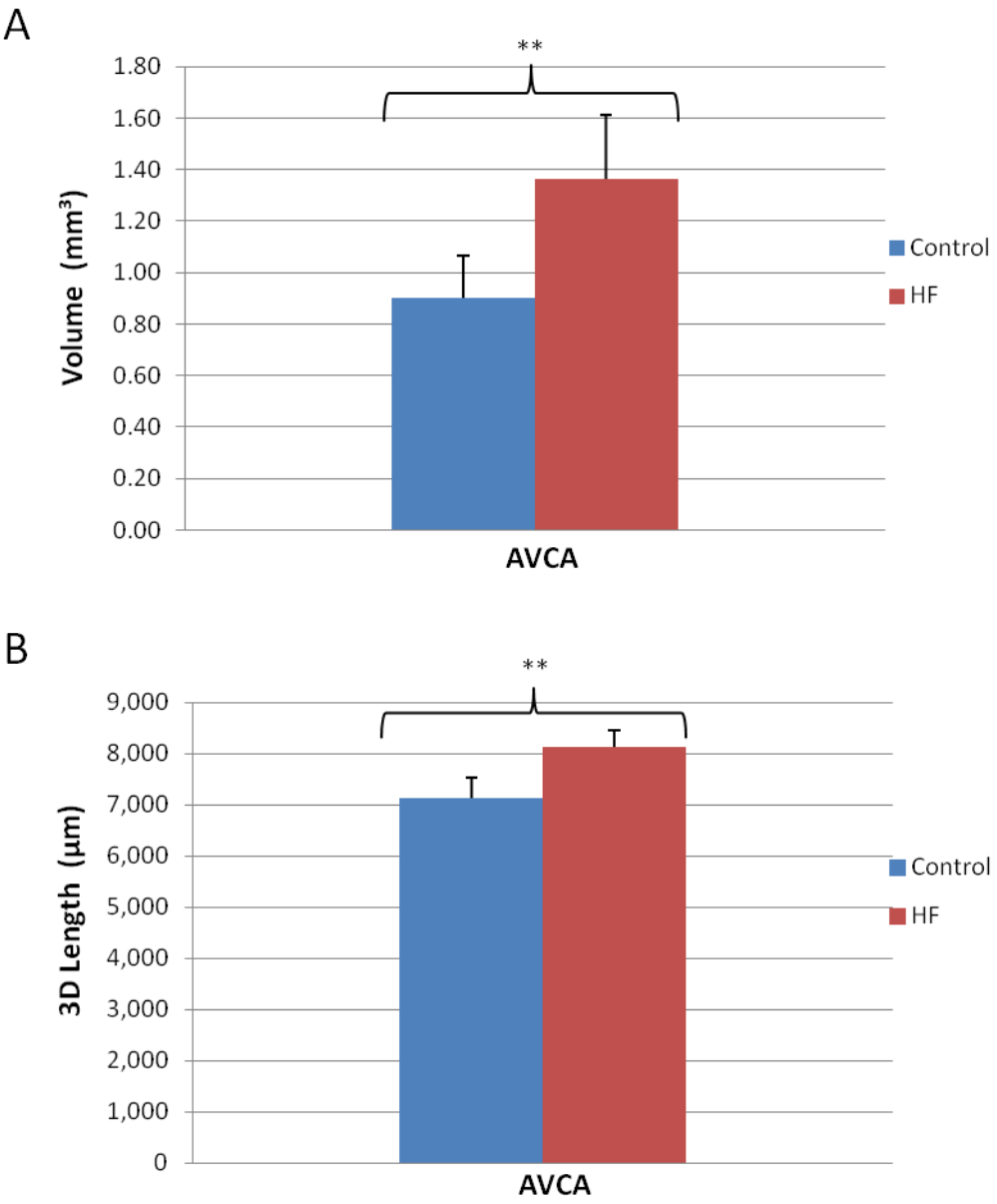

Figure 7.4 Tissue volume and 3D length of the atrioventricular conduction axis segmented from micro-CT data of control and heart failure samples. Mean tissue volume (A) and 3D length (B). (Control n=5, HF n= 5, **p=<0.05). Error bars indicate standard error of the mean (SEM).

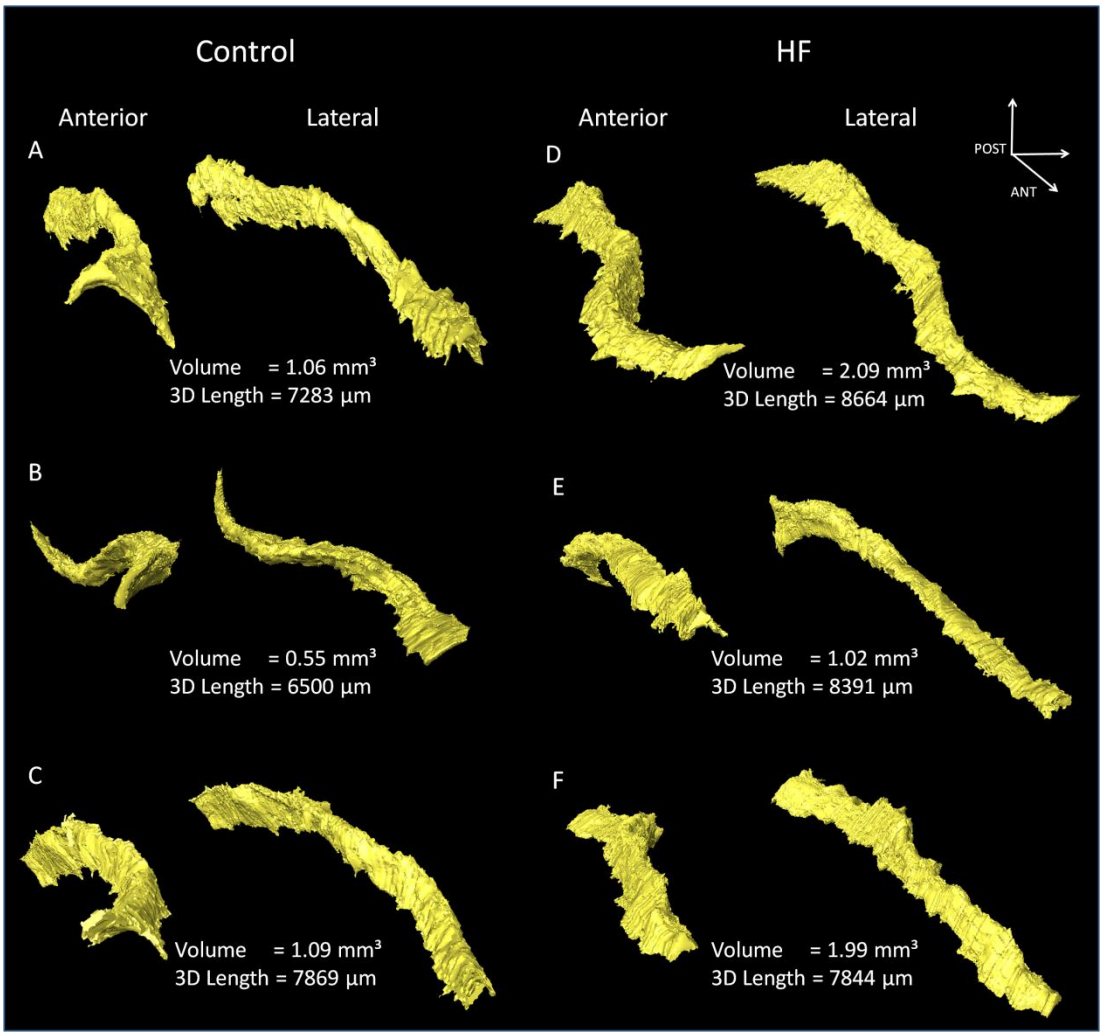

Figure 7.5 3D surfaces of the atrioventricular conduction axis in control and heart failure samples. Isosurfaces segmented from micro-CT data of control (A,B,C) and heart failure (D,E,F) samples. For each sample, anterior and right lateral views are shown, and tissue volumes and 3D lengths given.

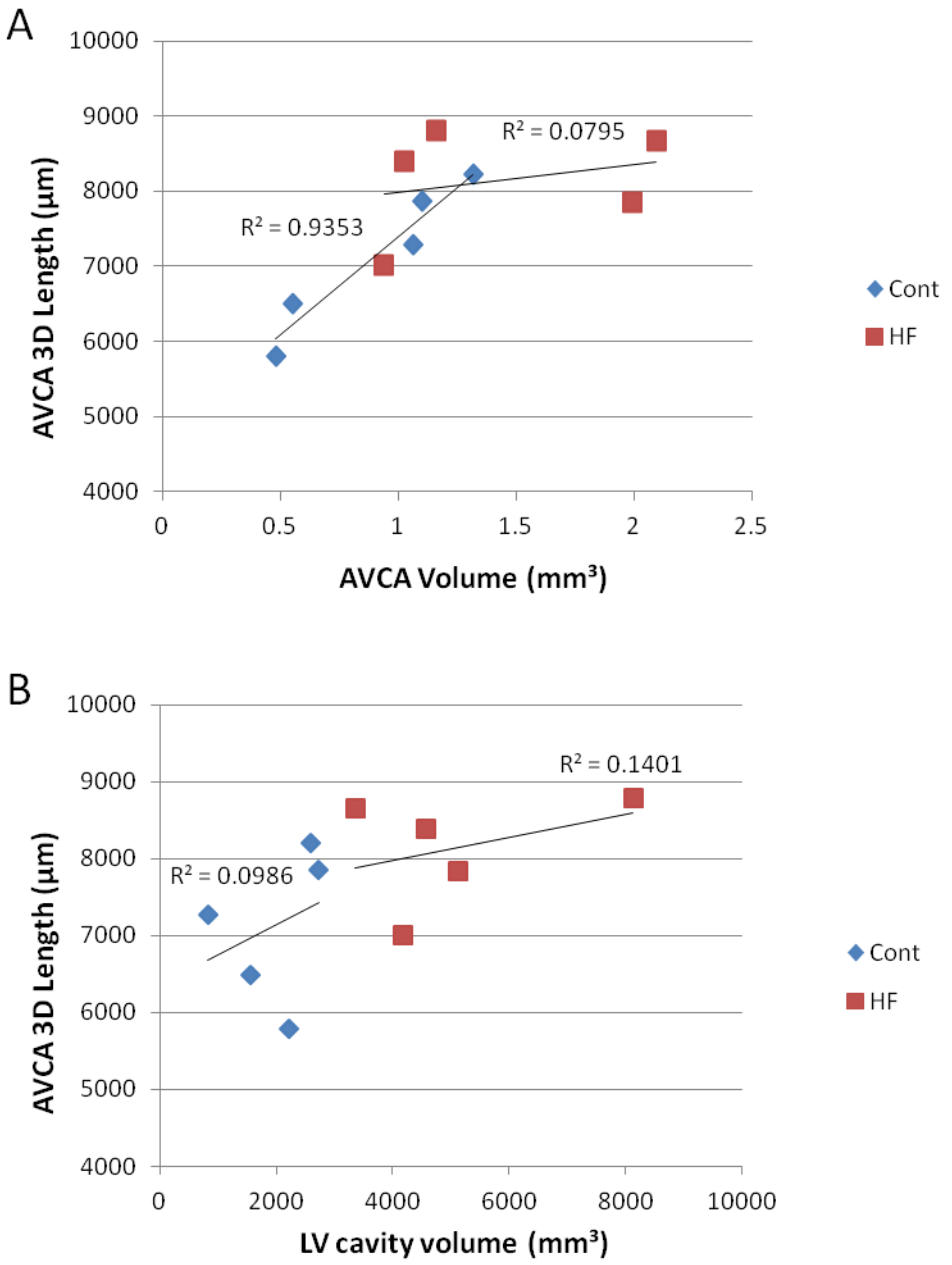

Figure 7.6 Coefficient of determination (R^2) analysis of the atrioventricular conduction axis in control and heart failure. Showing the morpholoigcal relationship between 3D length and tissue volume (A), and 3D length and left ventricular cavity volume (B). Cont-control, HF-heart failure, AVCA- atrioventricular conduction axis, LV-left ventricle.

7.4 Volumetric changes to the Purkinje network in heart failure

The Purkinje network is continuous with the AVCA, and forms a web-like network of conducting fibres within the ventricles responsible for the synchronisation of ventricular contraction. To assess morphological changes to the free running Purkinje network in control and HF animals, whole intact rabbit hearts were stained with I_2KI and micro-CT scanned in optimal conditions. From whole heart scans of perfusion fixed samples, the ventricles were reconstructed separately at 100% resolution. This allows fine details to be resolved in computationally manageable data sets. Ventricle data (control n= 6, HF n=6) was segmented from surrounding fat and fascia, and semi-automatic segmentation II (methods 2.4.2) was carried out to isolate the free running LV Purkinje network. Fibres were deemed free running up until they made contact with the endocardium; fibres running on the endocardial surface as digitations were therefore excluded from analysis. As described previously sub-endocardial Purkinje fibres were not identified in the micro-CT or whole mount immunohistochemical data of rabbit hearts (Chapter 6 and Stephenson et al., 2012, Atkinson et al., 2011). From the segmented data, volumes were then extracted (Amira 5.4.0). Figure 7.7 shows the mean Purkinje network volume was significantly increased in HF samples (85% increase: 7.29±0.49 mm^3 vs 13.5 ±3.60 mm^3) ($p=<0.05$). LV Purkinje fibre preparations from control and HF samples were processed for histology, and cell diameters were measured and means taken. Analysis showed a significant increase in cell diameter in HF samples (15.1± 0.7 µm vs 19.1± 0.9 µm) ($p=<0.05$). Histology was conducted by Dr Xue Cai, The University of Manchester.

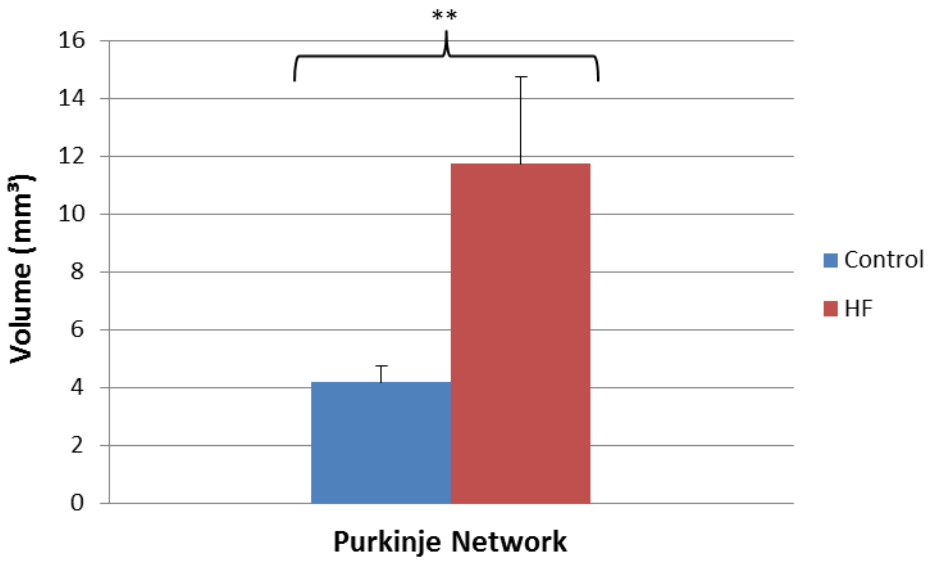

Figure 7.7 Mean tissue volume of the free running Purkinje network segmented from micro-CT data of control and heart failure samples. (Control n=5, HF n= 6, **p=<0.05). HF-heart failure. Error bars indicate standard error of the mean (SEM).

7.4.1 Detailed morphological changes to the Purkinje network in heart failure

To investigate the morphological changes accounting for the dramatic increase in total network volume, segmented data was analysed using 3D filament analysis (Amira 5.4.0) (methods 2.4.3). This technique allows quantification of volume, length, and width variations within a network, and the number of segments, nodes and branching points can also be extracted. In this method, segmented Purkinje networks were first binarized and then dilated two-fold (Image J 1.47a). Dilation was required as the algorithm for filament extraction could not accurately trace/detect the fine fibres in the high resolution micro-CT data. Without dilatation pre-analysis, the number of segments and nodes within a volume were unrealistic, often exceeding 2000. Also the tracing results for flattened regions of the thickest fibres appeared as meshes made up of numerous nodes and segments, rather than a single fibre (see explanatory figure 7.1). Filament analysis results were then qualitatively compared with 3D isosurfaces of the respective segmented Purkinje networks. Excellent correspondence was observed between the two sets of data.

Analysis showed the mean free running length of the Purkinje network was significantly increased in HF (221±24 mm vs 359±59 mm) (p=<0.05) (figure 7.8A).

The longest single segment within each network was recorded, and the means for each group calculated. The mean longest segment was seen to be ~2.5 mm longer in HF compared to control (5.78±0.43 mm vs 8.22±0.30 mm) (p=<0.001) (figure 7.8B). Coefficient of determination (R^2) analysis analysis was carried out to investigate the correlation between free running Purkinje length and LV cavity volume (figure 7.9). Analysis showed in HF there was a strong positive correlation between the two variables (R^2= 0.937), in contrast a weak correlation was observed in control samples (R^2=0.174) (figure 7.9). This Suggests dilatation of the LV is a contributing factor to the increased free running length of the Purknje network in HF.

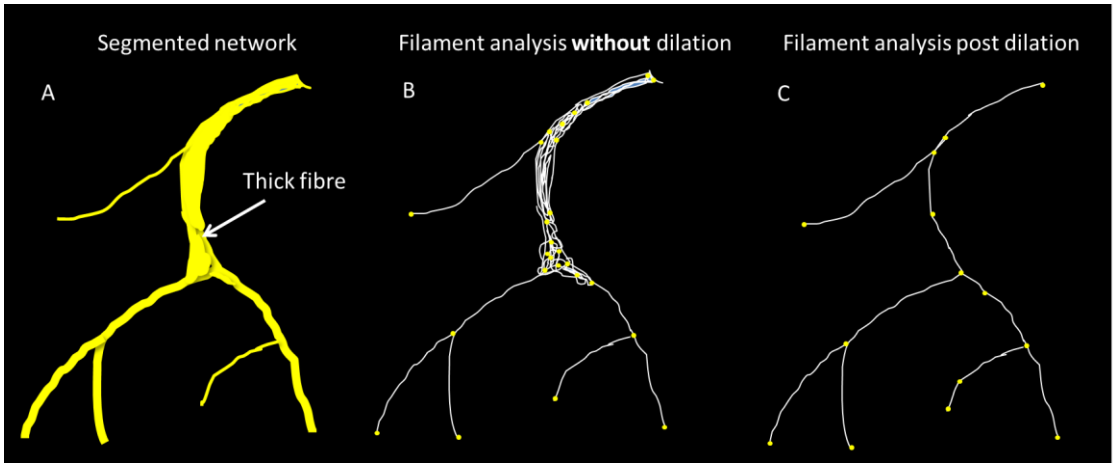

Explanatory figure 7.1 The importance of dilation in Purkinje fibre filament analysis. The segmented network (A), without dilatation of the segmented network filament analysis produced unrealistic results, with thick fibres appearing as meshes with many nodes and segments (B). Filament analysis post dilatation produced a more accurate representation of the network (C). white lines indicate segments, yellow dots indicate nodes.

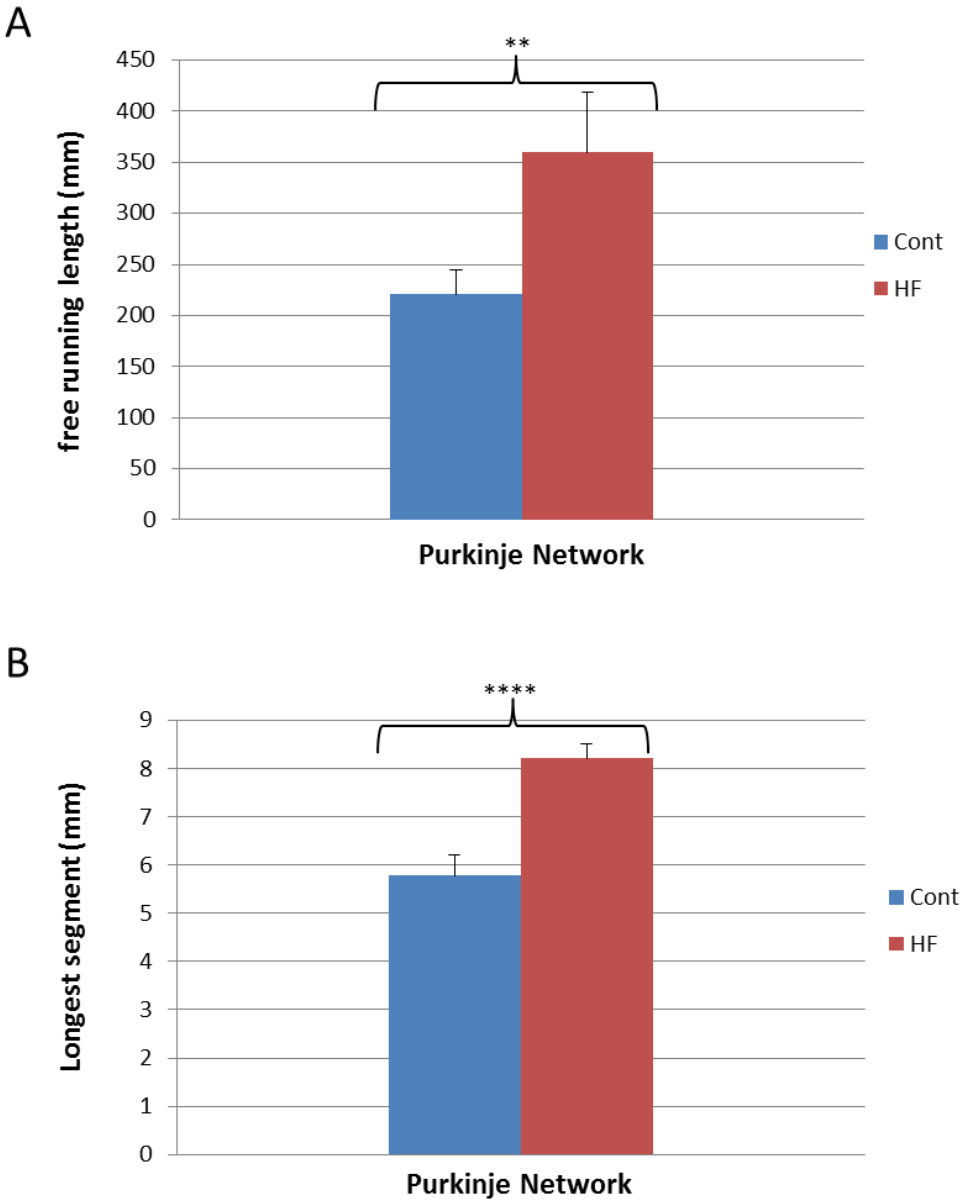

Figure 7.8 Free running length and mean longest segment of the free running Purkinje network segmented from micro-CT data of control and heart failure samples. Mean total free running length (A) and mean longest single segment (B). (Control n=6, HF n= 6, **p=<0.05, ****p=<0.001). Cont- control, HF-heart failure. Error bars indicate standard error of the mean (SEM).

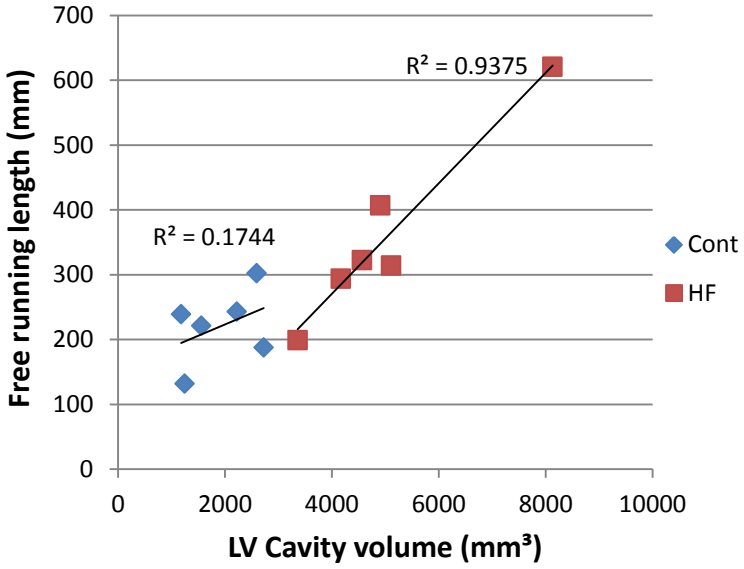

Figure 7.6 Coefficient of determination (R^2) analysis of the free running Purkinje network in control and heart failure. Showing the morpholoigcal relationship between free running length and left ventricular cavity volume. (Control n=6, HF n= 6). Cont- control, HF-heart failure, LV-left ventricle.

From 3D filament analysis, information on individual segment widths can be extracted, this data was used as a measure for hypertrophy of the Purkinje network. As dilatation was conducted in the transverse plane, the quantification of segment widths was down sampled by a factor of two. Although increased in HF, the mean fibre radius across the whole network was not significantly different when comparing the two groups (control- 30.02±4.55 μm, HF- 34.6±3.28 μm) (figure 7.10). There was no difference when the mean minimum fibre radius was analysed (control- 10.66±2.59 μm, HF- 10.12±2.55 μm). However, a significant increase in mean maximum fibre radius was observed in HF (31% increase- 49.89±4.07 μm vs 65.17±6.17 μm) (p=<0.05) (figure 7.10). These results suggest some, but not all Purkinje cells have undergone hypertrophy in HF. The radius measurements are consistent with previous histological studies of Purkinje fibre morphology (Stankovicová et al., 2003), which validates the method of analysis used here. The mean number of segments and nodes both increased in HF samples, however statistical significance was only seen for segment number (p=<0.05). The number of loops within the networks was calculated. A loop is best defined as a 'roundabout'

within the free running network which consists of multiple exit lanes. Loop size varied considerably within networks. The mean number of loops in a network was similar in both control (14.7 ±1.8) and HF (16.0 ±3.3), however the size and circumference of the loops was increased in HF (Figure 7.11). Figure 7.11 shows scaled 3D isosurfaces of Purkinje networks from representative control and HF samples, their corresponding volumes and free running lengths are given. The 3D isosurfaces allow visualisation of the aforementioned morphological changes to the LV Purkinje network in HF. The increase in total network volume and regional hypertrophy is clear, and the correlation between increased LV dilatation and increased free running length and increased loop size can be appreciated. Figure 7.11 also shows the variation of the morphological changes in HF, and the intra-species variation of the Purkinje network (as previously described in chapter 6 and Stephenson et al., 2012).

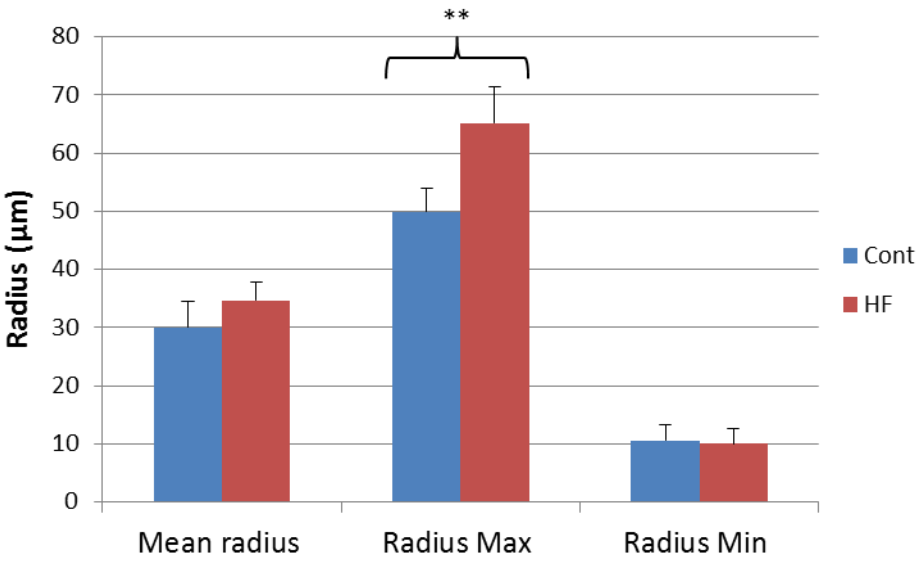

Figure 7.10 Mean, minimum and maximum segment radius in the free running Purkinje network segmented from micro-CT data of control and heart failure samples. (Control n=6, HF n= 6, **p=<0.05). Cont- control, HF-heart failure. Error bars indicate standard error of the mean (SEM).

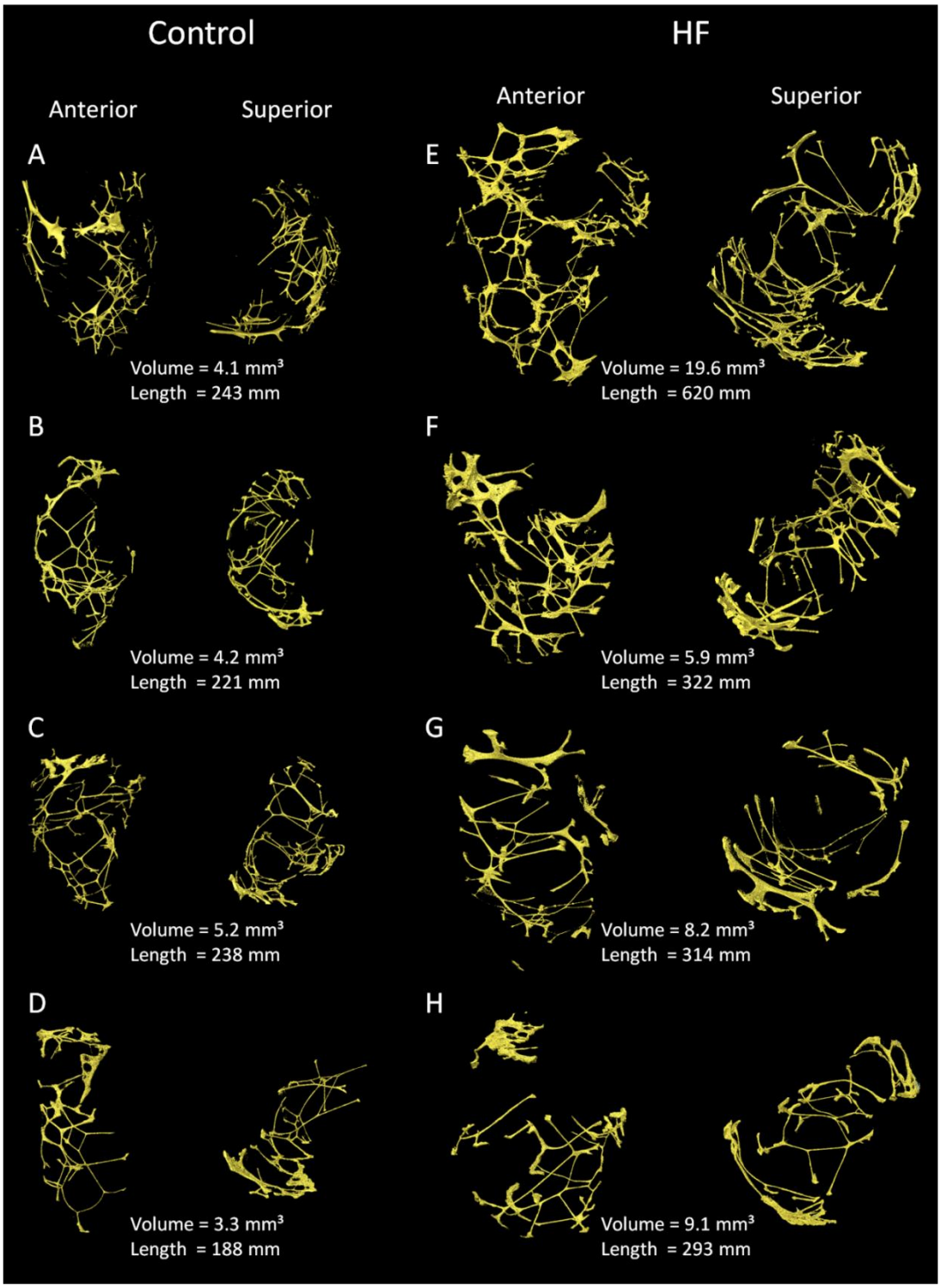

Figure 7.11 3D surfaces of the left ventricular free running Purkinje network in control and heart failure samples. Scaled 3D isosurfaces segmented from micro-CT data of control (A,B,C,D) and heart failure (E,F,G,H) samples. For each sample, anterior and superior views are shown, and tissue volumes and total network lengths given.

7.5 Discussion

Previously we have used contrast enhanced micro-CT to non-invasively image the major regions of the CCS (Stephenson et al., 2012 and Chapter 6). Here using an experimental model of HF developed in rabbit, the effects of both volume and pressure overload on the morphology of the CCS were investigated. Contrast enhanced micro-CT was used to image whole, perfusion fixed hearts *ex vivo*. Subsequent image and histological analyses of the SAN, AVCA and Purkinje network were used to investigate morphological changes in HF. Analysis showed all major regions of the CCS underwent morphological changes in HF, the observed changes and their possible effects on function are discussed below.

7.5.1 The advantages of Micro-CT for analysis of the CSS

Comparison with Traditional techniques

Much of our knowledge regarding the CCS and its responses to disease come from histological, immunohistochemical and quantitative PCR (Atkinson et al., 2011, Chandler et al., 2011, Li et al., 2008). Such studies have transformed our understanding of the anatomy and pathophysiology of the CCS (Boyett, 2009), however our knowledge of 3D morphological changes in disease is limited. Although 3D reconstruction have been made of the SAN and AVN in healthy hearts from serial sections, their resolution is poor, particularly in the z-plane (~100-300 μm), and results from concatenation of sections into a 3D volume are subject to error. In contrast, Micro-CT data is made up fully isometric voxels which are automatically aligned. In comparison with micro-CT, histological analysis of the CCS is very time consuming and analysis of the free running Purkinje nework is almost impossible. Processing, sectioning, staining, segmentation and concatenation of a single preparation can take several weeks using histology. In contrast, using micro-CT a whole heart can be scanned at high resolution (20μm) in ~20 minutes, then segmented, presented in 3D and quantified in hours rather than weeks. This facilitates the analysis of a sample size of adequate number for statistical analysis. We were the first to non-invasively image the major regions of the CCS in whole

hearts (Stephenson et al., 2012), and to our knowledge are the first to analyse the 3D morphology of the major regions of the CSS in HF.

At present, micro-CT scans of whole hearts do not allow sufficient resolution to resolve single cells (as resolution is proportionate to sample size), therefore measurements, for example cell diameter, cannot be made. However we have shown single cell resolution is attainable in muscle preparations (Jeffery et al., 2011), and have shown previously scanned samples can be subsequently processed for standard histology (Stephenson et al., 2012).

Inferences regarding CCS function and dysfunction are commonly made from immunohistochemisty and quantitative PCR analysis of connexin and ion channel expression (Dobrzynski et al., 2013). Although high resolution morphological data is obtained using micro-CT, in the method presented here it is not possible to detect changes in specific protein expression. However, we have worked on the development of TCE micro-CT for imaging the heart (presented and discussed in Chapter 6), a technique which has the potential to provide information on specific protein expression across the whole heart in 3D.

High fidelity morphological data

The I_2KI contrast agent is differentially taken up by different tissue types, this allows nodal tissue to be distinguished from the surrounding myocardium and connective tissue with contrast and spatial resolutions superior (Stephenson et al., 2012) to rival imaging techniques (discussed in Chapters 4 and 6). Furthermore perfusion fixation allows the appreciation of cardiac anatomy with the heart in a naturally inflated state, not confounded by folding of structures or accumulation of blood (Chapter 3.5) (Jarvis and Stephenson, 2013). This makes micro-CT data ideal for integration into mathematical models of the heart. Although experimental data exists on the remodelling of the CCS in HF at a cellular and protein level, little is known on how the 3D morphology of these specialised tissues is affected. This is well illustrated by current mathematical models of the cardiac function; multi cell models of electrical propagation offer highly detailed functional modelling, however model fidelity is confounded by low resolution and often inaccurate morphological data (Aslanidi et al., 2009, Aslanidi et al., 2011, Butters et al., 2010, Inada et al., 2009). This is due to the fact that until recently (Stephenson et al., 2012), data regarding the true 3D

anatomy of the CCS and its relationships with the surrounding myocardium was poor. Current models of cardiac function often integrate poor morphological data derived from histology (Aslanidi et al., 2009), and in some cases from multi species (Aslanidi et al., 2011, Butters et al., 2010). This highlights the advantage of the current study in which data from whole hearts is acquired. Furthermore, with the path and velocity of the cardiac impulse strongly dictated by fibre orientation, the ability to extract 3D fibre orientation in the CCS from micro-CT data promises to further improve the fidelity of cardiac modelling. Fibre orientation in regions of the CCS has been described previously (Chandler et al., 2011, Dobrzynski et al., 2005, Ambrosi et al., 2012, Ambrosi et al., 2009). Although it can be argue that resolution is finer in a 2D plane using optical coherence tomography (5-15 μm), data is only presented in 2D, z-plane depth and resolution is poor, and only small sample preparation can be analysed.

7.5.2 Morphological changes to the CCS in heart failure

The CCS has been confirmed as plastic (Boyett, 2009), and has been shown to be more sensitive to change than myocardium (Chandler et al., 2009). The data presented in this chapter provides novel insight into morphological changes across all major regions of the CCS in HF. Analysis showed all major regions of the CCS (SAN, AVN and Purkinje network) underwent morphological changes in HF.

Impulse propagation across the heart depends on; the physiology of individual cardiomyocytes, impulse transmission between adjacent cells, and the 3D arrangement of cells (Smaill et al., 2013). Perturbation in the function of any of these factors can give rise to rhythm disturbances and reentry activation (Smaill et al., 2013). Here we will discuss the morphological changes to the CCS in HF and how they may affect function.

The sinoatrial node

Previous analysis of the SAN in rabbit, by us and others, confirmed that it is not so much a localised compact node, but an extended thin layer of conducting cells, with a smear like appearance (Dobrzynski et al., 2005, Stephenson et al., 2012, Chapter

6.3). The volume of the SAN was increased in HF, and this corresponded with an increase in cell diameter. This hypertrophic response was accompanied by dilatation of the SAN; a significant increase in surface area was observed. In HF fibres had an increased verticality in the superior and inferior regions ($p=<0.05$), and there appeared to be a trend towards fibre orientation been more ordered in HF, but this observation did not reach conventional significance in the group size available. Analysis revealed very complex and regionally variable fibre orientation in the SAN consistent with other studies (Chandler et al., 2011, Dobrzynski et al., 2005, Ambrosi et al., 2012). However, some fibre patterns were repeated across all samples; the lateral border which is adjacent to the crista terminalis was predominantly made up of vertically running fibres. Superiorly the SAN had fibres running into and following the curvature of the SVC, and radiating from central regions fibres ran transversely towards the IAS. The reduced fibre disarray and increased verticality observed in HF may be attributed to longitudinal stretching of the fibres caused by the considerable global dilatation of the atria (see Chapter 8.3). Such a phenomenon has been described in the myofibrils of the Purkinje fibres which have undergone mechanical stretch (Thornell et al., 1976).

Simulations of electrical activation demonstrate that ordered alignment of myocytes plays an important role in normal activation spread (Smaill et al., 2013), and that conduction velocity (CV) is strongly dependent on fibre orientation (Spach and Kootsey, 1983). The more ordered and vertically orientated fibres in the SAN in HF would suggest CV will be increased, however there is a suggestion that changes in ion channel remodelling compensates for these structural changes to slow propagation (Verkerk et al., 2003, Zicha et al., 2005). Models have shown that increased complexity of fibre orientation can increase the risk of arrhythmias (Zhao et al., 2012), thus the SAN maybe have a 'safer' structural phenotype in HF. However, tissue that has undergone dilatation is more prone to the generation of rotors associated with arrhythmogenic activity (Yamazaki et al., 2012). Furthermore, hypertrophy is also associated with conduction abnormalities in clinical practice (Mercadier, 2007) .

The atrioventricular conduction axis

The general anatomy of the AVCA is well described in the literature (Li et al., 2008, Tawara, 2000), and histological studies have been conducted to investigate changes to its morphology in disease at a cellular level (Okada and Fukuda, 1981, Harris et al., 2012). Using micro-CT it is possible to identify all major regions of the AVCA; the inferior nodal extension, penetrating bundle, and non-branching and branching bundles (Stephenson et al., 2012). Tissue volume, cell size and 3D length were investigated. The methodology used here for measuring 3D length of micro-CT data offers increased accuracy over the method adopted in histology, in which the slice thickness is multiplied by slice number and thus the curvature of the AVCA is not considered.

The AVCA was seen to significantly increase in both volume and 3D length in HF. Histological analysis suggested cell diameter was not increased however cell length was not investigated. Changes in cell size were greater in other regions of the CCS, it is postulated that stress, shown to induce hypertrophy in myocytes (Blaauw et al., 2010, Ruwhof and van der Laarse, 2000), is reduced in the region of the AVCA because of its association with the rigid fibrous skeleton. Coefficient of determination (R^2) analysis conducted here suggests varying morphological changes occur in HF, including hypertrophy, stretch and a combination of both. The observed increase in 3D length did not cause an increase in volume, but 3D length was more closely correlated with LV cavity volume, suggesting the AVCA is stretched in HF. It is expected stretch reduces cell coupling which can cause retrograde propagation (Rohr et al., 1998) and slow conduction which can support re-entry (Shaw and Rudy, 1997). In addition it has been suggested increased size, particularly in the region of the INE, is associated with the increased prevalence of AVN re-entry tachycardia with age (Ko et al., 1992, Van Hare, 2008).

Conduction in all regions of the heart is determined by the balance between current source and passive current load, known as source-sink matching (Smaill et al., 2013). Depolarised cells act as the source of current, which diffuses into surrounding polarised tissues- the sink (Nikolaidou et al., 2012). Abrupt changes in wall thickness and fibre orientation have been shown to contribute to source sink mismatch (Zhao et al., 2012, Hocini et al., 2002, Klos et al., 2008). In addition abrupt tissue expansions

result in a change in wave front curvature (Auerbach et al., 2011), conduction slowing (Cabo et al., 1994) and even conduction block (Auerbach et al., 2011). Reverse source-sink occurs at the proximal region of the AVCA; impulses from the myocardium (source) need to be funnelled into the narrow entrances to the AVCA (sink) (Nikolaidou et al., 2012). In this region safety is increased by the presence of a transitional zone of myocytes, which allows a smoother transition from the fast conducting myocardium into the slow conducting AVCA. This transitional zone is not present at the junction of the AVCA and Purkinje system; where the AVCA gives branches to the fine right and left bundle branches. Therefore it can be anticipated that the increased vulnerability to ventricular tachycardias (VT) described previously in this HF model (Pogwizd, 1995), may be associated with hypertrophy and stretch of the AVCA, acting to increase reverse source-sink mismatch and electrical dysfunction at the distal aspect of the AVCA.

The Purkinje fibre network

The free running aspect of the Purkinje network has previously been understated (Ansari et al., 1999, Drake et al., 2005, Atkinson et al., 2011), this is likely due to the destructive nature of traditional techniques (discussed above). Micro-CT has the ability to resolve these fine structures in 3D, allowing for detailed analysis of how they respond to HF. The mean Purkinje network volume was significantly increased in HF samples (85%). This was supported by histological analysis of cell diameters, which also showed a significant increase in HF (26%). The variation in the results of the two methods is likely due to the difficulty in selecting a representative fibre in histological analysis. However it also highlights the possibility that although hypertrophy is evident, the major increase in volume may be due to an increased deposition of extracellular matrix (fibrosis). We have shown TCE micro-CT allows differentiation of Purkinje cells from their surrounding connective tissue sheaths (see Chapter 6), this technique could therefore be employed to elucidate both the hypertrophic and fibrotic response of the Purkinje fibres to HF.

Quantification of control samples using 3D filament analysis showed a mean fibre radius of 30 μm, this is consistent with previous histological studies of Purkinje fibre morphology (Stankovicová et al., 2003) and thus validates the technique. In HF the mean fibre radius across the whole network was increased, but did not reach

statistical significance. However a significant increase in mean maximum radius was observed in HF. These results suggest some, but not all Purkinje cells, have undergone hypertrophy in HF. The mean free running length of the Purkinje network was significantly increased, and the mean longest segment was ~2.5 mm longer in HF compared to control. Furthermore, in HF there was a strong correlation between free running length and LV cavity volume, suggesting dilatation of the LV is a contributing factor to the increased free running length of the Purkinje network. It is generally accepted that cardiomyocytes cannot divide, at least in the short term (Bergmann et al., 2009), therefore we hypothesise that free ruuning fibres are stretched and fibres normally running on the surface of the endocardium are stretched/pulled away from the wall to become free running. These longer and stretched free running networks will have slower CVs due to increased conduction distance and reduced cell coupling. Together these factors will increase the likelihood of slow conduction, re-entry, and conduction block in HF samples (Smaill et al., 2013).

We have shown previously the Purkinje network in rabbit is a very complex web-like structure with many branches, connections and loops (Stephenson et al., 2012). It is anticipated the anatomy of the free running Purkinje network could act as a morphological substrate for re-entry, and changes in HF seem to only extenuate this problem. However, modelling of electrical propagation through cultures show repetitive tissue branching may contribute to slow stable conduction (Kucera et al., 1998, Kucera and Rudy, 2001). This increased safety factor is thought to occur in two ways; 1) the multiple branches act as ‘sinks’ for the approaching wave of propagation; 2) once excited the branching provides a depolarisation current that supports downstream activation. However such studies did not consider loops in their models; loops in the Purkinje network are best described as roundabouts within the networks with multiple exits. These loops were numerous in both groups. In HF samples overall loop size was increased and the mean number of loops within the LV network was increased. It is expected if modelled these loops, especially in HF, would increase the chance of early depolarisation, conduction block and reduce safety factor (Zhao et al., 2009).

7.5.3 The vulnerability of heart failure samples to early after depolarisation (EAD)

EADs trigger premature activation of cells, and are caused by reactivation of L-type calcium channels during APD prolongation (Smaill et al., 2013). APD has been shown to be prolonged in our model of HF (Jones et al unpublished data), but the structural changes to the CSS in HF also provide potential support to EADs. How the influx of calcium is synchronised across large areas to allow for sufficient current to trigger EADs has been studied by Xie et al (Xie et al., 2010). It was found that 2D structures were more prone to EADs than complex 3D myocardium. This is because the number of cells required to reach threshold was about 100 times lower in 2D structures. Therefore, the probability that unstable calcium handling will successfully reach threshold is greater in quasi-2D structures (Nikolaidou et al., 2012, Smaill et al., 2013) such as the SAN, AVN and Purkinje network. Reduced cell coupling as a result of dilatation and stretching, and marked spatial variation in the 3D arrangement of cells will further reduce these figures (Smaill et al., 2013, Xie et al., 2010), and will prolong APD, making EADs even more probable in these structures in HF.

7.5.4 The other conducting tissues

The major regions of the CCS develop from the primary myocardium. Recently other vestiges of primary myocardium consisting of nodal-like cells have been discovered. These include the retroaortic node, right and left atrioventricular rings and the dead end tract (Yanni et al., 2009a). Although their role in normal conduction is yet to be elucidated, it is believed they play a role in cardiac dysfunction and arrhythmogenesis (Boyett, 2009, Kistler et al., 2006). These structures are not investigated here, but it is expected that such regions would undergo similar morphological changes as the other regions of the CCS in HF, and would also play a role in the pathophysiologies associated with HF.

7.5.5 Variation of the CSS in health and disease

From analysis conducted here it is clear that the morphology of the CCS is highly variable in both health and disease. Interspecies variation is well documented

(Dobrzynski et al., 2013, Nikolaidou et al., 2012), but intraspecies variation is less well known, especially in rabbit. This is due to the inability to distinguish the CCS using gross dissection, and the difficulty of investigating a representative number of samples histologically. We have previously shown the large degree of variation in control Purkinje fibre networks (Stephenson et al., 2012), with volume, branching, and free running length highly variable. Variation was considerably increased in HF compared to control, with all regions of the CCS showing increased coefficient of variance for measures of tissue volume, surface area, and length. Volume renderings revealed the SAN node as a heterogeneous structure, with highly variable interdigitations into the atrial myocardium. Analysis revealed a very complex and regionally variable fibre orientation exists in the SAN, and although some common patterns exist, fibre orientation was highly variable between samples. The AVN morphology was also highly variable; a range of 3D lengths and volumes were recorded, and the two measurements were weakly correlated, especially in HF. 3D Visualisation of the AVN revealed considerable variation in the curvature of the conduction axis as it passes through the central fibrous body, round the curvature of the aortic annulus, culminating anteriorly as the branching bundle. On some occasions the AVN appeared as an elongated 's', and on others seemed to run almost straight. Such variation needs to be considered when producing mathematical models of cardiac function, and also in a clinical setting, for example in surgical planning.

7.5.6 Clinical implications

This data has many clinical implications; the novel findings regarding 3D morphology will improve the knowledge and understanding of structural and functional changes to the CSS in HF, which in turn could aid drug discovery and the accuracy of surgical procedures. The observed intra species variation highlights the need for patient specific interventions, and shows the importance of developing a technique for non-invasive imaging of the CCS *in vivo*. The application of the technique presented here could be used to analyse other disease states, and also non-diseased states such as the electrophysiology of trained hearts (Boyett, 2009). As discussed previously high resolution 3D morphological data will also improve the fidelity of functional mathematical models of the heart (Chapter 4,5,6). Furthermore

combination of the data presented here (morphological and molecular) will allow highly accurate models of HF to be developed.

7.6 Summary

Using an experimental model of HF developed in rabbit, the combined effects of both volume and pressure overload on the morphology of the CCS were investigated. Contrast enhanced micro-CT was employed to image whole hearts *ex vivo*, and subsequent image and histological analysis of the SAN, AVN and Purkinje network was used to investigate morphological changes in HF.

Here we present a method for 3D morphological analysis of the CCS, which has clear advantages over traditional methods. Contrast enhanced micro-CT is a fast, non-invasive technique, which produces automatically aligned tomographic data sets with isometric resolutions of ~5 μm attainable. This data allowed appreciation of the true 3D morphology of the CSS in HF, along with highly accurate quantification. To our knowledge this is the first time such analysis of the CCS has been conducted in experimental groups of adequate size for statistical analysis.

All major regions of the CCS underwent morphological changes in HF. The SAN showed an increase in volume and surface area, confirming dilatation and hypertrophy in this model of HF. The SAN was shown to be a complex and heterogeneous structure. Intricate and disordered fibre orientation was observed within the node, although some regional similarities between samples were evident. The volume and 3D length of the AV conduction axis was increased in HF. However, varying morphological changes were observed, including hypertrophy, stretch and a combination of both. Dramatic changes to the free running Purkinje network were evident in HF, with changes strongly correlated to global changes in ventricular morphology (dilatation). Increase in total network volume and regional thickening was observed, along with an increase in total free running length. Suggesting both mechanical stress and tissue hypertrophy are contributing to the morphological changes seen in HF. Although dramatic changes to the CCS were observed clear intra species variation was apparent in all regions of CCS.

The data presented in this chapter provides novel insight into morphological changes across the major regions of the CCS in HF, and provides insight into possible causes for the vunerabilty of failing hearts to electrical dysfunction.

CHAPTER 8

The Effects of Volume and Pressure overload on the Morphology and Function of the Rabbit Heart

8.1 Introduction

Heart failure (HF) is a syndrome characterised by the heart's inability to pump sufficient blood to meet the metabolic requirements of the body. HF and the associated morphological and functional abnormalities are a major contributor to morbidity and mortality in the western world. HF is often categorised by how fast symptoms present themselves (chronic or acute), and the impact abnormalities have on the heart (volume or pressure overload). The morphological and functional effects of volume or pressure overload on the ventricles are well documented in the scientific literature. However, the effects that a combination of both volume and pressure overload have on the whole heart (atria and ventricles) is not so well understood. The majority of morphological studies focus on the ventricles, with the atria often overlooked. This is in part due to the atria's morphological heterogeneity, structural instability, and the difficulty to maintain them in a naturally inflated state for examination. Gross structural modifications and alterations in gene expression in HF are well known, but how these changes affect fibre orientation in 3D is unclear. Existing data is often from small regions and based on serial 2D sections or low resolution imaging. The development of a high resolution non-invasive imaging technique, with the ability to improve current knowledge, and provide new insight into morphological and functional changes to the heart in disease, would be of considerable value. Contrast enhanced micro-CT is a non-destructive imaging technique that can resolve fine structures within soft tissue. We have recently shown the ability of micro-CT to provide high resolution images of cardiac tissue, and to allow visualisation of 3D fibre orientation, which in turn directly influences cardiac contraction and therefore pump function. Here using *in vivo* and *ex vivo* imaging, we investigate the global and regional effects of volume and pressure overload on the rabbit heart. We investigate the morphological and functional changes across the whole heart (atria and ventricles), and assess the validity of micro-CT to investigate cardiac morphology *ex vivo.* This chapter is made up of 3 sections: section 1 reviews the development of our experimental HF model using longitudinal *in vivo* echocardiography (performed in collaboration with Dr Caroline Jones). Section 2 investigates changes in cardiac morphology *ex vivo* using contrast enhanced micro-CT. Section 3 assesses the effects of HF on fibre orientation within the ventricles,

with emphasis placed on areas of dilatation (primarily in collaboration with Dr Jichao Zhao).

Some of the work in the following chapter regarding atrial morphology has been published as:

Inherent Vulnerability of Atrial Appendages to Atrial Fibrillation. Jichao Zhao, Robert S. Stephenson, George Hart, Mark R. Boyett, Jonathan C. Jarvis, Henggui Zhang, Bruce H. Smaill. Heart Rhythm Society conference proceedings, Denver, CO, USA, 2013

8.2 Morphological and functional changes in experimental heart failure revealed by longitudinal *in vivo* echocardiography

Experimental HF was induced in adult rabbits by the means of aortic valve disruption (figure 8.1C,D) and subsequent aortic banding (3 weeks later). This enabled us to investigate morphological and functional changes in hearts exposed to both volume and pressure overload (methods 2.2). *In vivo* echocardiography was performed weekly (for ~12 weeks) to investigate longitudinal functional and morphological changes in HF (n=24) and sham control (n=21) subjects. Transthoracic echocardiography was performed, and 2D images were obtained in the parasternal long axis view. The M mode cursor was placed at the tip of the mitral valve leaflets, perpendicular to the interventricular septum (IVS). Images were stored and measurements of the left ventricular internal dimension (LVID), IVS thickness, and left ventricular posterior wall thickness (LVPW) were made in both systole (s) and diastole (d) (figure 8.1A,B). Each measurement was recorded on 3 separate cardiac cycles and the mean taken. Left ventricular fractional shortening (FS) and ejection fraction (EF) were then calculated from these measurements. Colour Doppler was used to assess aortic and mitral valve regurgitation (figure 8.1E). Surgery was performed by Dr Antonio Corno, and Dr Xue Cai; echocardiography was performed by Dr Caroline Jones.

Statistical analysis was performed in collaboration with Professor Stanley Salmons and Professor Jonathan Jarvis using T-tests and regression analysis (graphical

presentations by Professor Salmons). All morphological and functional measurements from baseline (pre-intervention) to pre-termination (~12 weeks post intervention) were included in the analysis. For control animals, no loss of function was observed over the time course. Only LVIDs and LVIDd showed a significant increase ($p=<0.05$), however these changes did resemble natural growth, with a ~0.5mm increase in both systole and diastole observed (see table 8.1). Comparing pre-termination measurements for both groups revealed LVID was increased in HF both in systole (80% increase: 9.08±0.37 mm vs 17.23±1.23 mm) and diastole (49% increase: 15.44±0.47 mm vs 22.94±0.96 mm) ($p=<0.0001$) (table 8.2). The high LVIDs observed in HF was reflected in a ~50% reduction in FS compared to control (41.28±1.23% vs 25.33±2.9%) ($p=<0.0001$). All wall measurements were increased in HF (except LVPWs), although IVSd was the only wall measurement to significantly increase ($p=<0.001$). Figure 8.1A,B shows an example of the LVIDd increase from baseline (panel A) to pre-termination (panel B) (~12 weeks post intervention) measured in M mode, LVIDd in this example increases from 15.6 mm to 22.5 mm. This morphological change is characteristic of volume overload brought about by regurgitation at the aortic valve (artificially induced here by surgical intervention). An example of a control (healthy) and surgically destructed aortic valve can be seen in figure 8.1C and D respectively. The technique damages and creates perforations in the valve leaflets preventing effective occlusion, thus simulating a ‘leaky’ valve. Figure 8.1E shows a colour Doppler image confirming the loss of aortic valve function post intervention, red indicates regurgitated blood.

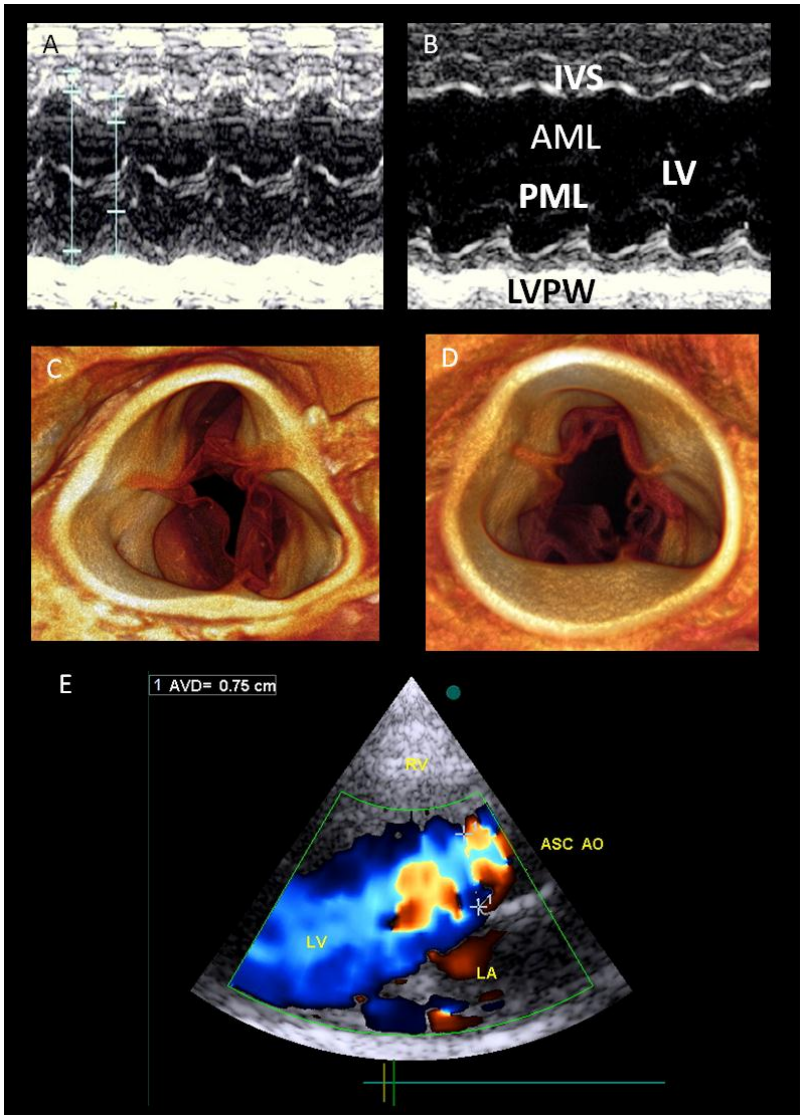

Figure 8.1 Echocardiography, micro-CT and colour doppler to asses model of experimental heart failure. *In vivo* echocardiography was performed weekly (for ~12 weeks) to investigate longitudinal functional and morphological changes in HF (n=24) and sham control (n=21) rabbits. A and B shows parasternal long axis view of a HF animal pre-intervention and pre-termination respectively. Volume renderings (micro-CT data) of the Aortic valve from sham control (C) and HF (surgical aortic valve disruption) (D) rabbits. Colour Doppler was used to assess aortic and mitral valve regurgitation (red indicates regurgitation) (E). AML- anterior mitral leaflet, AVD- aortic valve distance, IVS- interventricular septum, LA- left atrium, LV- left ventricle, LVPW- left ventricular posterior wall, PML- posterior mitral leaflet, RV- right ventricle.

Table 8.1 - Baseline and pre-termination echocardiographic parameters in sham and heart failure (HF) groups

	Sham animals n= 21		P value	HF animals n= 24		P value
	Baseline	Pre-termination		Baseline	Pre-termination	
IVSd (mm)	2.57 ± 0.21	2.68 ± 0.16	NS	2.51 ± 0.13	3.19 ± 0.24	0.000
LVIDd (mm)	14.89 ± 0.46	15.44 ± 0.47	0.024	14.85 ± 0.36	22.94 ± 0.96	0.000
LVPWd (mm)	2.62 ± 0.22	2.57 ± 0.17	NS	2.48 ± 0.14	2.73 ± 0.25	0.05
IVSs (mm)	3.24 ± 0.25	3.32 ± 0.28	NS	3.03 ± 0.18	3.65 ± 0.30	0.000
LVIDs (mm)	8.64 ± 0.39	9.08 ± 0.37	0.013	8.53 ± 0.29	17.23 ± 1.23	0.000
LVPWs (mm)	4.14 ± 0.28	4.24 ± 0.23	NS	4.02 ± 0.3	3.79 ± 0.38	0.334
FS (%)	42.08 ± 1.21	41.28 ± 1.23	NS	42.68 ± 0.91	25.33 ± 2.9	0.000

Values represent mean and 95% confidence intervals. (Control n=21, HF n= 24). IVSd and IVSs- interventricular septum in diastole and systole, LVIDd and LVIDs- left ventricular internal dimension in diastole and systole, LVPWd and LVPWs- left ventricular posterior wall thickness in diastole and systole, FS- fractional shortening.

Table 8.2- Pre-termination echocardiographic parameters in sham and heart failure (HF) groups

	Sham animals n= 21	HF animals n= 24	P value
IVSd (mm)	2.68 ± 0.16	3.19 ± 0.24	0.001
LVIDd (mm)	15.44 ± 0.47	22.94 ± 0.96	0.000
LVPWd (mm)	2.57 ± 0.17	2.73 ± 0.25	NS
IVSs (mm)	3.32 ± 0.28	3.65 ± 0.30	NS
LVIDs (mm)	9.08 ± 0.37	17.23 ± 1.23	0.000
LVPWs (mm)	4.24 ± 0.23	3.79 ± 0.38	NS
FS (%)	41.28 ± 1.23	25.33 ± 2.9	0.000
EF (%)	79.72 ± 0.60	57.10 ± 2.27	0.000

Values represent mean and 95% confidence intervals. (Control n=21, HF n= 24). IVSd and IVSs- interventricular septum in diastole and systole, LVIDd and LVIDs- left ventricular internal dimension in diastole and systole, LVPWd and LVPWs- left ventricular posterior wall thickness in diastole and systole, FS- fractional shortening, EF- ejection fraction.

This experimental model of heart failure is acute therefore symptoms can manifest quickly; as a result body weights were monitored daily to ensure animals remained healthy. Analysis of body weights throughout the entire study revealed there was no significant difference between HF and control animals, with all animals showing growth curves within the normal range (figure 8.2). Therefore normalising quantification for body weight was not required for echocardiography or micro-CT data.

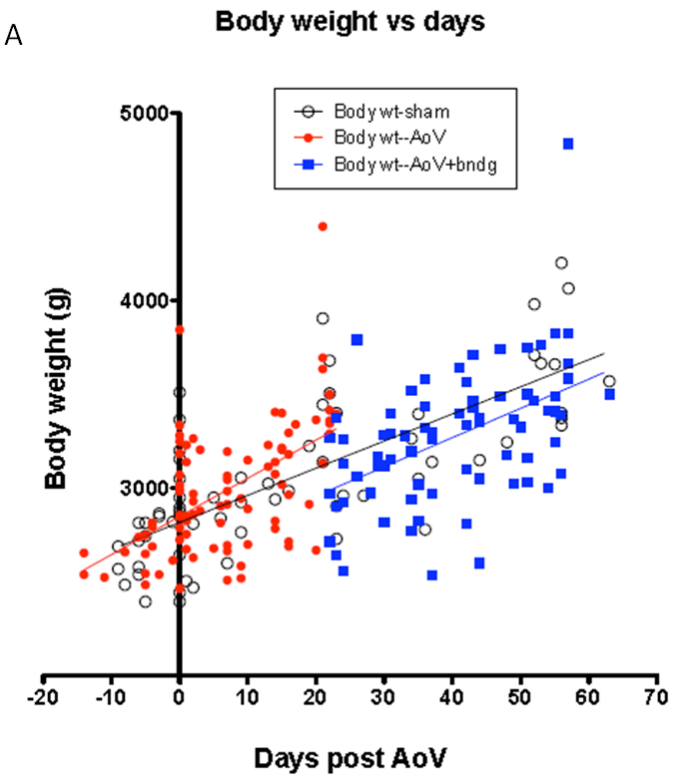

Figure 8.2 Regression analysis of the effect of experimental heart failure on body weight. Showing no significant difference between HF and control animals, with all animals showing growth curves within the normal range. (Control n=21, HF n= 24). AoV- aortic valve disruption.

LVID was measured at aortic valve disruption, aortic banding and pre-termination. Increased dilatation of the LV was evident in HF animals at both, aortic banding and pre-termination in both systole and diastole (figure 8.3A,B). There was no difference in LVID between groups at aortic valve disruption, confirming dilatation occurred post-intervention (figure 8.3A,B). To illustrate the progressive nature of the dilatation in the LV in HF, LVPW was plotted as a fraction of LVID (relative wall thickness) in both diastole and systole against days post aortic valve disruption (figure 8.3C). Dilatation was progressive in both diastole and systole. The change was most dramatic in systole, representing the progressive inability of the myocardium to reduce the LV cavity, and produce the sufficient systolic myocardial bulking needed for a healthy stroke volume. The data did not show evidence of an

inflection at the time of aortic banding (~21 days), suggesting the model produces progressive morphological changes (figure 8.3C).

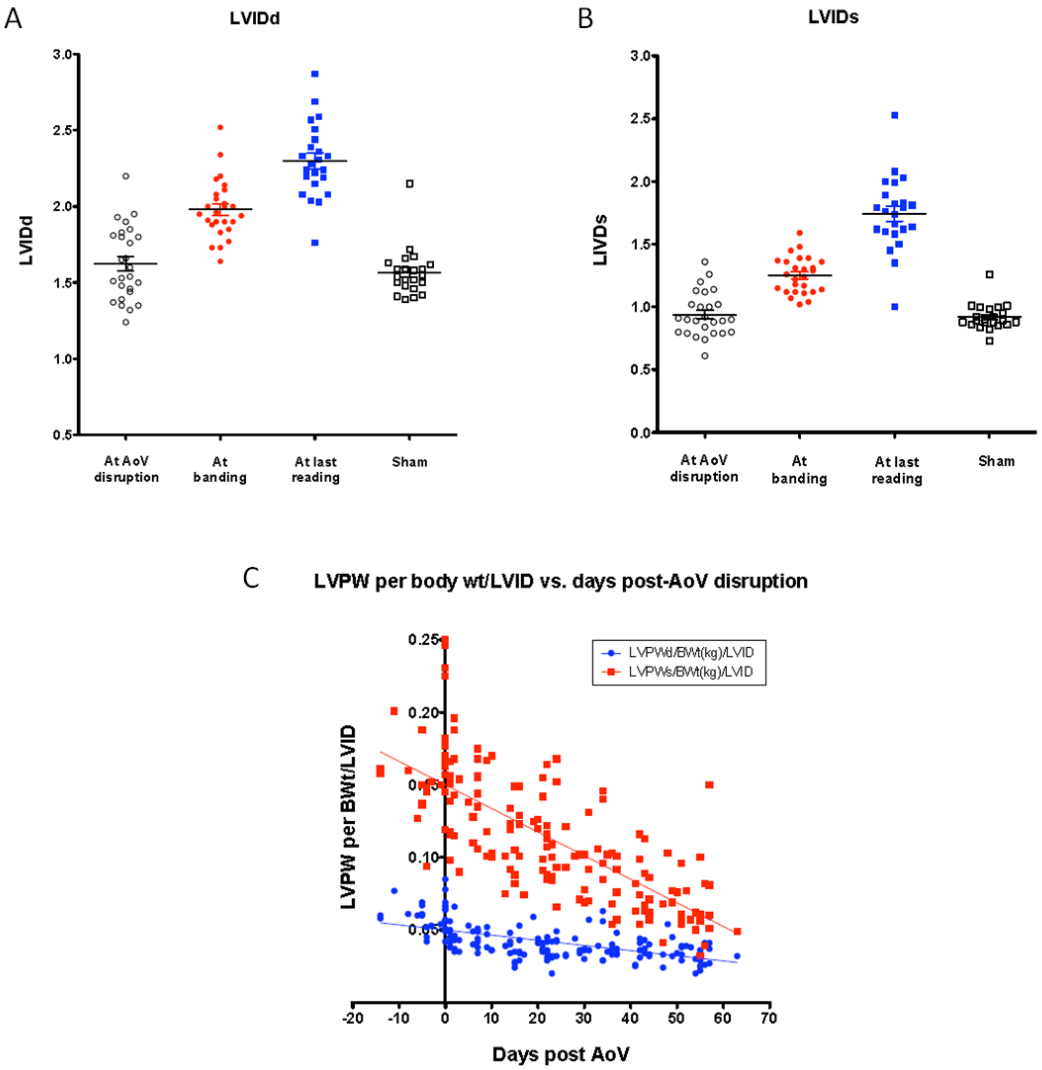

Figure 8.3 Progressive dilatation of the left ventricle in experimental heart failure assessed by echocardiography. Left ventricular internal dimension at aortic valve disruption, aortic banding and pre-termination in diastole (A) and systole (B). There was no difference in LVID between groups at aortic valve disruption (A,B). Regression analysis showing dilatation was progressive in both diastole and systole in heart failure (C). (Control n=21, HF n= 24). AoV- aortic valve disruption, LVIDd and LVIDs- left ventricular internal dimension in diastole and systole, LVPW- left ventricular posterior wall thickness. Error bars indicate standard error of the mean (SEM).

To analyse functional changes throughout the study, FS and EF of the LV was calculated at every performed scan. At termination EF was significantly reduced in HF (79.72±0.60 % vs. 57.10±2.27 %) (p=<0.0001) (table 8.2, figure 8.4A). 22 of 24 HF animals showed reduced FS over the study (baseline: 42.68±0.91 %, pre-termination: 25.33±2.9 %) (p=<0.0001) (table 8.1, figure 8.4A). Reduced FS (loss of function) in the LV was evident in HF animals after both aortic banding and aortic valve disruption, confirming loss of function post-intervention (figure 8.4B). Investigating FS post aortic valve disruption and up to pre-termination, confirmed control animals showed no loss of LV function (figure 8.4C). HF animals showed a steady decline in FS after both interventions (figure 8.4C), although outliers were evident. Again FS data does not show evidence of an inflection at the time of aortic banding (~ 21 days), suggesting the model produces progressive loss of function. Regression Analysis showed there was little evidence of correlations between functional and morphological changes. There is a weak correlation (p=<0.1) between LVPW post interventions and FS.

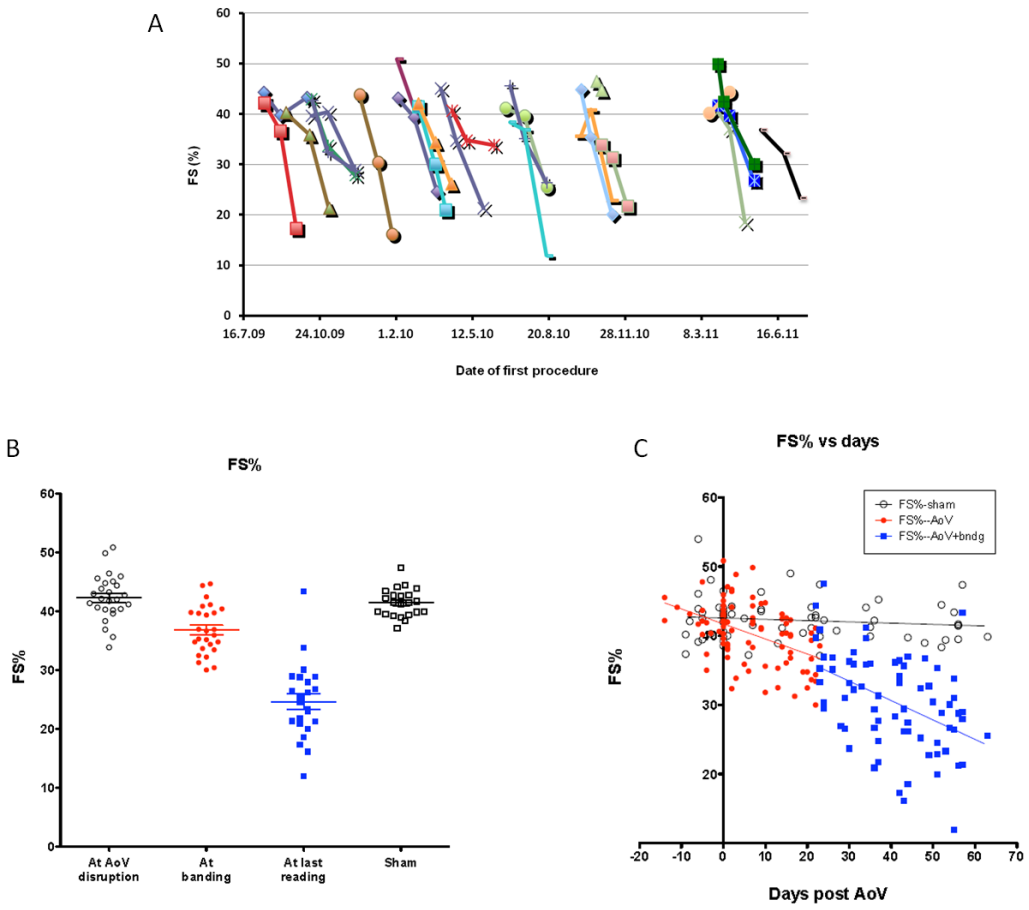

Figure 8.4 Progressive loss of fractional shortening in experimental heart failure assessed by echocardiography. Fractional shortening of left ventricle in individual heart failure rabbits measured at aortic valve disruption, aortic banding and pre-termination (n=24) (A). Data from (A) is pooled in (B) and mean values given (wide horizontal lines). There was no difference in ejection fraction between groups at aortic valve disruption (B). Regression analysis of progressve change in sham control and heart failure rabbits (C) (Control n=21, HF n= 24). AoV- aortic valve disruption, FS- fractional shortening, LV- left ventricle. Error bars indicate standard error of the mean (SEM).

8.3 The effects of experimental heart failure on the morphology of the atria, revealed by *ex vivo* contrast enhanced micro-CT

To assess morphological changes in control and HF animals, whole intact rabbit hearts were stained with I_2KI and scanned for micro-CT in optimal conditions. *In situ* heparinisation followed by perfusion fixation, accompanied with careful monitoring during fixation (see methods 2.2.4), produced naturally inflated hearts, with no residing blood in the atrial or ventricular cavities. From whole heart scans atria and ventricles were reconstructed separately at 100% resolution, allowing fine details to be resolved in computationally manageable data sets. This section will concentrate on changes seen in the atria.

8.3.1 Is the atrial myocardial volume changed in heart failure?

Atria data (control n= 5, HF n=5) was segmented from surrounding fat and fascia, and the total atrial volumes calculated. To investigate regional changes, further segmentation (semi-automatic segmentation II- see methods 2.4.2) was conducted to isolate the RA, LA and IAS. Here the IAS is defined as the wall dividing the two atrial chambers as viewed in transverse sections. T-tests were used to analyse statistical significance of results. The overall atrial myocardial volume was increased in HF (67% increase: 648±32 mm^3 vs 1085±239 mm^3) (figure 8.5A). All sub regions showed a volume increase in HF (RA- 59%: 297±18 mm^3 vs 472±109 mm^3, LA- 93%: 304±30 mm^3 vs 587±159 mm^3, IAS- 91%: 45±6 mm^3 vs 86±30 mm^3) (figure 8.5A). The biggest increase was seen in the LA, which is to be expected in a model directly affecting the left side of the heart. Variation (standard error) was much higher in HF atria than in control data (figure 8.5A). Scaled volume renderings of a typical control and HF atria (figure 8.5B and C respectively) allows visualisation of the dramatic change in atrial morphology. RA preparations from control and HF samples were processed for histology, and cell diameters were measured and means taken. Analysis showed an increase in cell diameter in HF samples in the RA (60% increase: 12.7±0.5 μm vs 20.3±0.8 μm) ($p=<0.05$), the LA was not tested. Histology was conducted by Dr Xue Cai, The University of Manchester.

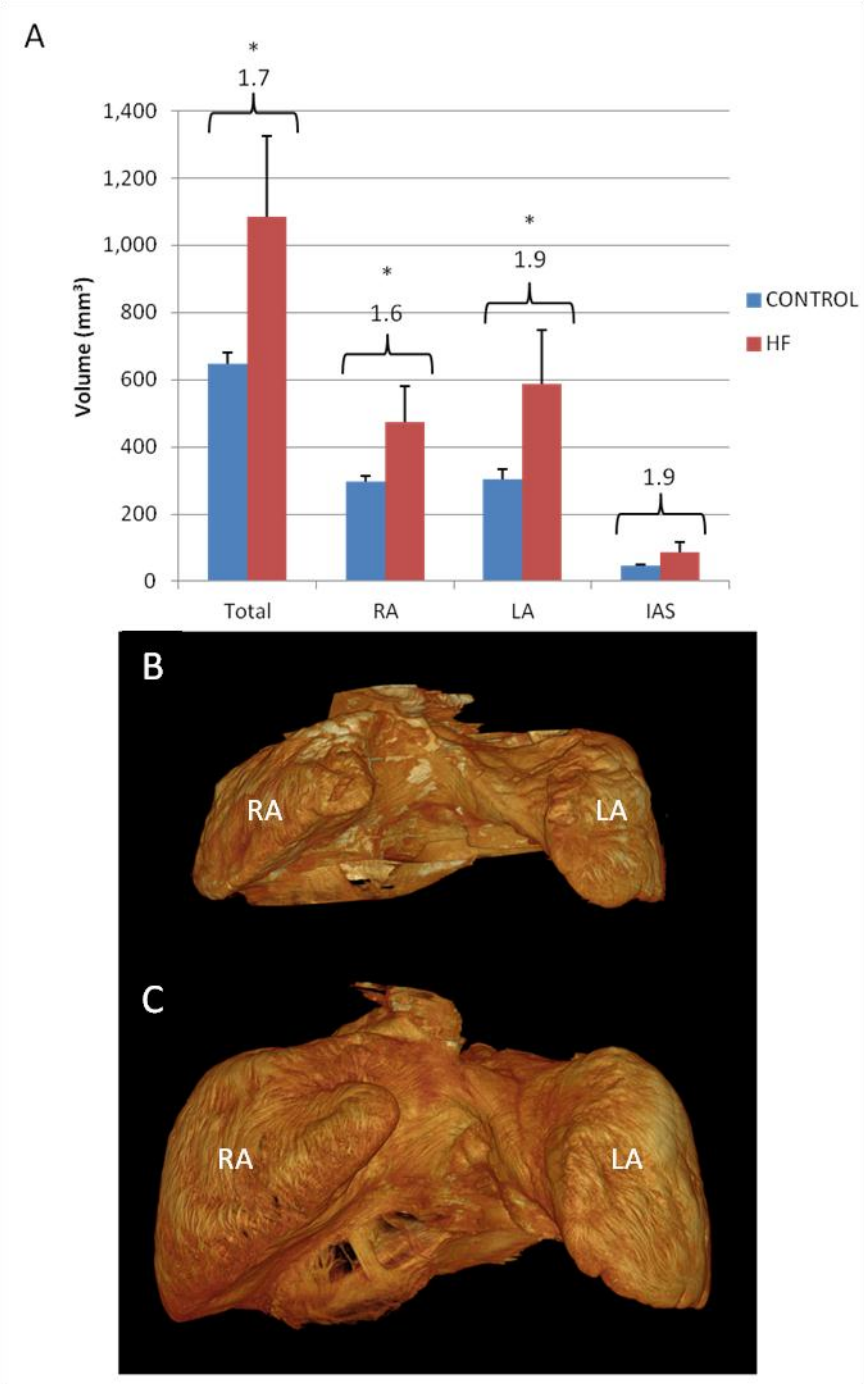

Figure 8.5 Changes in total and regional atrial tissue volume in experimental heart failure assessed by micro-CT. Mean tissue volume of segmented atria, right atrium, left atrium and interatrial septum (A). Scaled volume renderings of atria (anterior view) from representative control (B) and HF (C) samples. (Control n=5, HF n= 5, *p=<0.1). Values in A represent times increase. Error bars indicate standard error of the mean (SEM). IAS- interatrial septum, LA- left atrium, RA- right atrium.

8.3.2 Is atrial hypertrophy uniform across the atria?

To investigate how the observed hypertrophy of the atria (figure 8.5) affects wall and PcM thickness, atria (control n=5, HF n=5) were orientated on their respective valve vestibules so the PcMs were predominantly in a vertical orientation. Free wall and PcM width measurements (4 measurements for each) were made from transverse sections at 6 intervals (inferior-superior) through the atrial wall, resulting in a total of 42 measurements per atrium. At each interval measurements were made at the anterior, posterior and free wall of the atria ensuring a representative measure of wall and PcM thickness across the entire atria. If a PcM cross section appeared ellipsoidal its short axis width was taken.

The mean wall thickness in control and HF samples was not significantly different in the RA (245±34.4 μm vs 241±40.7 μm) or LA (330±29.1 μm vs 291±38.6 μm) (figure 8.6, figure 8.7), although a suggestion of wall thinning in regions of the LA was evident in HF (figure 8.6B). In contrast, an increase in mean PcM width was observed in HF in both the RA (379±29.5 μm vs 527±91.4 μm) ($p=<0.1$) and LA (607±26.8 μm vs 733±38.1 μm) ($p=<0.05$) (figure 8.6, 8.7). Distribution curves of control and HF PcM widths in both the RA and LA are shown in figure 8.9. In HF, a shift of the distribution to the right was observed in both the RA and LA, this was accompanied by an increased number of PcMs with widths exceeding the mode. This suggests the mean and maximum PcM widths are increased in HF. Figure 8.6 and figure 8.8 suggest the increased PcM width in HF is more considerable in the mid-wall of the atria than the extreme inferior and superior intervals. This suggests that the free running portions of PcM are more prone to hypertrophy than their insertion points. The observed morphological changes to the PcMs can be appreciated in the volume renderings shown in figure 8.8. The PcM width to atrial wall width ratio (PcM:W) was calculated for all samples. PcM:W was increased in HF in both the RA (1.6 ±0.14 vs 2.3 ±0.25) ($p=<0.05$) and LA (1.9 ±0.15 vs 2.7 ±0.34) ($p=<0.05$) (figure 8.7), with the biggest increase seen the LA. The higher ratio seen in the LA in comparison to the RA in both groups is due to the inherent increased thickness of the LA PcMs as discussed in Chapter 5.2.

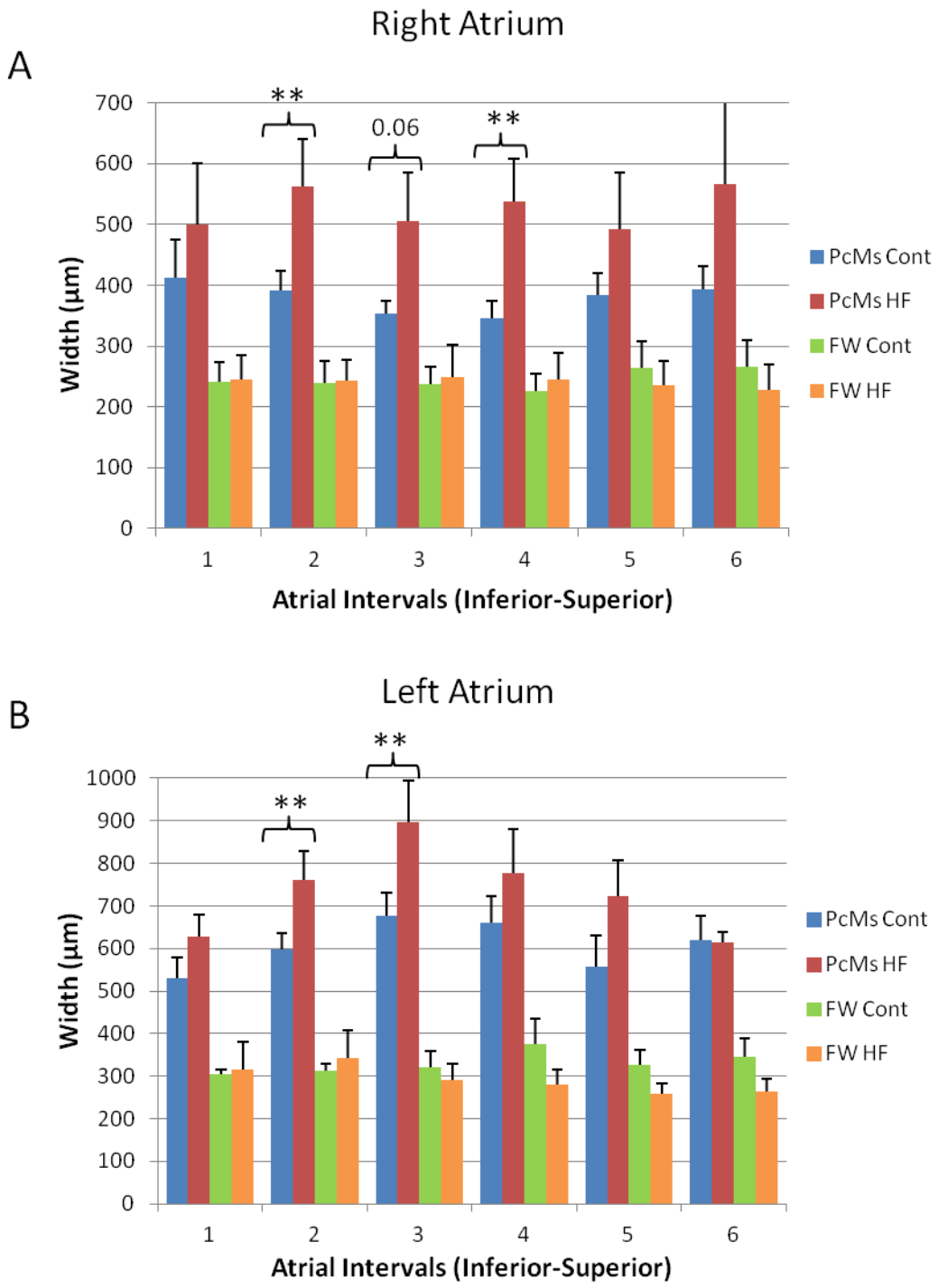

Figure 8.6 Regional changes in pectinate muscle and atrial free wall widths in experimental heart failure assessed by micro-CT. Mean width of pectinate muscles and atrial free wall measured from transverse micro-CT images at 6 intervals through the right (A) and left (B) atria. (Control n=5, HF n= 5, **p=<0.05). Error bars indicate standard error of the mean (SEM). PcMs- pectinate muscles, FW- atrial free wall, Cont- control, HF- heart failure.

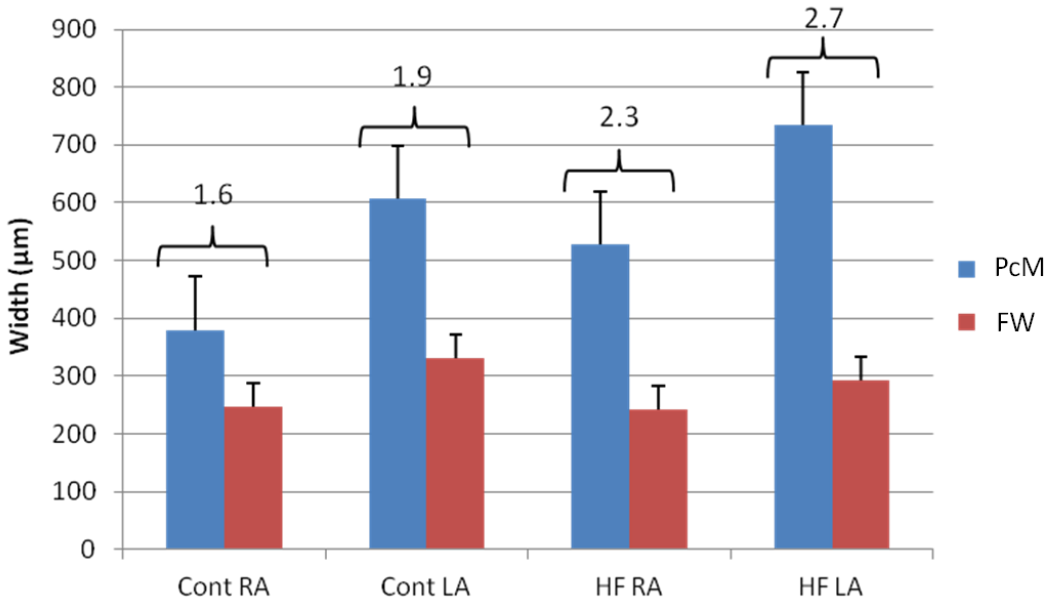

Figure 8.7 Changes in pectinate muscle and atrial free wall widths in experimental heart failure assessed by micro-CT. Raw data from figure 8.6 was pooled and total mean widths calculated for control and heart failure samples. Values above bars indicate pectinate muscle : atrial free wall ratios. (Control n=5, HF n= 5). Error bars indicate standard error of the mean (SEM). FW- atrial free wall, LA- left atrium, PcM- pectinate muscle, RA- right atrium.

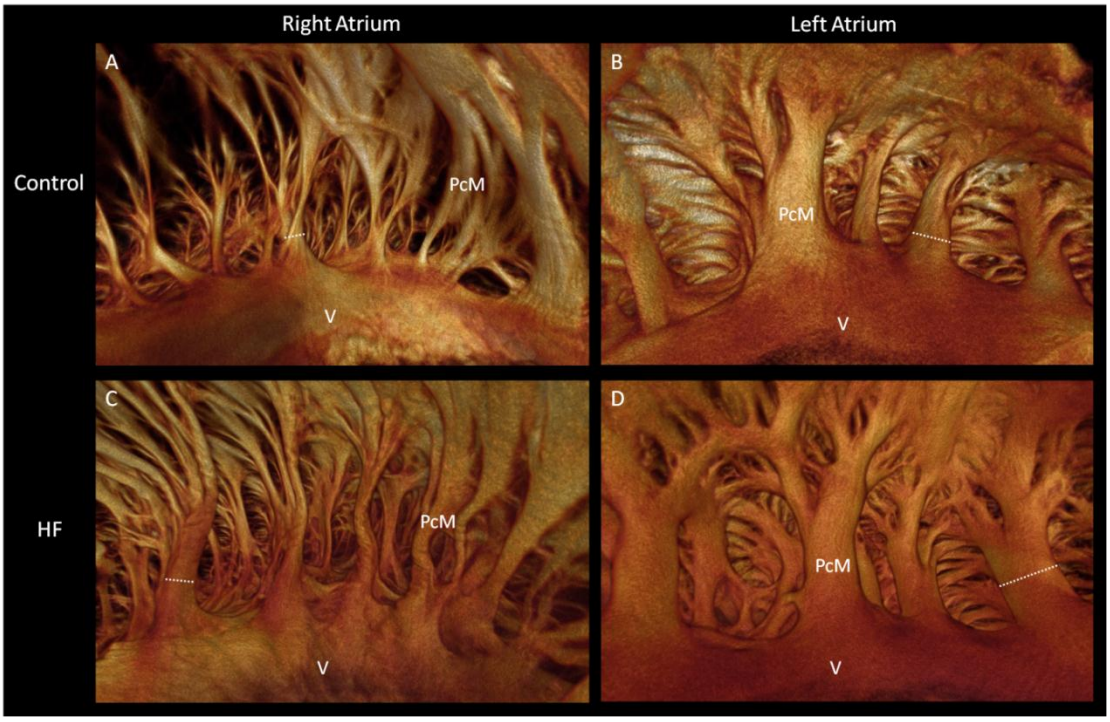

Figure 8.8 Volume renderings of the pectinate muscle in a control and heart failure rabbit. Scaled volume renderings from endocardial view of PcMs in the free wall of right atrium (A,C) and left atrium (B,D) from control (A,B) and heart failure (C,D) samples. Dotted lines represent pectinate muscle widths: A= 554µm, B= 851µm, C= 674µm, D= 1672µm. Images derived from micro-CT data. PcM- pectinate muscle, V- vestibule.

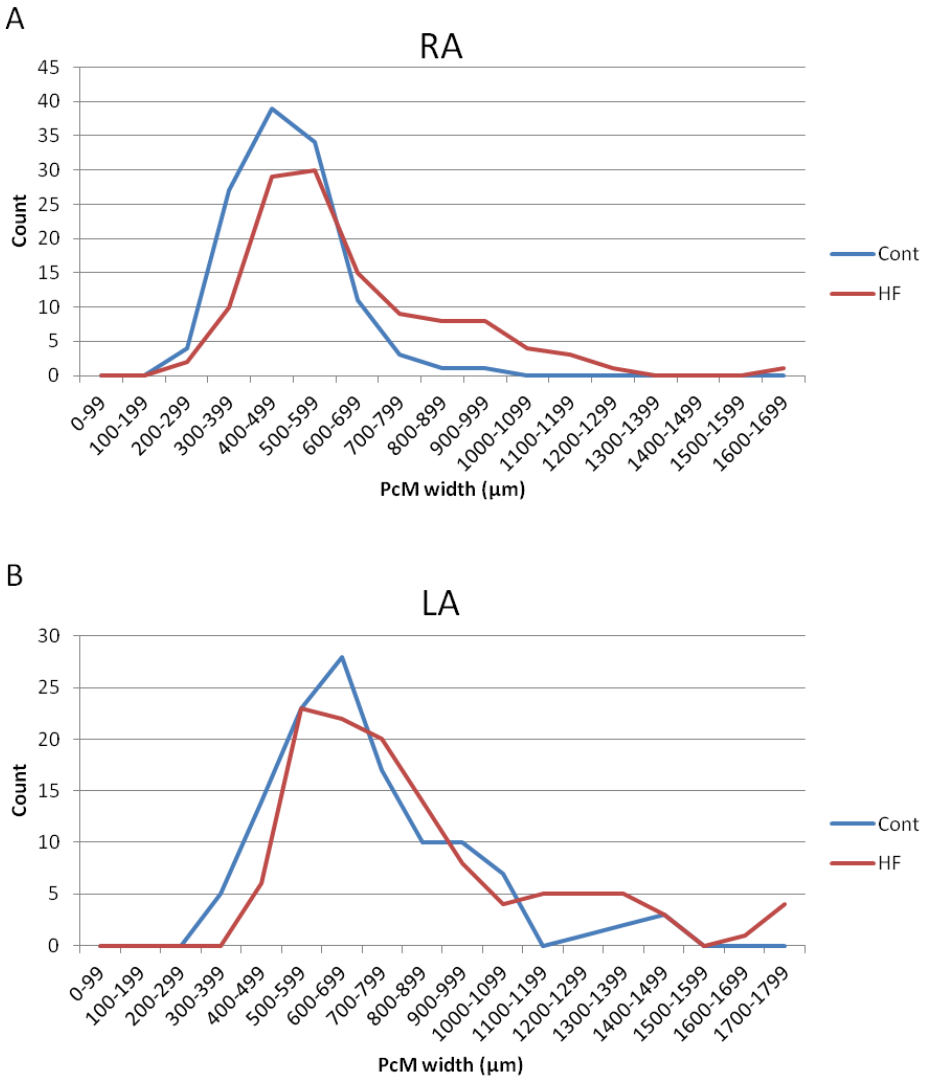

Figure 8.9 Distribution of pectinate muscle widths in control and heart failure rabbit atria. Raw data from figure 8.6 was pooled and histograms plotted for the right atrium (A) and left atrium (B). In heart failure a shift of the distribution curve to the right was observed in both the RA (A) and LA (B), this was accompanied by an increased number of PcMs with widths exceeding the mode (A,B). (Control n=5, HF n= 5). Cont- control, HF- heart failure.

8.3.3 Does heart failure cause dilatation?

Atrial dilatation in HF was investigated in collaboration with Dr Jichao Zhao (the University of Auckland). Atrial cavities (space) of control and HF samples (n=4 each) were segmented from the surrounding myocardium, the atrial appendages were then isolated, and the respective volumes extracted. Total atrial cavity volume more than doubled in HF (119% increase: 932±243 mm^3vs 2040±1297 mm^3) (p=<0.05).

However, morphological changes between the RA and LA were not uniform; in the RAA the tissue (113% increase: 79±16 mm^3vs 169±59 mm^3) and cavity (307% increase: 28±4 mm^3 vs 114±32 mm^3) (p=<0.05) volumes both increased in HF. The same trend was seen for the LAA, with both tissue (84% increase: 221±48 mm^3 vs 406±107 mm^3) and cavity (233% increase: 189±64 mm^3 vs 630±330 mm^3) (p=<0.1) volumes increasing in HF. Therefore experimental HF induced a greater increase in dilatation than hypertrophy, with the greatest relative dilatation observed in the RA.

8.4 The effects of experimental heart failure on the morphology of the ventricles, revealed by *ex vivo* contrast enhanced micro-CT

To assess morphological changes in control and HF animals, whole intact rabbit hearts were stained with I_2KI and scanned for micro-CT in optimal conditions. *In situ* heparanisation followed by perfusion fixation produced naturally inflated hearts, with no residing blood in the ventricular cavities. From whole heart scans atria and ventricles were reconstructed separately at 100% resolution, allowing fine details to be resolved in computationally manageable data sets. This section will concentrate on changes seen in the ventricles.

8.4.1 Do the ventricles undergo hypertrophy in heart failure?

Ventricle data (control n= 7, HF n=7) was segmented from surrounding fat and fascia, and the total volumes calculated. Further segmentation (semi-automatic segmentation II- see methods) was conducted to isolate the RV, LV and IVS, to allow investigation of regional changes. T-tests were used to analyse the statistical significance of results. The total myocardial volume was increased in HF compared to control (28% increase: 3558±276 mm^3 vs 4564±556 mm^3) (p=<0.01) (figure 8.10). Regional analysis showed significant myocardial volume increase in the RV (84% increase: 603±63 mm^3 vs 1115±132 mm^3) (p=<0.05), IVS (62% increase: 1006±96 mm^3vs 1630±117 mm^3) (p=<0.001) and LV (64% increase: 1514±178 mm^3 vs 2478±260 mm^3) (p=<0.01) (figure 8.10). The volume increase in HF was relatively uniform (RV- 1.8x, IVS- 1.6x, LV- 1.6x), showing evidence of a compensated response across the ventricles, that is the ventricles followed the expected primary

response to HF by undergoing hypertrophy. Ventricle preparations from control and HF samples were processed for histology, and cell diameters were measured and means taken. Analysis showed an increase in cell diameter in HF samples in the RV (21 % increase: 15.6±0.7 µm vs 18.9±1.9µm) (p=<0.05) and LV (25% increase: 16.7±0.8 µm vs 20.8±0.5 µm) (p=<0.05). Histology was conducted by Dr Xue Cai, The University of Manchester.

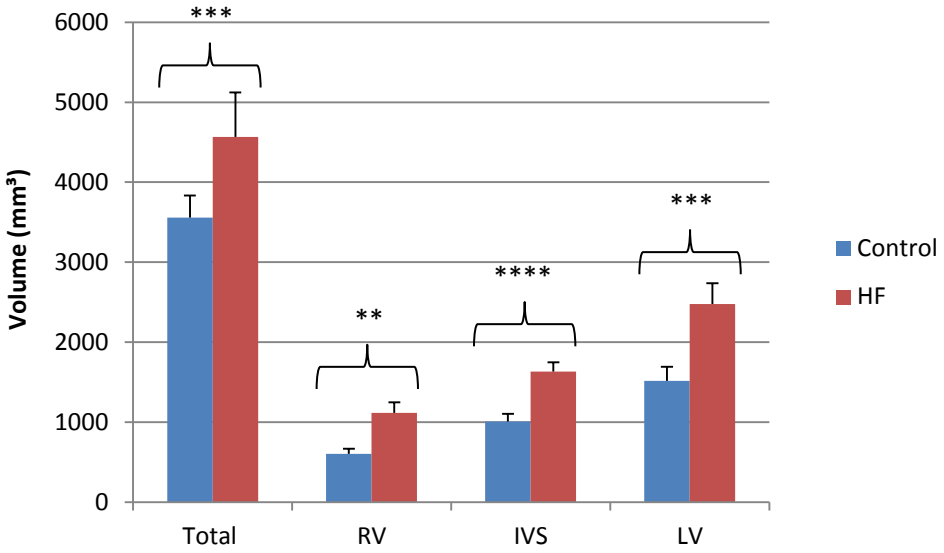

Figure 8.10 Changes in total and regional ventricular tissue volume in experimental heart failure assessed by micro-CT. Mean tissue volume of segmented ventricles, right ventricle, interventricular septum and left ventricle. (Control n=7, HF n= 7, **p=<0.05, ***p=<0.01, ****p=<0.001). Error bars indicate standard error of the mean (SEM). IVS- interventricular septum, LV- left ventricle, RV- right ventricle.

8.4.2 Are the ventricles dilated in heart failure, and does this affect ventricular shape?

To investigate dilatation, ventricular cavities (space) of control and HF samples (n=7 each) were segmented from the surrounding myocardium. In control hearts, as expected, the mean RV cavity volume exceeded that of the LV, however this relationship was dramatically reversed in HF (figure 8.11A). The LV cavity volume was significantly increased in HF compared to control (231% increase: 1426±344 mm^3 vs 4716±651 mm^3) (p=<0.001). Although an increase in the RV cavity was observed in HF (1906±323 mm^3 vs 2650±686 mm^3), data was not statistically significant (figure 8.11A). Dramatic changes in ventricular cavities can affect the overall shape of the LV, therefore ventricular sphericity index (SI) was calculated (figure 8.11B). Data sets were resliced longitudinally and orientated on the apex of the ventricles, creating a four chamber view. At the midpoint of the valve plane a base-apex length was taken spanning from the midpoint of mitral valve to the tip of the apex. A second measurement was taken perpendicular to the midpoint of the base-apex measurement, spanning from the IVS to the LVFW, this length was then divided by the base-apex length to give the hearts SI. Small SI values correspond to an ellipsoidal LV, while values closer to 1 indicate a spherical LV. An increase in LV sphericity is a predictor of LV dysfunction and HF. There was no difference between control and HF, with mean values appearing almost identical (0.674 ±0.04 mm^3 vs 0.679±0.03 mm^3) (figure 8.11B). This suggests that although hearts in HF have undergone considerable LV dilatation (non-compensated), compensated morphological changes have occurred to maintain an ellipsoidal LV.

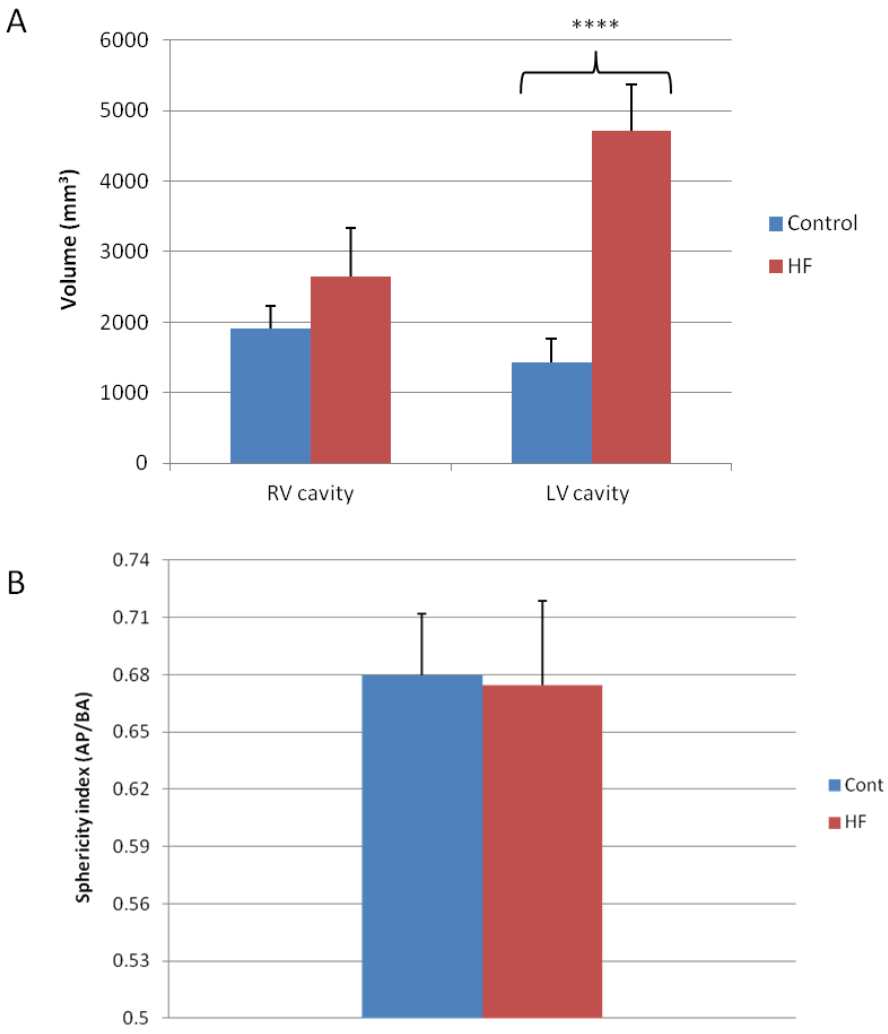

Figure 8.11 Changes in cavity volume and sphericity of the ventricles in experimental heart failure assessed by micro-CT. Mean volume of segmented right ventricular and left ventricular cavites (A)**.** Left ventricular sphericity index (see text for methodology) in control and heart failure rabbits (B). (Control n=7, HF n=7, ****p=<0.001). Error bars indicate standard error of the mean (SEM). Cont- control, HF- heart failure.

Scaled 3D isosurfaces of the RV and LV cavity volumes allow a visual appreciation of the aforementioned morphological changes in HF (figure 8.12). Figure 8.12 shows scaled 3D isosurfaces of RV and LV cavities in 3 control and 3 HF hearts. The dramatic changes in cavity volumes are clearly shown, and the maintenance of a normal SI can be appreciated. The effect of HF on the endocardial trabeculation cannot be appreciated in statistical analysis, however, the 3D isosurfaces revealed a

reduction in the depth and complexity of endocardial trabeculae in the LV of HF samples (figure 8.12). This suggests dilatation of the ventricles in HF stretches and flattens the trabeculae carnae.

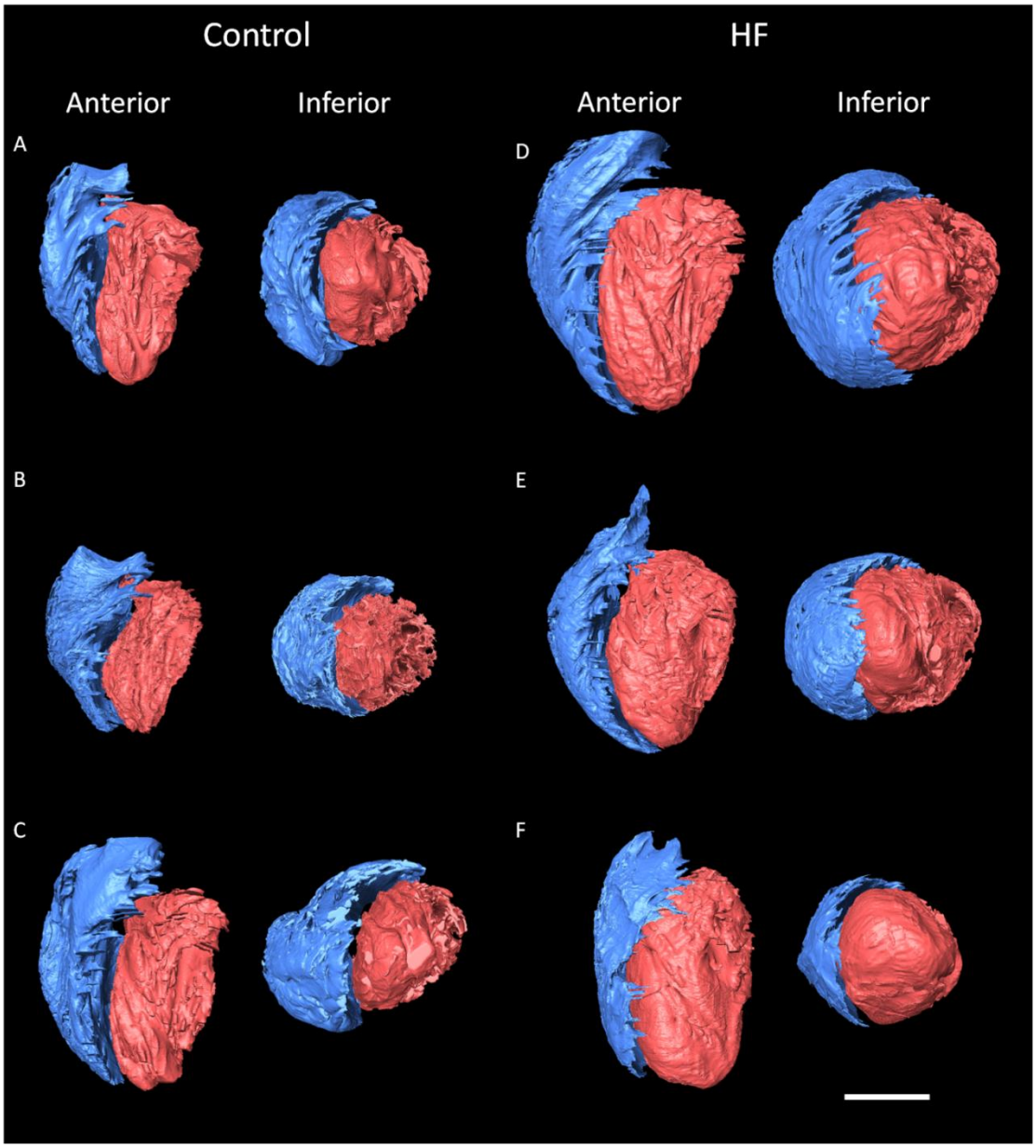

Figure 8. 12 3D isosurfaces of the ventricular cavities in control and heart failure rabbits. Scaled 3D isosurfaces segmented from micro-CT data showing the right ventricle (blue) and left ventricle (red) cavity volumes. The 3D isosurfaces reveal a reduction in the depth and complexity of endocardial trabeculae in the LV of HF samples. Note there was no significant difference in the sphericity index of control and HF hearts. (Scale bar represents ~1 cm)

8.4.3 Are morphological changes uniform across the ventricles?

To investigate regional changes in wall thickness throughout the ventricles, data sets were resliced longitudinally and orientated on the apex of the ventricles to two orthogonal planes. Then the mean wall thicknesses for the RV, IVS and LV regions were calculated from transverse sections at 8 evenly spaced intervals from base to apex. Interval 1 was anatomically defined as the first slice in which all 3 walls were visible. Interval 8 was defined as the final slice in which all 3 walls were still visible. Mean wall thickness for each regional interval was calculated by averaging 4 measurements (anterior, posterior and 2 free wall), resulting in 32 measurements per region, per heart. Significant thickening of the RV wall was observed at all intervals in HF, with the greatest RV wall thickness seen at the base (figure 8.13A). In contrast, in HF the IVS showed thinning at the base, mid-wall and apical intervals, with significant thinning seen in the mid-wall (figure 8.13B). An interesting relationship was observed in the LV wall thickness of HF hearts. Thinning was observed in the base and mid-wall, followed by thickening of the wall towards and including the apex (figure 8.13C). This is a reverse of the relationship usually observed in control hearts (Ho 2009).

To assess whether the anterior or posterior LV wall was more susceptible to change, in both groups the anterior and posterior mean wall thicknesses were compared at each interval using T-tests. There was no significant difference between anterior and posterior LV wall measurements within an interval in control or HF, apart from at interval 8 in control. Comparision of free wall meausremnts showed there was no significant difference between LV free wall measurements within an interval in control or HF. To assess whether the LV free wall was more susceptible to change, in both groups the anterior and posterior wall thicknesses were compared with the 2 free-wall wall thicknesses at each interval using analysis of variance (anova). The only significant difference was seen in HF at interval 5. This shows the observed changes in response to experimental HF are uniform throughout the LV wall at each interval.

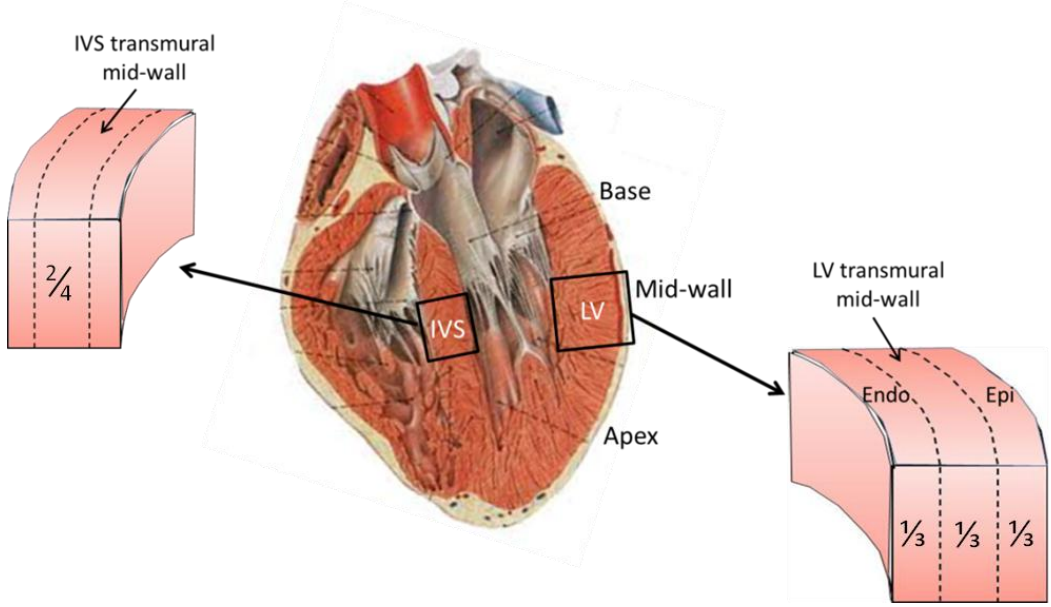

Explanatory figure 8.1 Anatomical classification of the ventricles. Schematic indicating regional (base, mid-wall, apex) and transmural anatomical classification of the ventricles, as used in volumetric, wall thickness and fibre orientation analysis.

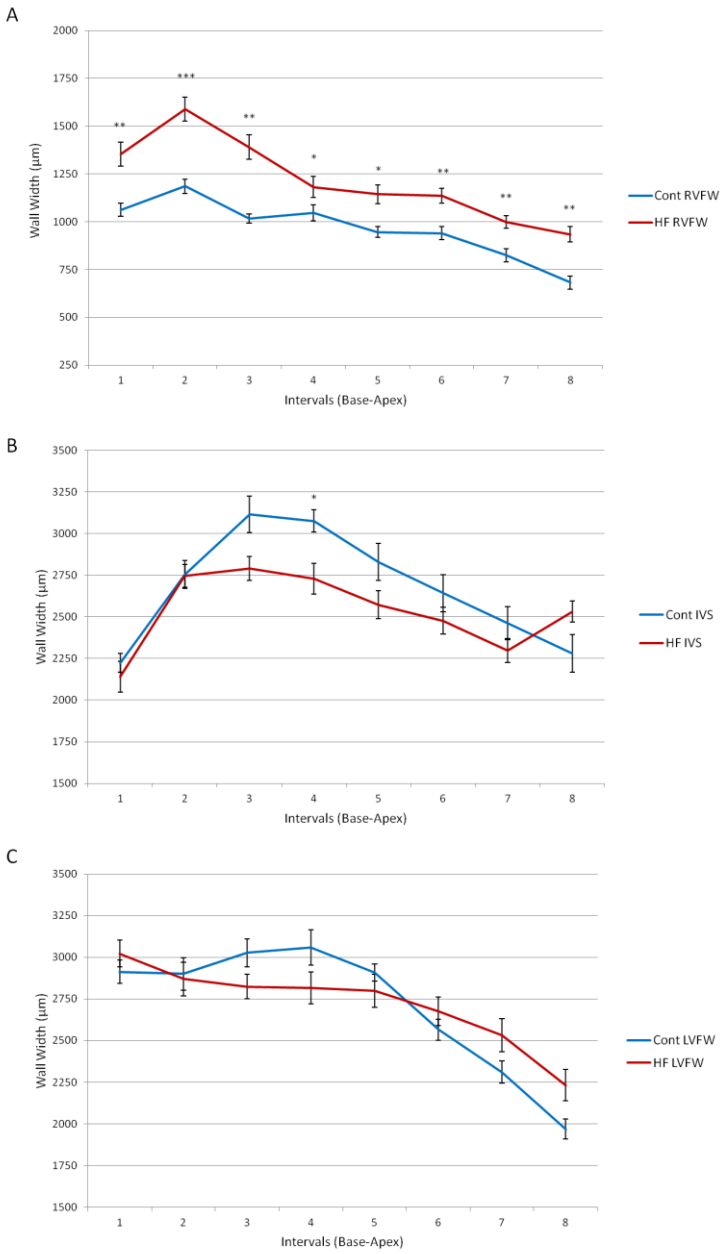

Figure 8.13 Changes in regional wall thickness of the ventricles in experimental heart failure assessed by micro-CT. Mean width of the right ventricular (A) and left ventricular (C) free walls, and interventricular septum (B) measured from transverse micro-CT images at 8 intervals through the ventricles (base-apex). (Control n=7, HF n= 7,*p=<0.1, **p=<0.05, ***p=<0.01). Error bars indicate standard error of the mean (SEM). IVS- interventricular septum, LVFW- left ventricular free wall, RV- right ventricular free wall.

To investigate regional changes in cavity size throughout the ventricles, scan data was prepared as for wall thickness analysis, and cavity cross sectional areas for the RV and LV were recorded at the same 8 intervals (base-apex) used for wall thickness analysis. Figure 8.14A shows mean RV cavity cross sectional area was increased in HF from intervals 2-8 (base-apex), however, only interval 8 was statistically significant ($p=<0.05$). This suggests concentric remodelling of the RV in HF (figure 8.13A and 8.14A). Significant increase in cavity cross sectional area was observed at all intervals of the LV in HF. The most dramatic changes occur at the base and mid-wall (intervals 2-5) (figure 8.14B), corresponding to regions where LV wall thinning was observed (figure 8.13C). A decline in cavity cross sectional area was seen in the apical region (intervals 7,8) (figure 8.14B), corresponding to areas of LV wall thickening (figure 8.13C). This suggests regional specific morphological changes occur in the LV of HF samples. Consequently, data was analysed using the coefficient of determination (R^2) to look for correlations between LV wall thickness and LV cavity cross sectional area (figure 8.15). Weak correlations for both control and HF samples were observed for whole heart analysis, and showed the dramatic dilatation observed in HF had little effect on wall thickness (figure 8.15A). The same trend was observed when the apical regions (intervals 6-8) were analysed (figure 8.15B). However at the base (intervals 2-5), a negative correlation was observed in both control and HF, suggesting dilatation is causing LV wall thinning (figure 8.15C). Figure 8.15 therefore further clarifies that regional specific morphological changes occur in HF.

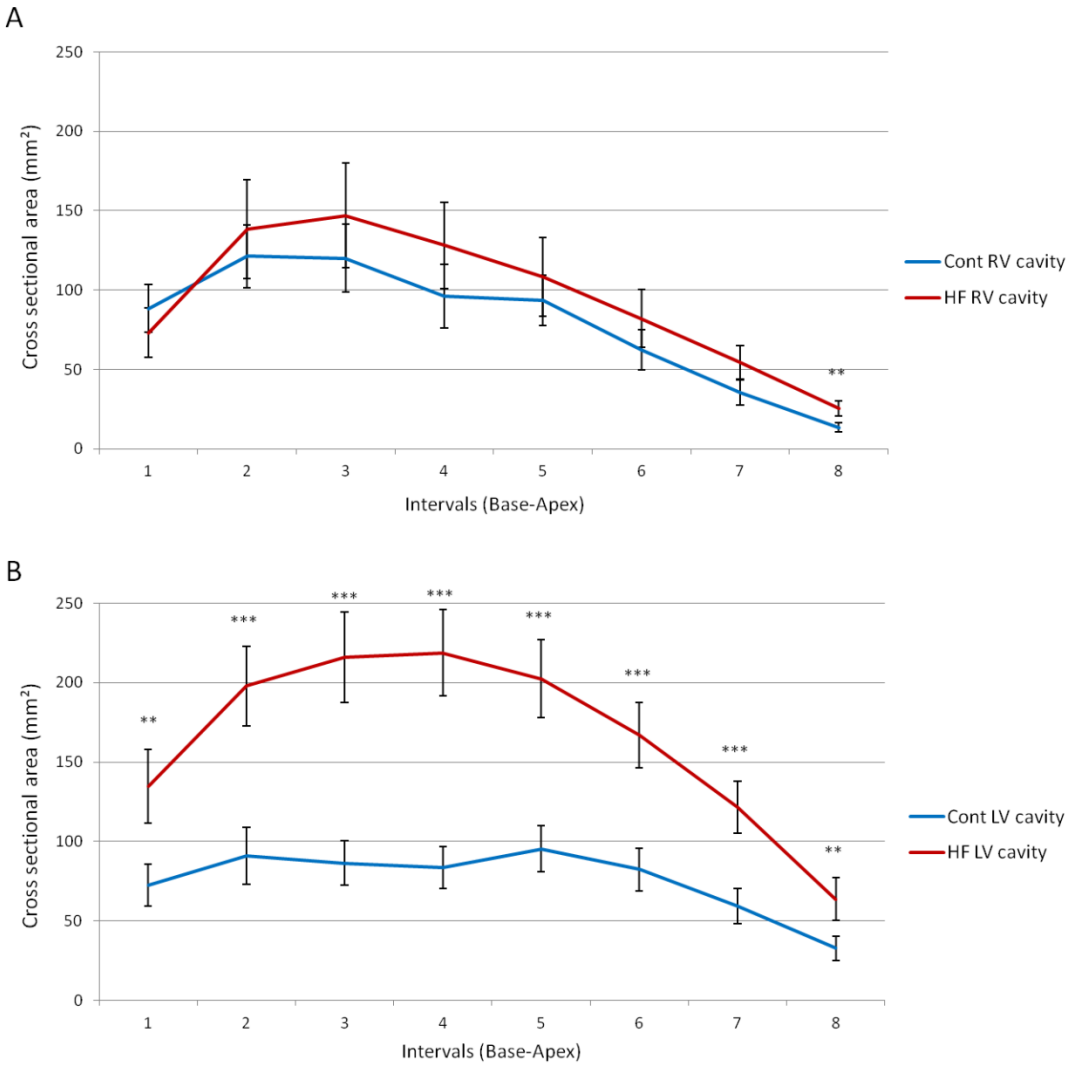

Figure 8.14 Changes in regional cross sectional area of the ventricular cavities in experimental heart failure assessed by micro-CT. Mean cross sectional area of right ventricular (A) and left ventricular (B) cavities measured from transverse micro-CT images at 8 intervals through the ventricles (base-apex). (Control n=7, HF n= 7, **p=<0.05, ***p=<0.01). Error bars indicate standard error of the mean (SEM). Cont- control, HF-heart failure, LV-left ventricle.

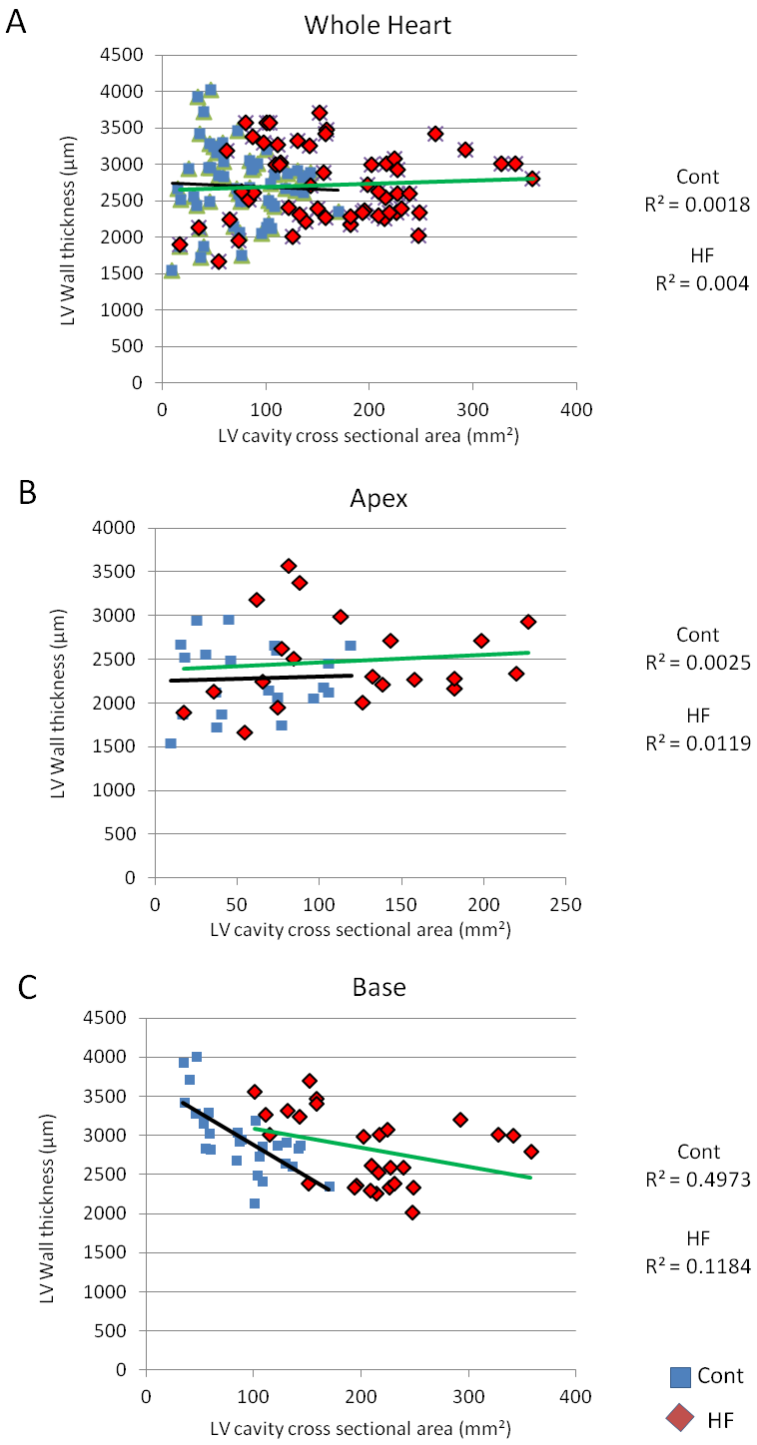

Figure 8.15 Regional coefficient of determination (R^2) analysis of the left ventricular wall and cavity in control and heart failure. Showing the morpholoigcal relationship between left ventricular wall thickness (individual sample means from analysis in figure 8.13) and cavity cross sectional area (individual sample means from analysis in figure 8.14) in the whole heart (intervals 1-8) (A), apical region (intervals 6-8) (B) and basal region (intervals 2-5) (C). (Control n=7, HF n= 7). Cont- control, HF-heart failure, LV-left ventricle.

8.5 The effects of experimental heart failure on fibre orientation within the ventricles.

Contrast enhanced micro-CT has been shown to non-invasively resolve the 3D arrangement of single muscle fibres (Chapter 4.3, 5.5 and Jeffery et al., 2011). Consequently novel structure tensor and fibre tracking analysis was carried out on micro-CT data (methods 2.4.4) of adult rabbit hearts, to visualise and quantify 3D myofibre orientation of the ventricles in control (n=5) and HF (n=6). Data sets (18-24 μm isometric resolution) were resliced longitudinally and orientated on the apex of the ventricles in two orthogonal planes, making the IVS vertical and ensuring each heart was in the same orientation. Inclination and transverse fibre angles (figures 2.1,2.2) for LVFW, LVPW and IVS regions were then extracted (with the epicardial wall from each region forming the x plane) from 7 transverse sections at evenly spaced intervals (base-apex). Data was subsequently smoothed using coherence-enhancing anisotropic diffusion to allow better appreciation of transmural trends. Interval 1 was anatomically defined as the first slice in which all 3 walls were visible. Interval 7 was defined as the final slice in which all 3 walls were still visible. Interval 1 was excluded from analysis due to the large variation in morphology at this region. In each region at every interval, a ~650μm (~30 voxels) wide transmural segment was taken for analysis, resulting in ~3000 readings (voxels) per transmural segment. The papillary muscles were excluded from analysis as they predominantly consist of vertically running fibres, which if included, would give a skewed representation of fibre orientation in the endocardium. All values corresponding to space were removed, and means and standard deviations for the whole transmural segment, and at each transmural plane (parallel to epicardial wall) within a segment, were calculated. Then transmural fibre orientation plots and histograms of fibre distribution were plotted. All samples were normalised for wall thickness. For explanatory figures of 3D fibre orientation see figures 2.1 and 2.2.

8.5.1 The global changes to fibre orientation in heart failure

The LVFW showed a gradual increase in inclination angle from base to apex in both groups (figure 8.16A). However, in HF the difference in mean inclination compared to control gradually increased from base to apex, with significant increase observed at interval 7 (figure 8.16A). The LVPW showed a gradual decrease in inclination

angle from base to apex in HF (figure 8.16B), this was in contrast to the gradual increase from base to apex seen in control (matching the trend seen in control LVFW) (figure 8.16B). A significant increase in mean inclination angle was seen in the base and mid-wall regions (intervals 2-4) of the LVPW in HF (figure 8.16B). No significant difference was observed in the apical region. There was no base to apex trend evident in fibre orientation of the IVS, although, like in the LVPW, a significant increase in mean inclination angle was seen in the basal region of the IVS in HF (figure 8.16C). The LVPW and IVS both showed a mean increase in inclination angle at the base and mid-wall, and in contrast to the LVFW, showed a shift to a mean decrease in inclination angle at the apex (figure 8.16B,C). The observed differences reveal that changes in fibre orientation are regional, with subtle changes in some regions but dramatic in others. This is probably a reflection of the acute nature of the HF model. It is expected that such changes would be exacerbated in a chronic model of HF.

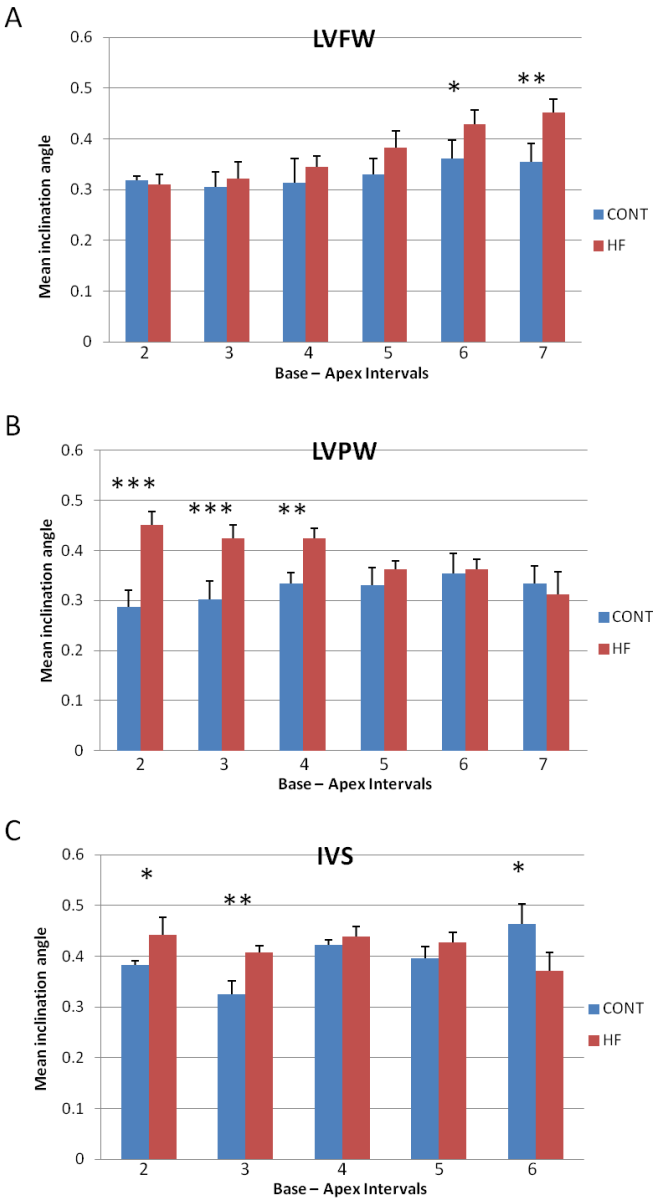

Figure 8.16 Regional changes in inclination angle of fibres across the ventricles in control and heart failure. Mean Inclination angles from left ventricular free wall (A) and posterior wall (B), and interventricular septum (C) regions extracted from micro-CT data at 7 transverse intervals base-apex (intervals 2-7 shown). In each region at every interval a ~650µm (~30 voxels) wide transmural segment was taken for analysis, resulting in ~3000 readings (voxels) per transmural segment. (Control n=5, HF n= 6, *p=<0.1, **p=<0.05, ***p=<0.01). Error bars indicate standard error of the mean (SEM). IVS- interventricular septum, LVFW- left ventricular free wall, LVPW- left ventricular posterior wall.

8.5.2 Regional transmural changes in fibre orientation

Further analysis was carried out to investigate regional transmural changes in fibre orientation from intervals 2-6. Previously analysed LVFW and LVPW transmural segments were divided evenly into 3 regions, allowing the epicardium, transmural mid-wall and endocardium to be analysed separately (explanatory figure 8.1). The mid-wall of the IVS was also analysed; transmural segments were divided evenly into 4, the transmural mid-wall was deemed to be the 2 central regions (explanatory figure 8.1). For inclination angle percentage calculations, values ranging from 0.1-0.3 were classified circumferential, and values 0.8-1.0 classified vertical.

8.5.3 Regional transmural changes in fibre orientation in the left ventricular free wall

In HF the LVFW endocardial mean inclination angle showed a small and gradual increase from base to apex (figure 8.17A). A considerable increase was observed at interval 3 (figure 8.17A), this corresponded with a significant increase in the percentage of vertical fibres at the same interval (figure 8.17C). Analysis of the transmural mid-wall region revealed similar fibre orientation (predominantly circumferential) in both control and HF at the base and mid-wall (intervals 2-4) (figure 8.17B,D). However, at intervals 5 and 6 an increase in mean inclination was observed (figure 8.17B), coupled with a dramatic decrease in the percentage of circumferential fibres in the region (figure 8.17D). Further clarifying major changes in the LVFW are localised to the apex in HF. The lack of statistically significant change in the LVFW throughout the LV is illustrated in figure 8.18. Transmural plots (~650 μm segment) and colour maps of inclination angles from intervals 2-7 of two representative samples illustrate that the normal transmural helical arrangement was largely preserved in HF samples (figure 8.18).

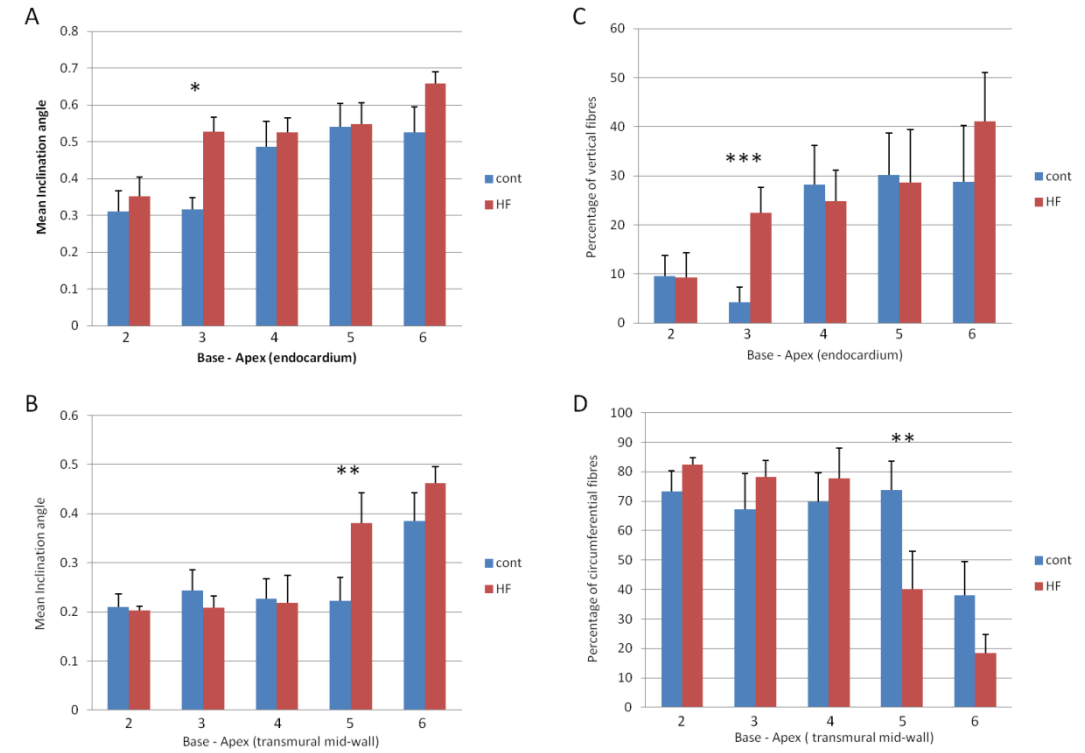

Figure 8.17 Regional changes in inclination angle of fibres in the endocardium and transmural mid-wall of the left ventricular free wall in control and heart failure. Mean Inclination angles from the endocardium (inner ⅓ of wall) (A) and transmural mid-wall (middle ⅓ of wall) (B) extracted from micro-CT data at 7 transverse intervals base-apex (intervals 2-6 shown). Corresponding percentage of vertical (values 0.8-1.0) and circumferential (values 0.1-0.3) fibres in the endocardium and transmural mid-wall respectivley (C,D). In each region at every interval a ~650µm (~30 voxels) wide transmural segment was taken for analysis. (Control n=5, HF n= 6, *p=<0.1, **p=<0.05, ***p=<0.01). Error bars indicate standard error of the mean (SEM).

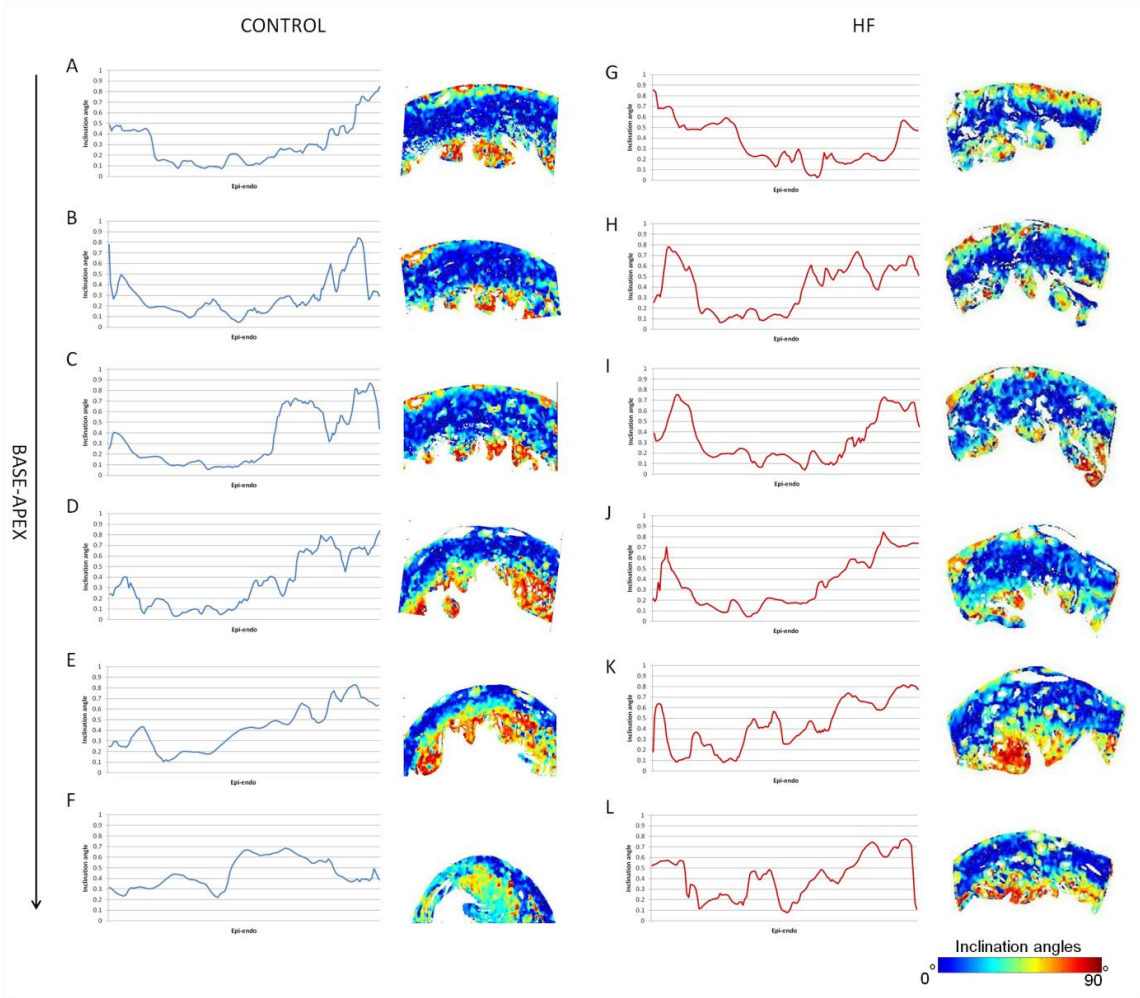

Figure 8.18 Transmural plots and colour maps of fibre inclination angle in the left ventricular free wall in control and heart failure. Mean inclination angles from each transmural plane (parallel to epicardial wall) within a segment were extracted from micro-CT data at 7 transverse intervals base-apex (intervals 2-7 shown); a representative control (A-F) and heart failure (G-L) sample are shown. In each region at every interval a ~650µm (~30 voxels) wide transmural segment was taken for analysis. (Colour bar indicates inclination angles).

8.5.4 Regional transmural changes in fibre orientation in the posterior wall of the left ventricle

Regional transmural analysis of the LVPW, on the other hand, revealed considerable changes in fibre orientation in HF. The LVPW endocardial mean inclination angle increased at all intervals in HF, with significant increases observed at the base and mid-wall (intervals 2 and 4) (figure 8.19A). This was coupled with a dramatic increase in the percentage of vertical fibres in the endocardium (figure 8.19C). The same trend was seen in the transmural mid-wall of the LVPW. Mean inclination increased at all intervals in HF, with significant increase observed at the base and mid-wall (intervals 2 -4) (figure 8.19B). This was coupled with a striking decrease in the percentage of circumferential fibres in the transmural mid-wall (figure 8.19D), indicating more vertical fibres are present in HF. Transmural plots (~650μm wide segment) and colour maps of inclination angles from intervals 2-7 illustrate these findings in two representative samples (figure 8.20). Panels G,H and I in figure 8.20 represent data from intervals 2-4 and clearly show an increase in vertical fibres at the endocardium and transmural mid-wall in HF.

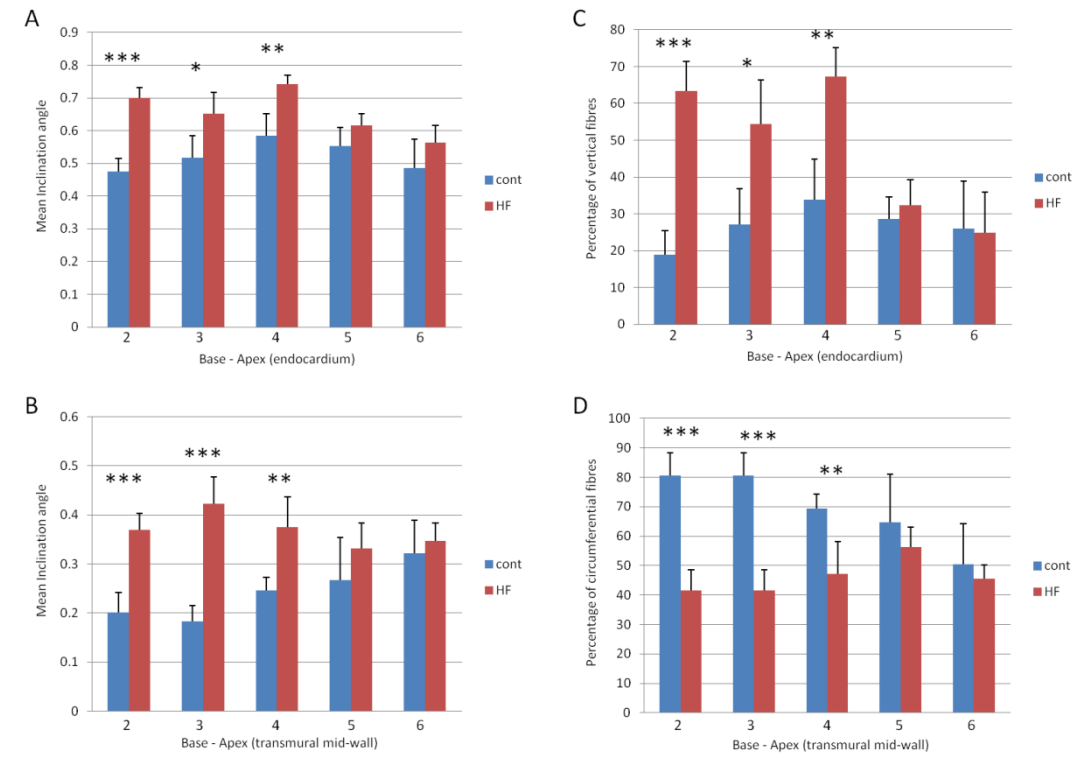

Figure 8.19 Regional changes in inclination angle of fibres in the endocardium and transmural mid-wall of the left ventricular posterior wall in control and heart failure. Mean Inclination angles from the endocardium (inner ⅓ of wall) (A) and transmural mid-wall (middle ⅓ of wall) (B) extracted from micro-CT data at 7 transverse intervals base-apex (intervals 2-6 shown). Corresponding percentage of vertical (values 0.8-1.0) and circumferential (values 0.1-0.3) fibres in the endocardium and transmural mid-wall respectivley (C,D). In each region at every interval a ~650µm (~30 voxels) wide transmural segment was taken for analysis. (Control n=5, HF n= 6, *p=<0.1, **p=<0.05, ***p=<0.01). Error bars indicate standard error of the mean (SEM).

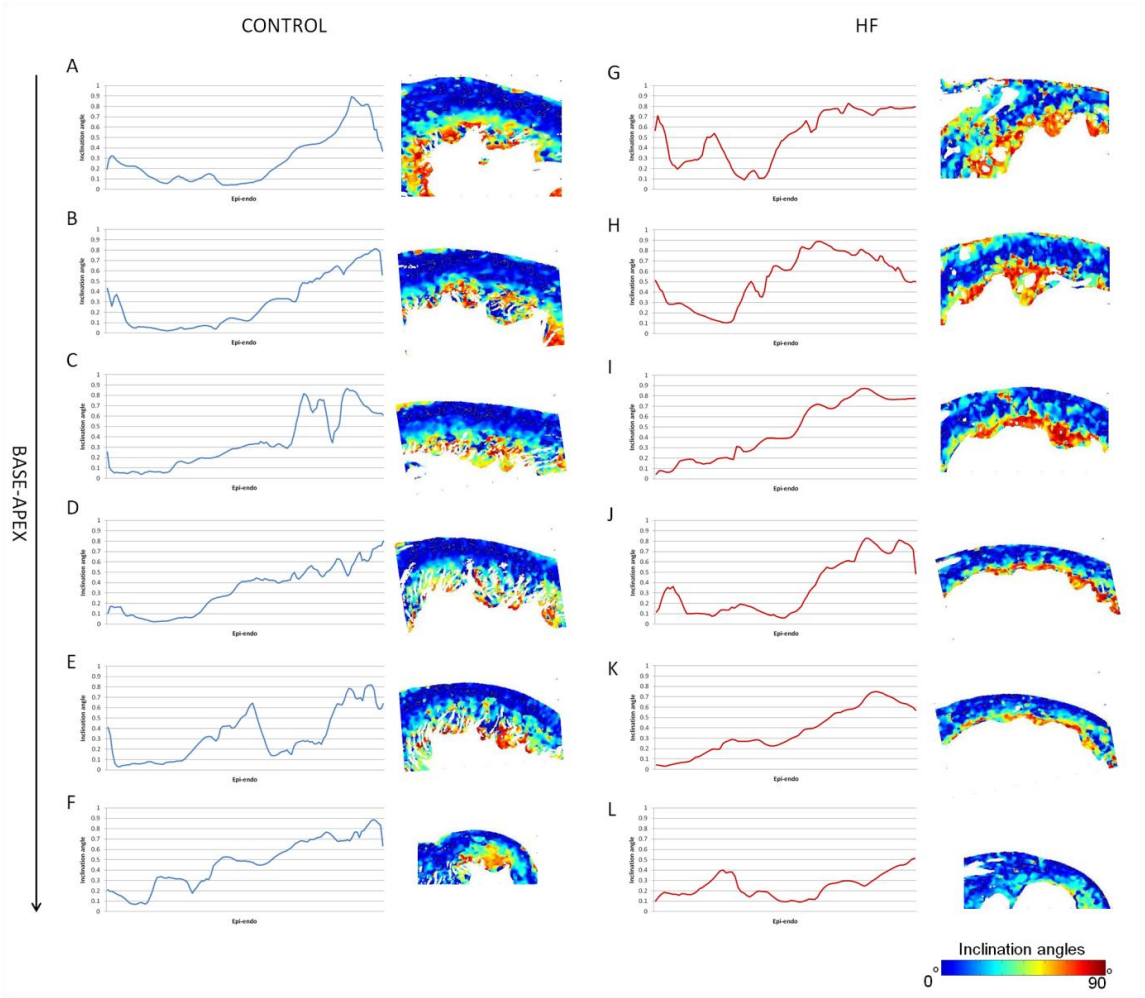

Figure 8.20 Transmural plots and colour maps of fibre inclination angle in the left ventricular posterior wall in control and heart failure. Mean inclination angles from each transmural plane (parallel to epicardial wall) within a segment were extracted from micro-CT data at 7 transverse intervals base-apex (intervals 2-7 shown); a representative control (A-F) and heart failure (G-L) sample are shown. In each region at every interval a ~650µm (~30 voxels) wide transmural segment was taken for analysis. (Colour bar indicates inclination angles).

8.5.5 Regional transmural changes in fibre orientation in the interventricular septum

As with the full transmural analysis, there was no base to apex trend evident in the IVS transmural mid-wall fibre orientation. In a healthy heart the transmural mid-wall should predominantly consist of circumferential running fibres. In HF the transmural mid-wall mean inclination increased at all intervals in HF (except interval 6), with significant increase observed at intervals 3 and 5 (figure 8.21A). The percentage of circumferential fibres in the transmural mid-wall was similar in both control and HF, the only significant decrease in HF was at the base (interval 3) (figure 8.21B). This suggests that although there is a similar percentage of fibres falling under the circumferential classification (0.1-0.3), fibres falling outside of this classification are more vertical in HF. To illustrate this point, histograms showing the distribution of inclination fibre angles at intervals (2-4) were plotted; two representative samples are shown in figure 8.22. There is a clear increase in the number of fibres with an inclination angle ranging from 0.4-0.7, and clear decrease in the number of circumferential fibres (0.1-0.3) in HF. Transmural plots (~650μm wide segment) and colour maps of inclination angles from intervals 2-7 illustrate the findings in two representative samples (figure 8.23). Colour maps indicate a reduced number of circumferential fibres (dark blue) within the transmural mid-wall in HF, and this is reflected as disordered inflections at the mid-wall and LV endocardial region in the transmural plots (figure 8.23). So, in HF the central band of circumferential running fibres within the transmural mid-wall became narrower, and fibres outside the central band became more vertical (figure 8.23).

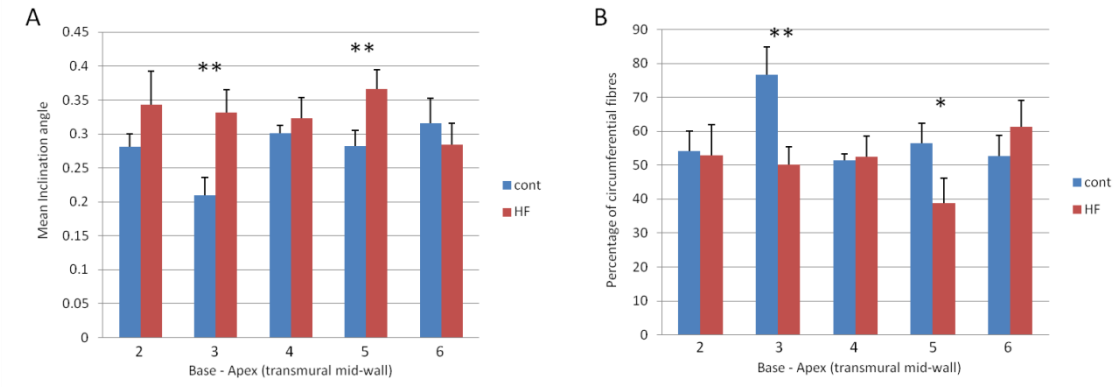

Figure 8.21 Regional changes in inclination angle of fibres in the transmural mid-wall of the interventricular septum in control and heart failure. Mean Inclination angles from the transmural mid-wall (middle $^{2}/_{4}$ of wall) (A) extracted from micro-CT data at 7 transverse intervals base-apex (intervals 2-6 shown). Corresponding percentage of circumferential (values 0.1-0.3) fibres in the transmural mid-wall (B). In each region at every interval a ~650µm (~30 voxels) wide transmural segment was taken for analysis. (Control n=5, HF n= 6, *p=<0.1, **p=<0.05). Error bars indicate standard error of the mean (SEM).

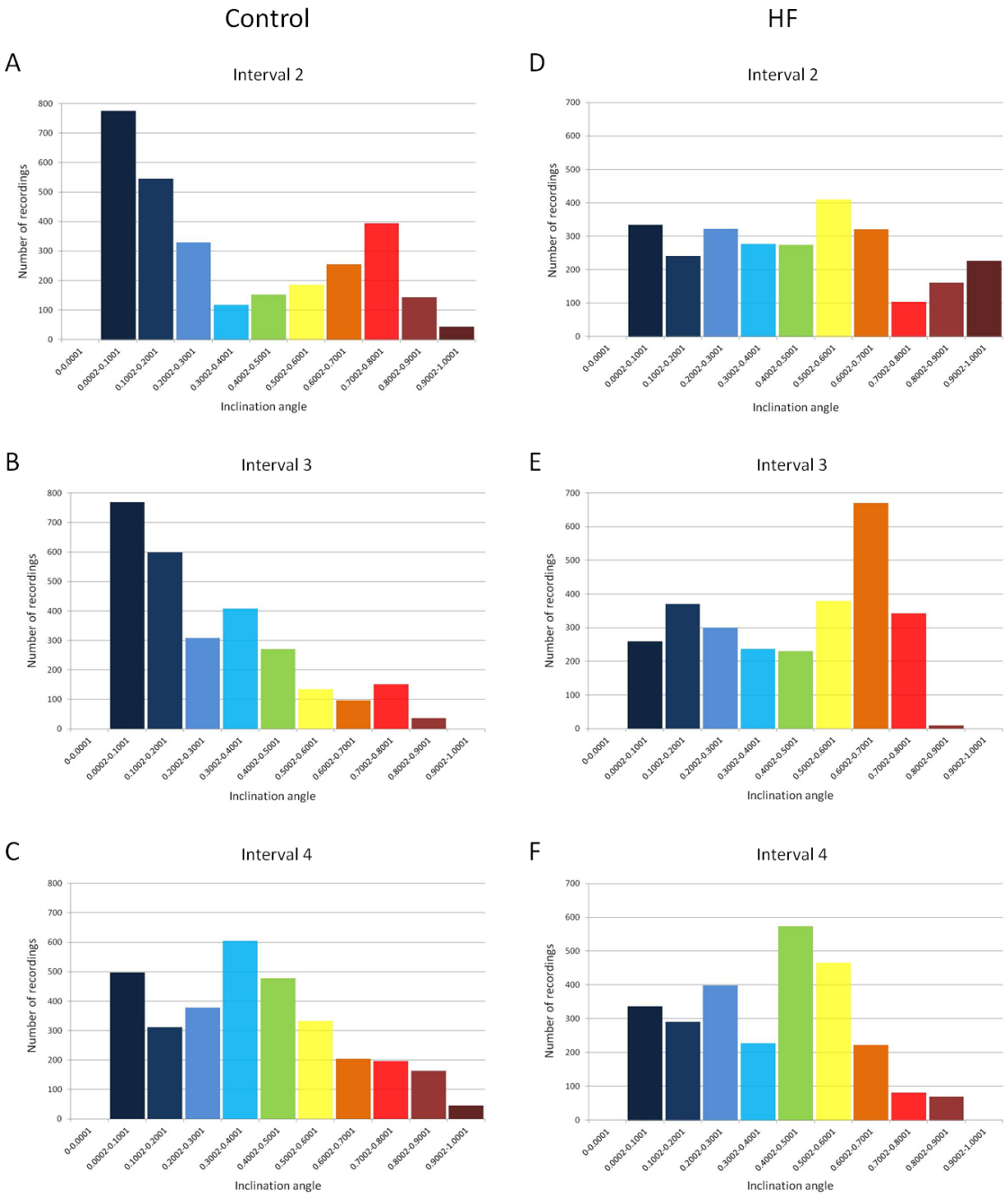

Figure 8.22 Distribtion of inclination fibre angles in the interventricular septum in control and heart failure. Histograms showing the distribution of inclination fibre angles at the base and mid-wall (intervals 2-4) in two representative samples; control (A-C), heart failure (D-F).

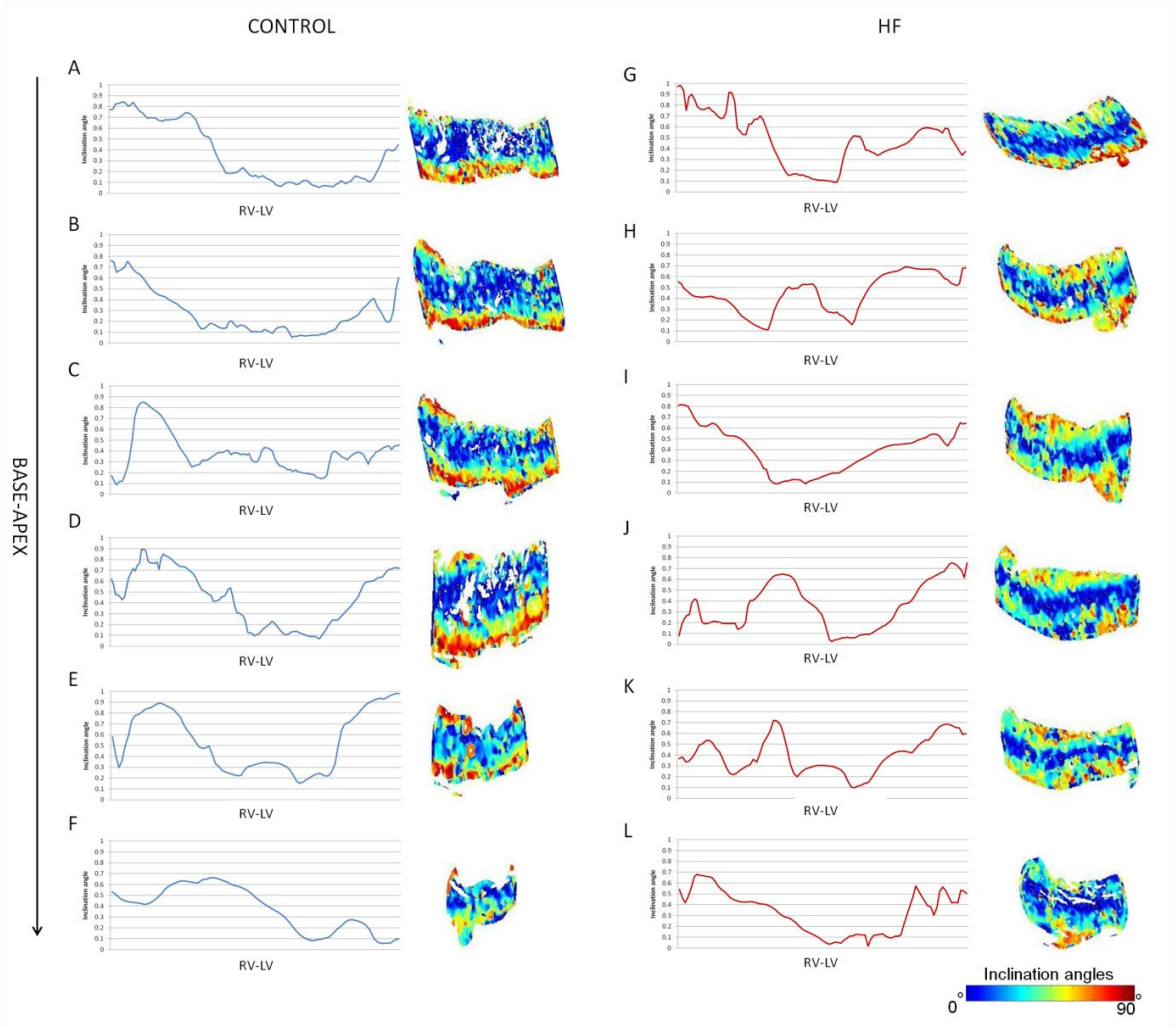

Figure 8.23 Transmural plots and colour maps of fibre inclination angle in the interventricular septum in control and heart failure. Mean inclination angles from each transmural plane (parallel to endocardial wall) within a segment were extracted from micro-CT data at 7 transverse intervals base-apex (intervals 2-7 shown); a representative control (A-F) and heart failure (G-L) sample are shown. In each region at every interval a ~650µm (~30 voxels) wide transmural segment was taken for analysis. (Colour bar indicates inclination angles).

8.5.6 Changes in fibre orientation at the base and mid-wall in heart failure

3D scatter graphs were plotted using both inclination and transverse angles, this allowed for a true impression of the 3D course of fibres transmurally. Inclination and transverse angles were extracted for each pixel from identical ~650μm wide transmural segments. The mean angles at each transmural plane within a segment were then calculated and plotted using 'excel 3D scatter plot' v.2.0 (excel 2007). Figure 8.24 shows 3D plots of data taken from the LVPW at the basal region (interval 3) of 3 control (figure 8.24 A,B,C) and 3 HF (figure 8.24 D,E,F) samples. 3D fibre orientation in control samples appeared as expected; the classical transmural helical arrangement was observed, with small transmural deviation in the mean tilt (transverse angle) of fibres. In HF inclination angles at the endocardium, subendocardium and transmural mid-wall were increased considerably. In HF, the regions of increased inclination angle were accompanied by a reduction in transverse angle, particularly at the subendocardium and transmural mid-wall (figure 8.24 D,E,F). This suggests the LVPW is prone to changes in fibre orientation in dilatated remodelling (seen at the base and mid-wall). Muscle fibres in dilated regions became more vertical in orientation accompanied by a reduction in tilt in relation to the longitudinal plane (figure 8.26 A,B). These changes in morphology are a possible cause of the observed loss of LV function seen in HF samples.

Figure 8.25 shows 3D plots of data taken from the IVS at the basal region (interval 3) of 3 control (figure 8.25 A,B,C) and 3 HF samples (figure 8.25 D,E,F). 3D Fibre orientation in the IVS was less ordered in HF samples. Inclination angles at the transmural mid-wall were seen to be increased in HF, this was accompanied by irregular changes in corresponding transverse angles. These sharp changes in transverse angles at the transmural mid-wall were not observed in control samples. In control there was an apparent increase in transverse angle at the transmural mid-wall and subendocardium, transverse angles were smaller in these regions in HF (figure 8.25). This suggests that the usually circumferential fibres of the transmural mid-wall have become more vertical and disordered, with a reduction in tilt in HF (figures 8.25 D,E,F, 8.26 C,D). (Mean fibre angles and significance values for the regions investigated using 3D plots can be found in the appendix)

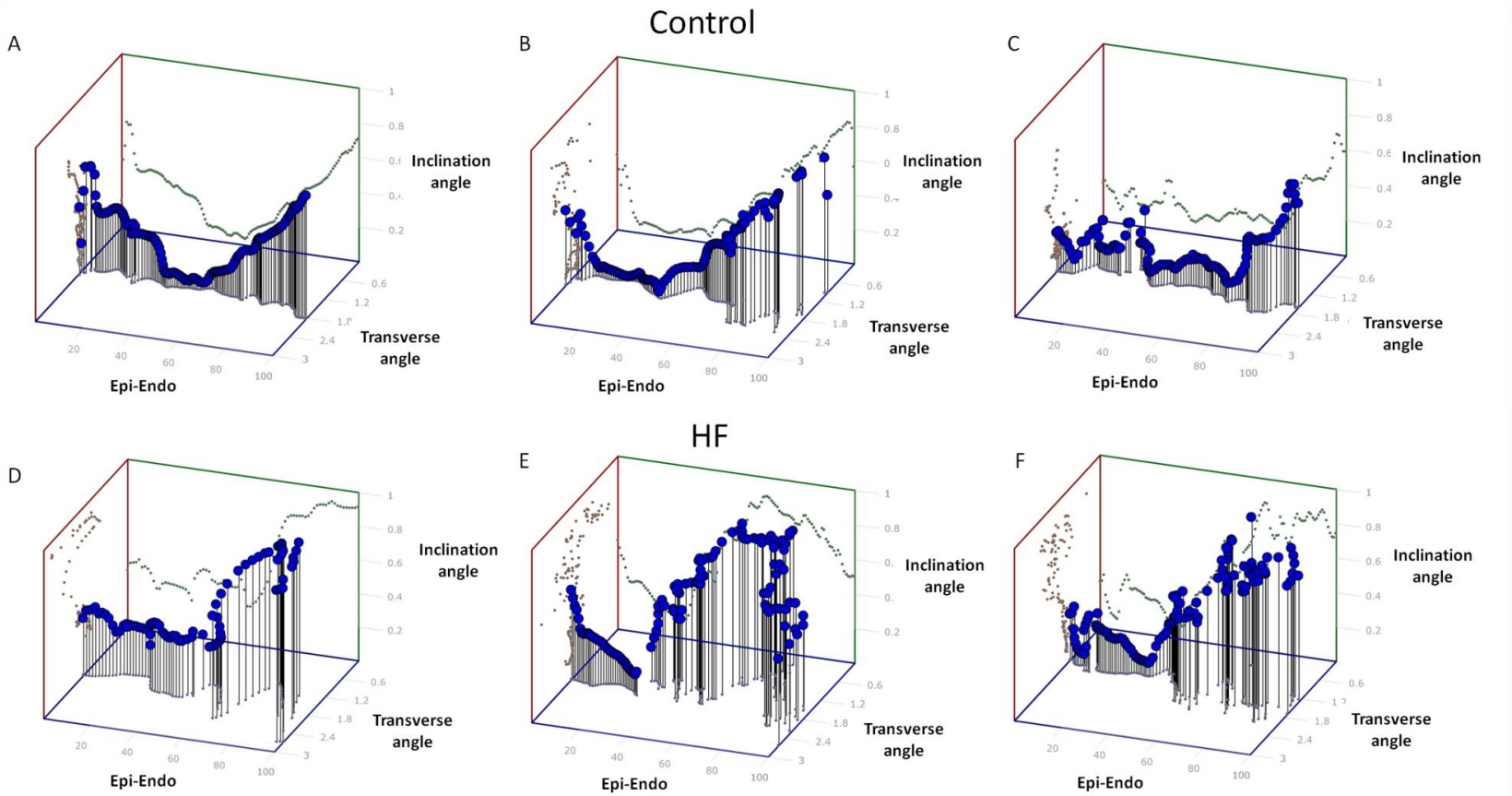

Figure 8.24 Transmural 3-D scatter plots of changes in inclination and transverse fibre angles at the basal region of the LVPW in heart failure. Mean inclination and transverse angles from each transmural plane (parallel to epiocardial wall) within the LVPW segment were extracted from micro-CT data at interval 3 and plotted; representative samples from control (A,B,C) and HF (D,E,F) samples are shown. 3D fibre orientation in control samples appeared as expected; the classical transmural helical arrangement (A,B,C). In HF muscle fibres in the endocardium became more vertically orientated, accompanied by a reduction in transverse angle. LVPW- left ventricular free wall.

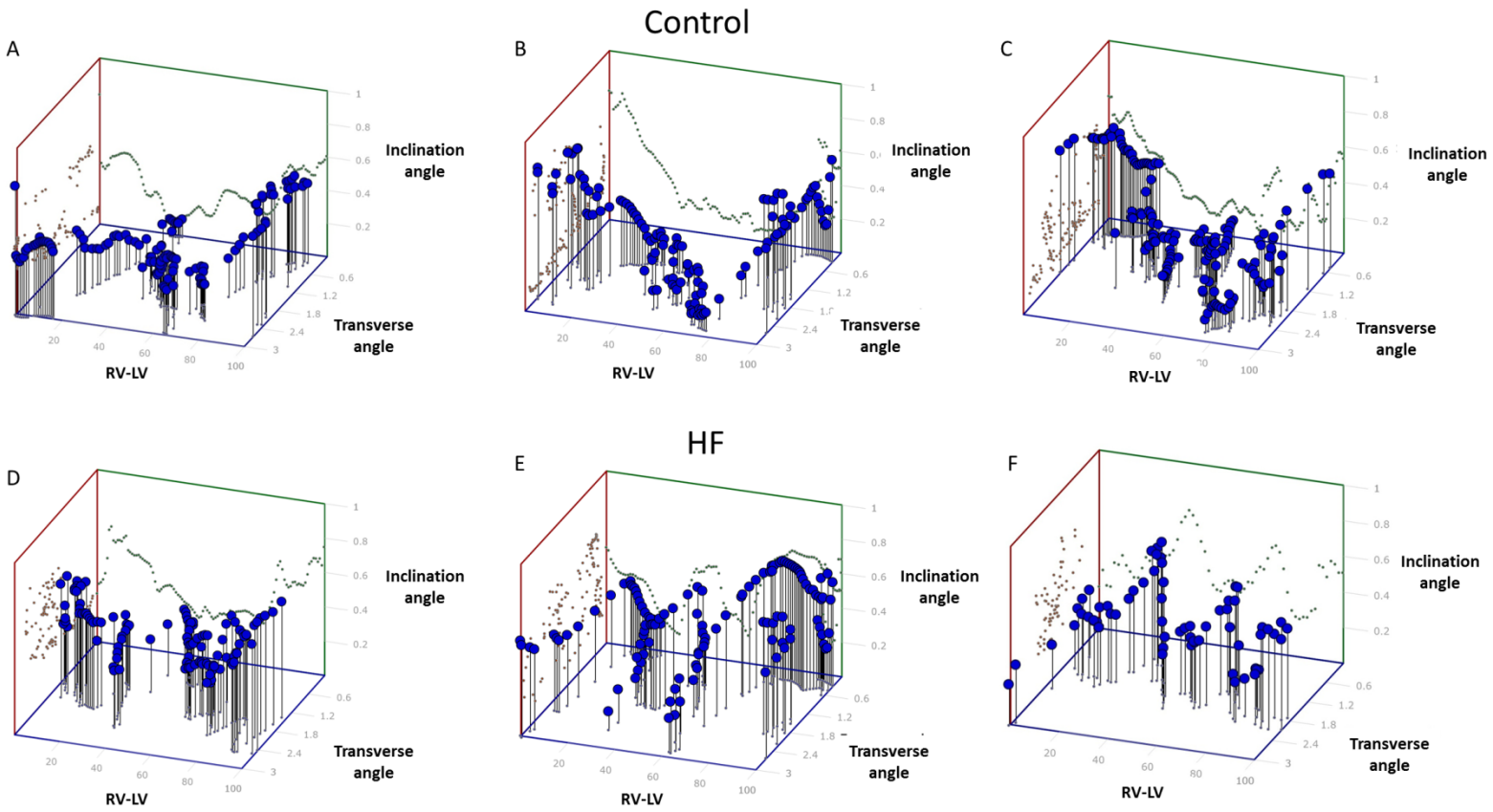

Figure 8.25 Transmural 3-D scatter plots of changes in inclination and transverse fibre angles at the basal region of the IVS in heart failure. Mean inclination and transverse angles from each transmural plane (parallel to endocardial wall) within the IVS segment were extracted from micro-CT data at interval 3 and plotted; representative samples from control (A,B,C) and HF (D,E,F) samples are shown. 3D Fibre orientation of the IVS was less ordered in HF. Inclination angles at the transmural mid-wall were seen to be increased in HF, this was accompanied by irregular changes in corresponding transverse angles (D,E,F). IVS- interventricular septum.

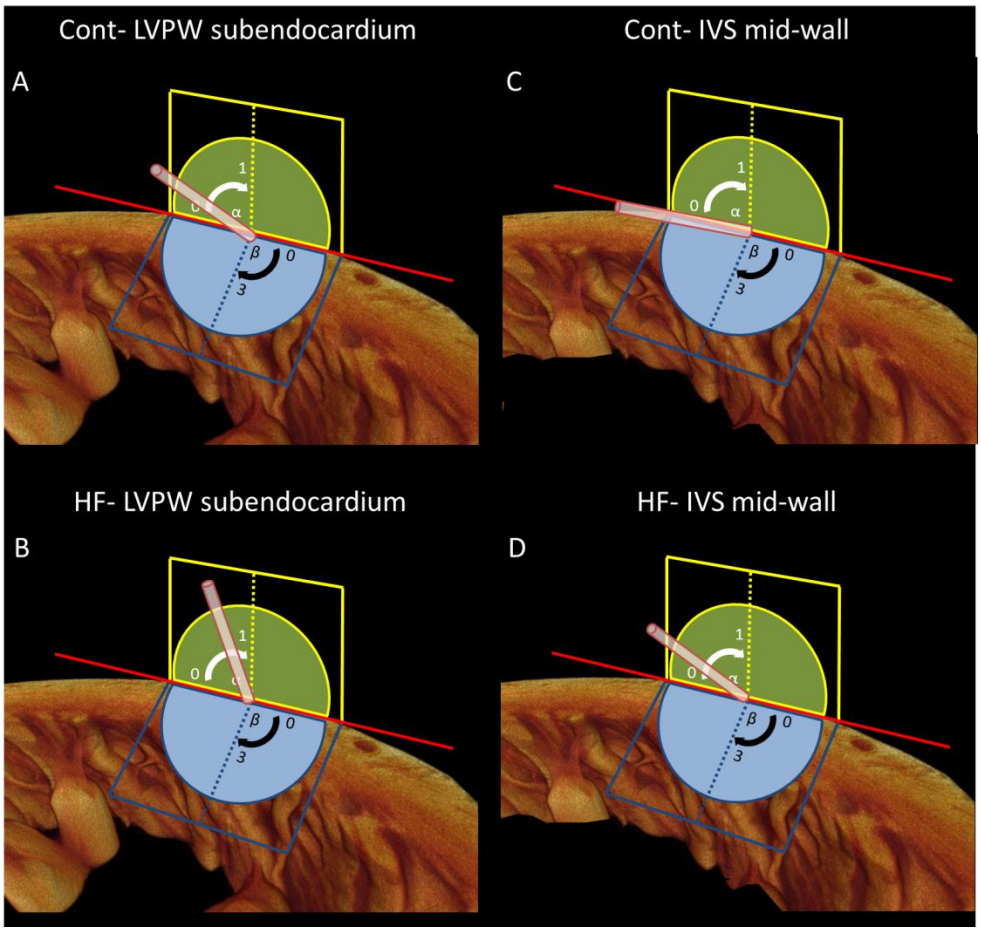

Figure 8.26 3-dimensional schematic representations of general changes in fibre orientation at the left ventricular posterior wall and interventricular septum in heart failure. General 3D fibre orientation at the base and mid-wall (intervals 2-4) in the subendocardium of the LVPW (A,B) and IVS transmural mid-wall (C,D) in control (A,C) and HF (B,D). IVS- interventricular septum, LVPW- left ventricular posterior wall.

8.6 Validation of the use of contrast enhanced micro-CT to investigate cardiac morphology *ex vivo*.

To assess the validity of using micro-CT to investigate morphological changes in cardiac tissue *ex vivo*, micro-CT data (n=9) was compared with corresponding pre-termination echocardiography readings. Micro-CT data was manipulated into a position that reflected the parasternal long axis view used for echocardiography, and measurements were made corresponding to the LVID, IVS and LVPW echo readings. Micro-CT measurements were compared with both systolic (s) and diastolic (d) echo readings, and t-tests were used to analyse statistical significance of

results. In both control and HF hearts micro-CT LVID measurements closely resembled LVIDs (figure 8.27), and were significantly different from LVIDd (control- p=<0.05, HF- p=<0.005). However, wall thickness measurements (IVS, LVPW) revealed the myocardium was in a diastolic state (figure 8.27). Measurements were significantly different from IVSs (control- p=<0.01, HF- p=<0.05) and LVPWs (control- p=<0.001, HF- p=<0.05) echo readings. To assess the level of agreement between micro-CT and echocardiography measurements Bland Altman analysis was conducted (table 8.3); low bias values with small standard deviation (SD), and a small confidence interval indicates good reproducibilty. Low bias levels were observed when micro-CT IVS and IVSd, and micro-CT LVPW and LVPWd were compared (-0.02 and 0.02 respectively), this was accompanied by small confidence intervals (-0.09 to 0.04 and -0.13 to 0.017 respectively). In contrast, a high level of bias (-0.64) and large confidence interval (-1.26 to -0.01) was seen when micro-CT LVID and LVIDd echo measurements were compared. This suggests, when scanned the hearts are in a relaxed state which is not over inflated.

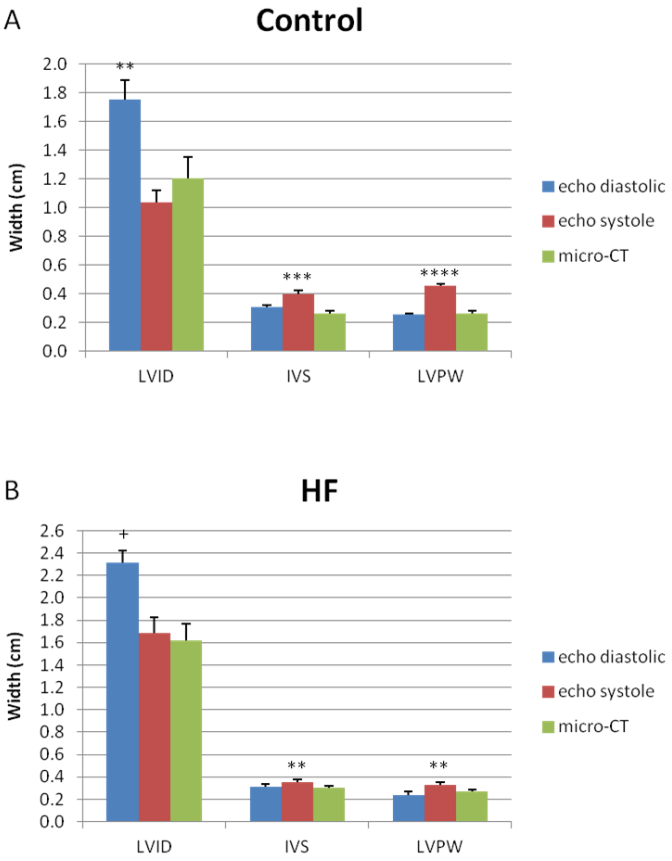

Figure 8.27 Comparison of left ventricular cavity and wall widths obtained by echocardiography and micro-CT. To assess the validity of using micro-CT to investigate morphological changes in cardiac tissue *ex vivo*, pre-termination echocardiography readings from systole and diastole were compared with corresponding micro-CT measurements (n=9). (**p=<0.05, ***p=<0.01, +p=<0.005, ****p=<0.001). Error bars indicate standard error of the mean (SEM). LVID- left ventricular internal dimension, IVS- interventricular septum, LVPW- left vetricular posterior wall.

Table 8.3- Bland-Altman analysis investigating level of agreement between micro-CT and echocardiographic morphological measurements.

	Bias	SD of Bias	95% confidence interval of difference between micro-CT and echo measurements
LVID micro-CT **vs** LVIDd	-0.64	0.31	-1.26 to -0.01
IVS micro-CT **vs** IVSd	-0.02	0.03	-0.09 to 0.04
LVPW micro-CT **vs** LVPWd	0.02	0.07	-0.13 to 0.17

IVS-CT and IVSd- interventricular septum width from micro-CT and echo diastolic measurements, LVID-CT and LVIDd- left ventricular internal dimension from micro-CT and echo diastolic measurements, LVPW-CT and LVPWd- left ventricular posterior wall width from micro-CT and echo diastolic measurements. SD- standard deviation.

8.7 Discussion

HF and the associated morphological and functional abnormalities are a major contributor to morbidity and mortality in the western world (Leonard et al., 2012, McDonagh et al., 2011). The morphological and functional effects of volume or pressure overload on the ventricles are well documented in the scientific literature (Gaasch and Zile, 2011, Opie et al., 2006). However, the effects of a combination of both volume and pressure overload on the whole heart (atria and ventricles) is not so well documented (Hasenfuss, 1998). Here using *in vivo* and *ex vivo* imaging, we investigated the global and regional effects of volume and pressure overload on the whole rabbit heart (atria and ventricles).

8.7.1 Is the gross morphology of the heart changed in heart failure?

Changes in cardiac morphology due to overload usually involve chamber dilatation and/or hypertrophy; a process often referred to as cardiac remodelling (Hunt et al., 2005, Opie et al., 2006). Pressure overload is traditionally characterised by myocardial hypertrophy with little chamber dilation, and is often categorised as concentric hypertrophy. In contrast, volume overload brings about myocyte stretching and only modest hypertrophy, causing dilatation of the ventricle cavity, and is categorised as eccentric hypertrophy (Opie et al., 2006). However studies have revealed cardiac remodelling is a complex process, which is progressive and unique

to the inciting overload (Grossman et al., 1975). As a result numerous attempts to better categorise cardiac remodelling have been presented (Opie et al., 2006). The effects of pressure and volume overload are often assessed as separate entities, with few investigating a combination effect (Gilson et al., 1990, Pogwizd, 1995, Hasenfuss, 1998). Furthermore, studies often ignore the remodelling effects of overload on the atria (Gilson et al., 1990, Pogwizd, 1995). Here we look at the morphological effects of both pressure and volume overload on the whole heart, and show the necessity to categorise the observed remodelling regionally.

Atria-

In the literature there are few detailed descriptions of the remodelling of atrial morphology in HF. This may be due to the fact that 3D high resolution morphological data of the whole atria is only achievable with *ex vivo* imaging techniques, and also requires the atria to be fixed in their naturally inflated state, which is technically difficult. We have previously shown a perfusion fixation technique which facilitates imaging of the detailed morphology of the atria (Chapter 5) (Jarvis and Stephenson, 2013). Here we assess changes to atrial morphology in HF and present data that is consistent with clinical data (Corradi et al., 2011, Sallach et al., 2009, Tsang et al., 2002), and provide novel insight into atrial remodelling. All regions of the atria showed an increase in tissue volume in HF, the biggest increase was observed in the LA, this is to be expected in a model directly affecting the left side of the heart, and consistent with previous studies (Tsang et al., 2002, Corradi et al., 2011). Remodelling of the PcMs and the corresponding atrial wall in HF is poorly represented in the literature, here we show these structures are modified in HF, and reveal contrasting remodelling in the right and left atria. Wall thickness was not increased in HF, although there was a suggestion of wall thinning in regions of the LA. The lack of a hypertrophic response (in contrast to the ventricles) may be due to the atria's inherent structural weakness compared to the ventricles (see Chapter 5) making them more susceptible to stretch, also the atrial wall has been shown to be more prone than the ventricles to apoptosis and myocyte death in HF (Hanna et al., 2004). In contrast, hypertrophy of the PcMs was observed in both the RA and LA in HF. Data suggests the mean and maximum PcM widths are increased in HF. Increased PcM width in HF was more considerable in the mid-wall of the atria than the extreme inferior and superior intervals. This suggests that the free running

portions of PcMs are more prone to hypertrophy than their insertion points, possible due to stretch induced hypertrophy (Blaauw et al., 2010, Ruwhof and van der Laarse, 2000).

Total atrial cavity volume more than doubled in HF, clearly showing dilatation. This is probably due to an increase in atrial pressure because of increased end systolic volume, and therefore congestion upstream, leading to increased wall tension which increases myocardial stretching (Corradi et al., 2011, Spotnitz, 2000). However, morphological changes between the RA and LA were not uniform. The RAA showed greater relative dilatation than the LAA. This could be attributed to the reduced structural integrity of the RAA compared to the LAA; the RAA has comparably thin walls, and thin PcMs which have weaker connections with the atrial free wall (see Chapter 5). Also an excessive increase in central venous pressure due to LV dysfunction could increase wall tension in the RA, enhancing myocardial stretch. LAA dilatation is probably due to the observed hypertrophy of the RV which will increase LA preload, thus increasing wall tension (Levick, 2003, Loushin et al., 2009, Spotnitz, 2000).

Ventricles-

In vivo echocardiography showed all wall measurements were increased in HF (except LVPWs). Micro-CT data revealed the total myocardial volume was significantly increased in HF compared to control (28%). Regional analysis showed significant increases in the RV (84%), IVS (62%) and LV (64%). This level of hypertrophy is consistent with previous studies using a similar model of HF (Gilson et al., 1990, Pogwizd et al., 2001). Pre-termination measurements revealed LVID was significantly increased in HF in both systole and diastole. This morphological change is characteristic of volume overload brought about by regurgitation at the aortic valve (Gaasch and Zile, 2011, Opie et al., 2006). Increased dilatation of the LV was evident in HF at aortic banding and pre-termination in both systole and diastole. There was no inflection at aortic banding, therefore dilatation was progressive for both diastole and systole. The change was most dramatic in systole, representing the progressive inability of the myocardium to reduce the LV cavity, and produce the systolic myocardial bulking needed for a healthy stroke volume. This is supported by the progressive loss of function observed (progressive reduction in EF and FS) and

suggests that the acute nature of the model did not allow for a compensated response; rather changes resembled chronic decompensated HF (Opie et al., 2006).

8.7.2 Do changes in cell morphology match gross changes in volume?

The percentage increase in cell size in the RA (60%) in HF matched closely with the percentage increase in volume calculated from micro-CT data (59%). However in the ventricles the percentage increases in cell size were considerable different to the total volume increases (LV- 25% vs 64%, RV- 21% vs 84%). This suggests an increased deposition of extracellular matrix or fibrosis in the ventricles. Increased fibrosis is well documented in HF (Leonard et al., 2012), but histological analysis conducted by colleagues on samples from the same HF model suggests there is no increase in extracellular matrix in the atria or ventricles at post termination (Quigley et al., unpublished data). However, PCR analysis did show upregulation of markers for fibrosis (Quigley et al., unpublished data).

8.7.3 Are there regional differences in cardiac remodelling in heart failure?

Ventricles-

Many studies of cardiac remodelling ignore regional changes in cardiac morphology (Gilson et al., 1990, Pogwizd, 1995). The results presented here highlight the need to assess changes across the whole heart. Although the observed scaled hypertrophy suggests a compensated response, this does not accurately represent the heart's response to HF; further analysis revealed a region specific response. In HF the IVS showed thinning in the base, mid-wall and apical intervals, with significant thinning seen in the mid-wall. An interesting relationship was observed in the LV wall thickness in HF; thinning was observed in the base and mid-wall, followed by thickening of the wall towards and including the apex, this is a reverse of the relationship seen in normal hearts (Ho, 2009). There were no regional differences in wall thickness within a single interval (transverse plane), showing the observed changes in response to experimental HF are uniform throughout the LV wall at each interval. Significant increase in cavity cross sectional area was observed at all

intervals of the LV in HF. The most dramatic changes occur at the base and mid-wall, which corresponded to regions where LV wall thinning was observed. A decline in cavity cross sectional area was seen in the apical region, which corresponded to areas of LV wall thickening. This clearly shows regional specific morphological changes occur in the LV in response to volume and pressure overload. This data suggests HF samples can be classified regionally, with the base and mid-wall (majority of the heart) undergoing eccentric hypertrophy, and the apex undergoing mixed hypertrophy (Gaasch and Zile, 2011). Plastic dilatation (dilatation without hypertrophy) (Linzbach, 1960) was observed at intervals 5-6, which demarcates the transition from the mid-wall to apex. Data suggests the base and mid-wall are more prone to stress, while the apex can produce a more compensated response. Remodelling at the base and mid-wall is an example of when maladaptive responses overpower adaptive responses (Meerson, 1962) (see section 8.7.7).

8.7.4 How is the shape of the ventricles affected in heart failure?

Volume overload has been shown to induce the heart to become more spherical, a morphological changed linked to dilatation and ventricular dysfunction (Kono et al., 1992, Opie et al., 2006). Here there was no difference in sphericity between control and HF, with mean values appearing almost identical. This suggests that although HF hearts have undergone considerable LV dilatation, compensated shape changes have occurred to maintain a healthy ellipsoidal shaped heart. Although sphericity did not change in HF across the whole heart, regional LV cavity cross sectional area and coefficient of determination (R^2) analysis suggests region specific changes in sphericity did occur. With the heart becoming more spherical at the base, while the apex remained within the normal range. Data from Donato et al 2006 shows the method implicated in the present study cannot identify regional changes, as a result apical conicity index (ACI) should be employed in future analysis (Di Donato et al., 2006).

The effect of HF on the endocardial trabeculation cannot be appreciated in statistical analysis presented here. However, 3D isosurfaces revealed a reduction in the depth and complexity of endocardial trabeculae in the LV of HF samples. This suggests dilatation of the ventricles in HF stretches and flattens the trabeculae carnae. Studies

into trabeculae morphology (Fernandez-Golfin et al., 2009) show hypertrophy takes place in disease, however these studies do not asses shape change.

8.7.5 Variation in the degree of remodelling in heart failure

The morphological changes observed among the HF samples were considerably variable. This is thought to be attributed to the aortic valve disruption procedure, as remodelling depends on severity and duration of overload (Gaasch and Meyer, 2008), and the procedure is difficult to standardise. However, varying responses to volume and pressure overload have been previously documented (Pogwizd, 1995).

8.7.6 What are the changes to the right side of the heart in left sided heart failure?

In investigations of HF, the main focus is traditionally on the morphology and function of the left ventricle. Therefore, information on cardiac remodelling and the pathophysiology of the RV in left sided HF is limited in the current literature (Brieke and DeNofrio, 2005). It is suggested that the RV response to chronic pressure overload is similar to that of the LV; RV hypertrophy is observed in response to increased wall stress and eventually dilatation develops, and as afterload increases RV dysfunction and failure follow (Brieke and DeNofrio, 2005). In the present study the response of the RV was contrasting to the LV. In control hearts, as expected the mean RV cavity volume exceeded the LV, however this relationship was dramatically reversed in HF. An increase in the RV cavity volume was observed but data was not statistically significant. RV cavity cross sectional area was increased in HF from intervals 2-8 (base-apex), however, only interval 8 was statistically significant. However, significant thickening of the RV wall was observed at all intervals in HF, with the greatest wall thickness seen at the base. These results suggest concentric remodelling of the RV in HF. The lack of regional differences confirms concentric hypertrophy occurred across the whole of the RV. This is in contrast to the LV where substantial regional differences were observed (see above). This response is to be expected as LV dysfunction is linked with increased pulmonary pressure, which has been shown to induce RV hypertrophy due to increased afterload (Levick, 2003, Loushin et al., 2009, Spotnitz, 2000). The RV appears to produce a chronic compensated response in HF in contrast to the chronic

decompensated response generally seen in LV. This could be explained by the model having an acute effect on the left side of the heart, while the effect on the right side of the heart develops more slowly.

8.7.7 What are the functional implications of the observed cardiac remodelling?

Atria-

Heart failure has a structural basis and causes substantial myocardial remodelling of the atria. It is well known that increased LA size (dilatation) is a major risk factor for various pathological conditions including; atrial fibrillation and death in subjects with dilated cardiomyopathy (Benjamin et al., 1995, Muller et al., 2003, Solti et al., 1989, Corradi et al., 2011). LA size also increases in the presence of volume and pressure overload, and LV dysfunction (Abhayaratna et al., 2006). This supports our findings and suggests the changes in morphology seen in the HF samples make them more prone to pathology. Furthermore LA volume increase (hypertrophy) and dilatation have been shown as accurate markers for HF (Gottdiener et al., 2006).

Global morphological changes to the myocardium are strongly linked to arrhythmogenesis and electrical dysfunction (Smaill et al., 2013), and the morphological changes observed here are likely to make the atria more prone to such electrical abnormalities. Tissue that has undergone dilatation has been shown to have increased vulnerability to the generation of rotors associated with arrhythmogenic activity (Yamazaki et al., 2012). In addition pressure overload which elicits hypertrophy is clinically associated with conduction abnormalities (Harris et al., 2012). Furthermore it is expected that stretch reduces cell coupling which can cause retrograde propagation (Shaw and Rudy, 1997) and slow conduction which can support re-entry (Rohr et al., 1998).

Changes in morphology on a small scale can also affect electrical function. Conduction in all regions of the heart is determined by the balance between current source and passive current load, known as source-sink matching (Smaill et al., 2013). Abrupt changes in wall thickness and fibre orientation has been shown to contribute to source sink mismatch and electrical dysfunction (Zhao et al., 2012, Auerbach et al., 2011, Cabo et al., 1994). Reverse source-sink has also been describe at the

proximal region of the AVN (Nikolaidou et al., 2012). However transitional tissues increase the safety factor in these regions (Dobrzynski et al., 2013). We postulate that reverse source sink mismatch is increased at the PcM-atrial wall interface in HF. The pectinate muscle width to atrial wall width ratio (PcM:W) was considerably increased in both the RA and LA in HF, meaning the difference between the thick PcMs and thin atrial walls increased. Therefore the atria in HF will be more prone to reverse source sink mismatch and thus electrical dysfunction and arrhythmias. The biggest increase in PcM:W was seen in the LA, suggesting the LA is more vulnerable to electrical dysfunction than the RA, and this notion is supported by clinical data (Letsas et al., 2011).

Ventricles-

Cardiac remodelling can be compensated or decompensated (Gaasch and Zile, 2011, Opie et al., 2006), but how alterations in structure truly affect function is an on-going discussion (Anderson et al., 2006, Anderson et al., 2008, Gaasch and Zile, 2011). Early stage remodelling to both pressure (Grossman et al., 1975, Gaasch and Zile, 2011) and volume overload (Gaasch and Meyer, 2008, Opie et al., 2006) has been shown to be compensated, in that normal EF% is maintained. However such remodelling is usually due to the progressive nature of the overload presented (Lamb et al., 2002, Opie et al., 2006). Therefore the decompensated remodelling observed here is likely to be due to the acute nature of the model, and the fact that remodelling is associated with the severity and duration of overload (Grossman et al., 1975, Roeske et al., 1976). In the current study no compensated response was evident in the LV from *in vivo* echocardiography data. Reduced FS (~ 50% loss of function) in the LV was observed in HF.

Our morphological data shows HF samples can be classified regionally, with the majority of the heart undergoing eccentric hypertrophy, which is strongly associated with a low EF% (Khouri et al., 2010), and thus decompensated HF. At termination EF was significantly reduced in HF (28% reduction). However, due to Starling's law (see introduction 1.4.3.1) dilatation can act as a compensated response in HF (Levick, 2003, Spotnitz, 2000). But excessive preload in the absence of hypertrophy causes; overdistension due to increased wall stress, and loss of contractility due to the length tension relationship, ultimately causing a reduction in stroke volume. In

the current model excessive preload will be present in the LV due to both aortic regurgitation and increased pulmonary pressure. This offers an explanation for the observed dilatation, wall thinning and loss of function in HF samples. The idea of a compensated response occurring at the apex of the LV is supported by the presence of reduced dilatation and more importantly hypertrophy, this will increase contractility and in the presence of increased preload will bring stroke volume back towards the normal range. However it is postulated the overall loss of LV function is probably due to the majority of the heart (base and mid-wall) having a decompensated phenotype, which outweighs the compensated response at the apex. Laplace's law (see introduction 1.4.3.1) therefore dominates the majority of the heart in HF samples.

Afterload-velocity and afterload-shortening curves suggest contractility is reduced in the presence of excessive afterload (see introduction 1.4.3.1). Therefore, in the current model aortic banding will be a major contributor to the observed loss of function (Levick, 2003, Loushin et al., 2009). To supress the effect of increased afterload, the LV must increase its contractility through a hypertrophic response. This further supports the thought that a decompensated response has occurred at the base/mid-wall and a compensated response at the apex.

8.7.8 Is fibre orientation changed in Heart failure?

The detailed study of Pettigrew (Pettigrew, 1864) showed that the long axis of myocytes changes in angulation across the ventricular wall relative to the ventricular equator. This so-called helical arrangement came to prominence due to the investigations of Streeter (Streeter and Bassett, 1966, Streeter et al., 1969). The angle of fibres rotates clockwise from -80° at the epicardium to +80° at the endocardium, with the mid-wall consisting of fibre running primarily circumferentially (Greenbaum et al., 1981, Streeter et al., 1969). The 3D morphology of fibre orientation cannot be fully appreciated using histology (Greenbaum et al., 1981, Streeter et al., 1969) or peeling (Dorri et al., 2007) due to the inability to view the long axis of the myocytes in all their orthogonal planes. Fibre orientation must be described in terms of both inclination (helical) and transverse (intrusion) angle, and should be considered as an anisotropic mesh of fibres (Anderson et al., 2008,

Bovendeerd et al., 1994, Geerts et al., 2002, Smerup et al., 2009). Here we have extracted 3D fibre angles, including both helical and transverse angles, from the ventricles of control and experimental HF hearts. Our findings show consistencies with previous descriptions of fibre orientation in control hearts (Dorri et al., 2007, Geerts et al., 2002, Lunkenheimer et al., 1997a, Streeter et al., 1969), and provide novel insight into how fibre orientation is changed regionally in response to cardiac remodelling. Emphasis is placed on regions of dilatation.

3D fibre orientation analysis showed that the regions which underwent the greatest amount of dilatation and wall thinning (the base and mid-wall), were the most prone to changes in fibre orientation. Fibres of LV and IVS in these regions became more vertically orientated, accompanied by a reduction in tilt (transverse angle). Findings show consistent patterens with other studies of fibre orientation in HF using histology and DT-MRI (Carew and Covell, 1979, Clayton et al., 2010, Eggen et al., 2009, Kuribayashi and Roberts, 1992), but are conflicting with others {Schmitt, 2009 #432}, and some studies report no difference (Nielsen et al., 2009, Pearlman et al., 1981). Regional transmural analysis revealed significant changes at the base and mid-wall in the failing LVPW. The regions of increased inclination angle were accompanied by a reduction in transverse angle, particularly at the subendocardium and transmural mid-wall. In the IVS the fibres running within in the transmural mid-wall changed significantly; in HF the central band of circumferential running fibres within the transmural mid-wall became narrower and disorganised, and fibres outside the central band became more vertical. These changes in HF could be a substrate for the observed loss of ventricular systolic function, but it is postulated they will also contribute to diastolic dysfunction (see below).

Most studies of fibre orientation in pathological hearts concentrate on changes in the helical angle. The few studies that have looked at changes in the transverse or intrusion angle have looked at hypertrophic hearts; Lunkenheimer et al. suggests these intruding fibres become more erect in the LV in response to hypertrophy (Lunkenheimer et al., 2006b). Using DT-MRI Schmitt et al. 2009 described regional differences in hypertrophic hearts; an increase in intruding angle was observed at the base, mid-wall, and apex (Schmitt et al., 2009). It should be noted studies of hypertrophy often assume universal change to the myocardium, results presented here regarding regional remodelling suggest this may be erroneous.

Here we show the transverse angled fibres become less erect at the subendocardium in regions of dilatation (LVPW and IVS). To our knowledge this is first time changes in fibre orientation in response to both pressure and volume overload have been investigated, and the first time the change in transverse angle in response to dilatation has been described.

8.7.9 The relationship between fibre orientation and structure in heart failure

Interesting relationships are therefore revealed when changes in fibre orientation are compared to morphological changes. The biggest changes were seen in regions of dilatation and wall thinning (base and mid-wall). While in regions of hypertrophy and moderate dilatation (apex) changes were smaller. The change in fibre orientation in response to dilatation is poorly represented in the literature, with most studies concentrating on the effects of hypertrophy. Our data suggests dilated regions could be the main foci for contractile dysfunction in dilated cardiomyopathies and should a target for therapeutic interventions.

8.7.10 What are the functional implications of the observed changes in fibre orientation?

Systolic dysfunction-

It is difficult to directly relate anatomy to function (Anderson et al., 2008), but the key to understanding true cardiac function in health and disease is in defining the underlying architecture responsible for the contractile mechanism- narrowing, shortening, lengthening, widening and twisting of the heart (Buckberg et al., 2008). In the present study we have observed changes in fibre orientation in HF, below we discuss how such changes may have contributed to the observed loss of function (reduced EF and FS). Due to its homogenous arrangement the functional implications of morphological changes in skeletal muscle are often assessed using the physiological cross sectional area principle (Campbell et al., 2013). This simplistic approach cannot be applied to cardiac muscle due to its heterogeneous structure and dualistic function (Lunkenheimer et al., 1997b, Lunkenheimer et al., 2004). However, insights into cardiac function from traditional studies (Streeter et al., 1969, Lunkenheimer et al., 2006b, Lunkenheimer et al., 2004) and more recently

from high resolution echo to show regional strain (Notomi et al., 2008, Sengupta et al., 2006), speckle tracking to look at torsion (Thomas and Popovic, 2006) and DT-MRI to assess fibre orientation (Geerts et al., 2002), means information is available that allows inferences to made from our data regarding the dilatation and contractile dysfunction of the LV.

Mural thickening is essential to effective ejection, and is achieved in part by realignment of myocytes over one another (Spotnitz et al., 1966, Anderson et al., 2008). We postulate that the increase in verticality and reduced tilt of fibres in HF may reduce their plane of movement in this fashion, and thus transmural thickening will be reduced. MRI tagging studies have highlighted the importance of circumferential radial shear in wall thickening (Young et al., 1994b, Young et al., 1994a). Circumferential radial shear occurs due to increased rotation of the endocardium relative to the epicardium (Young et al., 1994b), a motion which will be reduced in HF due to the increased verticality of fibres in the endocardium. In addition, the reduction in circumferential fibres in the transmural mid-wall will also reduce transmural thickening and constriction, and because circumferential fibres make the greatest contribution to pressure generation, stroke volume will also be reduced (Buckberg et al., 2008). During the ejection phase, transverse circumferential fibres are thought to counteract outward forces generated by the oblique epi and endocardium fibres, preventing outward 'explosion' of the ventricle (Buckberg et al., 2008). The reduction in number and increase in verticality of circumferential fibres at the base in HF suggests outward forces will be increased, leading to contractile dysfunction and a vulnerability to dilatation.

We also propose the changes in fibre orientation will have an affect on the 'wringing' or torsion of the heart (Ingels, 1997). Coordinated counter-clockwise and clockwise twisting of apex and base respectively occurs during ejection (Notomi et al., 2008), leading to efficient blood expulsion and stress equalisation (Arts et al., 1984, Arts et al., 1979). Increased torsion is associated with increased EF (Ahmed et al., 2012). But *In vivo* studies have shown torsion is reduced in a variety of pathologies including; dilated cardiomyopathy, eccentric hypertrophy and increased sphericity (Ennis et al., 2009, Kanzaki et al., 2006, van Dalen et al., 2009), all features observed here in the base and mid-wall in HF samples. We propose data presented here provides reasoning for the reduced function associated with dilated phenotypes. It is

postulated changes in fibre orientation in HF will reduce circumferential and radial shear in the LV, particularly at the base of the heart. Therefore the coordinated process of ventricular torsion will be disturbed (Schmitt et al., 2009, Buckberg et al., 2008, Lunkenheimer et al., 2004) causing reduced EF (Ahmed et al., 2012). In addition stresses will be less equalised thus increasing the susceptibility of the LV base to dilatation.

The complex motion of torsion requires two opposing forces which are produced by two separate populations of myocytes (Lunkenheimer et al., 2004). (1) The helical arrangement of myocytes acts to uniquely constrict the LV, (2) transverse angled or intruding fibres (often ignored in studies of cardiac dynamics and fibre orientation) equalise myocyte strains during systole, confine ventricular compliance, support both ventricular constriction and dilation, and can be functionally antagonistic to the helical fibres (Lunkenheimer et al., 2004, Smerup et al., 2013b). A mathematical model developed by Smerup et al. 2013 has shown the angle of intruding fibres is specific to their function; larger angles antagonise mural contriction, while smaller angles act to equalise strain and contribute to constriction (Smerup et al., 2013b). Therefore it can be postulated that the reduction in transverse angles observed at the base in HF would allow for increased mural constriction. However it is expected these changes will reduce the resistance of the region to compliance (Lunkenheimer et al., 2004), causing a succeptability to dilatation. In addition any increase in contractility in the region will be nullified by the reduction in circumferential strain (described above) and loss of contractility due to dramatic change in relative wall thickness (see section 8.7.7).

As described above, models of cardiac mechanics can be used to investigate how 3D fibre orientation affects cardiac function (Dorri et al., 2010). Dorri et al. 2010 showed cardiac function was robust in the presence of small changes in fibre orientation. But highlighted severe loss of function at angle deviations of ~30°, and showed transverse angles exceeding 45° cause mural contraction that counteracts systolic thickening and reduces EF%. This level of deviation in 3D fibre angle was observed in HF samples at the base and mid-wall in the LV and IVS, supporting the hypothesis that changes observed here have contributed to the observed loss of function. However other studies suggest changes of only ~5-10° can substantially affect ventricular torsion and performance (Sallin, 1969).

Diastolic dysfunction

Originally HF was thought to be characterised by a loss of systolic function, however, recently increasing emphasis has been placed on the role of diastolic dysfunction in HF (Gaasch and Zile, 2004, Zile and Brutsaert, 2002a, Zile and Brutsaert, 2002b). The changes in fibre orientation we have observed in HF suggest diastolic function may also be affected. The dualistic ventricular function of the heart proposed by Brachet (Anderson et al., 2008), suggests a separate component of radially orientated myocytes exist to sustain ventricular dilation and diastolic reopening (Anderson et al., 2006). Therefore the reduction in the transverse angle of fibres observed in HF suggests sustained dilatation will be impaired, reducing ventricular filling and thus reducing stroke volume. Furthermore, elastic energy generated in systolic torsion is released during diastole through mechanical recoil, facilitating rapid filling (Rademakers et al., 1992, Ashikaga et al., 2004). Therefore with torsion expected to be reduced in HF, filling will be impaired due to reduced mechanical recoil.

8.7.11 Limitations of fibre orientation analysis

We recognize the limitations of the current study, in particulary the inability to distinguish between the positive and negative angle of fibres. In addition fibre angles were not normalised to the LV curvature in the longitudinal plane, but this can be rectified by using the epicardial tagent plane as a reference plane. It should also be noted that individual myocytes are not resolved, the term 'fibre' refers to aggregations of individual myocytes adjoined axially. Although there are technical limitations to the present study, the superior resolution over similar studies using MRI (20 μm vs 1300 μm) (Nielsen et al., 2009, Smerup et al., 2009), shows the huge potential of the technique to elucidate the complex morphology and function of the heart in health and disease.

8.8 Summary

The effects of both volume and pressure overload on the function and morphology of the heart were investigated using *in vivo* and *ex vivo* imaging. An experimental HF model was developed in rabbit. To assess longitudinal changes animals were imaged at various time points using *in vivo* echocardiography and functional and morphological measurements were made. To investigate changes *ex vivo*, perfusion fixed rabbit hearts were scanned using contrast enhanced micro-CT. Scan data was then used to investigate global and regional changes to cardiac morphology across the whole heart.

In vivo echocardiography showed significant changes in morphology and function in HF. Significant and progressive dilatation of the LV was accompanied with hypertrophy in all regions of the ventricles. These dramatic changes in morphology corresponded with significant and progressive loss of LV function (~50% loss at termination), suggesting that this acute model of HF brings about dramatic progressive changes to the heart, and would be suitable for a wide range of scientific investigation into HF.

Contrast enhanced micro-CT provided excellent high resolution images, which facilitated investigation of gross and regional changes in morphology, and also allowed extraction of 3D fibre orientation. Hypertrophy was observed in all regions of the atria (RA, IAS and LA) in HF. In depth analysis of hypertrophy revealed atrial wall thickness was unchanged but the PcMs showed significant hypertrophy. The normal morphology of the RA and LA seemed to influence their response to HF, in that the thin walled RA with its slender PcMs was more prone to dilatation. It is postulated that the changes to the atria in HF make them more vulnerable to electrical dysfunction. The ventricles showed hypertrophy in all regions (RV, IVS and LV), with significant dilatation of the LV observed in HF. Traditionally the RV cavity is greater than the thick walled LV but in HF this relationship was reversed. Regional analysis of the ventricular morphology reveal hypertrophy throughout the RV, accompanied with no significant dilatation. However regional changes were observed in the LV and IVS in HF, with thinning of the wall at basal and mid-wall regions, and wall thickening seen in the apical region. In the LV areas of wall thinning (base and mid-wall) corresponded to regions were the greatness degree of

dilatation was observed, and areas of wall thickening corresponded to the areas of low dilatation. This suggests for this model of HF, decompensated (eccentric) remodelling takes place at the base and mid-wall, while compensated (concentric) remodelling occurs at the apical region.

Novel 3D fibre orientation analysis showed that in HF the regions which underwent the greatest amount of dilatation and wall thinning (the base and mid-wall), were the most prone to changes in fibre orientation. In HF fibres in the LV and IVS became more vertically orientated, accompanied by a reduction in tilt (transverse angle). The most significant changes were observed at the base and mid-wall of the LV and IVS. Regional transmural analysis revealed significant changes occurred at the endocardium and transmural mid-wall in the LV, while in the IVS the fibres running within in the transmural mid-wall changed significantly. These changes in HF could be a substrate for the observed loss of ventricular function, but could also contribute to diastolic dysfunction.

Data presented here suggests morphological changes in HF are non-uniform throughout the whole heart, and highlights the important contribution of regional changes, and thus the need for regional assessment in the clinical setting. Novel information on 3D fibre orientation in the failing heart has been presented, which will aid the development of functional and mechanical models of the heart in health and disease.

References

Abhayaratna WP, Seward JB, Appleton CP, et al. (2006) Left Atrial Size: Physiologic Determinants and Clinical Applications. *Journal of the American College of Cardiology,* **47,** 2357-2363.

Adhyapak S, Parachuri VR (2009) Architecture of the left ventricle: insights for optimal surgical ventricular restoration. *Heart Failure Reviews,* **15,** 73-83.

Ahmed MI, Desai RV, Gaddam KK, et al. (2012) Relation of Torsion and Myocardial Strains to LV Ejection Fraction in Hypertension. *JACC: Cardiovascular Imaging,* **5,** 273-281.

Airey JA, Almeida-Porada G, Colletti EJ, et al. (2004) Human Mesenchymal Stem Cells Form Purkinje Fibers in Fetal Sheep Heart. *Circulation,* **109,** 1401-1407.

Almajdub M, Magnier L, Juillard L, Janier M (2008) Kidney volume quantification using contrast-enhanced in vivo X-ray micro-CT in mice. *Contrast Media & Molecular Imaging,* **3,** 120-126.

Ambrosi CM, Fedorov VV, Schuessler RB, Rollins AM, Efimov IR (2012) Quantification of fiber orientation in the canine atrial pacemaker complex using optical coherence tomography. *Journal of Biomedical Optics,* **17,** 071309-071309.

Ambrosi CM, Moazami N, Rollins AM, Efimov IR (2009) Virtual histology of the human heart using optical coherence tomography. *Journal of Biomedical Optics,* **14,** 054002-054002-7.

Anderson R, Boyett M, Dobrzynski H, Moorman AM (2013) The Anatomy of the Conduction System: Implications for the Clinical Cardiologist. *Journal of Cardiovascular Translational Research,* **6,** 187-196.

Anderson RH, Becker AE, Cosio FG (2000) Consensus Statement from the Cardiac Nomenclature Study Group of Arrhythmias of the European Society of Cardiology, and the Task Force on Cardiac Nomenclature from the North American Society of Pacing and Electrophysiology on Living Anatomy of the Atrioventricular Junctions. *Journal Of Cardiovascular Electrophysiology,* **11,** 1297-1297.

Anderson RH, Cook AC (2007) The structure and components of the atrial chambers. *Europace,* **9,** vi3-vi9.

Anderson RH, Devine WA, Ho SY, Smith A, McKay R (1991) The myth of the aortic annulus: The anatomy of the subaortic outflow tract. *The Annals of Thoracic Surgery,* **52,** 640-646.

Anderson RH, Ho SY (1998) The architecture of the sinus node, the atrioventricular conduction axis, and the internodal atrial myocardium. *Journal Of Cardiovascular Electrophysiology,* **9,** 1233-1248.

Anderson RH, Ho SY, Redmann K, Sanchez-Quintana D, Lunkenheimer PP (2005) The anatomical arrangement of the myocardial cells making up the ventricular mass. *European Journal of Cardio-Thoracic Surgery,* **28,** 517-525.

Anderson RH, Ho SY, Sanchez-Quintana D, Redmann K, Lunkenheimer PP (2006) Heuristic problems in defining the three-dimensional arrangement of the ventricular myocytes. *The Anatomical Record Part A: Discoveries in Molecular, Cellular, and Evolutionary Biology,* **288A,** 579-586.

Anderson RH, Ho SY, Smith A, Becker AE (1981) The internodal atrial myocardium. *The Anatomical Record,* **201,** 75-82.

Anderson RH, Mohun TJ, Moorman AFM (2011) What is a ventricle? *Cardiology in the Young,* **21,** 14-22.

Anderson RH, Sanchez-Quintana D, Niederer P, Lunkenheimer PP (2008) Structural-functional correlates of the 3-dimensional arrangement of the myocytes making up the ventricular walls. *The Journal of thoracic and cardiovascular surgery,* **136,** 10-18.

Ansari A, Yen Ho S, Anderson RH (1999) Distribution of the Purkinje fibres in the sheep heart. *The Anatomical Record,* **254,** 92-97.

Arts T, Meerbaum S, Reneman RS, Corday E (1984) Torsion of the left ventricle during the ejection phase in the intact dog. *Cardiovascular Research,* **18,** 183-193.

Arts T, Reneman R, Veenstra P (1979) A model of the mechanics of the left ventricle. *Annals of Biomedical Engineering,* **7,** 299-318.

Ashikaga H, Criscione JC, Omens JH, Covell JW, Ingels NB (2004) Transmural left ventricular mechanics underlying torsional recoil during relaxation. *American Journal of Physiology - Heart and Circulatory Physiology,* **286,** H640-H647.

Aslanidi O, Nikolaidou T, Zhao J, et al. (2012) Application of Micro-Computed Tomography with Iodine Staining to Cardiac Imaging, Segmentation and Computational Model Development. *Medical Imaging, IEEE Transactions on,* **PP,** 1-1.

Aslanidi OV, Boyett MR, Dobrzynski H, Li J, Zhang H (2009) Mechanisms of Transition from Normal to Reentrant Electrical Activity in a Model of Rabbit Atrial Tissue: Interaction of Tissue Heterogeneity and Anisotropy. *Biophysical journal,* **96,** 798-817.

Aslanidi OV, Colman MA, Stott J, et al. (2011) 3D virtual human atria: A computational platform for studying clinical atrial fibrillation. *Progress in Biophysics and Molecular Biology,* **107,** 156-168.

Atkinson A, Inada S, Li J, et al. (2011) Anatomical and molecular mapping of the left and right ventricular His–Purkinje conduction networks. *Journal of Molecular and Cellular Cardiology,* **51,** 689-701.

Atkinson AJ, Logantha SJRJ, Hao G, et al. (2013) Functional, Anatomical, and Molecular Investigation of the Cardiac Conduction System and Arrhythmogenic Atrioventricular Ring Tissue in the Rat Heart. *Journal of the American Heart Association,* **2**.

Auerbach DS, Grzda KR, Furspan PB, Sato PY, Mironov S, Jalife J (2011) Structural heterogeneity promotes triggered activity, reflection and arrhythmogenesis in cardiomyocyte monolayers. *The Journal of Physiology,* **589,** 2363-2381.

Axelsson M, Svensson S (2010) 3D pore structure characterisation of paper. *Pattern Analysis and Applications,* **13,** 159-172.

Badea CT, Fubara B, Hedlund LW, Johnson GA (2005) 4-D micro-CT of the mouse heart. *Mol Imaging,* **4,** 110-6.

Badea CT, Hedlund LW, Wheeler CT, Mai W, Johnson GA (2004) Volumetric microCT system for in vivo microscopy. In *Biomedical Imaging: Nano to Macro, 2004. IEEE International Symposium on*), pp. 1377-1380 Vol. 2.

Badea CT, Schreibmann E, Fox T (2008) A registration based approach for 4D cardiac micro-CT using combined prospective and retrospective gating. *Medical Physics,* **35,** 1170-1179.

Barnett V, Iaizzo PA (2009) Cellular Myocytes. In *Handbook of Cardiac Anatomy, Physiology, and Devices*), pp. 147-158. Humana Press.

Bartlett DW, Su H, Hildebrandt IJ, Weber WA, Davis ME (2007) Impact of tumor-specific targeting on the biodistribution and efficacy of siRNA nanoparticles measured by multimodality in vivo imaging. *Proceedings of the National Academy of Sciences,* **104,** 15549-15554.

Bartling SH, Stiller W, Semmler W, Kiessling F (2007) Small Animal Computed Tomography Imaging. *Current Medical Imaging Reviews,* **3,** 45-59.

Bateman M, Quill J, Hill A, Iaizzo P (2013) The Clinical Anatomy and Pathology of the Human Atrioventricular Valves: Implications for Repair or Replacement. *Journal of Cardiovascular Translational Research,* **6,** 155-165.

Bearden JA, Burr AF (1967) Reevaluation of X-Ray Atomic Energy Levels. *Reviews of Modern Physics,* **39,** 125-142.

Beauchamp P, Yamada KA, Baertschi AJ, et al. (2006) Relative Contributions of Connexins 40 and 43 to Atrial Impulse Propagation in Synthetic Strands of Neonatal and Fetal Murine Cardiomyocytes. *Circulation Research,* **99,** 1216-1224.

Benjamin EJ, D'Agostino RB, Belanger AJ, Wolf PA, Levy D (1995) Left Atrial Size and the Risk of Stroke and Death: The Framingham Heart Study. *Circulation,* **92,** 835-841.

Berenfeld O, Jalife J (1998) Purkinje-Muscle Reentry as a Mechanism of Polymorphic Ventricular Arrhythmias in a 3-Dimensional Model of the Ventricles. *Circulation Research,* **82,** 1063-1077.

Bergmann O, Bhardwaj RD, Bernard S, et al. (2009) Evidence for Cardiomyocyte Renewal in Humans. *Science,* **324,** 98-102.

Bers DM (2002) Cardiac excitation-contraction coupling. *Nature,* **415,** 198-205.

Beutel J, Kundel HL, Van Metter RL (2000) *Handbook of medical imaging. Vol. 1, Physics and psychophysics [electronic book] / Jacob Beutel, Harold L. Kundel, and Richard L. Van Metter, editors,* Bellingham : SPIE, 2000.

Bhowmik B, Jendrasiak GL (1967) Molecular structure charge transfer complexes of lipids with iodine *Nature,* **215**.

Blaauw E, van Nieuwenhoven FA, Willemsen P, et al. (2010) Stretch-induced hypertrophy of isolated adult rabbit cardiomyocytes. *American Journal of Physiology - Heart and Circulatory Physiology,* **299,** H780-H787.

Bojsen-Moller F, Tranum-Jensen J (1971) Whole-mount demonstration of cholinesterase-containing nerves in the right atrial wall, nodal tissue, and atrioventricular bundle of the pig. *J. Anat,* **108,** 375-386.

Bojsen-Moller F, Tranum-Jensen J (1972) Rabbit heart nodal tissue, sinuatrial ring bundle and atrioventricular connxions identified as a neuromuscular system. *J Anat,* **112,** 367-382.

Bordas R, Gillow K, Lou Q, et al. (2011) Rabbit-specific ventricular model of cardiac electrophysiological function including specialized conduction system. *Progress in Biophysics and Molecular Biology,* **107,** 90-100.

Bovendeerd PHM, Huyghe JM, Arts T, van Campen DH, Reneman RS (1994) Influence of endocardial-epicardial crossover of muscle fibers on left ventricular wall mechanics. *Journal of Biomechanics,* **27,** 941-951.

Boyde A (2012) Title: Staining plastic blocks with triiodide to image cells and soft tissues in backscattered electron SEM of skeletal and dental tissues. *European Cells and Materials,* **24,** 154-161.

Boyett M, Inada S, Yoo S, et al. (2006) Connexins in the Sinoatrial and Atrioventricular Nodes. *Cardiovascular Gap Junctions. Adv Cardiol.,* **42,** 175-197.

Boyett MR (2009) 'And the beat goes on' The cardiac conduction system: the wiring system of the heart. *Experimental Physiology,* **94,** 1035-1049.

Boyett MR, Honjo H, Kodama I (2000) The sinoatrial node, a heterogeneous pacemaker structure. *Cardiovascular Research,* **47,** 658-687.

Boyett MR, Honjo H, Yamamoto M, Nikmaram MR, Niwa R, Kodama I (1999) Downward gradient in action potential duration along conduction path in and around the sinoatrial node. *American Journal of Physiology - Heart and Circulatory Physiology,* **276,** H686-H698.

Boyett MR, Li J, Inada S, et al. (2005) Imaging the heart: computer 3-dimensional anatomic models of the heart. *Journal of Electrocardiology,* **38,** 113-120.

Brieke A, DeNofrio D (2005) Right ventricular dysfunction in chronic dilated cardiomyopathy and heart failure. *Coronary Artery Disease,* **16,** 5-11.

Brooks AG, Stiles MK, Laborderie J, et al. (2010) Outcomes of long-standing persistent atrial fibrillation ablation: A systematic review. *Heart rhythm : the official journal of the Heart Rhythm Society,* **7,** 835-846.

Brown AM, Cleland JGF (1998) Influence of concomitant disease on patterns of hospitalization in patients with heart failure discharged from Scottish hospitals in 1995. *European Heart Journal,* **19,** 1063-1069.

Buckberg G, Hoffman JIE, Mahajan A, Saleh S, Coghlan C (2008) Cardiac Mechanics Revisited: The Relationship of Cardiac Architecture to Ventricular Function. *Circulation,* **118,** 2571-2587.

Buckberg GD, Mahajan A, Jung B, Markl M, Hennig J, Ballester-Rodes M (2006) MRI myocardial motion and fiber tracking: a confirmation of knowledge from different imaging modalities. *European Journal of Cardio-Thoracic Surgery,* **29,** S165-S177.

Butters TD, Aslanidi OV, Inada S, et al. (2010) Mechanistic Links Between Na+ Channel (SCN5A) Mutations and Impaired Cardiac Pacemaking in Sick Sinus Syndrome. *Circulation Research,* **107,** 126-137.

Cabo C, Pertsov AM, Baxter WT, Davidenko JM, Gray RA, Jalife J (1994) Wave-front curvature as a cause of slow conduction and block in isolated cardiac muscle. *Circulation Research,* **75,** 1014-28.

Campbell EL, Seynnes OR, Bottinelli R, et al. (2013) Skeletal muscle adaptations to physical inactivity and subsequent retraining in young men. *Biogerontology,* **14,** 247-259.

Carew TE, Covell JW (1979) Fiber orientation in hypertrophied canine left ventricle. *American Journal of Physiology - Heart and Circulatory Physiology,* **236,** H487-H493.

Catani M, Bodi I, Dell'Acqua F (2012) Comment on "The geometric structure of the brain fiber pathways". *Science,* **337,** 1605.

Chandler N, Aslanidi O, Buckley D, et al. (2011) Computer Three-Dimensional Anatomical Reconstruction of the Human Sinus Node and a Novel Paranodal Area. *The Anatomical Record: Advances in Integrative Anatomy and Evolutionary Biology,* **294,** 970-979.

Chandler NJ, Greener ID, Tellez JO, et al. (2009) Molecular Architecture of the Human Sinus Node: Insights Into the Function of the Cardiac Pacemaker. *Circulation,* **119,** 1562-1575.

Chauvin M, Shah DC, Haissaguerre M, Marcellin L, Brechenmacher C (2000) The Anatomic Basis of Connections Between the Coronary Sinus Musculature and the Left Atrium in Humans. *Circulation,* **101,** 647-652.

Christoffels VM, Smits GJ, Kispert A, Moorman AFM (2010) Development of the Pacemaker Tissues of the Heart. *Circulation Research,* **106,** 240-254.

Clayton R, Abdalhamid S, Bloor R, et al. (2010) Transmural Changes in Fibre Helix Angle in Normal and Failing Canine Ventricles *IEEE computing in cardiology***,** 915−918.

Colaco CA, Evans WH (1981) A biochemical dissection of the cardiac intercalated disk: isolation of subcellular fractions containing fascia adherentes and gap junctions. *Journal of Cell Science,* **52,** 313-325.

Corradi D, Maestri R, Macchi E, Callegari S (2011) The Atria: From Morphology to Function. *Journal Of Cardiovascular Electrophysiology,* **22,** 223-235.

Cosio FG, Anderson RH, Kuck K-H, et al. (1999) Living Anatomy of the Atrioventricular Junctions. A Guide to Electrophysiologic Mapping: A Consensus Statement from the Cardiac Nomenclature Study Group, Working Group of Arrhythmias, European Society of Cardiology, and the Task Force on Cardiac Nomenclature from NASPE. *Circulation,* **100,** e31-e37.

Costa KD, Takayama Y, McCulloch AD, Covell JW (1999) Laminar fiber architecture and three-dimensional systolic mechanics in canine ventricular myocardium. *American Journal of Physiology - Heart and Circulatory Physiology,* **276,** H595-H607.

Cox PG, Jeffery N (2011) Reviewing the Morphology of the Jaw-Closing Musculature in Squirrels, Rats, and Guinea Pigs with Contrast-Enhanced MicroCt. *Anat Rec (Hoboken),* **294,** spc1-spc1.

Cryer CW, Navidi-Kasmai H, Lunkenheimer PP, Redmann K (1997) Computation of the alignment of myocardial contractile pathways using a magnetic tablet and an optical method. *Technology and Health Care,* **5,** 79-93.

Damon BM, Buck AKW, Ding Z (2011) Diffusion-tensor MRI-based skeletal muscle fiber tracking. *Imaging in Medicine,* **3,** 675-687.

Desplantez T, Dupont E, Severs N, Weingart R (2007) Gap Junction Channels and Cardiac Impulse Propagation. *Journal of Membrane Biology,* **218,** 13-28.

Di Donato M, Dabic P, Castelvecchio S, et al. (2006) Left ventricular geometry in normal and post-anterior myocardial infarction patients: sphericity index and 'new' conicity index comparisons. *European Journal of Cardio-Thoracic Surgery,* **29,** S225-S230.

Dobrzynski H, Anderson RH, Atkinson A, et al. (2013) Structure, function and clinical relevance of the cardiac conduction system, including the atrioventricular ring and outflow tract tissues. *Pharmacology & Therapeutics,* **139,** 260-288.

Dobrzynski H, Li J, Tellez J, et al. (2005) Computer Three-Dimensional Reconstruction of the Sinoatrial Node. *Circulation,* **111,** 846-854.

Dolber PC, Spach MS (1987) Picrosirius red staining of cardiac muscle following phosphomolybdic acid treatment. **62,** 23-26.

Dorri F, Niederer PF, Lunkenheimer PP, Anderson RH (2010) The architecture of the left ventricular myocytes relative to left ventricular systolic function. *European Journal of Cardio-Thoracic Surgery,* **37,** 384-392.

Dorri F, Niederer PF, Redmann K, Lunkenheimer PP, Cryer CW, Anderson RH (2007) An analysis of the spatial arrangement of the myocardial aggregates making up the wall of the left ventricle. *European Journal of Cardio-Thoracic Surgery,* **31,** 430-437.

Drake RL, Vogl W, Mitchell AWM (2005) Grays Anatomy for students.). Philadelphia, USA: Elsevier.

Drazner MH (2011) The Progression of Hypertensive Heart Disease. *Circulation,* **123,** 327-334.

Driehuys B, Nouls J, Badea A, et al. (2008) Small Animal Imaging with Magnetic Resonance Microscopy. *Ilar Journal,* **49,** 35-53.

Eggen MD, Swingen CM, Iaizzo PA (2009) Analysis of fiber orientation in normal and failing human hearts using diffusion tensor MRI. In *Biomedical Imaging: From Nano to Macro, 2009. ISBI '09. IEEE International Symposium on*), pp. 642-645.

Eliška O (2006) Purkinje fibers of the Heart Conduction System *The History and Present Relevance of the Purkinje discoveries*. *ČASOPIS LÉKAŘŮ ČESKÝCH,,* **145**.

Elliott JC, Dover SD (1982) X-ray microtomography. *Journal of Microscopy,* **126,** 211-213.

Ennis DB, Nguyen TC, Itoh A, et al. (2009) Reduced Systolic Torsion in Chronic "Pure" Mitral Regurgitation. *Circulation: Cardiovascular Imaging,* **2,** 85-92.

Faraj KA, Cuijpers VMJI, Ronnie G. Wismans, et al. (2009) Micro-Computed Tomographical Imaging of Soft Biological Materials Using Contrast Techniques. *Tissue Engineering Part C: Methods,* **15**.

Fedorov VV, Glukhov AV, Chang R, et al. (2010) Optical Mapping of the Isolated Coronary-Perfused Human Sinus Node. *Journal of the American College of Cardiology,* **56,** 1386-1394.

Fedorov VV, Schuessler RB, Hemphill M, et al. (2009) Structural and Functional Evidence for Discrete Exit Pathways That Connect the Canine Sinoatrial Node and Atria. *Circulation Research,* **104,** 915-923.

Feldkamp LA, Davis LC, Kress JW (1984) Practical cone-beam algorithm. *Journal of the Optical Society of America A,* **1,** 612-619.

Fernandez-Golfin C, Pachon M, Corros C, et al. (2009) Left ventricular trabeculae: quantification in different cardiac diseases and impact on left ventricular morphological and functional parameters assessed with cardiac magnetic resonance. *Journal of Cardiovascular Medicine,* **10,** 827-833 10.2459/JCM.0b013e32832e1c60.

Flannery BP, Deckman HW, Roberge WG, D'amico KL (1987) Three-Dimensional X-ray Microtomography. *Science,* **237,** 1439-1444.

Fleming CP, Ripplinger CM, Webb B, Efimov IR, Rollins AM (2008) Quantification of cardiac fiber orientation using optical coherence tomography. *Journal of Biomedical Optics,* **13,** 030505-030505-3.

Frangi AF, Niessen WJ, Viergever MA (2001) Three-dimensional modeling for functional analysis of cardiac images, a review. *Medical Imaging, IEEE Transactions on,* **20,** 2-5.

Gaasch WH, Meyer TE (2008) Left Ventricular Response to Mitral Regurgitation: Implications for Management. *Circulation,* **118,** 2298-2303.

Gaasch WH, Zile MR (2004) Left Ventricular Diastolic Dysfunction and Diastolic Heart Failure. *Annual Review of Medicine,* **55,** 373-394.

Gaasch WH, Zile MR (2011) Left Ventricular Structural Remodeling in Health and Disease: With Special Emphasis on Volume, Mass, and Geometry. *Journal of the American College of Cardiology,* **58,** 1733-1740.

Galban CJ, Maderwald S, Stock F, Ladd ME (2007) Age-Related Changes in Skeletal Muscle as Detected by Diffusion Tensor Magnetic Resonance Imaging. *The Journals of Gerontology Series A: Biological Sciences and Medical Sciences,* **62,** 453-458.

Ganesan AN, Shipp NJ, Brooks AG, et al. (2013) Longterm Outcomes of Catheter Ablation of Atrial Fibrillation: A Systematic Review and Meta-analysis. *Journal of the American Heart Association,* **2**.

Geerts L, Bovendeerd P, Nicolay K, Arts T (2002) Characterization of the normal cardiac myofiber field in goat measured with MR-diffusion tensor imaging. *American Journal of Physiology - Heart and Circulatory Physiology,* **283,** H139-H145.

Gerneke DA, Sands GB, Ganesalingam R, et al. (2007) Surface imaging microscopy using an ultramiller for large volume 3D reconstruction of wax- and resin-embedded tissues. *Microscopy Research and Technique,* **70,** 886-894.

Gilbert SH, Benoist D, Benson AP, et al. (2012) Visualization and quantification of whole rat heart laminar structure using high-spatial resolution contrast-enhanced MRI. *American Journal of Physiology - Heart and Circulatory Physiology,* **302,** H287-H298.

Gilbert SH, Bernus O, Holden A, Benson A (2009) A Quantitative Comparison of the Myocardial Fibre Orientation in the Rabbit as Determined by Histology and by Diffusion Tensor-MRI. In *Functional Imaging and Modeling of the Heart*), pp. 49-57. Springer Berlin Heidelberg.

Gillis TE, Marshall CR, Tibbits GF (2007) Functional and evolutionary relationships of troponin C. *Physiological Genomics,* **32,** 16-27.

Gilson N, el Houda Bouanani N, Corsin A, Crozatier B (1990) Left ventricular function and beta-adrenoceptors in rabbit failing heart. *American Journal of Physiology - Heart and Circulatory Physiology,* **258,** H634-H641.

Glukhov AV, Hage LT, Hansen BJ, et al. (2013) Sinoatrial Node Reentry in a Canine Chronic Left Ventricular Infarct Model: Role of Intranodal Fibrosis and Heterogeneity of Refractoriness. *Circulation: Arrhythmia and Electrophysiology,* **6,** 984-994.

Gottdiener JS, Kitzman DW, Aurigemma GP, Arnold AM, Manolio TA (2006) Left Atrial Volume, Geometry, and Function in Systolic and Diastolic Heart Failure of Persons > or =65 Years of Age (The Cardiovascular Health Study). *The American Journal of Cardiology,* **97,** 83-89.

Gourdie RG, Severs NJ, Green CR, Rothery S, Germroth P, Thompson RP (1993) The spatial distribution and relative abundance of gap-junctional connexin40 and connexin43 correlate to functional properties of components of the cardiac atrioventricular conduction system. *Journal of Cell Science,* **105,** 985-991.

Greenbaum RA, Ho SY, Gibson DG, Becker AE, Anderson RH (1981) Left ventricular fibre architecture in man. *British Heart Journal,* **45,** 248-263.

Grossman W, Jones D, McLaurin LP (1975) Wall stress and patterns of hypertrophy in the human left ventricle. *The Journal of Clinical Investigation,* **56,** 56-64.

Gupta R, Grasruck M, Suess C, et al. (2006) Ultra-high resolution flat-panel volume CT: fundamental principles, design architecture, and system characterization. *European Radiology,* **16,** 1191-1205.

Hanna N, Cardin S, Leung T-K, Nattel S (2004) Differences in atrial versus ventricular remodeling in dogs with ventricular tachypacing-induced congestive heart failure. *Cardiovascular Research,* **63,** 236-244.

Harman JW, Gwinn RP (1949) The recovery of skeletal muscle fibers from acute ischemia as determined by histologic and chemical methods. *The American journal of pathology,* **25,** 741-755.

Harrild DM, Henriquez CS (2000) A Computer Model of Normal Conduction in the Human Atria. *Circulation Research,* **87,** e25-e36.

Harris BS, Baicu CF, Haghshenas N, et al. (2012) Remodeling of the peripheral cardiac conduction system in response to pressure overload. *American Journal of Physiology - Heart and Circulatory Physiology,* **302,** H1712-H1725.

Hasenfuss G (1998) Animal models of human cardiovascular disease, heart failure and hypertrophy. *Cardiovascular Research,* **39,** 60-76.

Hay GA, Hughes D (1983) First-year physics for radiographers.). London: Bailliere Tindall.

Hayat MA (1970) Principles and techniques of electron microscopy: biological applications.). New York: Van Nostrand Reinhold.

Heart Failure Society of America (2006) Executive Summary: HFSA 2006 Comprehensive Heart Failure Practice Guideline. *Journal of cardiac failure,* **12,** 10-38.

Helm P, Beg MF, Miller MI, Winslow RL (2005a) Measuring and Mapping Cardiac Fiber and Laminar Architecture Using Diffusion Tensor MR Imaging. *Annals of the New York Academy of Sciences,* **1047,** 296-307.

Helm PA, Tseng H-J, Younes L, McVeigh ER, Winslow RL (2005b) Ex vivo 3D diffusion tensor imaging and quantification of cardiac laminar structure. *Magnetic Resonance in Medicine,* **54,** 850-859.

Hill A, Iaizzo P (2009) Comparative Cardiac Anatomy. In *Handbook of Cardiac Anatomy, Physiology, and Devices*), pp. 87-108. Humana Press.

Hiraoka M, Sano T (1976) Role of sinoatrial ring bundle in internodal conduction *American journal of physiology,* **231,** 319-325.

Ho SY (2009) Anatomy and myoarchitecture of the left ventricular wall in normal and in disease. *European Journal of Echocardiography,* **10,** iii3-iii7.

Ho SY, Anderson RH, Sanchez-Quintana D (2002) Gross structure of the atriums: more than an anatomic curiosity? *PACE,* **25,** 342-350.

Ho SY, Cabrera JA, Sanchez-Quintana D (2012) Left Atrial Anatomy Revisited. *Circulation: Arrhythmia and Electrophysiology,* **5,** 220-228.

Ho SY, Kilpatrick L, Kanal T, Germroth P, Thompson RP, Anderson R (1995) The Architecture of the atrioventricular conduction axis in dog compared to Man. *J cardiovasc electrophysiol,* **6,** 26-39.

Ho SY, Sánchez-Quintana D (2009) The importance of atrial structure and fibers. *Clinical Anatomy,* **22,** 52-63.

Ho SY, Sanchez-Quintana D, Cabrera JA, Anderson RH (1999) Anatomy of the left atrium: implications for radiofrequency ablation of atrial fibrillation. *j. Cardiovasc Electrophysiol,* **10,** 1525-1533.

Hoagland CL, Shank RE, Lavin GI (1944) The Histopathology Of Progressive Muscular Dystrophy as Revealed by Ultraviolet Photomicroscopy. *The Journal of Experimental Medicine,* **80,** 9-18.

Hocini Mlz, Ho SY, Kawara T, et al. (2002) Electrical Conduction in Canine Pulmonary Veins: Electrophysiological and Anatomic Correlation. *Circulation,* **105,** 2442-2448.

Hocini Mlz, Loh P, Ho SY, et al. (1998) Anisotropic Conduction in the Triangle of Koch of Mammalian Hearts: Electrophysiologic and Anatomic Correlations. *Journal of the American College of Cardiology,* **31,** 629-636.

Holdsworth DW, Thornton MM (2002) Micro-CT in small animal and specimen imaging. *Trends in Biotechnology,* **20,** S34-S39.

Hooks DA, Trew ML, Caldwell BJ, Sands GB, LeGrice IJ, Smaill BH (2007) Laminar Arrangement of Ventricular Myocytes Influences Electrical Behavior of the Heart. *Circulation Research,* **101,** e103-e112.

Hoshino M, Uesugi K, Yagi N (2012) Phase-contrast X-ray microtomography of mouse fetus. *Biology Open,* **1,** 269-274.

Hucker WJ, Fedorov VV, Foyil KV, Moazami N, Efimov IR (2008a) Optical Mapping of the Human Atrioventricular Junction. *Circulation,* **117,** 1474-1477.

Hucker WJ, McCain ML, Laughner JI, Iaizzo PA, Efimov IR (2008b) Connexin 43 Expression Delineates Two Discrete Pathways in the Human Atrioventricular Junction. *The Anatomical Record: Advances in Integrative Anatomy and Evolutionary Biology,* **291,** 204-215.

Hunt SA, Abraham WT, Chin MH, et al. (2005) ACC/AHA 2005 Guideline Update for the Diagnosis and Management of Chronic Heart Failure in the Adult: A Report of the American College of Cardiology/American Heart Association Task Force on Practice Guidelines (Writing Committee to Update the 2001 Guidelines for the Evaluation and Management of Heart Failure): Developed in Collaboration With the American College of Chest Physicians and the International Society for Heart and Lung Transplantation: Endorsed by the Heart Rhythm Society. *Circulation,* **112,** e154-e235.

Iaizzo PA, Weinhaus A, Roberts K (2009) Anatomy of the Human Heart. In *Handbook of Cardiac Anatomy, Physiology, and Devices*), pp. 59-85. Humana Press.

Immel S (1995) The Hydrophobic Topography of Amylose.), pp. Chapter 11. Darmstadt University of Technology.

Inada S, Hancox JC, Zhang H, Boyett MR (2009) One-Dimensional Mathematical Model of the Atrioventricular Node Including Atrio-Nodal, Nodal, and Nodal-His Cells. *Biophysical journal,* **97,** 2117-2127.

Ingels NBJ (1997) Myocardial fiber architecture and left ventricular function. *Technology and Health Care,* **5,** 45-52.

Inoue S, Becker AE (1998) Koch's Triangle sized up: Anatomical landmarks in perspective of catheter ablation procedures. *PACE,* **21,** 1553-1558.

Irisawa H (1987) Membrane currents in cardiac pacemaker tissue. *Experientia,* **43,** 1131-1135.

James TN (1963) The connecting pathways between the sinus node and A-V node and between the right and the left atrium in the human heart. *American Heart Journal,* **66,** 498-508.

Jarvis J, Stephenson RS (2013) Studying the microanatomy of the heart in 3 dimensions: a practical update. . *Frontiers in Paediatric Cardiology,* **In press**.

Jeffery NS, Stephenson RS, Gallagher JA, Jarvis JC, Cox PG (2011) Micro-computed tomography with iodine staining resolves the arrangement of muscle fibres. *Journal of Biomechanics,* **44,** 189-192.

Jessup M, Brozena S (2003) Heart Failure. *New England Journal of Medicine,* **348,** 2007-2018.

Jeyaraj D, Wilson LD, Zhong J, et al. (2007) Mechanoelectrical Feedback as Novel Mechanism of Cardiac Electrical Remodeling. *Circulation,* **115,** 3145-3155.

Johnson GA, Cofer GP, Fubara B, Gewalt SL, Hedlund LW, Maronpot RR (2002) Magnetic resonance histology for morphologic phenotyping. *Journal of Magnetic Resonance Imaging,* **16,** 423-429.

Jorgensen SM, Demirkaya O, Ritman EL (1998a) Three-dimensional imaging of vasculature and parenchyma in intact rodent organs with X-ray micro-CT. *American Journal of Physiology - Heart and Circulatory Physiology,* **275,** H1103-H1114.

Jorgensen SM, Demirkaya O, Ritman EL (1998b) Three-dimensional imaging of vasculature and parenchyma in intact rodent organs with X-ray micro-CT. *American Journal of Physiology,* **275,** H1103-H1114.

Jouk PS, Usson Y, Michalowicz G, Grossi L (2000) Three-dimensional cartography of the pattern of the myofibres in the second trimester fetal human heart. *Anatomy and Embryology,* **202,** 103-118.

Jung B, Markl M, Foll D, Hennig Jr (2006) Investigating myocardial motion by MRI using tissue phase mapping. *European Journal of Cardio-Thoracic Surgery,* **29,** S150-S157.

KachelrieiB M, Semmler W, Schwaiger M (2008) Micro-CT. In *Molecular Imaging I*), pp. 23-52. Springer Berlin Heidelberg.

Kanzaki H, Nakatani S, Yamada N, Urayama S-i, Miyatake K, Kitakaze M (2006) Impaired Systolic torsion in dilated cardiomyopathy: Reversal of apical rotation at mid-systole characterized with magnetic resonance tagging method. *Basic Research in Cardiology,* **101,** 465-470.

Kaplan SR, Gard JJ, Protonotarios N, et al. (2004) Remodeling of myocyte gap junctions in arrhythmogenic right ventricular cardiomyopathy due to a deletion in plakoglobin (Naxos disease). *Heart rhythm : the official journal of the Heart Rhythm Society,* **1,** 3-11.

Keith A, Flack M (1907) The form and nature of the muscular connections between the primary divisions of the vertebrate heart. *J Anat,* **41,** 172-89.

Kerem D, Hammond DD, Elsner R (1973) Tissue glycogen levels in the Weddell seal, Leptonychotes weddelli: A possible adaptation to asphyxial hypoxia. *Comparative Biochemistry and Physiology Part A: Physiology,* **45,** 731-736.

Khand A, Gemmel I, Clark AL, Cleland JGF (2000) Is the prognosis of heart failure improving? *Journal of the American College of Cardiology,* **36,** 2284-2286.

Khandelwal GS (1968) Characteristic X-Ray Production in the Atomic K Shell. *Physical Review,* **167,** 136-138.

Khouri MG, Peshock RM, Ayers CR, de Lemos JA, Drazner MH (2010) A 4-Tiered Classification of Left Ventricular Hypertrophy Based on Left Ventricular Geometry: The Dallas Heart Study. *Circulation: Cardiovascular Imaging,* **3,** 164-171.

Kinney JH, Ryaby JT, Haupt DL, Lane NE (1998) Three-dimensional in vivo morphometry of trabecular bone in the OVX rat model of osteoporosis. *Technology and Health Care,* **6,** 339-350.

Kistler PM, Roberts-Thomson KC, Haqqani HM, et al. (2006) P-Wave Morphology in Focal Atrial TachycardiaDevelopment of an Algorithm to Predict the Anatomic Site of Origin. *Journal of the American College of Cardiology,* **48,** 1010-1017.

Klos M, Calvo D, Yamazaki M, et al. (2008) Atrial Septopulmonary Bundle of the Posterior Left Atrium Provides a Substrate for Atrial Fibrillation Initiation in a Model of Vagally Mediated Pulmonary Vein Tachycardia of the Structurally Normal Heart. *Circulation: Arrhythmia and Electrophysiology,* **1,** 175-183.

Ko JK, Deal BJ, Strasburger JF, Benson Jr DW (1992) Supraventricular tachycardia mechanisms and their age distribution in pediatric patients. *The American Journal of Cardiology,* **69,** 1028-1032.

Ko Y-S, Yeh H-I, Ko Y-L, et al. (2004) Three-Dimensional Reconstruction of the Rabbit Atrioventricular Conduction Axis by Combining Histological, Desmin, and Connexin Mapping Data. *Circulation,* **109,** 1172-1179.

Kono T, Sabbah HN, Rosman H, Alam M, Jafri S, Goldstein S (1992) Left ventricular shape is the primary determinant of functional mitral regurgitation in heart failure. *Journal of the American College of Cardiology,* **20,** 1594-1598.

Krause M, Hausherr JM, Burgeth B, Herrmann C, Krenkel W (2010) Determination of the fibre orientation in composites using the structure tensor and local X-ray transform. *Journal of Materials Science,* **45,** 888-896.

Kucera JP, Kleber AG, Rohr S (1998) Slow Conduction in Cardiac Tissue, II: Effects of Branching Tissue Geometry. *Circulation Research,* **83,** 795-805.

Kucera JP, Rudy Y (2001) Mechanistic Insights Into Very Slow Conduction in Branching Cardiac Tissue: A Model Study. *Circulation Research,* **89,** 799-806.

Kuribayashi T, Roberts WC (1992) Myocardial disarray at junction of ventricular septum and left and right ventricular free walls in hypertrophic cardiomyopathy. *The American Journal of Cardiology,* **70,** 1333-1340.

Lamb HJ, Beyerbacht HP, de Roos A, et al. (2002) Left ventricular remodeling early after aortic valve replacement: differential effects on diastolic function in aortic valve stenosis and aortic regurgitation. *Journal of the American College of Cardiology,* **40,** 2182-2188.

Lansdown DA, Ding Z, Wadington M, Hornberger JL, Damon BM (2007) Quantitative diffusion tensor MRI-based fiber tracking of human skeletal muscle. *Journal of Applied Physiology,* **103,** 673-681.

Laske T, Shrivastav M, Iaizzo P (2009) The Cardiac Conduction System. In *Handbook of Cardiac Anatomy, Physiology, and Devices*), pp. 159-175. Humana Press.

Le Bihan D, Mangin J-F, Poupon C, et al. (2001) Diffusion tensor imaging: Concepts and applications. *Journal of Magnetic Resonance Imaging,* **13,** 534-546.

Lecker DN, Kumari S, Khan A (1997) Iodine binding capacity and iodine binding energy of glycogen. *Journal of Polymer Science Part A: Polymer Chemistry,* **35,** 1409-1412.

LeGrice IJ, Smaill BH, Chai LZ, Edgar SG, Gavin JB, Hunter PJ (1995) Laminar structure of the heart: ventricular myocyte arrangement and connective tissue architecture in the dog. *American Journal of Physiology - Heart and Circulatory Physiology,* **269,** H571-H582.

Lehto H, Tirri R (1980) Characterization of contractions in mechanically disaggregated myocardial cells from the rat. *Acta Physiologica Scandinavica,* **110,** 385-389.

Leonard BL, Smaill BH, LeGrice IJ (2012) Structural Remodeling and Mechanical Function in Heart Failure. *Microscopy and Microanalysis,* **18,** 50-67.

Leroux O, Leroux F, Bellefroid E, et al. (2009) A new preparation method to study fresh plant structures with X-ray computed tomography. *Journal of Microscopy,* **233,** 1-4.

Letsas KP, Efremidis M, Charalampous C, Tsikrikas S, Sideris A (2011) Current Ablation Strategies for Persistent and Long-Standing Persistent Atrial Fibrillation. *Cardiology Research and Practice,* **2011**.

Levick JR (2003) An Introduction to Cardiovascular Physiology.). Hodder Headline Group.

Li J, Greener ID, Inada S, et al. (2008) Computer Three-Dimensional Reconstruction of the Atrioventricular Node. *Circ Res,* **102,** 975-985.

Li J, Schneider JE, Yamamoto M, et al. (2005) A detailed 3D model of the rabbit right atrium including the sinoatrial node, atrioventricular node, surrounding blood vessels and valves. In *Computers in Cardiology, 2005*), pp. 603-606.

Linzbach AJ (1960) Heart failure from the point of view of quantitative anatomyâˆ—. *The American Journal of Cardiology,* **5,** 370-382.

Liu J, Dobrzynski H, Yanni J, Boyett MR, Lei M (2007) Organisation of the mouse sinoatrial node: structure and expression of HCN channels. *Cardiovascular Research,* **73,** 729-738.

Loukas M, Tubbs RS, Tongson JM, et al. (2008) The clinical anatomy of the crista terminalis, pectinate muscles and the teniae sagittalis. *Annals of Anatomy - Anatomischer Anzeiger,* **190,** 81-87.

Loushin MK, Quill JL, Iaizzo PA (2009) Mechanical Aspects of Cardiac Performance. In *Handbook of Cardiac Anatomy, Physiology, and Devices*), pp. 271-296. Humana Press.

Lunkenheimer PP, Niederer P (2012) Hierarchy and inhomogeneity in the systematic structure of the mammalian myocardium: Towards a comprehensive view of cardiodynamics. *Technology and Health Care,* **20,** 423-434.

Lunkenheimer PP, Redmann K, Dietl KH, et al. (1997a) The heart's fibre alignment assessed by comparing two digitizing systems. Methodological investigation into the inclination angle towards wall thickness. *Technology and Health Care,* **5,** 65-77.

Lunkenheimer PP, Redmann K, Dietl KH, et al. (1997b) The assessment of intramural stress alignment on the beating heart in situ using micro-ergometry: functional implications. *Technology and Health Care,* **5,** 115-122.

Lunkenheimer PP, Redmann K, Florek J, et al. (2004) The forces generated within the musculature of the left ventricular wall. *Heart,* **90,** 200-207.

Lunkenheimer PP, Redmann K, Kling N, et al. (2006a) Three-dimensional architecture of the left ventricular myocardium. *The Anatomical Record Part A: Discoveries in Molecular, Cellular, and Evolutionary Biology,* **288A,** 565-578.

Lunkenheimer PP, Redmann K, Westermann P, et al. (2006b) The myocardium and its fibrous matrix working in concert as a spatially netted mesh: a critical review of the purported tertiary structure of the ventricular mass. *European Journal of Cardio-Thoracic Surgery*, **29,** S41-S49.

Maguy A, Le Bouter S, Comtois P, et al. (2009) Ion Channel Subunit Expression Changes in Cardiac Purkinje Fibers: A Potential Role in Conduction Abnormalities Associated With Congestive Heart Failure. *Circulation Research,* **104,** 1113-1122.

Marin-Garcia J (2010) Cardiac Remodeling and Cell Death in Heart Failure. In *Heart Failure*), pp. 213-231. Humana Press.

Masuda MO, Paes de Carvalho A (1975) Sinoatrial transmission and atrial invasion during normal rhythm in the rabbit heart. *Circulation Research,* **37,** 414-21.

Matsuyama T-a, Inoue S, Kobayashi Y, et al. (2004) Anatomical diversity and age-related histological changes in the human right atrial posterolateral wall. *Europace,* **6,** 307-315.

Mazgalev TN, Ho SY, Anderson RH (2001) Anatomic-Electrophysiological Correlations Concerning the Pathways for Atrioventricular Conduction. *Circulation,* **103,** 2660-2667.

McCracken T, Kainer R, Carlson D (2008) Color Atlas of Small Animal Anatomy. , .). Blackwell Publishing, USA.

McDonagh T, Cleland J, Dargie H, Whittaker T, Standing M, Cunningham D (2011) National Heart Failure Audit. *National Institute for Cardiovascular Outcomes Research*.

Meerson FZ (1962) Compensatory Hyperfunction of the Heart and Cardiac Insufficiency. *Circulation Research,* **10,** 250-258.

Mercadier JJ (2007) Determinants of cardiac remodeling and progression to
heart failure. In: *Congestive Heart Failure*, edited by Hosenpud JD,
. (ed Greenberg BH). Philadelphia: Lippincott Williams and Wilkins.

Metscher B (2009a) MicroCT for comparative morphology: simple staining methods allow high-contrast 3D imaging of diverse non-mineralized animal tissues. *BMC Physiology,* **9,** 11.

Metscher BD (2009b) MicroCT for Developmental Biology: A Versatile Tool for High-Contrast 3D Imaging at Histological Resolutions. *Developmental Dynamics,* **238,** 632-640.

Metscher BD, Müller GB (2011) MicroCT for molecular imaging: Quantitative visualization of complete three-dimensional distributions of gene products in embryonic limbs. *Developmental Dynamics,* **240,** 2301-2308.

Miquerol L, Meysen S, Mangoni M, et al. (2004) Architectural and functional asymmetry of the Hisâ€“Purkinje system of the murine heart. *Cardiovascular Research,* **63,** 77-86.

Mohun TJ, Weninger WJ (2011) Imaging heart development using high-resolution episcopic microscopy. *Current Opinion in Genetics & Development,* **21,** 573-578.

Monfredi O, Anderson R, Boyett M, Dobrzynski H (2010) Nodal-like cells exist in the right ventricular outflow tract. *THE EUROPEAN HEART JOURNAL.* , **31,** 696-696.

Mouchess ML, Sohara Y, Nelson MDJ, DeClerck YA, Moats RA (2006) Multimodal Imaging Analysis of Tumor Progression and Bone Resorption in a Murine Cancer Model. *Journal of Computer Assisted Tomography,* **30,** 525-534.

Muir A, Smith G, Burton F, Rankin A, Cobbe S (2005) Increased a-h interval in isolated av node from rabbits with lv dysfunction due to myocardial infarction. *Journal of molecular and cellular cardiology***,** (abstract).

Muller JE, Hillis GS, Oh JK, et al. (2003) Left Atrial Volume: A Powerful Predictor of Survival After Acute Myocardial Infarction. *Circulation,* **107,** 2207-2212.

Myers DC, Fishman GI (2003) Molecular and Functional Maturation of the Murine Cardiac Conduction System. *Trends in Cardiovascular Medicine,* **13,** 289-295.

Narayan SM, Krummen DE, Rappel W-J (2012) Clinical Mapping Approach To Diagnose Electrical Rotors and Focal Impulse Sources for Human Atrial Fibrillation. *Journal Of Cardiovascular Electrophysiology,* **23,** 447-454.

National Collaborating Centre for Chronic Conditions (2006) Atrial Fibrillation: National Clinical Guideline for Management in Primary and Secondary Care. In *(NICE Clinical Guidelines, No. 36.)*). (UK) London: Royal College of Physicians (UK).

Nattel S, Maguy A, Le Bouter S, Yeh Y-H (2007) Arrhythmogenic Ion-Channel Remodeling in the Heart: Heart Failure, Myocardial Infarction, and Atrial Fibrillation. *Physiological Reviews,* **87,** 425-456.

NHS (2012) Heart Failure. In *http://www.nhs.uk/conditions/Heart-failure*).

Nielsen E, Smerup M, Agger P, et al. (2009) Normal Right Ventricular Three-Dimensional Architecture, as Assessed with Diffusion Tensor Magnetic Resonance Imaging, is Preserved During Experimentally Induced Right Ventricular Hypertrophy. *The Anatomical Record: Advances in Integrative Anatomy and Evolutionary Biology,* **292,** 640-651.

Nielsen PM, Le Grice IJ, Smaill BH, Hunter PJ (1991) Mathematical model of geometry and fibrous structure of the heart. *American Journal of Physiology - Heart and Circulatory Physiology,* **260,** H1365-H1378.

Nikolaidou T, Aslanidi OV, Zhang H, Efimov IR (2012) Structure-Function Relationship in the Sinus and Atrioventricular Nodes. *Pediatric Cardiology,* **33,** 890-899.

Notomi Y, Popovic ZB, Yamada H, et al. (2008) Ventricular untwisting: a temporal link between left ventricular relaxation and suction. *American Journal of Physiology - Heart and Circulatory Physiology,* **294,** H505-H513.

Okada R, Fukuda K (1981) A histopathological study on the hypertrophy of the atrioventricular conduction system. *Jpn Circ J,* **45,** 441-445.

Opie LH, Commerford PJ, Gersh BJ, Pfeffer MA (2006) Controversies in ventricular remodelling. *The Lancet,* **367,** 356-367.

Paes De Carvaho A, Carlos De Mello W, Hoffman BF (1953) Electrophysiological evidence for specialized fiber types in rabbit atrium. *Am J Physiol,* **196,** 483-8.

Paes De Carvalho A, Carlos De Mello W, Hoffman BF (1953) Electrophysiological evidence for specialized fiber types in rabbit atrium. *Am J Physiol,* **196,** 483-8.

Partridge JB, Anderson RH (2009) Left ventricular anatomy: Its nomenclature, segmentation, and planes of imaging. *Clinical Anatomy,* **22,** 77-84.

Pauwels E, Van Loo D, Cornillie P, Brabant L, Van Hoorebeke L (2013) An exploratory study of contrast agents for soft tissue visualization by means of high resolution X-ray computed tomography imaging. *Journal of Microscopy,* **250,** 21-31.

Pearlman E, Weber K, Janicki J (1981) Quantitative histology of the hypertrophied human heart. *Fed Proc,* **40,** 2042-7.

Pettigrew JB (1864) On the Arrangement of the Muscular Fibres in the Ventricles of the Vertebrate Heart, with Physiological Remarks. *Philosophical Transactions of the Royal Society of London,* **154,** 445-500.

Pogwizd SM (1995) Nonreentrant Mechanisms Underlying Spontaneous Ventricular Arrhythmias in a Model of Nonischemic Heart Failure in Rabbits. *Circulation,* **92,** 1034-1048.

Pogwizd SM, Schlotthauer K, Li L, Yuan W, Bers DM (2001) Arrhythmogenesis and Contractile Dysfunction in Heart Failure: Roles of Sodium-Calcium Exchange, Inward Rectifier Potassium Current, and Residual Î²-Adrenergic Responsiveness. *Circulation Research,* **88,** 1159-1167.

Pope AlJ, Sands GB, Smaill BH, LeGrice IJ (2008) Three-dimensional transmural organization of perimysial collagen in the heart. *American Journal of Physiology - Heart and Circulatory Physiology,* **295,** H1243-H1252.

Racker DK (2000) Consensus Statement from the Cardiac Nomenclature Study Group of Arrhythmias of the European Society of Cardiology, and the Task Force on Cardiac Nomenclature from the North American Society of Pacing and Electrophysiology on Living Anatomy of the Atrioventricular Junctions. *Journal Of Cardiovascular Electrophysiology,* **11,** 1297-1297.

Rademakers FE, Buchalter MB, Rogers WJ, et al. (1992) Dissociation between left ventricular untwisting and filling. Accentuation by catecholamines. *Circulation,* **85,** 1572-81.

Ritman EL (2004) Micro-computed tomography-current status and developments. *Annual Review of Biomedical Engineering,* **6,** 185-208.

Ritman EL (2011) Current Status of Developments and Applications of Micro-CT. *Annual Review of Biomedical Engineering,* **13,** 531-552.

Roberts DE, Hersh LT, Scher AM (1979) Influence of cardiac fiber orientation on wavefront voltage, conduction velocity, and tissue resistivity in the dog. *Circulation Research,* **44,** 701-12.

Roberts LA (1991) The sinoatrial ring bundle: A cardiac neural communication system? *American Journal of Anatomy,* **191,** 250-260.

Rodriguez EK, Hunter WC, Royce MJ, Leppo MK, Douglas AS, Weisman HF (1992) A method to reconstruct myocardial sarcomere lengths and orientations at transmural sites in beating canine hearts. *American Journal of Physiology - Heart and Circulatory Physiology*, **263,** H293-H306.

Roeske WR, O'Rourke RA, Klein A, Leopold G, Karliner JS (1976) Noninvasive evaluation of ventricular hypertrophy in professional athletes. *Circulation,* **53,** 286-91.

Rohmer D, Sitek A, Gullberg GT (2007) Reconstruction and Visualization of Fiber and Laminar Structure in the Normal Human Heart from Ex Vivo Diffusion Tensor Magnetic Resonance Imaging (DTMRI) Data. *Investigative Radiology,* **42,** 777-789 10.1097/RLI.0b013e3181238330.

Rohr S (2012) Arrhythmogenic Implications of Fibroblast-Myocyte Interactions. *Circulation: Arrhythmia and Electrophysiology,* **5,** 442-452.

Rohr S, Kucera JP, Kleber AG (1998) Slow Conduction in Cardiac Tissue, I: Effects of a Reduction of Excitability Versus a Reduction of Electrical Coupling on Microconduction. *Circulation Research,* **83,** 781-794.

Rowlatt U (1990) Comparative anatomy of the heart of mammals. *Zoological Journal of the Linnean Society,* **98,** 73-110.

Russel IK, Gotte MJW, Bronzwaer JG, Knaapen P, Paulus WJ, van Rossum AC (2009) Left Ventricular Torsion: An Expanding Role in the Analysis of Myocardial Dysfunction. *JACC: Cardiovascular Imaging,* **2,** 648-655.

Ruwhof C, van der Laarse A (2000) Mechanical stress-induced cardiac hypertrophy: mechanisms and signal transduction pathways. *Cardiovascular Research,* **47,** 23-37.

Saenger W (1984) The structure of the blue starch-iodine complex. *Naturwissenschaften,* **71,** 31-36.

Sallach JA, Tang WHW, Borowski AG, et al. (2009) Right Atrial Volume Index in Chronic Systolic Heart Failure and Prognosis. *JACC: Cardiovascular Imaging,* **2,** 527-534.

Sallin EA (1969) Fiber Orientation and Ejection Fraction in the Human Left Ventricle. *Biophysical journal,* **9,** 954-964.

Salmons S (1995) Muscle. *In:*. (ed.) *Gray's Anatomy.* 38 ed.). Churchill Livingstone.

Sanchez-Quintana D, Pizarro G, LÃ³pez-MÃnguez JRn, Ho S, Cabrera JA (2013) Standardized Review of Atrial Anatomy for Cardiac Electrophysiologists. *Journal of Cardiovascular Translational Research,* **6,** 124-144.

Sanchez-Quintana D, Wyn Davies D, Yen Ho S, Oslizlok P, Anderson RH (1997) Architecture of the Atrial Musculature In and Around the Triangle of Koch. *Journal Of Cardiovascular Electrophysiology,* **8,** 1396-1407.

Sanchez-Quintana D, Yen Ho S (2003) Anatomy of Cardiac Nodes and Atrioventricular Specialized Conduction System. *Revista Espanola de Cardiologia (English Version),* **56,** 1085-1092.

Sands GB, Gerneke DA, Hooks DA, Green CR, Smaill BH, Legrice IJ (2005) Automated imaging of extended tissue volumes using confocal microscopy. *Microscopy Research and Technique,* **67,** 227-239.

Sands GB, Gerneke DA, Smaill BH, Le Grice IJ (2006) Automated Extended Volume Imaging of Tissue using Confocal and Optical Microscopy. In *Engineering in Medicine and Biology Society, 2006. EMBS '06. 28th Annual International Conference of the IEEE*), pp. 133-136.

Schmid P, Lunkenheimer PP, Redmann K, et al. (2007) Statistical Analysis of the Angle of Intrusion of Porcine Ventricular Myocytes from Epicardium to Endocardium Using Diffusion Tensor Magnetic Resonance Imaging. *The Anatomical Record: Advances in Integrative Anatomy and Evolutionary Biology,* **290,** 1413-1423.

Schmitt B, Fedarava K, Falkenberg J, et al. (2009) Three-dimensional alignment of the aggregated myocytes in the normal and hypertrophic murine heart. *Journal of Applied Physiology,* **107,** 921-927.

Schotten U, Verheule S, Kirchhof P, Goette A (2011) Pathophysiological Mechanisms of Atrial Fibrillation: A Translational Appraisal. *Physiological Reviews,* **91,** 265-325.

Semwogerere D, Weeks ER (2005) Encyclopedia of Biomaterials and Biomedical Engineering. (ed Francis T).

Sengupta PP, Korinek J, Belohlavek M, et al. (2006) Left Ventricular Structure and Function: Basic Science for Cardiac Imaging. *Journal of the American College of Cardiology,* **48,** 1988-2001.

Severs NJ (2000) The cardiac muscle cell. *BioEssays,* **22,** 188-199.

Severs NJ, Bruce AF, Dupont E, Rothery S (2008) Remodelling of gap junctions and connexin expression in diseased myocardium. *Cardiovascular Research,* **80,** 9-19.

Shaw RM, Rudy Y (1997) Ionic Mechanisms of Propagation in Cardiac Tissue: Roles of the Sodium and L-type Calcium Currents During Reduced

Excitability and Decreased Gap Junction Coupling. *Circulation Research,* **81,** 727-741.

Smaill BH, Zhao J, Trew ML (2013) Three-Dimensional Impulse Propagation in Myocardium: Arrhythmogenic Mechanisms at the Tissue Level. *Circulation Research,* **112,** 834-848.

Smerup M, Agger P, Nielsen EA, et al. (2013a) Regional and Epi- to Endocardial Differences in Transmural Angles of Left Ventricular Cardiomyocytes Measured in Ex Vivo Pig Hearts: Functional Implications. *The Anatomical Record,* **296,** 1724-1734.

Smerup M, Nielsen E, Agger P, et al. (2009) The Three-Dimensional Arrangement of the Myocytes Aggregated Together Within the Mammalian Ventricular Myocardium. *The Anatomical Record: Advances in Integrative Anatomy and Evolutionary Biology,* **292,** 1-11.

Smerup M, Partridge J, Agger P, et al. (2013b) A mathematical model of the mechanical link between shortening of the cardiomyocytes and systolic deformation of the left ventricular myocardium. *Technology and Health Care,* **21,** 63-79.

Solti F, Vecsey T, kekesi V, Juhasz-nagy A (1989) The effect of atrial dilatation on the genesis of atrial arrhythmias. *Cardiovascular Research,* **23,** 882-886.

Sonnenblick E (1962) Force-velocity relations in mammalian heart muscle. *Am J Physiol,* **202,** 931-9.

Spach MS, Kootsey JM (1983) The nature of electrical propagation in cardiac muscle. *American Journal of Physiology - Heart and Circulatory Physiology,* **244,** H3-H22.

Spach MS, Miller WT, Dolber PC, Kootsey JM, Sommer JR, Mosher CE (1982) The functional role of structural complexities in the propagation of depolarization in the atrium of the dog. Cardiac conduction disturbances due to discontinuities of effective axial resistivity. *Circulation Research,* **50,** 175-91.

Spiers FW (1946) Effective Atomic Number and Energy Absorption in Tissues. *British Journal of Radiology,* **19,** 52-63.

Spotnitz HM (2000) Macro design, structure, and mechanics of the left ventricle. *The Journal of thoracic and cardiovascular surgery,* **119,** 1053-1077.

Spotnitz HM, Sonnenblick EH, Spiro D (1966) Relation of Ultrastructure to Function in the Intact Heart: Sarcomere Structure Relative to Pressure Volume Curves of Intact Left Ventricles of Dog and Cat. *Circulation Research,* **18,** 49-66.

Stankovicová T, Bito V, Heinzel F, Mubagwa K, Sipido KR (2003) Isolation and morphology of single Purkinje cells from the porcine heart. *Gen Physiol Biophys,* **22,** 329-40.

Stauber M, Mueller R (2008) Micro-computed tomography: A method for the non-destructive evaluation of the three-dimensional structure of biological specimens. In *Methods in Molecular Biology* (ed Westendorf JJ), pp. 273-292. Humana Press Inc.

Stephenson RS, Boyett MR, Hart G, et al. (2012) Contrast Enhanced Micro-Computed Tomography Resolves the 3-Dimensional Morphology of the Cardiac Conduction System in Mammalian Hearts. *PLoS ONE,* **7,** e35299.

Stewart S, MacIntyre K, Hole DJ, Capewell S, McMurray JJV (2001) More 'malignant' than cancer? Five-year survival following a first admission for heart failure. *European Journal of Heart Failure,* **3,** 315-322.

Streeter DD, Bassett DL (1966) An engineering analysis of myocardial fiber orientation in pig's left ventricle in systole. *The Anatomical Record,* **155,** 503-511.

Streeter DD, Spotnitz HM, Patel DP, Ross J, Sonnenblick EH (1969) Fiber Orientation in the Canine Left Ventricle during Diastole and Systole. *Circulation Research,* **24,** 339-347.

Sweeney LJ, Rosenquist GC (1979) The normal anatomy of the atrial septum in the human heart. *Am Heart J,* **98,** 194-199.

Szundi I (1978) The interaction of lipids with iodine in monomolecular films. *Chemistry and Physics of Lipids,* **22,** 153-161.

Tawara S (2000) *The conduction system of the Mammalian heart : an anatomico-histological study of the atrioventricular bundle and the purkinje fibers / S. Tawara ; foreword by L. Aschoff, translated by Kozo Suma, Munehiro Shimada, preface by R. H Anderson,* London : Imperial College Press, c2000.

Thomas JD, Popovic ZB (2006) Assessment of Left Ventricular Function by Cardiac Ultrasound. *Journal of the American College of Cardiology,* **48,** 2012-2025.

Thornell L-E, Sjostrom M, Andersson K-E (1976) The relationship between mechanical stress and myofibrillar organization in heart Purkinje fibres. *Journal of Molecular and Cellular Cardiology,* **8,** 689-695.

Torrent-Guasp F, Kocica MJ, Corno AF, et al. (2005) Towards new understanding of the heart structure and function. *European Journal of Cardio-Thoracic Surgery,* **27,** 191-201.

Tranum-Jensen J, Wilde AA, Vermeulen JT, Janse MJ (1991) Morphology of electrophysiologically identified junctions between Purkinje fibers and ventricular muscle in rabbit and pig hearts. *Circulation Research,* **69,** 429-37.

Trayanova NA (2011) Whole-Heart Modeling: Applications to Cardiac Electrophysiology and Electromechanics. *Circulation Research,* **108,** 113-128.

Tsang TSM, Barnes ME, Gersh BJ, Bailey KR, Seward JB (2002) Left atrial volume as a morphophysiologic expression of left ventricular diastolic dysfunction and relation to cardiovascular risk burden. *The American Journal of Cardiology,* **90,** 1284-1289.

Tseng W-YI, Dou J, Reese TG, Wedeen VJ (2006) Imaging myocardial fiber disarray and intramural strain hypokinesis in hypertrophic cardiomyopathy with MRI. *Journal of Magnetic Resonance Imaging,* **23,** 1-8.

Tunell GL, Hart M (1977) SImultaneous determination of skeletal muscle fiber, types i, iia, and iib by histochemistry. *Archives of Neurology,* **34,** 171-173.

Ueda A, McCarthy KP, Sánchez-Quintana D, Yen Ho S (2013) Right atrial appendage and vestibule: further anatomical insights with implications for invasive electrophysiology. *Europace,* **15,** 728-734.

van Dalen BM, Kauer F, Vletter WB, et al. (2009) Influence of cardiac shape on left ventricular twist. *Journal of Applied Physiology,* **108,** 146-151.

Van Hare GF (2008) Developmental aspects of atrioventricular node reentry tachycardia. *Journal of Electrocardiology,* **41,** 480-482.

Varela M, Zhao J, Aslanidi O, V (2013) Determination of Atrial Myofibre Orientation Using Structure Tensor Analysis for Biophysical Modelling. *FIMH,* 425–432.

Verkerk AO, Wilders R, Coronel R, Ravesloot JH, Verheijck EE (2003) Ionic Remodeling of Sinoatrial Node Cells by Heart Failure. *Circulation,* **108,** 760-766.

Vesalius A (1544) De humani corporis fabrica.). Basel: New York: The Metropolitan Museum of Art.

Vickerton P, Jarvis J, Jeffery N (2013) Concentration-dependent specimen shrinkage in iodine-enhanced microCT. *Journal of Anatomy,* **223,** 185-193.

Vigmond EJ, Clements C (2007) Construction of a Computer Model to Investigate Sawtooth Effects in the Purkinje System. *Biomedical Engineering, IEEE Transactions on,* **54,** 389-399.

Wang G, Vannier M (2001) Micro-CT scanners for biomedical pplications : an overview. *Adv Imaging***,** 18-27.

Wang K, Ho SY, Gibson DG, Anderson RH (1995) Architecture of atrial musculature in humans. *British Heart Journal,* **73,** 559-565.

Wedeen VJ, Rosene DL, Wang R, et al. (2012a) The Geometric Structure of the Brain Fiber Pathways. *Science,* **335,** 1628-1634.

Wedeen VJ, Rosene DL, Wang R, et al. (2012b) Response to comment on "the geometric structure of the brain fiber pathways". *Science,* **337,** 1605.

Weninger W, Geyer S, Mohun T, et al. (2006) High-resolution episcopic microscopy: a rapid technique for high detailed 3D analysis of gene activity in the context of tissue architecture and morphology. *Anatomy and Embryology,* **211,** 213-221.

Wise LD, Winkelmann CT, Dogdas B, Bagchi A (2013) Micro-computed tomography imaging and analysis in developmental biology and toxicology. *Birth Defects Research Part C: Embryo Today: Reviews,* **99,** 71-82.

Wisse E, Braet F, Duimel H, et al. (2010) Fixation methods for electron microscopy of human and other liver. *World journal of gastroenterology : WJG,* **16,** 2851-2866.

Xie Y, Sato D, Garfinkel A, Qu Z, Weiss JN (2010) So Little Source, So Much Sink: Requirements for Afterdepolarizations to Propagate in Tissue. *Biophysical journal,* **99,** 1408-1415.

Yamazaki M, Mironov S, Taravant Cm, et al. (2012) Heterogeneous atrial wall thickness and stretch promote scroll waves anchoring during atrial fibrillation. *Cardiovascular Research,* **94,** 48-57.

Yanni J, Boyett MR, Anderson RH, Dobrzynski H (2009a) The extent of the specialized atrioventricular ring tissues. *Heart rhythm : the official journal of the Heart Rhythm Society,* **6,** 672-680.

Yanni J, Tellez JO, MÄ…czewski M, et al. (2011) Changes in Ion Channel Gene Expression Underlying Heart Failure-Induced Sinoatrial Node Dysfunction. *Circulation: Heart Failure,* **4,** 496-508.

Yanni JF, Yamanushi TT, Dobrzynski H, Boyett MR (2009b) Remodelling of the extracellular matrix in the rat sinoatrial node in congestive heart failure. In *Proc Physiol Soc 15*). University College Dublin.

Yin RY, Gabriel OV, Pratt RH (1987) High-energy atomic photoelectric effect and bremsstrahlung. *Physical Review A,* **36,** 1207-1219.

Yohe HC, Rosenberg A (1972) Interaction of triiodide anion with gangliosides in aqueous iodine. *Chemistry and Physics of Lipids,* **9,** 279-294.

Young AA, Imai H, Chang CN, Axel L (1994a) Two-dimensional left ventricular deformation during systole using magnetic resonance imaging with spatial modulation of magnetization. *Circulation,* **89,** 740-52.

Young AA, Kramer CM, Ferrari VA, Axel L, Reichek N (1994b) Three-dimensional left ventricular deformation in hypertrophic cardiomyopathy. *Circulation,* **90,** 854-67.

Yu X, Houtman C, Atalla RH (1996) The complex of amylose and iodine. *Carbohydrate Research,* **292,** 129-141.

Zhang Y, Bharati S, Mowrey KA, Zhuang S, Tchou PJ, Mazgalev TN (2001) His Electrogram Alternans Reveal Dual-Wavefront Inputs Into and Longitudinal Dissociation Within the Bundle of His. *Circulation,* **104,** 832-838.

Zhao J, Butters TD, Henggui Z, LeGrice IJ, Sands GB, Smaill BH (2013a) Image-Based Model of Atrial Anatomy and Electrical Activation: A Computational Platform for Investigating Atrial Arrhythmia. *Medical Imaging, IEEE Transactions on,* **32,** 18-27.

Zhao J, Butters TD, Zhang H, et al. (2012) An Image-Based Model of Atrial Muscular Architecture: Effects of Structural Anisotropy on Electrical Activation. *Circulation: Arrhythmia and Electrophysiology,* **5,** 361-370.

Zhao J, Smaill BH, Pullan AJ (2009) A computer study of the effects of branching dimension on safety factor distribution and propagation in a cardiac conduction network. In *Engineering in Medicine and Biology Society, 2009. EMBC 2009. Annual International Conference of the IEEE*), pp. 3278-3281.

Zhao J, Stephenson RS, Sands GB, et al. (2013b) Atrial Fibrosis and Atrial Fibrillation: A Computer Simulation in the Posterior Left Atrium. *FIMH,* 400–408.

Zicha S, Fernández-Velasco M, Lonardo G, L'Heureux N, Nattel S (2005) Sinus node dysfunction and hyperpolarization-activated (HCN) channel subunit remodeling in a canine heart failure model. *Cardiovascular Research,* **66,** 472-481.

Zile MR, Brutsaert DL (2002a) New Concepts in Diastolic Dysfunction and Diastolic Heart Failure: Part I: Diagnosis, Prognosis, and Measurements of Diastolic Function. *Circulation,* **105,** 1387-1393.

Zile MR, Brutsaert DL (2002b) New Concepts in Diastolic Dysfunction and Diastolic Heart Failure: Part II: Causal Mechanisms and Treatment. *Circulation,* **105,** 1503-1508.

Zysk AM, Garson AB, Xu Q, et al. (2012) Nondestructive volumetric imaging of tissue microstructure with benchtop x-ray phase-contrast tomography and critical point drying. *Biomed. Opt. Express,* **3,** 1924-1932.

Appendix

LVPW

REGION	BASE											
INTERVAL	2						3					
	Transmural		Transmural mid-wall		Endocardium		Transmural		Transmural mid-wall		Endocardium	
	Inc. Angle	Trans. Angle	Inc. Angle	Trans. Angle	Inc. Angle	Trans. Angle	Inc. Angle	Trans. Angle	Inc. Angle	Trans. Angle	Inc. Angle	Trans. Angle
CONTROL	0.287±0.00	1.477±0.06	0.200±0.04	1.342±0.018	0.476±0.03	1.688±0.10	0.301±0.00	1.471±0.05	0.183±0.03	1.518±0.03	0.516±0.06	1.675±0.07
HF	0.450±0.00	1.573±0.06	0.369±0.03	1.534±0.05	0.699±0.03	1.698±0.13	0.423±0.00	1.401±0.10	0.423±0.05	1.489±0.06	0.651±0.06	1.346±0.10
P value	p=0.002		p=0.006		p=0.001		p=0.014		p=0.002		p=0.091	p=0.018

IVS

REGION	BASE							
INTERVAL	2				3			
	Transmural		Transmural mid-wall		Transmural		Transmural mid-wall	
	Inc. Angle	Trans. Angle	Inc. Angle	Trans. Angle	Inc. Angle	Trans. Angle	Inc. Angle	Trans. Angle
CONTROL	0.383±0.00	1.136±0.24	0.281±0.01	1.242±0.24	0.325±0.02	1.624±0.18	0.209±0.02	1.618±0.11
HF	0.441±0.03	1.302±0.10	0.343±0.04	1.301±0.15	0.407±0.01	1.321±0.12	0.331±0.03	1.325±0.15
	p=0.08				p=0.02	p=0.10	p=0.01	p=0.08

Fibre orientation analysis in the base of the failing heart- Tables showing the mean±SEM for mean inclination and transverse angles in the region of the base in control and heart failure samples. Means are calculated from the total transmural width, transmural mid-wall and endocardium. P-values are stated when significance or close to significance is reached. (n=5). LVPW- left ventricular posterior wall, IVS interventricular septum.

Published papers appended

Stephenson RS, Boyett MR, Hart G, et al. (2012) Contrast Enhanced Micro-Computed Tomography Resolves the 3-Dimensional Morphology of the Cardiac Conduction System in Mammalian Hearts. *PLoS ONE,* **7,** e35299.

Jeffery NS, **Stephenson RS**, Gallagher JA, Jarvis JC, Cox PG (2011) Micro-computed tomography with iodine staining resolves the arrangement of muscle fibres. *Journal of Biomechanics,* **44,** 189-192.

Jarvis J, **Stephenson RS.** (2013) Studying the microanatomy of the heart in 3 dimensions: a practical update. *Frontiers in Paediatric Cardiology,* doi: 10.3389/fped.2013.00026.

Zhao J, **Stephenson RS**, Sands GB, et al. (2013) Atrial Fibrosis and Atrial Fibrillation: A Computer Simulation in the Posterior Left Atrium. *FIMH,* 400–408.

Aslanidi O, Nikolaidou T, Zhao J, Smaill BH, Gilbert SH, Holden AV, Lowe T, Withers PJ, **Stephenson RS**, et al. (2012) Application of Micro-Computed Tomography with Iodine Staining to Cardiac Imaging, Segmentation and Computational Model Development. Medical Imaging, IEEE Transactions on, 32(1):8-17.

This text box is where the unabridged thesis included the following third party copyrighted material:

Stephenson RS, Boyett MR, Hart G, et al. (2012) Contrast Enhanced Micro-Computed Tomography Resolves the 3-Dimensional Morphology of the Cardiac Conduction System in Mammalian Hearts. *PLoS ONE,* **7,** e35299. DOI: 10.1371/journal.pone.0035299

This text box is where the unabridged thesis included the following third party copyrighted material:

Jeffery NS, **Stephenson RS**, Gallagher JA, Jarvis JC, Cox PG (2011) Micro-computed tomography with iodine staining resolves the arrangement of muscle fibres. *Journal of Biomechanics,* **44,** 189-192.
http://dx.doi.org/10.1016/j.jbiomech.2010.08.027

This text box is where the unabridged thesis included the following third party copyrighted material:

Jarvis J, **Stephenson RS.** (2013) Studying the microanatomy of the heart in 3 dimensions: a practical update. *Frontiers in Paediatric Cardiology,* doi: 10.3389/fped.2013.00026.

This text box is where the unabridged thesis included the following third party copyrighted material:

Zhao J, **Stephenson RS**, Sands GB, et al. (2013) Atrial Fibrosis and Atrial Fibrillation: A Computer Simulation in the Posterior Left Atrium. *FIMH***,** 400–408.
DOI: 10.1007/978-3-642-38899-6_47

This text box is where the unabridged thesis included the following third party copyrighted material:

Aslanidi O, Nikolaidou T, Zhao J, Smaill BH, Gilbert SH, Holden AV, Lowe T, Withers PJ, **Stephenson RS**, et al. (2012) Application of Micro-Computed Tomography with Iodine Staining to Cardiac Imaging, Segmentation and Computational Model Development. Medical Imaging, IEEE Transactions on, 32(1):8-17.
DOI: 10.1109/TMI.2012.2209183